DEDICATED TO MY PARENTS

VARIATION OF SHEET METAL FORMABILITY IN BIAXIAL STRETCHING PROCESSES

VARIATION OF SHEET METAL FORMABILITY IN BIAXIAL STRETCHING PROCESSES

by

HUYNH VAN MINH, M.Eng.

A Thesis

Submitted to the School of Graduate Studies

in Partial Fulfillment of the Requirements

for the Degree

Doctor of Philosophy

McMaster University

March 1974

DOCTOR OF PHILOSOPHY (1974) McMASTER UNIVERSITY
(Mechanical Engineering) Hamilton, Ontario.

TITLE: Variation of Sheet Metal Formability in Biaxial Stretching Processes

AUTHOR: Huynh Van Minh, B. Eng. (McGill University)
M. Eng. (McMaster University)

SUPERVISOR: Dr. J. L. Duncan

NUMBER OF PAGES: xix, 247

SCOPE AND CONTENTS:

The deformation of circular and elliptical steel diaphragms subjected to hydrostatic pressure is investigated and the different modes of failure of these diaphragms are analysed and compared.

An experimental program is carried out to determine the inherent variability of the forming-limit curves where a number of samples from different grades of deep drawing quality steel are hydrostatically bulged to failure. A quantitative metallographic analysis is also performed in an effort to establish a relationship between microstructural parameters and formability.

A hypothetical model of ductile fracture is proposed to predict the formability of a sheet which contains a population of voids and is subjected to a non-uniform biaxial straining process. A simulation process is developed for this model using the Marciniak analysis and the extreme value theory. Numerical solutions are obtained to show the influence of material defect parameters and process variables on the distribu-

tion of forming limits. Theoretical results are then compared with the experimentally determined forming limit curves.

RÉSUMÉ

Variation dans la Formabilité des Tôles Minces Soumises à une Expansion Biaxiale

La déformation de diaphragmes en acier, de formes circulaire et elliptique, soumis à une pression hydrostatique, ainsi que les divers modes d'échecs de ces diaphragmes ont été analysés et comparés.

On a réalisé un programme expérimental pour déterminer la variation intrinsèque des courbes limites de formage lorsque des échantillons de différents types d'aciers, de qualité emboutissage, sont soumis à une expansion hydrostatique jusqu'à rupture. Une analyse micrographique quantitative a été effectués afin de tenter d'établir un relation entre les caractéristiques de la microstructure et la formabilité.

Un modèle hypothétique de rupture ductile est proposé pour prédire la formabilité d'une tôle contenant une population de cavités et soumise à des déformations biaxiales non-uniformes. Un "processus de simulation" est developpé pour ce modèle à partir de l'analyse de Marciniak et de la théorie de "la valeur extrême". Des solutions ont été calculées pur faire ressortir l'influence des caractéristiques des défauts du matériau et des variables du procédé sur la distribution des limites de formage. Ces résultats théoriques ont été comparés aux courbes limites de formage obtenues expérimentalement.

ACKNOWLEDGEMENTS

The author would like to express his sincere thanks to Dr. J. L. Duncan for his continuous guidance and support throughout the course of this work. His understanding and helpfulness, not only in academic work but also in personal matters, is very much appreciated.

The author is also grateful to Dr. R. Sowerby for his valuable suggestions and assistance in analysing the problems encountered in this thesis.

Thanks are also due to Dr. G. Montgomery of the Steel Company of Canada for his suggestion of the replica technique as well as his expert advice on the metallurgical aspect of sheet steels.

The author is also thankful to the Steel Company of Canada for the supplying of the material and the assistance in performing the quantimet analysis.

Thanks are extended to Mr. John Hiam of the Dominion Foundries and Steel Company for his useful discussion on the influence of microstructure on sheet formability and especially for his help in obtaining the photo micrographs.

The material supplied and various assistance from the Dominion Foundries and Steel Company is gratefully acknowledged.

The author is also indebted to Professor W. R. Newcombe, Dr. B. Latto and Dr. A. E. Hamielec for their constructive criticism of this work.

Assistance from friends and colleagues to make this thesis possible is greatly appreciated,

Thanks are also due to Ms. B. A. Bedell for her expert typing of the manuscript.

The financial support of this work by both the National Research Council of Canada and the Mechanical Engineering Department of McMaster University is gratefully acknowledged.

TABLE OF CONTENTS

LIST OF SYMBOLS

a, b	Half-major and minor axes of the ellipse
A	Area
B_1, B_2	Limit-strain parameters (Equation 5.8)
C	Constants
D	Diameter
e	Engineering strain
E	Projected limit-strain vector on mean strain path
f_o	Inhomogeneity factor (t_B/t_A)
g	Distribution function
h	Dome height
ℓ	Length
F,G,H,L,M,N	Parameters characteristic of the anisotropy in Hill's model
m	Strain-rate sensitivity index
n	Strain-hardening index
N	Number
p	Pressure
P	Force
R	Coefficient of normal anisotropy
r	Radial distance
r_e	Radial distance to edge
$\bar{R}$	Average coefficient of normal anisotropy
ΔR	Coefficient of planar anisotropy
s	Critical subtangent
S	Standard deviation
t	Thickness

t_A , t_B	Thickness in adjacent zone and groove
X, Y, Z	Yield stresses in principal directions of anisotropy
Q, S, T	Yield stresses in shear with respect to the principal directions of anisotropy
(x,y), (u,v)	Cartesian coordinate systems
V	Volume fraction
w	Width
α	Stress ratio (σ_2/σ_1)
α'	Strain ratio (ϵ_2/ϵ_1)
β_1, β_2	Strain profile parameters (Equation 5.11)
γ	Probability level ($0<\gamma<1$)
Γ	Distribution function of elemental areas (Equation 5.10).
δ	Spatial defect density
ϵ	Natural strain
$\bar{\epsilon}$	Representative (or equivalent) strain
ϵ_t	Limit thickness strain
ϵ_{tm}	Thickness strain at the reference point
η	Student "t" statistics
θ	Angle
λ	Defect size distribution parameter (Equation 5.1)
ρ	Radius of curvature
σ	Principal stress
$\bar{\sigma}$	Representative (or effective) stress
τ	Shear stress
χ^2	Chi-square statistics
Ω	Uniformly distributed random number
ϵ_f	Fracture strain in thickness direction

Subscripts

a, b	Major and minor axes of the ellipse
o	Original state
x, y, z	Principal directions of anisotropy
xy, yz, zx	z, x and y planes
θ	Angle of inclination to the rolling direction
r, t	Radial and tangential direction
1, 2, 3	Principal directions of stress and strain
0, 45, 90	0, 45 and 90 degrees with respect to the rolling direction

Superscripts

*	Extreme or critical value

LIST OF FIGURES

CHAPTER 1

INTRODUCTION

Conversion of sheet metal into useful shapes at the least cost is the prime interest of press shops. Pressing operations normally involve a large plastic deformation of the sheet by stretching, drawing or by a combination of the two processes. The most critical problem encountered in these operations is the failure of the part due to the exhaustion of ductility of the material during the straining process. To predict failure, various testing methods such as fundamental property tests and simulative tests have been devised to assess the formability of a material for a particular forming operation. However, any one of these tests, by itself, cannot sufficiently predict how the material would behave under general pressing conditions. Recently, a concept of forming limit curve, proposed by Keeler [1.1] and Goodwin [1.2] and deriving from earlier work by Keeler and Backofen [1.3] has received appreciable attention in sheet metal industries. The premise behind this curve is that in a particular proportional straining process, there is a unique combination of maximum principal strains beyond which failure is imminent. The combination of maximum principal strains plotted in the principal strain diagram for various strain ratios defines the forming limit curve which can be applied to the failure

analysis of sheet metal in industrial pressings.

The forming-limit curve can be obtained by measuring the maximum uniform strains (or the limit strains) in sheets which are biaxially stretched to failure in different proportional straining processes. It has also been suggested that this can be predicted by using the instability criteria. The curve so obtained is normally regarded as a unique function of material properties. However, as proposed by Marciniak [1.4], failure of a material in a straining process is dependent on the severity of material inhomogeneity which, in turn, is subjected to a certain statistical variation; thus for a particular strain ratio, the forming limit cannot be described by a single value parameter but as a statistical quantity whose distribution depends on the severity, and distribution, of the inhomogeneity. Furthermore, the measured limit strains can be influenced by the testing method; it is observed that in regions of critical straining where there is a strain gradient, rupture does not necessarily occur at the point of maximum strain but can occur at points having a significantly lower strain. In addition, it is observed that in materials of apparently similar properties and deformed at similar strain ratios, the mean forming limit is effected by material thickness and overall strain gradient in the region.

The objective of this work is to investigate the inherent variability in measured limit strains and to study the influence of material defects as well as the process

variables on the forming-limit curves. This is carried out in three main divisions:

First, an experimental investigation of the hydrostatic bulging of elliptical diaphragms is made to study the feasibility of this process as a means of establishing the forming limit curves. The deformation of steel diaphragms in various elliptical dies is examined in terms of bulge profiles, strain paths and strain profiles. A theoretical prediction of failure in these diaphragms is also derived and the different modes of failure are then compared.

The second step is to determine the inherent variability of the experimentally established forming-limit curves for various materials. A distribution of forming-limits for a particular strain ratio is obtained from strain measurements on a number of diaphragms hydrostatically bulged to fracture in a certain elliptical die. The procedure is repeated for various elliptical dies and for different orientations of the rolling direction of the sheet with respect to the axis of the die. From these results, a comparison of the distributions of forming limits between various materials as well as between different strain ratios is made. A quantitative metallographic analysis is also carried out to relate the microstructure of the tested materials with their formabilities.

The third step in this work involves the proposal of a fracture model to explain the inherent variation of the forming-limit curves and also the influence of material thickness and strain gradient in the critical region. In this hypothesis, it is assumed that defects in the material are characterized by an equivalent population of voids existing at the start of the straining process. The population of these voids can be described by a constant spatial density and an exponential size distribution. It is also postulated that the inherent limit strain of an elemental area of the sheet is determined by the largest defect in that element. The distribution of limit strains in an infinite number of elements can then be determined using the theory of extreme value and the Marciniak analysis.

The deformation process considered in the analysis is a proportional straining process in which the critical area of straining is taken as being composed of a finite number of elements. A strain gradient exists everywhere in the critical region, and the strain level in each element is defined as a simple function of both the maximum strain in the region and the distance from the point of maximum strain.

A simulation technique is developed to determine the failure point in the region taking into account the overall strain gradient in the region, and the limit strain for the particular case is calculated. The procedure is repeated for a number of specimens and a frequency distribution of limit strains is established.

Numerical results are presented to demonstrate the effect of defect parameters, defect volume fraction, strain gradient and sheet thickness on the distribution of forming limits.

The analysis is then applied to simulate the hydrostatic bulging of elliptical diaphragms to predict the distribution of forming limits in mild steels in this particular process and the results are compared with the experimental data.

CHAPTER 2

FORMABILITY OF SHEET METALS - REVIEW

2.1. Historical Background

Formability can be defined as the ability of a material to be shaped into a particular configuration or design through a plastic deformation. During the past 50 years, various efforts have been made to devise a reliable means to assess this elusive quantity as applied to general sheet metal forming problems.

Empirical attempts to relate material properties to press performance have been made since the early days of pressing industry when Bessemer's converter steel had been drawn to cups [2.1]. Scientific analysis of press-forming operations was probably originated by Musiol [2.2] who first recognized the limiting-drawing ratio as a criterion for deep drawability. Another attempt to encompass material properties in the analysis of cup-drawing mechanics was the introduction of the concept of yield stress [2.3] into the calculation of drawing force. No advancement, however, could be made in relating material properties to drawability until the importance of anisotropic behaviour in material was fully recognized.

The observation of ear formation in cup-drawing led to the concept of directionality in sheet metal. Wilson

and Brick [2.4] demonstrated that earing would be expected to arise from preferred crystallographic orientation, and later Baldwin et al. [2.5] showed that this material behaviour could be observed in tensile tests. A study of plastic flow in anisotropic sheet steels was undertaken by Jackson et al. [2.6] where the stress-strain relationships between the tensile and hydrostatic bulge tests were compared. They found that the ratio of the width to thickness strain in tensile specimens was different for different materials and, in some instances, dependent upon the orientation of the specimen in relation to the rolling direction of the sheet.

The well known investigation by Lankford et al. [2.7] on the influence of material anisotropy on press performance set a landmark in the technology of sheet metal forming. In this work they indicated that a combination of favorable plastic anisotropy (which promotes resistance to thinning) and favorable strain-hardening characteristics gave good press performance. Whiteley [2.8], a few years later, illustrated the three dimensional effect of directionality and showed that there was a correlation between the limiting blank diameter for a small cupping press and the normal plastic anisotropy. He also demonstrated that anisotropic behaviour rather than material strength or ductility governs the deep drawability of the part.

Press operation normally consists not only of pure drawing but also of stretching or of a combination of the two. In pure stretching or in an operation where stretching predominates, Nelson and Winlock [2.9] found that the behaviour

of the sheet varies with the strain hardening capacity of the material. For steels, the strain-hardening capacity can be defined by the strain-hardening index. A subsequent series of experiments sponsored by ASTM committee E-26 [2.10] were carried out to correlate the press performance of steel sheets with the normal plastic anisotropy and the strain-hardening index. The results obtained from about one thousand stampings showed that press performance correlates best with normal anisotropy when the drawing operation is predominant; on the other hand, materials with high n-value performed better in forming operations which require mainly stretching.

A major contribution to the assessment of formability in sheet steels was made by Keeler [1.1]. He developed the concept of a limiting-strain curve (or forming-limit curve) in biaxial stretching and demonstrated that the incipient fracture is related to the biaxial major and minor strain in a unit area. He also showed that this curve can be applied to commercial stamping processes [2.11 to 2.13]. The original curve was generated primarily from the failure strain data of production stampings and laboratory tests of 20 gage low carbon steel sheets. It was shown that this curve applied to most ductile metals [1.3]. Subsequent work has been concentrated on the forming-limit curve as a diagnostic tool in press shops [2.13 to 2.15] and numerous studies of the effect of material parameters on the forming-limit curves have been conducted [2.15 to 2.21].

2.2. Methods of Assessing Sheet Metal Formability

The causes of failure in complex pressings of sheet metal are myriad, and neither the plastician nor the metallurgist has been completely successful in correlating the press performance with the mechanical properties or microstructural parameters of the material. There is a necessity, therefore, for a method predicting or evaluating the formability in a single, simple meaningful test. Tests for formability in this respect can be divided roughly into two main groups: "fundamental" and "simulative". The "fundamental" test is one which can be used to determine the fundamental properties of the material, while the "simulative" type of test is one which appears to be similar to the process that the sheet is expected to undergo.

2.2.1. Fundamental Tests

The most popular test in the fundamental group is the Rockwell hardness test. The reason for the popularity of this test is its simplicity; however, it serves only as a quality control test. In press forming research, the tensile test is probably the most important among the non-simulative tests. A variety of parameters derived from this test have been suggested as indicative of different aspects of press formability [2.22 and 2.23]. These include ultimate tensile strength, ratio of yield stress to ultimate tensile strength, uniform elongation, total elongation, circle-arc elongation, strain-hardening index and the normal anisotropy coefficient.

Several of the parameters derived from the tensile test are open to criticism if employed in any fundamental investigation. For instance, total elongation figures depend very much upon the geometry of the tensile test piece, and the ultimate tensile strength has very little meaning at all for ductile materials as it is based on the initial cross-section area of the specimens.

A disadvantage of the tensile test is that the total amount of deformation is limited by the tensile instability. However, it is fairly simple and straightforward and provides a means of assessing the two important parameters for formability: anisotropy coefficient and strain-hardening index.

a) Coefficient of Normal Anisotropy

Normal anisotropy refers to the difference between the stress-strain curves in the through-thickness direction and in the plane of the sheet while planar anisotropy indicates the variation of the stress-strain curves with orientation in the plane of the sheet.

The normal anisotropic coefficient is determined from the ratio of width to thickness strain for different orientations of the tensile test pieces to the rolling direction, i.e., $R = \frac{\ln (w/w_o)}{\ln (t/t_o)}$, where w_o and w are the original and current widths, and t_o and t are the original and current thicknesses respectively. As R is generally dependent on the orientation of the test piece, an average R-value for a given sheet is generally expressed as $\bar{R} = \frac{1}{4} (R_0 + 2R_{45} + R_{90})$ where the subscript refers to the angle of inclination of the test piece

with respect to the rolling direction. The planar anisotropy coefficient, in contrast, is defined by $\Delta R = \frac{1}{2}(R_0 + R_{90} - 2R_{45})$.

To find R-values, the early investigators [2.5 to 2.7] measured the thickness strain directly and it was reported that the R value varies along the gage length of the test piece. This inconsistency in the results is probably due to the inaccuracy in measuring the variation in thickness. Burns and Heyer's approach [2.24] was to avoid direct measurement of the thickness. By assuming constant volume throughout straining, the thickness strain can be calculated from the gage length measurement, and the coefficient of normal anisotropy was redefined as

$$R = \frac{\ln\left(\frac{w}{w_o}\right)}{\ln\left(\frac{w_o \ell_o}{w \ell}\right)}$$

where ℓ_o and ℓ are the original and current gage lengths respectively. This approach was adopted by Whiteley [2.8] and Atkinson and MacLean [2.25].

Variation of strain-ratio with the amount of straining of metals such as zinc and magnesium are well documented [2.26 and 2.27]. However, there is no clear indication of the manner in which R value may vary during the tensile tests of steel sheets. Upon further examination of this point, Atkinson and MacLean [2.25] suggested that average values of R may fall slightly in the strain range from 10 to 20% extension. (Elongation of more than 10% was recommended by the IDDRG conference at Liège in 1966 for mild steels).

There is no evidence that R values depend on strain rate, however, it is generally found that the R value for a specimen inclined at 45 degrees to the rolling direction of the sheet is less than that for any other direction. Bramley and Mellor [2.28] have also shown that even for steel sheets having similar R values at 0, 45 and 90 degrees, the distribution of R values between these angles can vary from sample to sample.

b) Strain-Hardening Index

The strain-hardening index is derived from the Ludwik relation, $\bar{\sigma} = \sigma_o \bar{\varepsilon}^n$ ($\bar{\sigma}$ and $\bar{\varepsilon}$ are true stress and true strain and σ_o and n are constants). This relationship is assumed to be a reasonable approximation of the stress and strain relationships of a wide range of metals and alloys. To determine n, stress and strain data are normally obtained from tensile tests and are plotted on a log-log scale. The value of n is then given by the slope of the curve.

Some recently developed testing techniques produce a value for n which is related to (but not equal to) the uniform elongation. One such method is the circle-arc elongation developed by Heyer and Newby [2.29]. The method requires a two-step tensile specimen or a tensile specimen with a slightly reduced cross-section. The major advantage of this is that no load elongation measurement is required during testing; the desired value is read directly from the broken specimen without calculation.

As with most properties, the n-values are influenced by testing technique, testing speed and the orientation of the tensile specimen with respect to the rolling direction. Bramley and Mellor [2.28] have shown that for steel exhibiting normal anisotropy, the value of n for the through-thickness direction may be different from that in the plane of the sheet.

Apart from the tensile tests, different laboratory tests have been devised to measure the plastic anisotropy and the strain-hardening characteristic of the material in various straining processes. The deformation of a circular diaphragm in a hydrostatic bulging process has been used to determine the strain-hardening characteristic of the material in balanced biaxial tension [2.30]. The same method can be utilized to derive the anisotropy coefficient. This was discussed in Reference [2.31].

A method of measuring n in pure shear deformation was developed by Metsis [2.32]. In this work, an in-plane torsion test was employed and the stress-strain characteristic was determined for a circular ring at different angles of twist. Marciniak [2.33] later devised an apparatus to measure directly the strain-hardening index of sheets tested in in-plane torsion and he found that there was a significant correlation between the results obtained and the n-values from tensile tests.

2.2.2. Simulative Tests

A large number of simulative tests have been designed for assessing the likely performance of sheet metal in press work. These can be divided into three main groups depending on the straining components of the operation: deep drawing, stretch forming and a combination of the two.

a) Deep-Drawing Tests

The Swift flat-bottomed cup drawing and Sach's wedge draw test are commonly used to simulate deep drawing, however, Swift's version is the best known in cup drawing tests.

Swift Cupping Test This test is used to determine the limiting drawing ratio (LDR) which can be correlated with the average value of the normal anisotropy ($\bar{R}$) for a material. This ratio is defined as the ratio of the largest successfully drawn blank diameter (D_c) to punch diameter. As there exists a diameter range within which blanks may break or may not break, the value of D_c is often defined as the diameter giving a particular proportion of successful draws, e.g., 90%.

The first significant attempt to deduce the influence of anisotropy on deep drawability appears to be Whiteley's work [2.8]. Whiteley demonstrated a correlation of normal plastic anisotropy and LDR for a Swift cupping press fitted with a 50-mm. flat nosed punch and dies designed according to BISRA specifications [2.34]. However, the dispersion of Whiteley's results was too wide to encourage the view that

anisotropy could be measured by the cupping test. Atkinson and MacLean [2.25] used thin polythene sheet to minimize friction and in a series of Swift flat-bottomed cupping tests on mild steels, showed that the manifestation of normal anisotropy in such tests is commonly masked by friction. They indicated that when the friction is reduced, $\bar{R}$ can be predicted from the LDR with an accuracy comparable to that of direct measurement, i.e., tensile tests. Figure 2.1 shows the relationship between limiting blank diameter and the normal anisotropy coefficient for different lubricants.

Engelhardt Test - An alternative method of assessing deep drawing performance which is now gaining popularity is the determination of maximum drawing load in relation to fracture load for flat-bottomed cup drawing. It was demonstrated by Schmidt [2.35] that the maximum drawing load (P_{max}) increases with blank diameter (D) until it coincides with the fracture load at the critical blank diameter. It is necessary, therefore, only to determine the fracture load and the slope of the P_{max} versus D curve to predict the critical blank diameter. This requires only 3 tests in total.

Recently Engelhardt has attempted to construct a simulative drawing test which needs only one blank size. The blank size in the test is much smaller than the critical one for the common deep drawing materials. The test is usually performed in a special hydraulic testing machine called TZP. This machine cuts a blank which is then automatically drawn into a cup. When the maximum drawing force is reached,

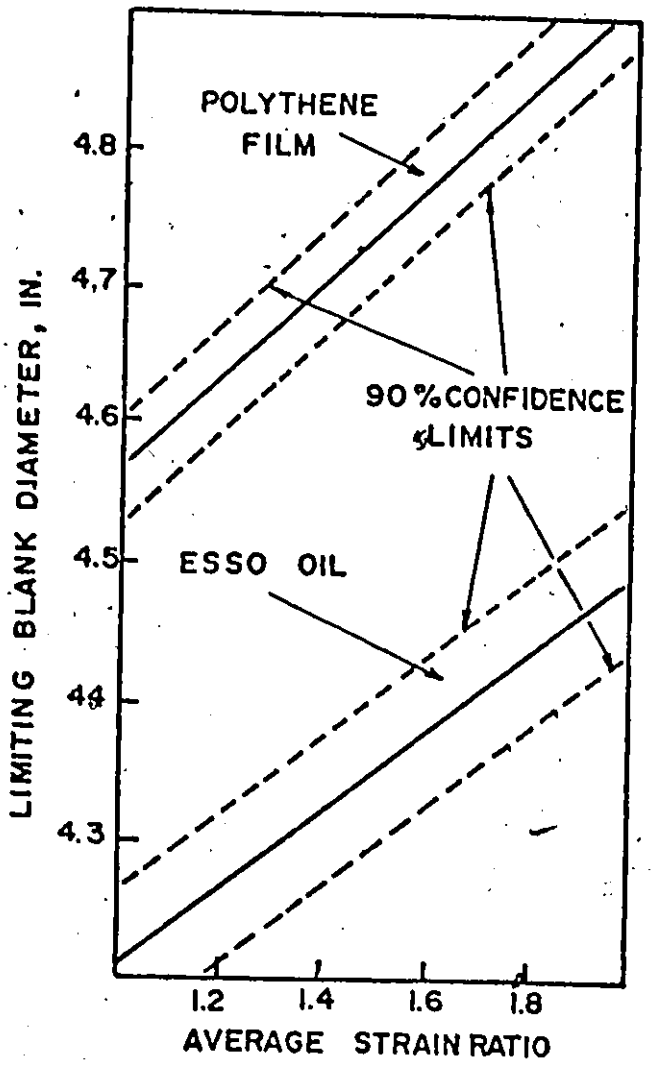

Figure 2.1. Relationship between Limiting Blank Diameter and Average Strain Ratio for Polythene Film Lubrication and Esso Oil TSD 926 Lubrication [2.25].

a second blank-holder is activated and clamps the ring section of a partly drawn cup so that there is no slip in the rim of the cup when the punch continues to move. The maximum drawing force (P_{max}) and the fracture load (P_f) are measured, and the T value is defined as

$$T = \frac{P_f - P_{max}}{P_f} \times 100\%$$

This indicates the load magnitude relative to the fracture load at the chosen drawing ratio.

This method offers the prospect of a simple testing procedure that can be used to evaluate normal anisotropy from one test result, however, the result may depend to a certain extent on the strain-hardening index [2.36].

b) Stretch-Forming Tests

The most common stretch-forming tests used in the press-shops are the Erichsen and Olsen tests in which punches of hemispherical ends are pressed into a securely clamped sheet. Circular hydrostatic bulge tests can also be classified in this category. The important indices in these tests are the height of the cup in the case of the cupping test and the depth of the cap (or circumspherential strain) in the case of the circular-bulge test. Heyer and Newby [2.37] studied the stretch forming of sheets using punches with ball ends of different diameters and found that improving lubrication or lowering the plastic strain ratio (R) had the similar effect of increasing the cup height at fracture. They also

observed that materials with a high strain-hardening capacity distribute the strain more uniformly and therefore had better biaxial stretchability.

c) Combination of Stretching and Drawing Tests

The combined stretching and drawing operation is simulated in the Fukui conical cup test. This test is based on forcing a disc of sheet metal into a cone with a hemispherical punch. Sheet clamping is not required in the test and the parameter measured is the average diameter of the base of the drawn cup at fracture.

Goodwin [2.38] has derived a "formability index" from a modified Fukui test where the index is based on the cup height or punch travel, and he showed that this quantity is related to the product of uniform elongation (or strain-hardening index) and the minimum value of strain ratio.

The value of the simulative tests lies in the ability to investigate the characteristics of deformation encountered in press work and in providing an easily controlled way of examining the influence of such factors as lubrication, forming speed and temperature. The fundamental tests, however, generally indicate the metallurgical quality of the product.

2.3. Forming-Limit Diagram

It is evident that no matter how perfect the test is, whether fundamental or simulative, it is, by itself, insufficient to accurately evaluate formability. Simulative

tests such as the Erichsen or Swift cup-drawing tests are in fact, non-simulative in terms of size and frictional restraint of the production tools, and only represent special cases of actual sheet forming processes.

A new concept of predicting formability of a material was introduced by Keeler in 1965 [1.1]. From laboratory punch stretching experiments and the production of automobile pressings, he proposed an empirical failure criterion based on the measurement of the largest principal surface strain and the surface strain perpendicular to it at some "critical failure" point of the part. The strain data from these tests for various materials were plotted on the principal strain diagram as shown in Figure 2.2. This is called a forming limit diagram (FLD).

The "critical failure" point where "failure strains" were measured was defined as the point where fracture would eventually occur and the "failure strains" were those which were obtained just before the onset of visible necking. These "failure strains" were determined from measuring the distortion of a pattern of circular grids, electrochemically marked on the metal surface. Keeler's first FLD is a line of critical strain level which is normally called the forming-limit curve (FLC). This defines the failure and safe regions in the strain diagram (see Figure 2.2). In later work [2.11, 2.13, 2.14], his results were presented as a band instead of a single curve (see Figure 2.3).

Further work on the FLD was performed by Goodwin [1.2], who, by means of tension tests and various cupping tests

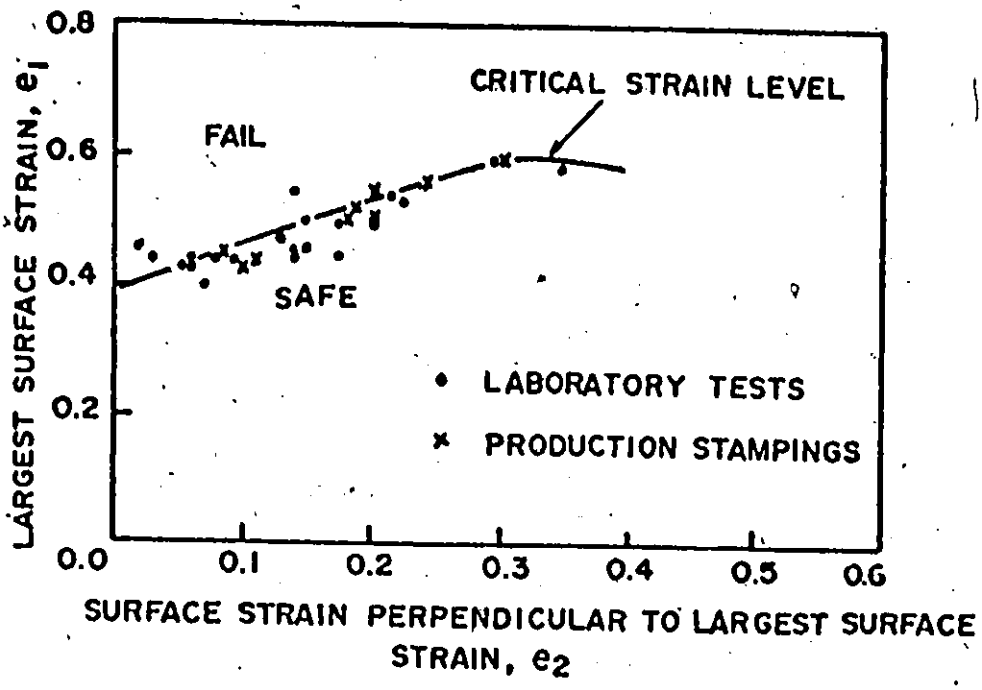

Figure 2.2. Keeler Original Forming-Limit Diagram [2.13].

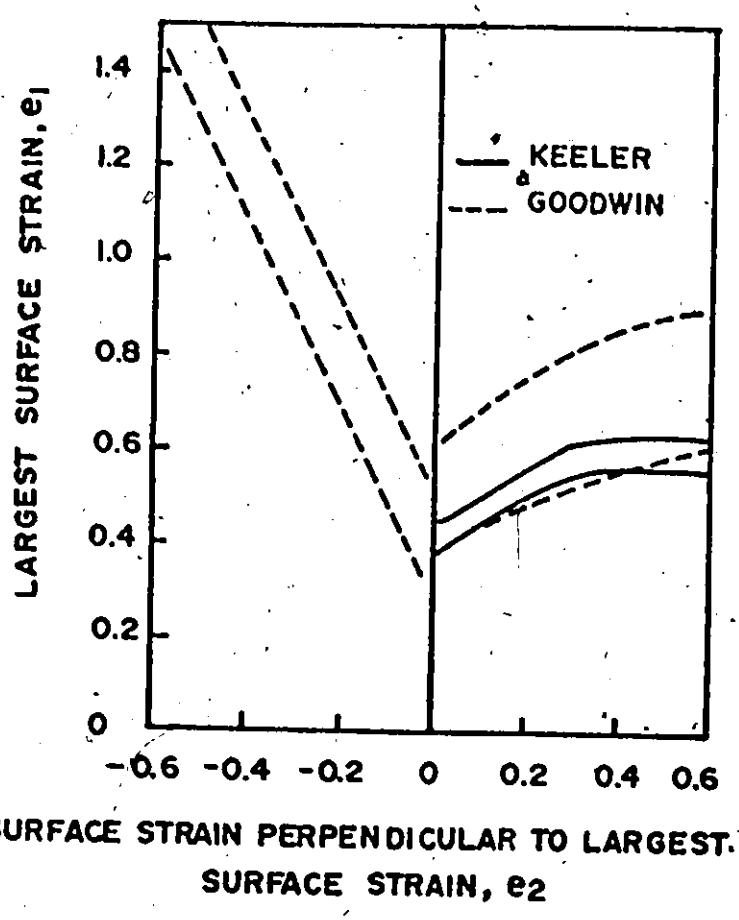

Figure 2.3. Keeler-Goodwin Forming-Limit Diagram [1.2].

from blanks of different shapes, obtained the value of "failure strains" in both tension-tension and tension-compression quardrants. The combined FLD is shown in Figure 2.3. Goodwin defined the failure strains as those which exist in the neck itself, thus the strain band has a higher upper limit than Keeler's results though the lower limits in both cases are approximately the same.

2.3.1. Determination of Forming-Limit Curves

In principle, the forming-limit curve is a measure of local ductility for all combinations of biaxial strains over which necking can occur. This curve is generally regarded as a unique function of strain ratio and has been applied to the strain analysis of sheet metal forming in press shops.

The forming limit curves are normally determined experimentally. Sheets are biaxially stretched to fracture in different strain ratios and strain data are obtained from the measurements of the deformed grids near fracture. The strain values determined this way are called the limit-strains which represent the maximum uniform elongation obtainable in a particular straining process. (It must be noted that the strain value measured at fracture is termed fracture strain and the curve obtained in this fashion is called the "intrinsic" forming-limit curve which is shown to be a straight line, see Figure 2.4).

Alternatively, forming-limit curves can be predicted by using the instability criteria applied to biaxially stretched

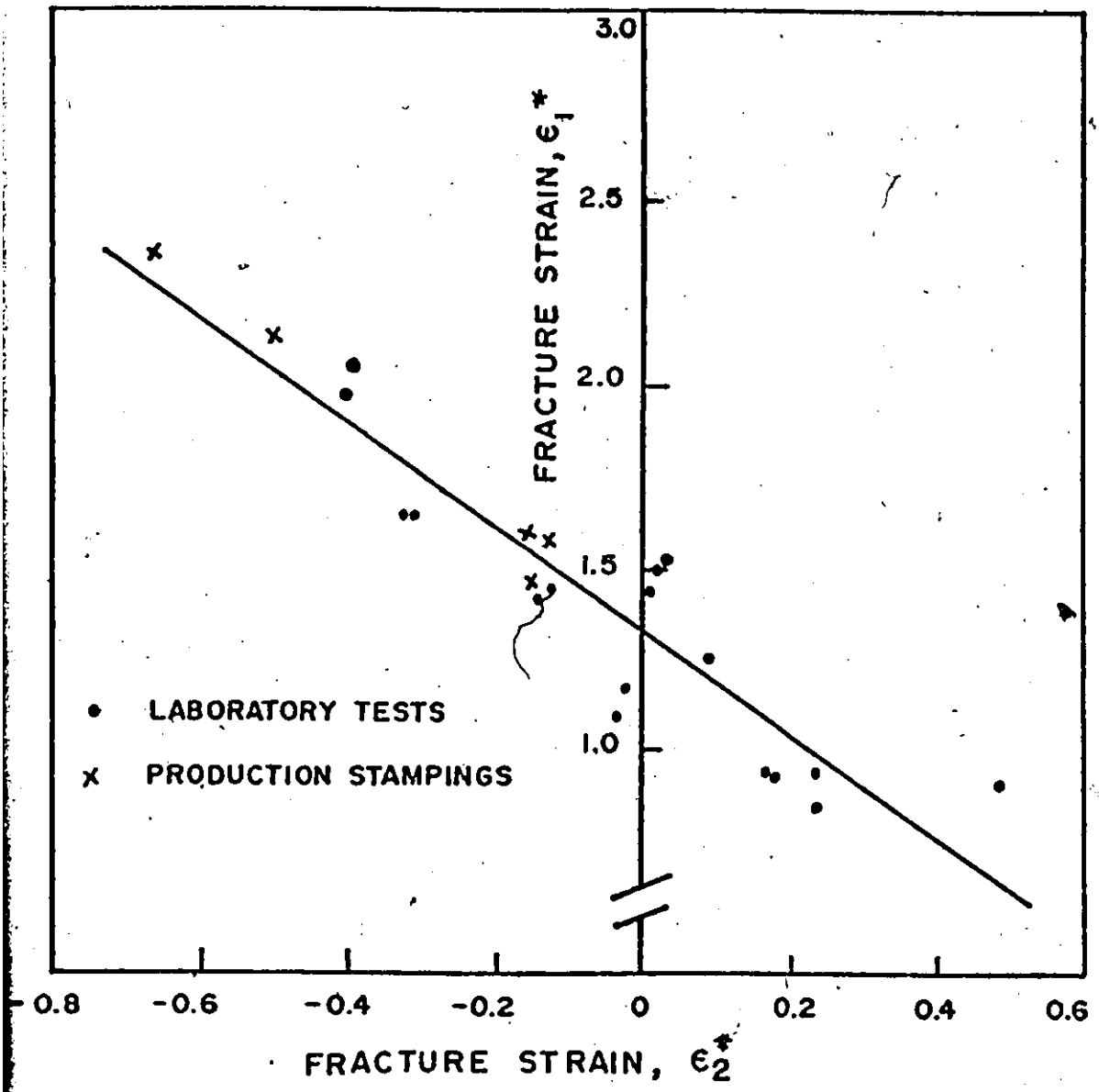

Figure 2.4. Intrinsic Forming-Limit Curve for Steels [2.17].

sheets. Straining in a deformation process is normally terminated by plastic instability and this has been the topic of discussion of various authors [2.39 to 2.42]. Their methods of predicting instability are essentially to determine the equivalent stress and strain which give rise to an unrestrained deformation without a further increase of load. There are two common modes of instability: diffuse necking and localized necking which are discussed in detail in Chapter 3.

Using the instability criteria, Keeler and Backofen [1.3] derived the conditions for unstable plastic flow in terms of the critical subtangent to the stress-strain curve. The value of the critical strains at instability can then be evaluated by using a particular stress-strain relationship. Moore and Wallace [2.43], Mir [2.44] and Venter [2.45] extended this analysis to take into account the anisotropic property of the material. A comparison of the critical strains at instability and the Keeler-Goodwin forming-limit curve is shown in Figure 2.5. It is found, in general, that the instability strains do not fall inside the Keeler-Goodwin strain band [2.45].

Forming-limit curves can also be predicted by using the Marciniak and Kuczynsky theory [2.46] in which a localized deformation mechanism similar to that of a localized neck was proposed to occur in a biaxial stretching process where all the strain components are positive. This theory will be discussed in detail in Chapter 3.

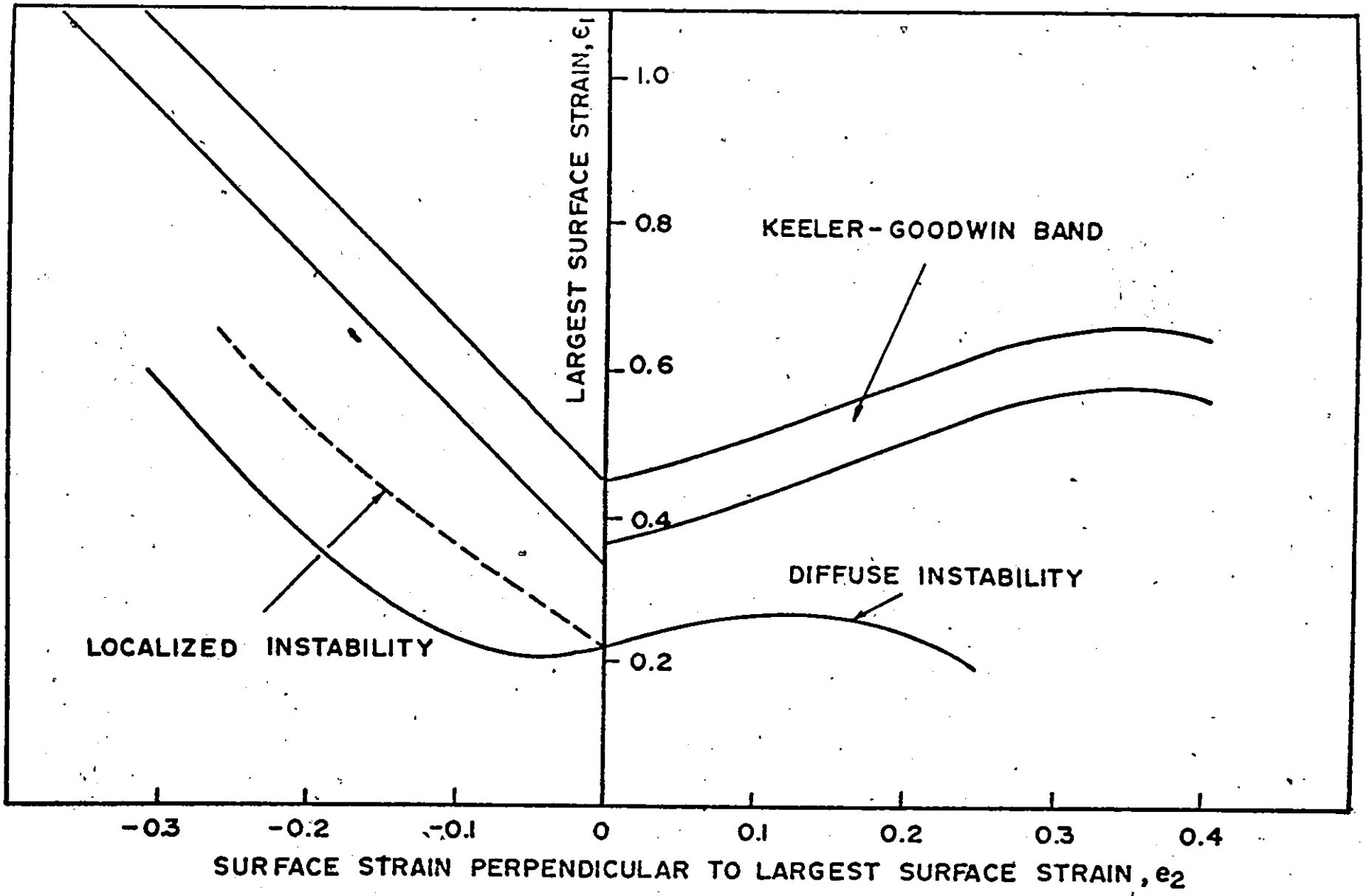

Figure 2.5. Comparison between Instability Strains for Aluminum Killed Steel ($\bar{R}$ = 1., n = 0.2, ϵ_o = 0) and Keeler-Goodwin Forming-Limit Curve [2.45].

2.3.2. Factors Affecting Forming-Limit Curves

The Keeler-Goodwin forming-limit curves were obtained from the analysis of failure strains of various materials, and it was believed that there was a universal forming-limit curve for all materials. However, subsequent researches indicated that the forming-limit curve is a function of material properties as well as the testing process.

a) Material Properties

As the ductility of metals varies with crystal structure and morphology, different materials should exhibit different forming-limit curves. Azrin and Backofen [2.21] indicated that metals such as copper, brass, austenitic stainless steels and zircalloy not only possess different scales of forming-limit curves but also their entire shapes are different. Various experimental as well as theoretical investigations [2.16, 2.17, 2.18, 2.46] have been performed to study the influence on the forming-limit curves of the important material parameters such as plastic properties and fracture properties. In applying the Marciniak-Kuczynsky theory to a biaxial-stretching process, Sowerby and Duncan [2.46] showed that the forming limit increases with an increase in strain-hardening index (see Figure 2.6), decreases with high $\bar{R}$ values (see Figure 2.7), and increases with increasing ductility (see Figure 2.8). Formability of a material also depends on material defects and strain-rate sensitivity. A high strain-rate sensitivity tends to increase the maximum uniform strain before instability (see Figure 2.9), while a

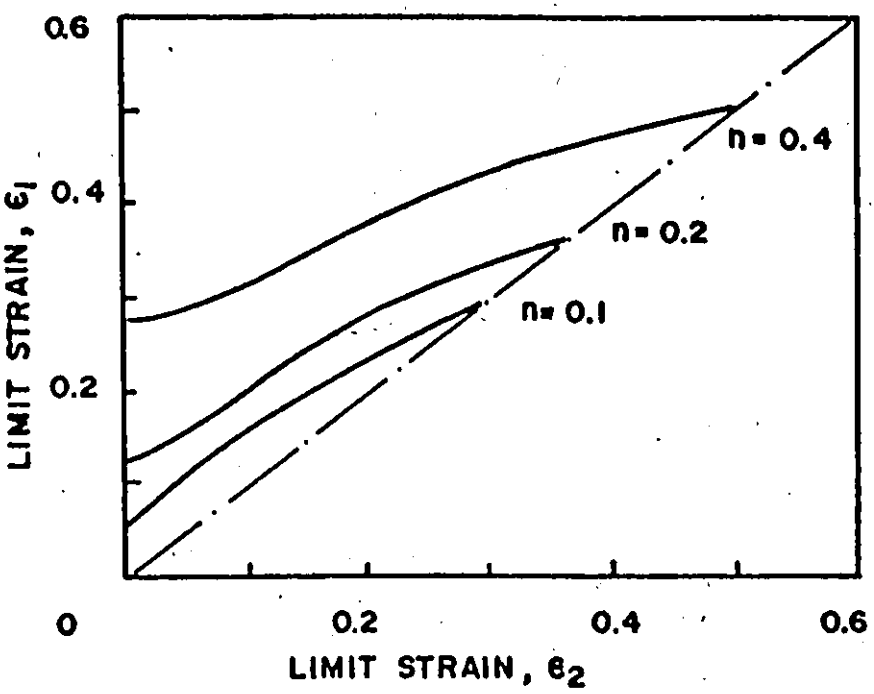

Figure 2.6. Influence of Strain-Hardening Index on Forming-Limit Curves (for R = 1., ϵ_o = 0.0014 and f_o = 0.98) [2.46].

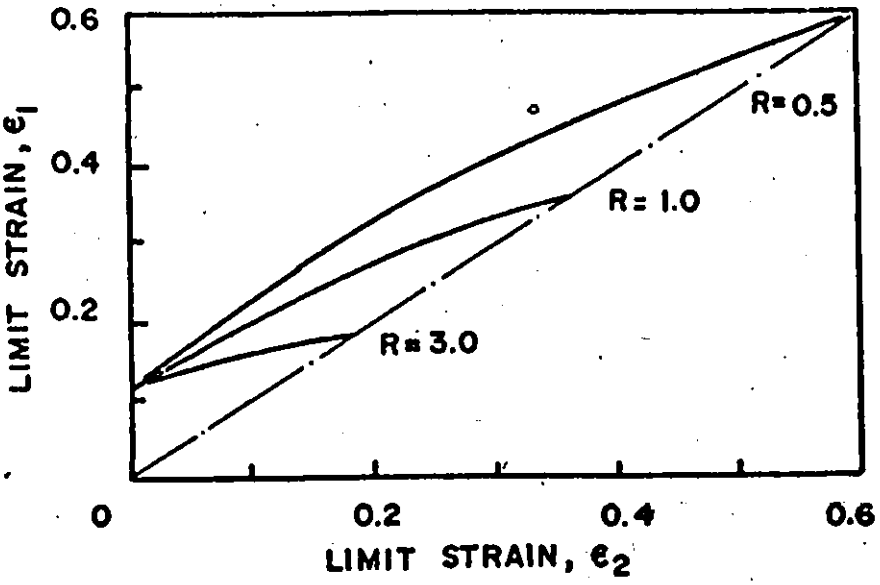

Figure 2.7. Influence of Normal Plastic Anisotropy on Forming-Limit Curve (for n = 0.2, ϵ_o = 0.0014 and f_o = 0.98) [2.46].

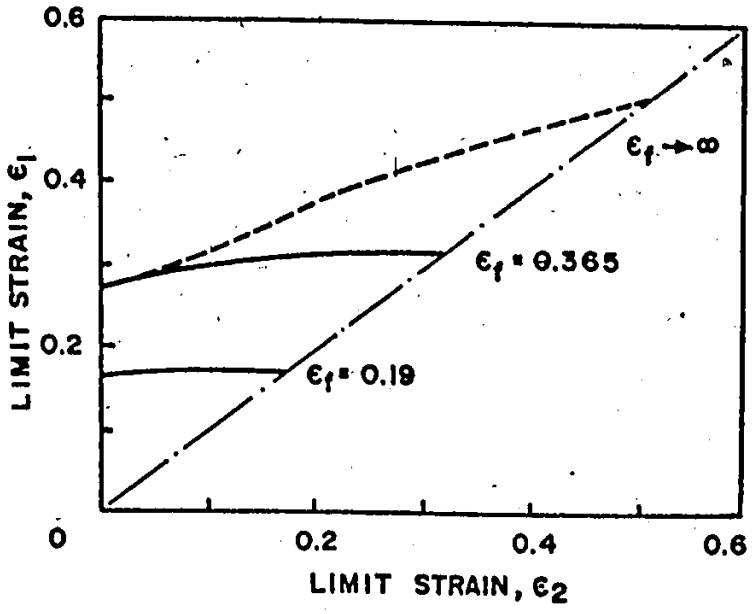

Figure 2.8. Influence of Ductility Parameter, ϵ_f, on Forming-Limit Curve (for $\bar{R} = 1$, $n = 0.4$ and $\epsilon_o = 0.0014$) [2.46].

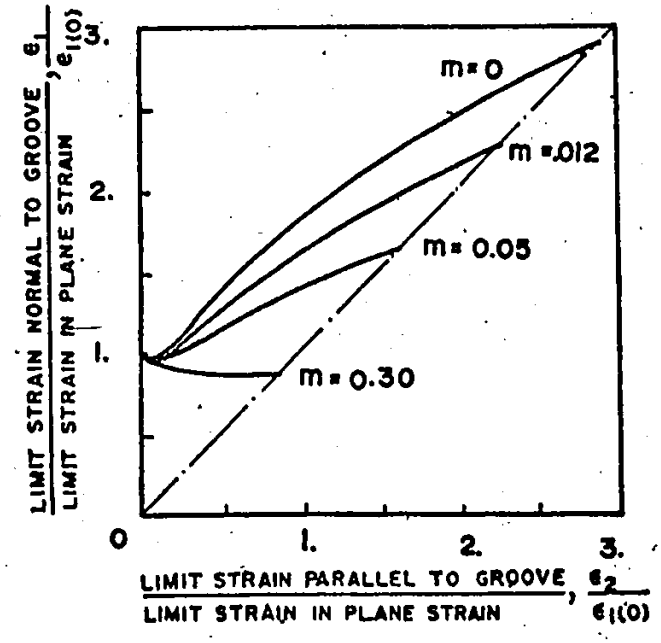

Figure 2.9. Influence of Strain-Rate-Sensitivity Index, m, on Forming-Limit Curve (for $\bar{R} = 1$, $n = 0.22$, $\epsilon_o = 0.01$, $f_o = 0.98$) [2.47].

material with large defects produces lower limit strains (see Figure 2.10).

b) Testing Process

Process variables can influence the forming-limit curves only indirectly through the change of straining path, deformation rate and strain gradient.

Yoshida et al. [2.18] have shown a pronounced influence of the strain path on the limit strains in biaxial stretching. In a similar work, Kobayashi et al. [2.20] found that the largest limit strain can be obtained by first applying a uni-axial tension and subsequently a balanced-biaxial tension, and also that the smallest limit strain is observed in the case of balanced-biaxial prestrain and subsequent plane-strain deformation.

The speed of the test and friction between the tool and the sheet may influence the amount of straining before failure of the sheet. It is also generally believed that specimen size, sheet thickness as well as the strain gradient of the process contributes a large part in changing the level of the forming-limit curves. A reduction of specimen size, or an increase of sheet thickness or strain gradient tends to increase the forming limit ..

2.4. Material Properties Affecting Formability - Metallurgical Considerations

The microstructure of a material determines its plastic and fracture properties. Material properties such as

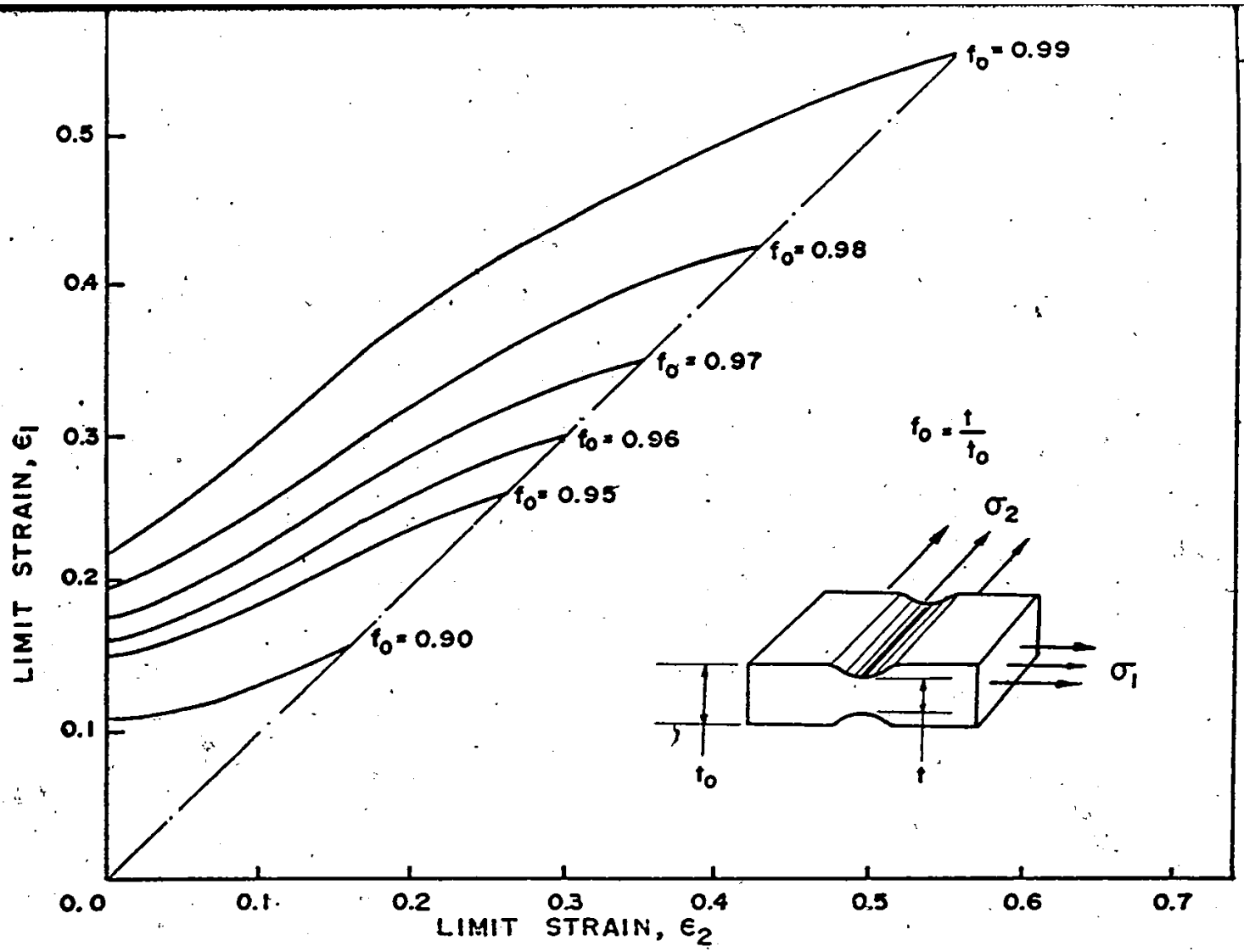

Figure 2.10. Effect of Inhomogeneity Factor, f_o, on Forming-Limit Curve (for $\bar{R} = 1$, $n = 0.29$, $\varepsilon_o = 0.015$) [2.45].

the strain-hardening characteristics and the anisotropic behaviour have been shown to influence material formability. These properties can be obtained from mechanical tests as described previously, however, a further insight into the behaviour of materials in forming can be obtained from a study of the underlying microstructure controlling the plastic deformation and fracture. From this, an assessment of the microstructural variables influencing the forming-limit curves can be derived.

2.4.1. Mechanism of Plastic Deformation

During the elastic straining of a single crystal, there is a slight displacement of the atoms in the lattice and this creates a change in the inter-atomic forces to balance the applied stress. In plastic deformation, however, a large scale slipping generally occurs in adjacent planes of atoms. The structure in the crystal lattice is maintained during the deformation and only the atoms change their relative position. The directions or the planes of slip are normally those of highest atomic density.

The mechanical deformation which occurs at ordinary speeds and temperatures in sheet-metal forming is concentrated in slip-bands, and the boundary separating the slipped and unslipped regions is called the dislocation line. This is a line of discontinuity in the atomic lattice and it must always form a closed loop within the crystal or end at its free surface. Imperfections within the crystals form a stress concentration from which the movement of a dislocation line

is initiated.

2.4.2. Yield Point and Strain-Hardening Characteristics

Low carbon steels in hot rolled or annealed condition normally display a sharp yield point. Cottrell [2.48] indicated that dislocations in these steels are so strongly pinned down by nitrogen and carbon atoms that they do not move during the initial stage of the plastic deformation. The applied stress increases instead until it reaches a point where new dislocations are formed at sources such as grain boundaries and by multiplication. The level of this stress is called the upper yield point. Plastic deformation then proceeds from grain to grain as the Lüder bands, which separate the yielded and unyielded part of the specimen, move across the specimen. In some applications where a sharp yield point is not desirable, skin rolling can be used to effectively remove this in most annealed steel sheets.

When the material is completely yielded a further increase of stress is necessary for the deformation to continue. This phenomenon is known as strain-hardening, which essentially is the result of the arresting of the slip bands at grain boundaries. Because the movement of the slip bands is impeded by another dislocation or an impurity, an increased stress is required to facilitate the movement of the dislocation.

It is well known that excess phases of increasing alloying elements in steels decreases the strain-hardening index. Lacy and Gensamer [2.49] indicated that the flow strength is related to the mean-free path of ferrite and thus

the strain-hardening index is related to this mean-free path. For steels which contain less than 0.1% carbon, Morrison [2.50] showed that the strain-hardening index, n, is related to grain size by

$$n = \frac{5}{10 + D^{-1/2}}$$

where D is the average grain diameter in millimeters.

2.4.3. Anisotropic Behaviour

The reduction of metal from ingots to sheets and the subsequent fabrication of these create various types of directionality of properties in almost all metals. Anisotropy can be traced to two common sources: crystallographic texture and mechanical fibering. Crystallographic texture, created by preferred orientation of available slip systems within the sheet, affects the overall shape of the stress-strain curve and the related properties such as yield strength, tensile strength and strain-hardening index. Mechanical fibering, on the other hand, involves alignment of particles, pores or weak interfaces and has considerably more influence on fracture behaviour.

a) Crystallographic-Texture Anisotropy

The strength of a single crystal varies with the crystallographic direction. For example, an iron crystal, which is essentially a body-center cubic structure, is strongest along the cube diagonal or <111>, and weakest along

the cube edge, <100>. Thus sheet steels would be isotropic only if the crystals were randomly oriented. Processing operations tend to rotate the individual crystals to one or more common orientations relative to the direction of deformation, thereby affecting the directionality of properties. The type and degree of preferred orientation depend upon the mode, magnitude and temperature of deformation, and the subsequent annealing treatment, all of which influence the crystallographic texture.

For steel sheets, the cube-on-corner texture (the cube diagonal of the body-cubic-center iron lattice is oriented normal to the plane of the sheet) favors development of high R value desirable for deep drawability [2.51]. Conversely, for the cube-on-face texture, with the weakest crystal direction, <100>, oriented normal to the sheet, the material yields low R value. The variation of strain ratio in the plane of the sheet is associated with textural changes and it is observed that ears normally occur in the direction where the intensity of the <100> component is the highest.

Cold rolling (after annealing) effects the anisotropic behaviour of steel sheets. Excess phases such as carbides, nitrides, oxides or sulphides have no direct effect on texture, however, finely divided excess phases have an indirect influence on the anisotropic behaviour through the influence on preferential growth of favorably oriented grains [2.10].

b) Mechanical Fibering Effects

Visual evidence for mechanical fibering abounds in

wrought materials; for example slag stringers in wrought iron, elongated grain structures and flow lines in deeply etched forging macrosections. Structural anisotropy of this type causes differences in strength, ductility, formability and toughness which are commonly observed in test samples oriented parallel and transverse to the direction of metal flow during processing.

A reasonable explanation of these effects can be made by assuming that the material, before deformation contains some kinds of internal flaw or defect. These are the structural elements which are distorted and aligned by plastic flow during deformation. In subsequent mechanical testing, the material's behaviour is influenced by the stress and strain concentration near the inclusions as well as the possibility of inclusion cracking or separation of the matrix-inclusion interface.

There are two prominent sources of fracture anisotropy in metals [2.52]. The first source is the relationship between the oriented weak interface and the principal tensile stresses. For example, when the applied stress is along the length of the flattened inclusions or elongated interfaces, there is no tendency for internal fracture until necking begins; however, when the tensile stress is applied normal to the length of the defect, internal fracturing can occur shortly after yielding because of the larger stress applied directly across the defect and metal interface. The second source of anisotropy is the difference in plastic pre-strain between inclusions and matrix accumulated during mechanical working. This anisotropic ductility

can be described by the ratio of the inclusion spacing to the size of the inclusion, and different ratios from different directions give different ductility.

A reduction of ductility as well as formability in a direction transverse to rolling has been observed in various steels containing inclusion stringers [2.53, 2.54]. By changing the morphology of the inclusion from stringers to globular, the tendency for transverse crack propagation can be reduced [2.55].

2.4.4. Effects of Inclusions

Second phase particles such as non-metallic inclusions play a primary role in influencing the ductile fracture resistance, hence formability, of metals and alloys. It is a general belief that inclusions (as well as cavities) introduce mechanical conditions favorable to local fracture, namely stress concentration and tri-axiality of the stress state.

Gurland and Plateau [2.56] found that cracks could appear simultaneously with the first plastic deformation lines which are preferentially located in the large inclusions and that, in general, the crack orientation tends to be normal to the direction of the applied stress. The cracks once formed, act, in effect, as cavities which grow by plastic deformation of the matrix. The condition for the formation of the micro-cracks depends on the ratio of the elastic moduli of the inclusions and the matrix, the difference in the coefficient of thermal expansion between the inclusions and the matrix, the inclusion shape and the orientation of the inclusion

in relation to the stress field.

It is recognised, however, that only inclusions larger than a certain critical size can cause stress concentration This leads to the concept of "micro" and "macro" inclusions proposed by Kiessling [2.57], who indicated that "macro"-inclusions are detrimental to material properties as they always result in a critical stress concentration. However, it is difficult to establish a critical size for the inclusions as this parameter can vary with the type, shape and distribution of the inclusions and also the heat treatment and the mechanical working on the material.

One of the important effects of inclusions on mechanical properties is the mechanical fibering effect discussed previously. Another effect is the reduction of ductility. Edelson and Baldwin [2.58] have shown that in copper, the resistance to ductile fracture where spherical inclusions are present is largely dependent on their volume fraction; as the volume fraction decreases, the plastic strain preceding fracture tends to increase in a hyperbolic fashion. Similar observations were reported by Gladman et al. [2.59] for sulphide inclusions in steels.

CHAPTER 3

DEFORMATION AND FAILURE OF ELLIPTICAL DIAPHRAGMS

3.1. Introduction

The deformation of thin circular and elliptical diaphragms has been the subject of extensive study by various researchers. Circular diaphragms have been used as bursting discs to protect pressure vessels or as devices to study the effect of explosive charges in underwater explosions [3.1]. Since the bulging process can produce larger strains in the sheet than the tensile test, this kind of deformation can be used for determining the stress-strain characteristics of the materials, especially for the less ductile ones [3.2].

Recently, more attention has been focussed on the use of elliptical diaphragms as a means of assessing material formability. In the bulging process, thin sheets are clamped in dies of elliptical aperture and pressure is applied to one side until failure. By varying the ratio of the major to minor axis of the aperture, it is possible to change the strain pattern on the sheet to simulate the straining conditions in various forming operations.

Failure in a straining process is generally preceded by plastic instability and for hydrostatic bulging processes both diffuse and localized necking can take place. The formation of a diffuse neck in the bulging of metal diaphragms coincides

with a pressure maximum and the diffusely necked area only appears at the pole of the deformed diaphragm. Localized necking, however, is the cause for edge failure of elliptical diaphragms and the criterion for instability is the maximum traction force in a certain direction.

The failure of elliptical and circular diaphragms may also be predicted using the Marciniak analysis. The maximum amount of straining in these diaphragms as calculated by this analysis is not only a function of strain-ratio and strain-hardening index but is also related to other material properties.

This chapter describes an experimental investigation of the deformation characteristics of mild steel diaphragms which was carried out to determine the strain path, diaphragm-profiles and strain-distribution. An attempt was also made to analyse the failure mode in the bulging of these diaphragms and the critical strain for each failure mode was evaluated.

3.2. Basic Plasticity Theory

The effective stress-strain relationships including the Levy-Mises theory of plastic flow provide a basis for the analysis of straining and failure of sheets in various forming operations. In most treatments of the instability of biaxial straining, it is stipulated that the straining process - at least up to the point of instability - is one of proportional straining. This is applicable to the case of hydrostatic bulging and it will be seen that the strain-ratio in the region at the top of the bulge is more or less constant during the deformation.

Material anisotropy is another consideration in predicting instability. Commercially available sheet normally exhibits some directional properties and this material characteristic is sometimes advantageous in retarding instability in forming processes.

3.2.1. Proportional Straining Processes

a) Yield Criteria

Assuming that the hydrostatic component of stress does not influence yielding and that there is no Bauschinger effect, the Von-Mises' yield criterion for an ideal isotropic material is written in terms of the principle stresses as

$$\bar{\sigma} = \sqrt{\frac{1}{2}\left((\sigma_1-\sigma_2)^2 + (\sigma_2-\sigma_3)^2 + (\sigma_3-\sigma_1)^2\right)}, \qquad (3.1)$$

where $\bar{\sigma}$ is the effective stress and σ_1, σ_2 and σ_3 are the three principal stresses.

In the case of hydrostatic bulging, the through thickness stress σ_3 of the diaphragm is small in magnitude relative to the other two; Equation (3.1) can thus be written as

$$\bar{\sigma} = \sigma_1 \left(\alpha^2 - \alpha + 1\right)^{1/2}, \qquad (3.2)$$

where

$$\alpha = \frac{\sigma_2}{\sigma_1} \qquad (3.3)$$

b) Stress-Strain Relation

For an isotropic and rigid-plastic material, the Levy-Mises flow equation for the three principal directions is given by

$$\frac{d\varepsilon_1}{2-\alpha} = \frac{d\varepsilon_2}{2\alpha-1} = -\frac{d\varepsilon_3}{1+\alpha} = \frac{\sigma_1\, d\bar{\varepsilon}}{2\bar{\sigma}}\,, \tag{3.4}$$

where $d\varepsilon_1$, $d\varepsilon_2$ and $d\varepsilon_3$ are the three principal strain increments which coincide with the axes of principal stress.

Similarly the equivalent strain increment is defined as

$$d\bar{\varepsilon} = \frac{2(\alpha^2-\alpha+1)^{1/2}}{(2-\alpha)}\, d\varepsilon_1\,. \tag{3.5}$$

In the case of proportional straining, the total strains are proportional to the incremental strains and the strain ratio can be derived from Equation (3.4) as

$$\alpha' = \frac{\varepsilon_2}{\varepsilon_1} = \frac{2\alpha-1}{2-\alpha}\,. \tag{3.6}$$

3.2.2 Empirical Strain Hardening Law

For a rigid plastic material, the Swift or Ludwik material equation may be used. This is given by

$$\bar{\sigma} = \sigma_o\, (\varepsilon_o + \bar{\varepsilon})^n\,, \tag{3.7}$$

where σ_o is the basic strength of the material, ε_o is the coefficient of prestrain and n is the strain-hardening index. For a fully annealed material, this reduces to

$$\bar{\sigma} = \sigma_o\, \bar{\varepsilon}^n\,. \tag{3.7a}$$

3.2.3. Plastic Anisotropy

As the material is being processed into sheets, the alignment of the crystallographic texture produces a variation

of material properties in different directions and this is manifested by ears in drawn cups. The degree of anisotropy is frequently determined from tensile tests with test pieces cut in different directions with respect to the rolling direction of the sheet. The anisotropic model proposed by Hill [3.3], assuming three orthogonal planes of symmetry in the material, has received appreciable attention and a brief summary of this theory is given.

a) Technological Definition of Anisotropy

A measure of normal plastic anisotropy is the Lankford coefficient [2.7] denoted by R which is defined as the ratio between the natural strains in the width and thickness directions for a specimen tested in tension. Algebraically

$$R_\theta = \frac{\ln \frac{w_\theta}{w_o}}{\ln \frac{t}{t_o}}, \qquad (3.8)$$

where R_θ is the coefficient of normal anisotropy in the direction θ with respect to the rolling direction, w_o and w_θ are the original and current width of specimen oriented at θ degree with respect to the rolling direction, and t and t_o are the current and original thickness of the specimen respectively.

Assuming that the volume of the material is constant during plastic deformation, the coefficient of normal anisotropy in direction θ can be expressed in terms of specimen's width and gage length as

$$R_\theta = \frac{\ln\left(\frac{w_\theta}{w_o}\right)}{\ln\left(\frac{w_o\, \ell_o}{w_\theta\, \ell_\theta}\right)}, \qquad (3.8a)$$

where ℓ_o and ℓ_θ are the original and current gage lengths respectively. The tensile specimens used for the determination of anisotropic behaviour of the material are normally aligned parallel, and normal to the rolling direction and at some intermediate orientation, usually 45 degrees.

To assess the press performance of the material in the drawing operation, an average value of R is chosen to indicate the normal anisotropy parameter of the sheet. This is taken as

$$\bar{R} = \frac{1}{4}\,(R_o + 2R_{45} + R_{90}), \qquad (3.9)$$

where R_o, R_{45} and R_{90} are the coefficients of normal anisotropy at 0, 45 and 90 degrees respectively to the rolling direction. Materials with a high $\bar{R}$ frequently perform better in drawing operations.

Equality in the R value in different directions in the plane of the sheet does not guarantee that the material is isotropic but only indicates that the material has rotational symmetry about the thickness direction (often called planar isotropy). Isotropy requires that all R values in a test piece cut from any direction equal unity. If $R_0 = R_{45} = R_{90} \neq 1$ then only planar isotropy is present. Planar anisotropy is normally responsible for earings in deep drawn cup and is defined as

$$\Delta R = \frac{1}{2}(R_0 - 2R_{45} + R_{90}). \qquad (3.10)$$

b) Hill's Model of Plastic Anisotropy

i) Yield Criteria and Plastic Anisotropy

Hill's model [3.3] for an anisotropic material is an extension of the Von-Mises' yield criteria for isotropic materials. In this model, the following assumptions are made:

i) the yield surface is always convex,

ii) there is no Bauschinger effect,

iii) hydrostatic stress does not cause yielding,

iv) plastic deformation occurs at constant volume and

v) there are three mutually orthogonal principal axes of anisotropy.

The yield criterion proposed is a quadratic function of the stress components containing six parameters, viz.,

$$2f(\sigma_{ij}) = F(\sigma_y-\sigma_z)^2 + G(\sigma_z-\sigma_x)^2 + H(\sigma_x-\sigma_y)^2 + 2L\,\tau_{yz}^2 +$$

$$2M\,\tau_{zx}^2 + 2N\,\tau_{xy}^2 = 1 \qquad (3.11)$$

where σ_x, σ_y, σ_z are the normal stress components,

τ_{xy}, τ_{yz}, τ_{zx} are the shear stress components,

F, G, H, L, M, N are parameters characteristic of the current state of anisotropy and are defined as

$$\frac{1}{X^2} = G + H ,$$

$$\frac{1}{Y^2} = H + F ,$$

$$\frac{1}{Z^2} = F + G ,$$

$$\frac{1}{Q^2} = 2L, \quad \frac{1}{S^2} = 2M, \quad \frac{1}{T^2} = 2N.$$

and X, Y, Z are the yield stresses in the principal axes of anisotropy and Q, S, T are the yield stresses in shear with respect to the principal axes of anisotropy.

If the principal stresses are acting in the principal directions of anisotropy then Equation (3.11) reduces to

$$2f(\sigma_{ij}) = F(\sigma_2-\sigma_3)^2 + G(\sigma_3-\sigma_1)^2 + H(\sigma_1-\sigma_2)^2 = 1. \qquad (3.12)$$

Using this model, the coefficient of normal anisotropy for a particular direction can be deduced from relationships between stress and strain increment, and is written as

$$R_\theta = \frac{H + (2N-F-G-4H)\ \sin^2\theta\ \cos^2\theta}{F\ \sin^2\theta + G\ \cos^2\theta} , \qquad (3.13)$$

where θ is the angle between the axis of the tensile specimen and the rolling direction of the sheet.

ii) Materials with Planar Isotropy

For materials which possess planar isotropy (R_θ is constant or F = G), the ratio of the yield stress in the thickness direction and in a principal direction in the plane of the sheet

is given by

$$\frac{Z}{X} = \left(\frac{1+R}{2}\right)^{1/2}, \tag{3.14}$$

where $R = \frac{H}{F}$.

The significance of this equation is apparent in the case of equal-biaxial stretching where the yield condition in the plane of the sheet is equivalent to yielding in uniaxial compression in the thickness direction. The strength of the sheet in this case is determined by that in the thickness direction and therefore a material with a high R-value seems to give a better formability because it resists thinning.

From Equation (3.12), the yielding of a planar isotropic material subjected to a biaxial stress system is

$$\sigma_1^2 \left[1 + \alpha^2 - \alpha\left(\frac{2R}{R+1}\right)\right] = X^2. \tag{3.15}$$

For different R values, Equation (3.15) describes a family of yield ellipses with the major axes inclined at 45 degrees with respect to the X-axis as shown in Figure 3.1. The major axes of these ellipses elongate as R increases and for R = 0, the ellipse becomes a circle.

The representative stress and strain derived from Hill's anisotropic model are given by

$$\bar{\sigma} = \sigma_1 \left[\frac{3}{2}\frac{1+R}{2+R}\left(1 - \frac{2R}{R+1}\alpha + \alpha^2\right)\right]^{1/2}, \tag{3.16}$$

and

$$d\bar{\varepsilon} = \left[\frac{2}{3}\frac{2+R}{1+2R}\left(d\varepsilon_1^2 + d\varepsilon_2^2 + R\, d\varepsilon_3^2\right)\right]^{1/2}. \tag{3.17}$$

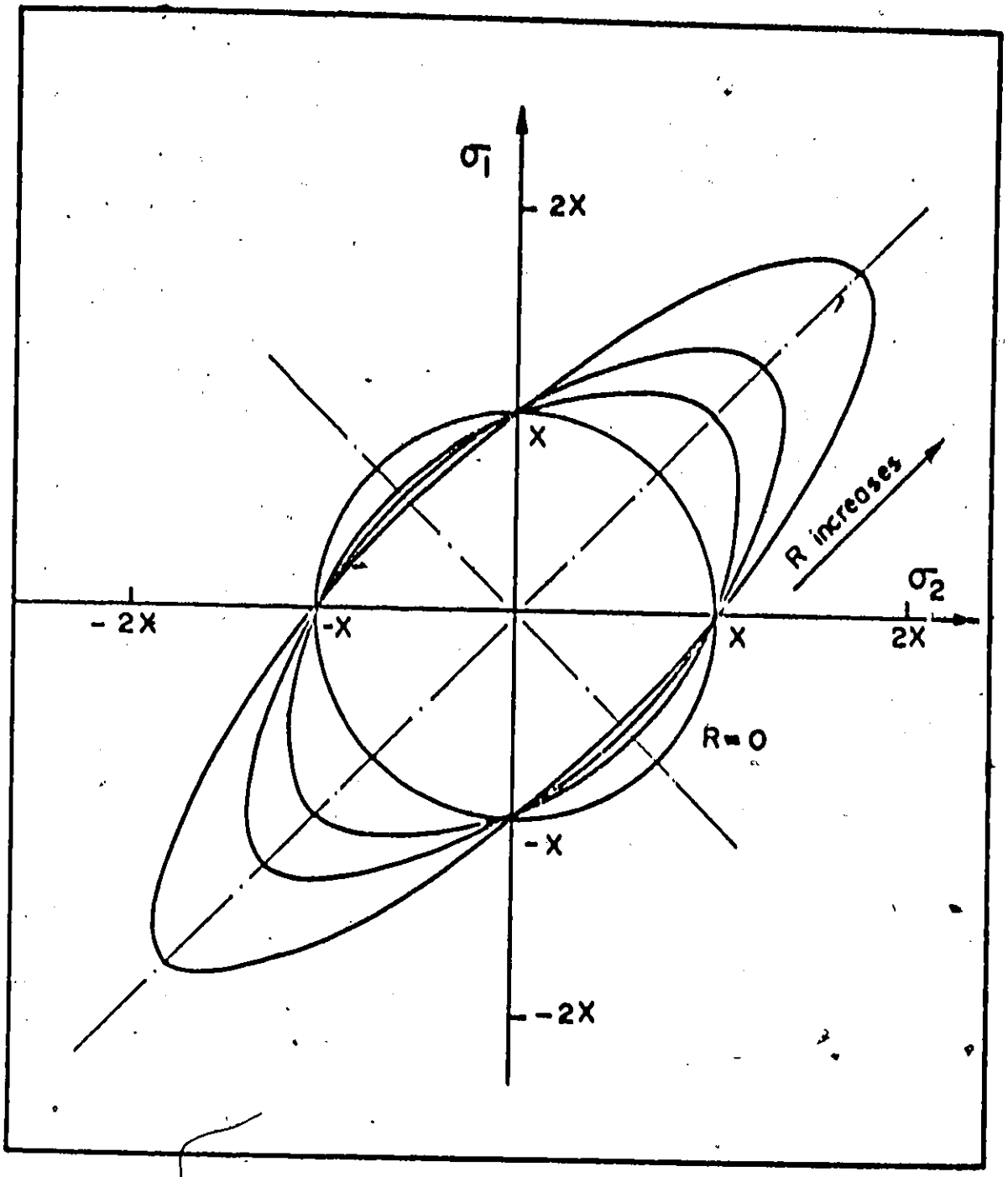

Figure 3.1. Yield Ellipses for Planar Isotropic Materials.

and the Levy-Mises' flow rule is

$$\frac{d\varepsilon_1}{(1+R)-\alpha R} = \frac{d\varepsilon_2}{\alpha(1+R)-R} = -\frac{d\varepsilon_3}{1+\alpha} = \frac{3}{2}\frac{\sigma_1\, d\bar{\varepsilon}}{(R+2)\bar{\sigma}} \qquad (3.18)$$

3.3. Theory of Instability

3.3.1. Modes of Instability in the Straining of an Element

It is well known that there are two modes of instability which terminate the stable straining of an element: diffuse and localized necking. Diffuse necking refers to a state in which the strain rate in the region of the strain concentration or "diffuse neck" increases more rapidly than that in the neighboring region. In most cases, this diffuse necking is associated with a maximum in the applied load. The material outside the neck may not cease straining as it may be subjected to a deformation due to the straining of the material in the "diffuse neck".

Localized necking, however, is a particular phenomenon described by Hill [3.4] which involves a discontinuity of the strain pattern in the straining process. In this mode of instability, strain concentrates in a groove along a direction parallel to the direction of zero extension, and the process of strain concentration is normally associated with a maximum force in the sheet in a direction perpendicular to the groove. The straining in the groove does not affect and cannot be influenced by the conditions outside the necking region.

Besides the two common modes of instability mentioned above, one can distinguish another localized straining or groove

forming process: the Marciniak groove. This groove can develop in a region where the principal components of strain are positive. As the groove is oriented along a line of positive straining, the formation of the groove is thus influenced by the straining in the surrounding area.

3.3.2. Instability in a Straining Process

a) Uni-axial Tension

In the tensile testing of a flat strip of specimen, there are two possible modes of instability: diffuse and localized instability.

i) Diffuse Instability

When the width of the test piece is small compared to the length, a diffuse neck can occur during the straining process. The onset of this mode of instability is generally considered to coincide with a load maximum as shown in Figure 3.2, and at this point an uncontrollable deformation starts.

If an applied load P produces a normal stress σ_1 on the current cross-section area A of a tensile strip, then

$$P = \sigma_1 A \ . \qquad (3.19)$$

Differentiating and noticing that at maximum load, $\frac{dP}{P} = 0$, Equation (3.19) becomes

$$\frac{d\sigma_1}{\sigma_1} = - \frac{dA}{A} \ . \qquad (3.20)$$

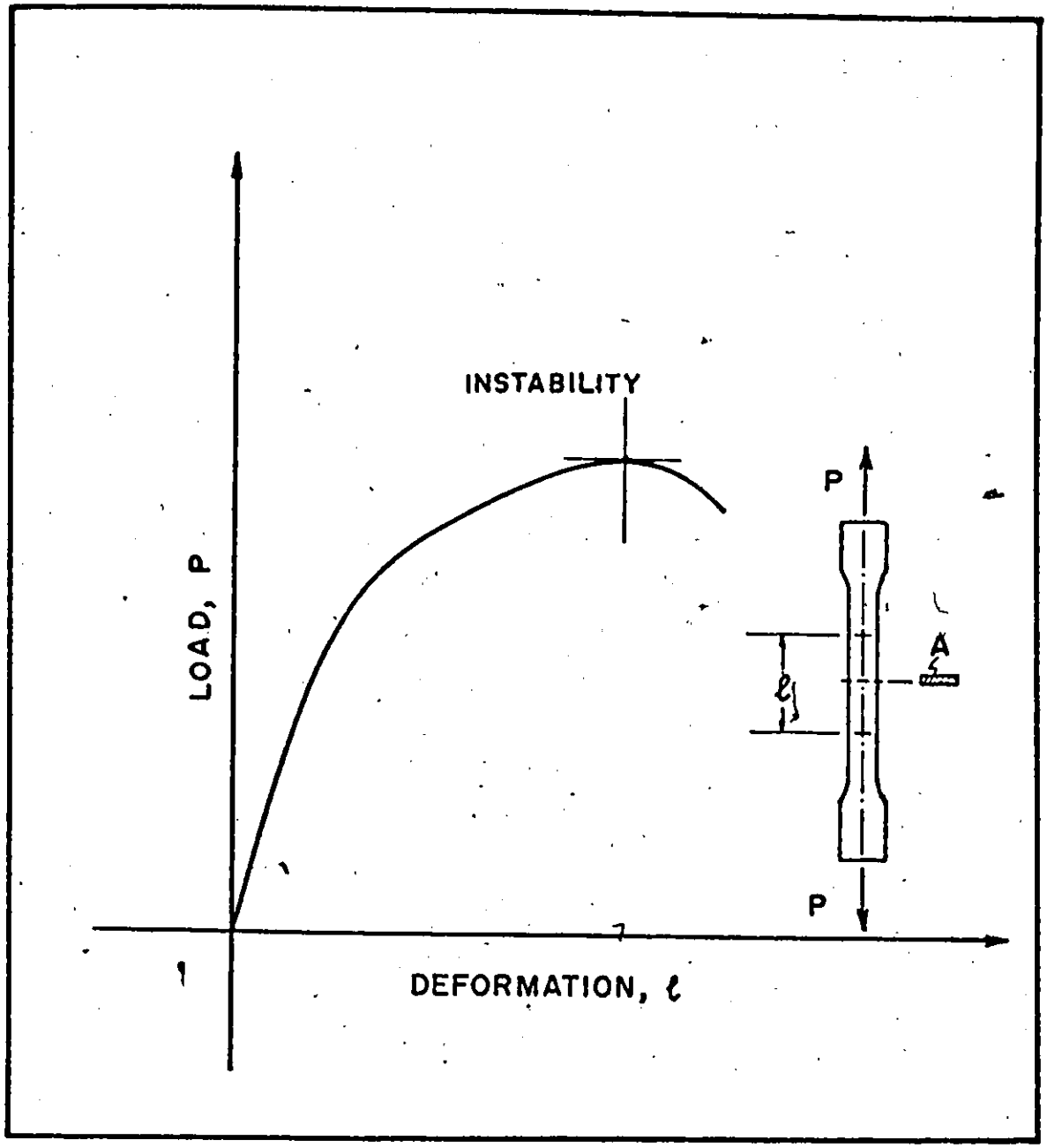

Figure 3.2. Instability Point on the Load-Elongation Curve for Tensile Test.

Assuming constant volume during deformation, Equation (3.20) can be written as

$$\frac{d\sigma_1}{\sigma_1} = \frac{d\ell}{\ell} = d\varepsilon_1,$$

where ℓ is the gage length of the specimen,

or

$$\frac{d\sigma_1}{\sigma_1 d\varepsilon_1} = 1. \tag{3.21}$$

The differential form of the representative stress from Equation (3.2) is

$$\frac{d\bar{\sigma}}{\bar{\sigma}} = \frac{d\sigma_1}{\sigma_1}. \tag{3.22}$$

However, for the uniaxial tension test ($\alpha=0$), the representative strain derived from Equation (3.18) is

$$d\bar{\varepsilon} = d\varepsilon_1 \sqrt{\frac{2}{3}\,\frac{(2+R)}{(1+R)}}. \tag{3.23}$$

By substituting $\frac{d\sigma_1}{\sigma_1}$ and $d\varepsilon_1$ from Equations (3.22) and (3.23) into Equation (3.21) the condition for instability can be written as

$$\frac{d\bar{\sigma}}{\bar{\sigma}\, d\bar{\varepsilon}} = \frac{1}{\sqrt{\frac{2}{3}\,\frac{2+R}{1+R}}} = \frac{1}{s}. \tag{3.24}$$

The factor "s" is called the critical subtangent to the stress-strain curve as shown in Figure 3.3, and the greater its value the greater the equivalent strain before instability.

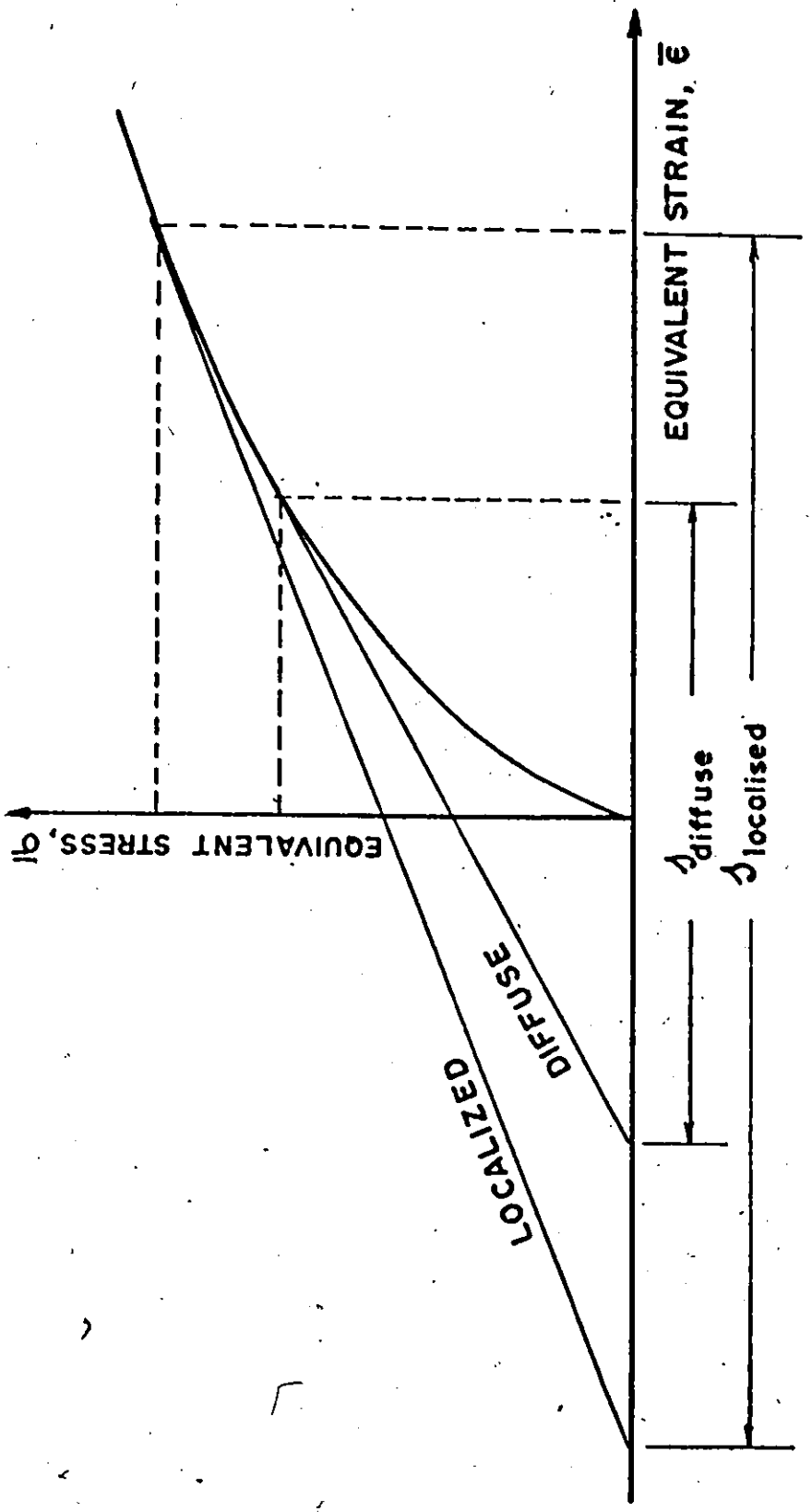

Figure 3.3. Instability Strain Obtained from the Critical Subtangent to the Equivalent Stress-Strain Curve.

The instability strain can be determined using the empirical stress-strain relationship given by Equation (3.7). It can be shown that

$$\frac{d\bar{\sigma}}{\bar{\sigma}\, d\bar{\varepsilon}} = \frac{n}{\varepsilon_o + \bar{\varepsilon}} .$$

Substituting into Equation (3.24) one can obtain the instability strain in the form

$$\bar{\varepsilon}^* = n \sqrt{\frac{2}{3}\frac{2+R}{1+R}} - \varepsilon_o . \tag{3.25}$$

Assuming a proportional loading, then the critical strains in the principal directions at instability are

$$\varepsilon_1^* = n - \frac{\varepsilon_o}{\sqrt{\frac{2}{3}(\frac{2+R}{1+R})}} ,$$

and (3.26)

$$\varepsilon_2^* = -\frac{R}{1+R}\left[n - \frac{\varepsilon_o}{\sqrt{\frac{2}{3}(\frac{2+R}{1+R})}}\right] .$$

These are the maximum value of strains for which the deformation process is stable.

ii) Localized Instability

For a thin tensile strip pulled in tension, there exists a direction along which the extension is zero. A localized neck proposed by Hill is formed along this direction. Let θ be the angle between the normal to the neck and the principal stress direction (as shown in Figure 3.4), it can be demonstrated that for an isotropic material, the angle θ is given by

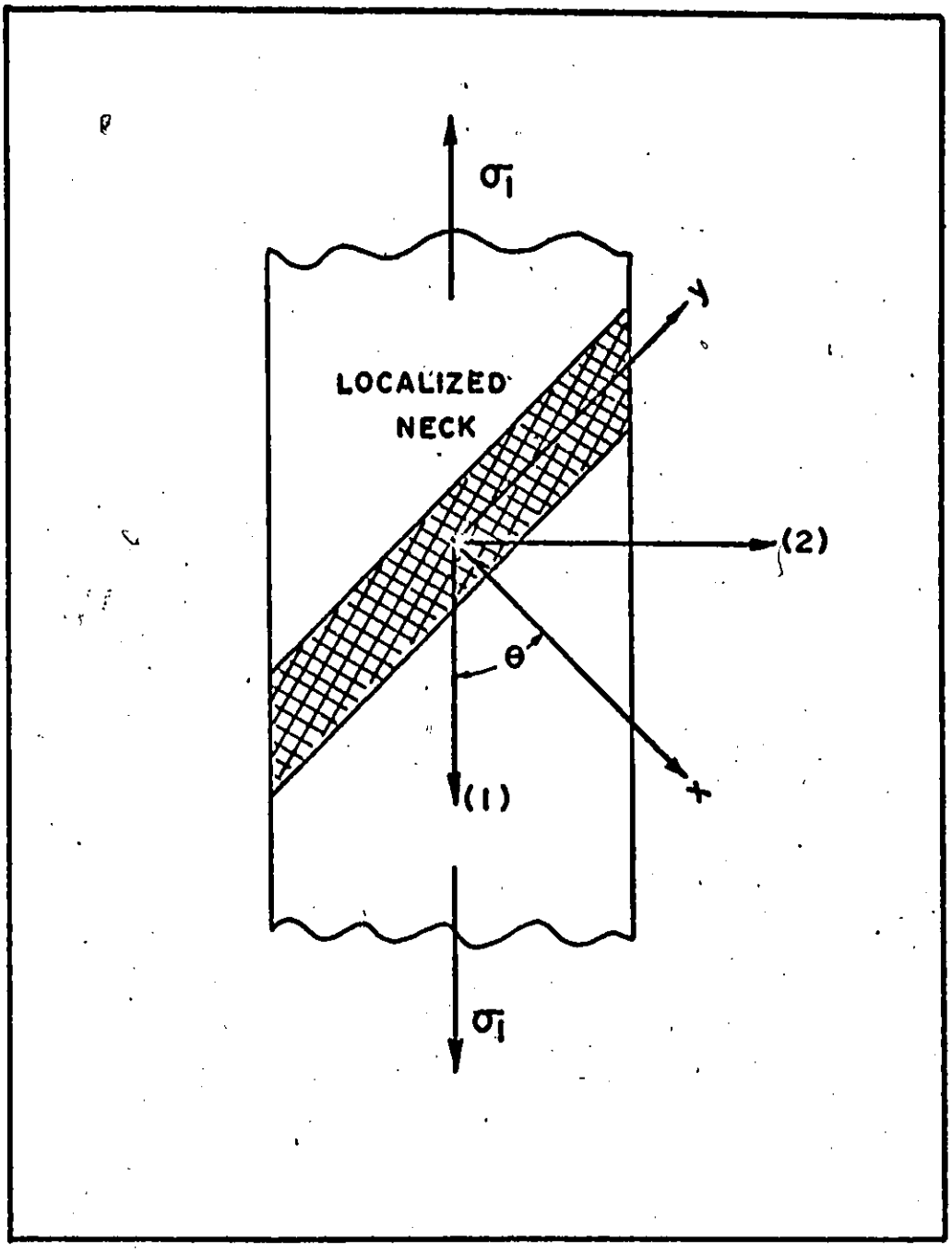

Figure 3.4. Localized Neck in Simple Tension Specimen.

$$\tan \theta = \pm \frac{\sqrt{2}}{2} .$$

This instability mode is associated with a maximum force normal to the groove, i.e.,

$$d(\sigma_x t_x) = 0,$$

or

$$\frac{d\sigma_x}{\sigma_x} = - \frac{dt_x}{t_x} = - d\varepsilon_3 \qquad (3.27)$$

where σ_x and t_x are the stress and thickness respectively in the x-direction.

From Equation (3.27) the critical subtangent can be proved to be

$$\frac{1}{s} = \frac{1}{2} , \qquad (3.28)$$

and the principal strains at the point of localized instability can be derived as

$$\varepsilon_1^* = 2n,$$

and (3.29)

$$\varepsilon_2^* = n.$$

In comparing the two instability modes, it is seen that the critical strains for the localized necking are twice as much as that in the diffuse mode, thus a localized neck may occur in a region where a diffuse neck has already developed.

b) Plane Strain Tension

If the width of the tensile test piece is very large compared to its thickness, the straining process in the specimen

can be approximated by a plane strain deformation. In this case, the two modes of instability coincide. A neck forms at the end of the stable straining where the load reaches a maximum. It can be shown that at this point, the critical strain is

$$\varepsilon_1^* = n,$$

and

$$\varepsilon_2^* = 0. \tag{3.30}$$

c) Biaxial Tension - Marciniak Hypothesis

For a load supporting element being stretched biaxially, load instability is commonly regarded as a limiting condition for the overall straining of the element. In a forming process, however, straining can continue after the load maximum until rupture. An examination of a sheet which has failed under biaxial tension reveals that there is a significant localized plastic deformation at the failure zone, and that the uniform strain measured at some point near fracture is less than that at fracture. This indicates a mechanism of localized deformation. The localized necking proposed by Hill does not apply in this case because there is no line of zero extension. The Marciniak hypothesis [3.5] however, provides an explanation for this mechanism of localized strain concentration.

In this hypothesis, it is assumed that a strain concentration which originates from an inhomogeneity in the sheet can develop into a groove oriented perpendicular to the direction of the greatest principal strain. The straining of a material

(A) having an inhomogeneity (B), characterized by a thickness reduction factor $f_o = \frac{t_B}{t_A}$ as shown in Figure 3.5, can be described in the following manner.

The strain increments in the direction of the groove (direction (2) in Figure 3.5) must be the same for the two regions (A) and (B) to satisfy the compatibility of deformation, i.e.,

$$(d\varepsilon_2)_A = (d\varepsilon_2)_B \,, \tag{3.31}$$

and in direction (1), the equilibrium of forces must be maintained, viz.

$$(\sigma_1 t)_A = (\sigma_1 t)_B \,, \tag{3.32}$$

where σ and t are the stress and thickness respectively. As the groove develops, the material in region (A) continues to strain until $(d\varepsilon_1)_B >> (d\varepsilon_2)_B$, then all straining is concentrated within the groove. This situation is illustrated in a principal strain diagram as shown in Figure 3.6. In this figure, the strain path of the material outside the neck is represented by a straight line as the process is assumed to be one of proportional straining, i.e., $(\frac{d\varepsilon_1}{d\varepsilon_2})_A$ = constant. For the groove, however, the strain increment $(d\varepsilon_1)_B$ increases at a faster rate than $(d\varepsilon_2)_B$, and consequently the straining in (B) is described by a curved path which approaches zero slope when a state of plane strain occurs in the groove. The current strain state for the two regions (A) and (B) is on a line parallel to the ε_1 axis; for example (A_1) and (B_1) as shown in Figure 3.6.

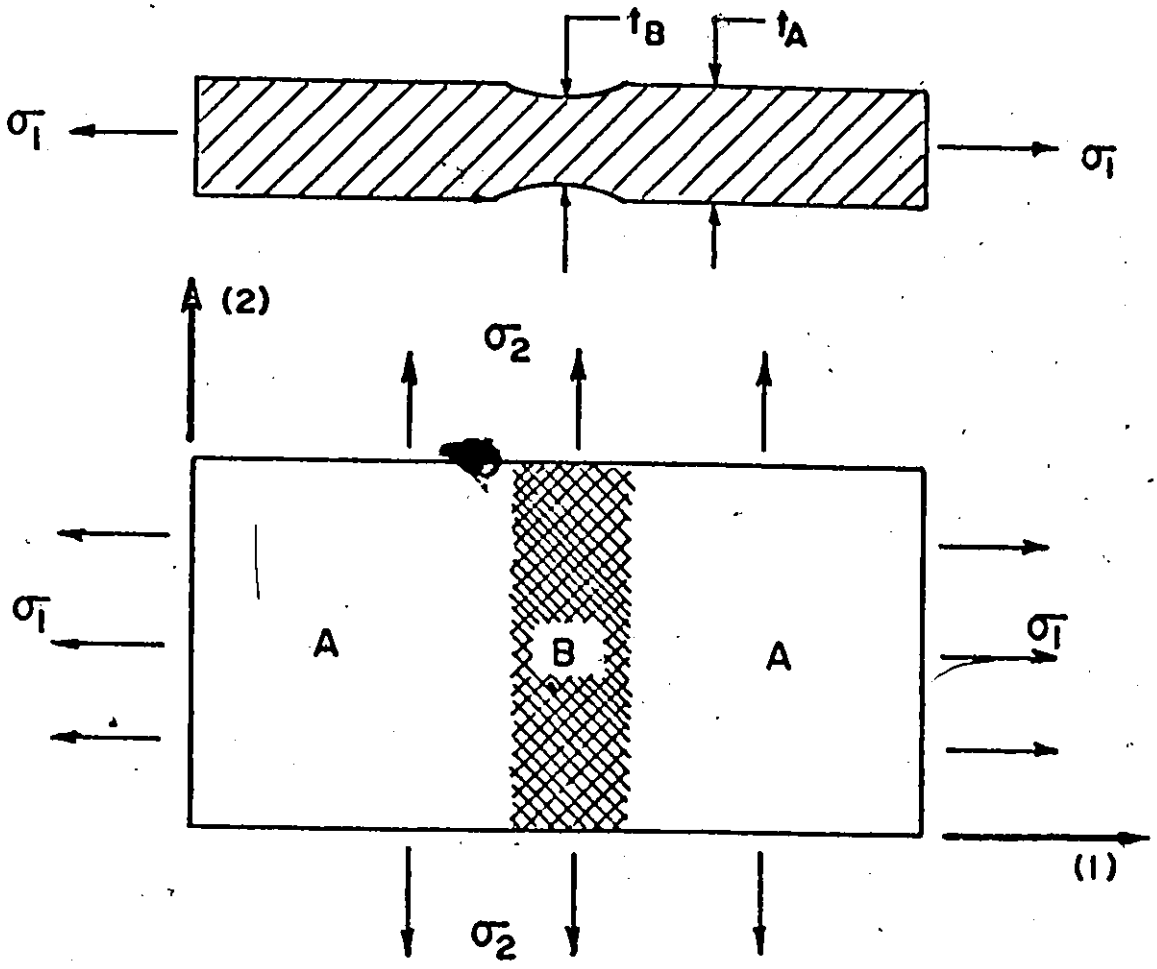

Figure 3.5. Schematic Presentation of Marciniak Groove in an Element.

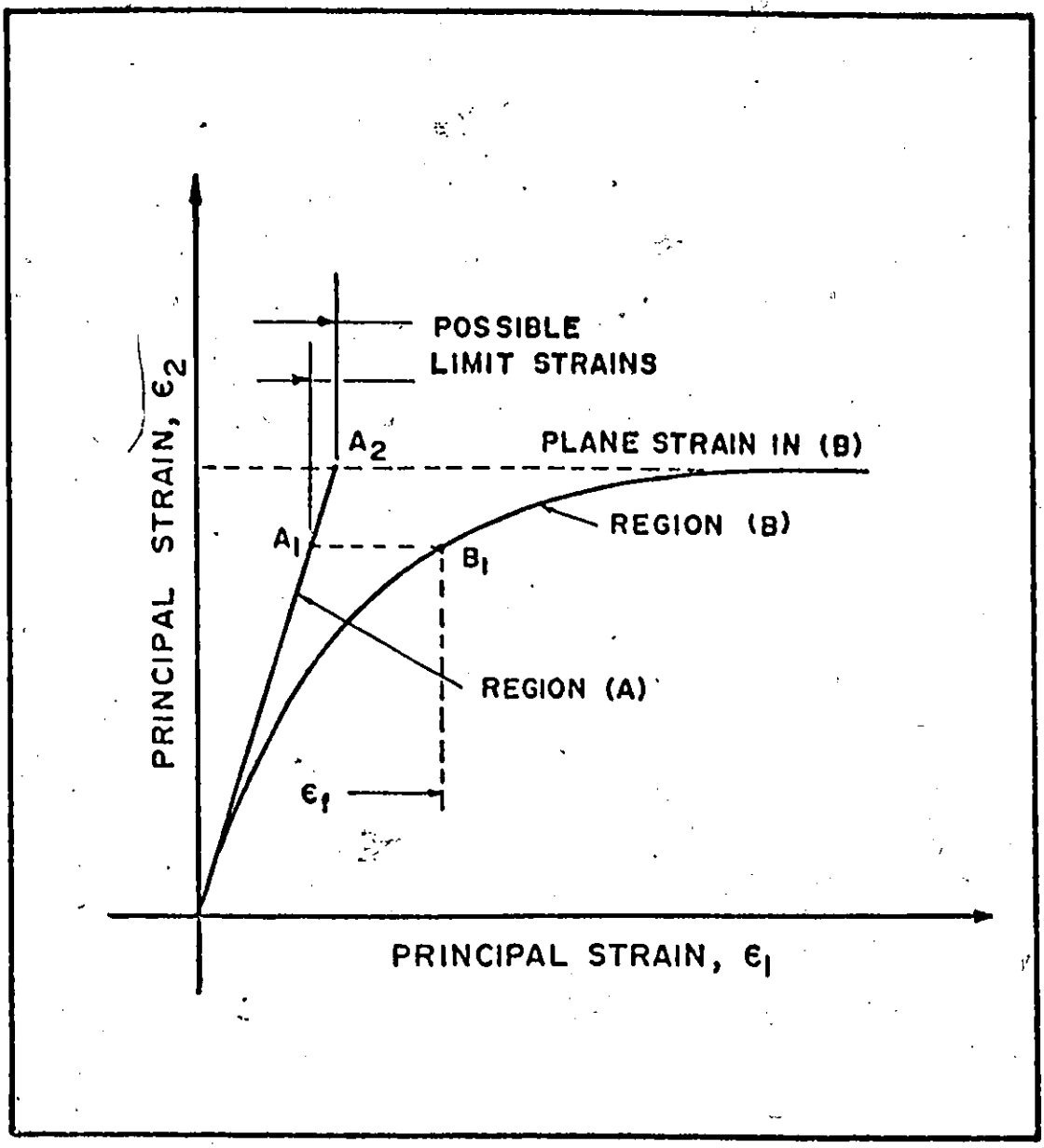

Figure 3.6. Straining Process Leading to Fracture of the Element Shown in Figure 3.5.

The criterion for material failure is that straining in the groove reaches the plane strain condition

$$\left(\frac{d\epsilon_2}{d\epsilon_1}\right)_B \to 0. \tag{3.33}$$

For less ductile materials, it is possible that fracture occurs in the groove before this condition is reached. A critical value of the thickness strain is thus selected as a condition for failure. This critical value is called the fracture strain and the additional criterion for failure is thus

$$(\epsilon_3)_B = (\epsilon_3)_f. \tag{3.34}$$

The limit strain in this hypothesis is defined by the strain measured in the region outside the localized strain concentration when rupture occurs in the groove.

Following the work of Marciniak [3.5], Sowerby and Duncan [2.46] extended the analysis and identified three cases within a straining process which leads to fracture. A numerical technique [2.45] was developed to compute the limit strain for a planar isotropic material where the parameters are:

- the Ludwik strain-hardening function, $\bar{\sigma} = \sigma_o (\bar{\epsilon}+\epsilon_o)^n$,
- the Von-Mises' yield criteria,
- the coefficient of anisotropy, $\bar{R}$,
- the initial inhomogeneity, $f_o = \frac{t_B}{t_A}$,
- the stress or strain ratio, and
- the material fracture strain, $(\epsilon_3)_f$.

Theoretical results were obtained for aluminum-killed steel and these were compared with the experimental data [3.6] as shown in Figure 3. 7.

The analysis was later modified by Marciniak and his co-workers [2.47] to assess the influence on limit strains of the strain-rate and the anisotropic behaviour of the material. The constitutive equation used in the analysis was of the form

$$\bar{\sigma} = \sigma_o \, (\bar{\varepsilon}+\varepsilon_o)^n \, \dot{\varepsilon}^m, \tag{3.35}$$

where $\dot{\varepsilon}$ is the strain rate and m is the strain-rate sensitivity index, and the thickness reduction factor was redefined as

$$f_o = \frac{(t_o\sigma_o)_B}{(t_o\sigma_o)_A}. \tag{3,36}$$

The plane-strain condition in the groove given by Equation (3.33) is unsatisfactory as a failure criterion when applied to a strain-rate sensitive material. Thus the condition described by Equation (3.34) was chosen as a criterion for failure. In using this criterion, a constant thickness strain at fracture was assumed for a particular material and this was supported by experimental evidence [2.47]. A numerical solution was found for the limit strains and it was observed that the strain-rate sensitivity index, m, influences the limit strain in a manner similar to the strain-hardening index.

Theoretical forming-limit curves taking into consideration the effect of m and R were obtained by Marciniak et al. [2.47] and were compared with the experimental results for various materials. A reasonably good agreement was found between experi-

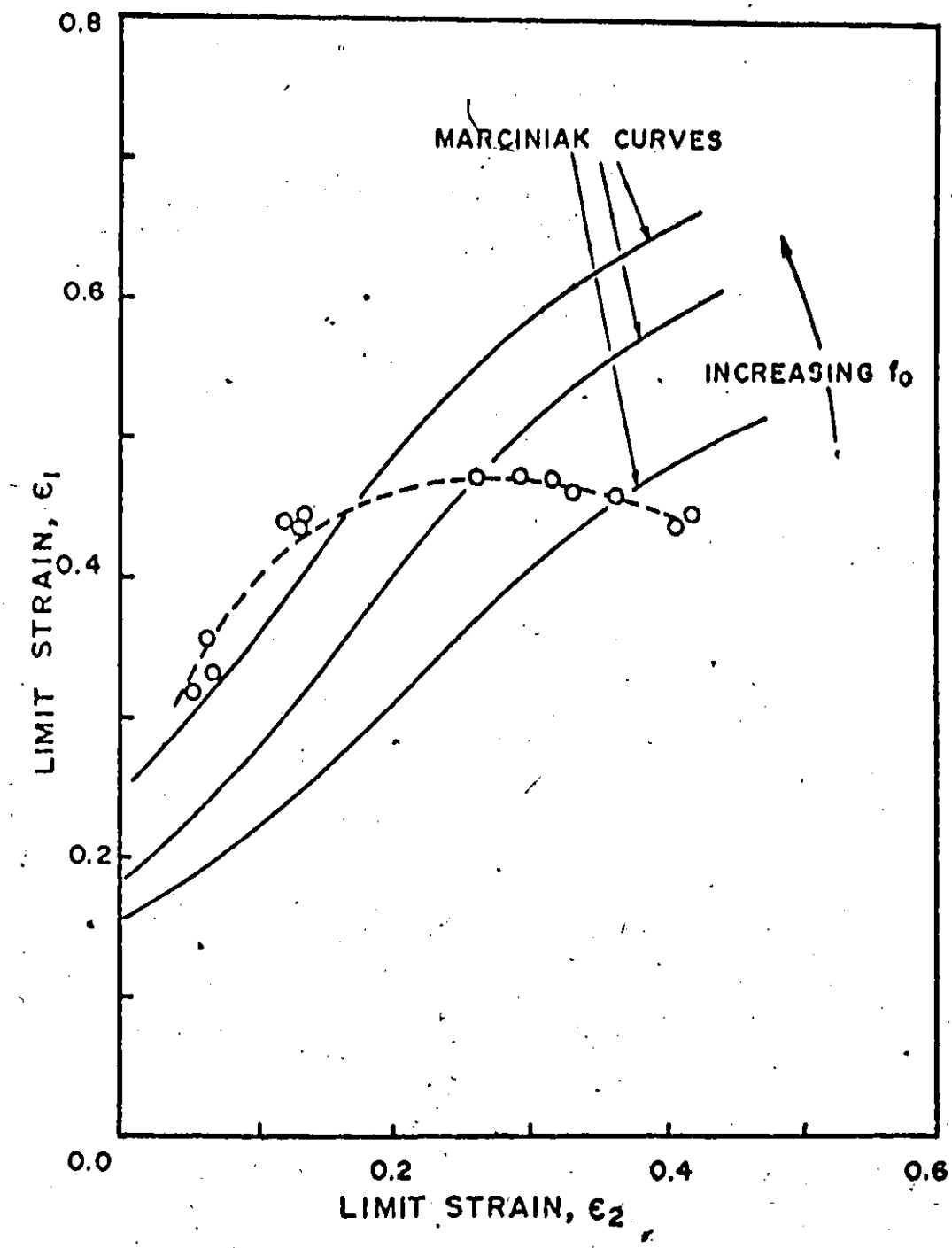

Figure 3.7. Comparison between Marciniak Limit-Strain Curves and Forming-Limit Curve for Aluminum-Killed Steel ($\bar{R}$ = 1.8, n = .24, ϵ_o = 0.013) [3.6].

mental and theoretical data for steel and copper as seen in Figures 3.8 and 3.9.

d) Hydrostatic Bulging Processes

The development of strain concentration which leads to failure at the pole in metal diaphragms subjected to a hydrostatic bulging process can be described in terms of a Marciniak groove. The limit-strain obtained from the analysis of the formation of this groove is, apart from the material properties, a function of the strain-ratio as mentioned earlier. Circular as well as elliptical diaphragms normally fail near the pole and the diffuse necking in these diaphragms is associated with a pressure maximum. In some elliptical diaphragms, however, pressure may not reach a maximum and failure can start at the edge due to a localized strain-concentration. Diffuse instability in circular diaphragms was first analysed by Hill [3.7] and Swift [2.30] and the following is a brief summary.

i) Diffuse Necking in Circular Bulge - Hill's Analysis

Hill [3.7] proposed a theory to predict the instability strains in a pressurized circular diaphragm in which failure occurs at the pole of the bulge.

Consider the deformation of a circular diaphragm by a pressure p as shown in Figure 3.10. It is assumed that the particle in the diaphragm describes a circular path orthogonal to the current profile of the diaphragm. At the pole, the profile of the diaphragm is approximately circular and the stress state

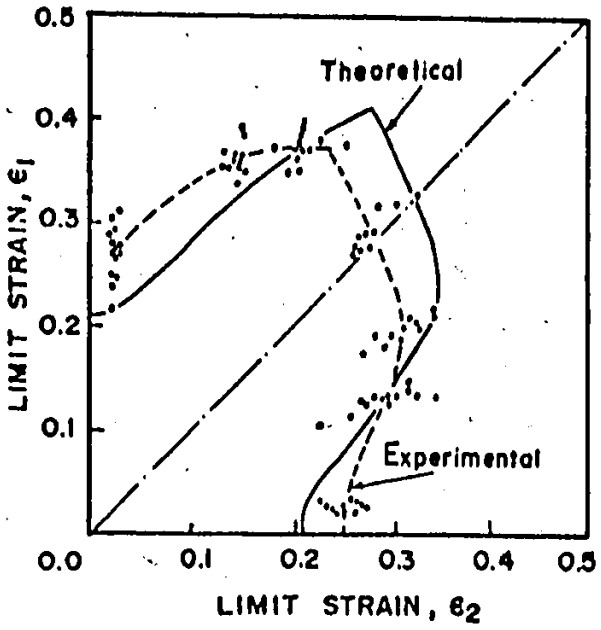

Figure 3.8. Marciniak Limit-Strain Curve and Experimental Forming-Limit Curve for Mild Steels [2.47].

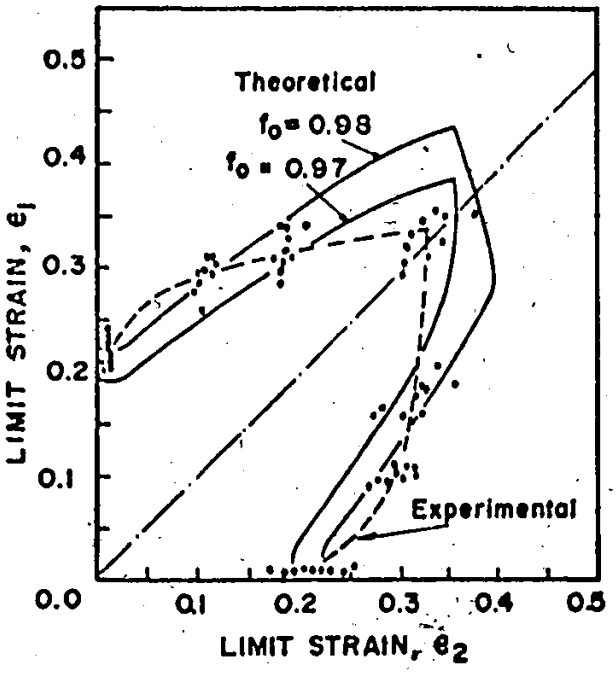

Figure 3.9. Marciniak Limit-Strain Curve and Experimental Forming-Limit Curve for Copper [2.47].

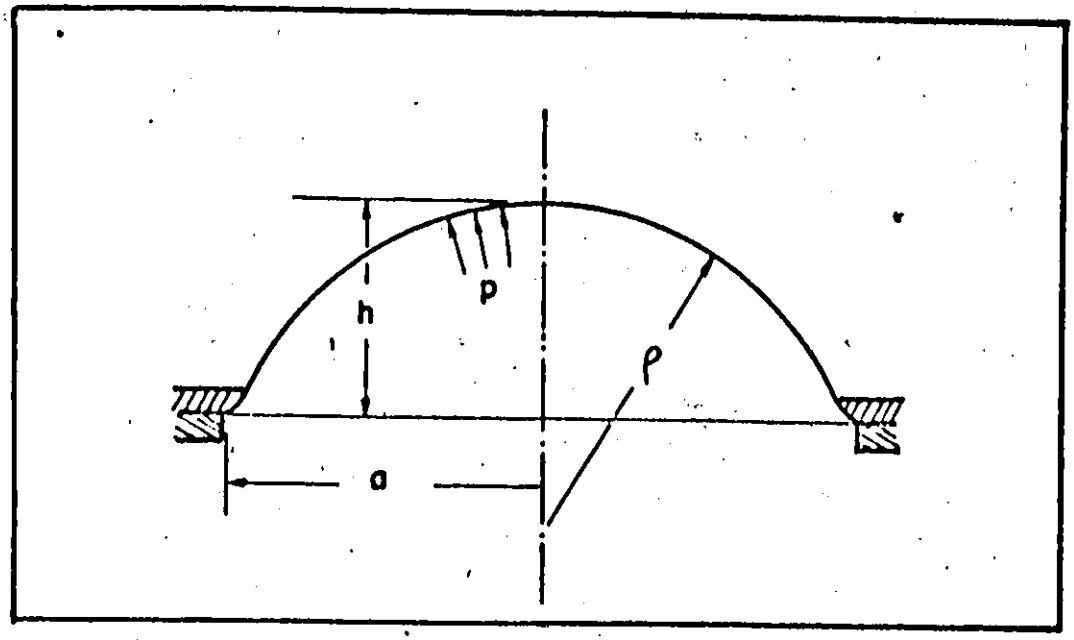

Figure 3.10. Schematic Presentation of the Deformation of Circular Diaphragm in Hill's Analysis.

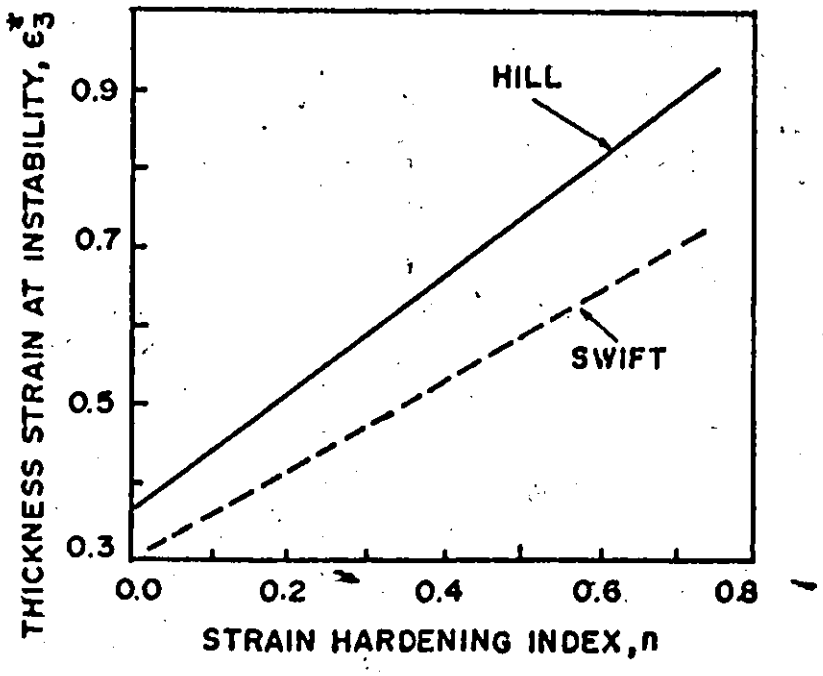

Figure 3.11. Hill's and Swift's Instability Strains in the Circular Bulge Test for different n-Values [3.11].

(for an isotropic material) is one of balanced-biaxial tension, i.e.,

$$\sigma_1 = \sigma_2 = \frac{p\rho}{2t}, \qquad (3.37)$$

and

$$\sigma_3 \doteq 0,$$

where ρ is the current radius of curvature and t is the current thickness.

For the deformation assumed by Hill, the strain at the pole is approximated by

$$\bar{\epsilon} = -\epsilon_3 = 2 \ln \left(1 + \frac{h^2}{a^2}\right), \qquad (3.38)$$

h and a being the pole height and original radius of the diaphragm respectively. The equation describing the geometry of the spherical cap is

$$\rho = \frac{a^2 + h^2}{2h} \qquad (3.39)$$

Using Equations (3.37) and (3.39) and noticing that at diffuse instability, dp = 0, one can derive

$$\frac{1}{\sigma_1}\frac{d\sigma_1}{d\bar{\epsilon}} = \frac{11}{8} + \frac{1}{2\bar{\epsilon}} - \frac{\bar{\epsilon}}{96} + \ldots \qquad (3.40)$$

Using the Ludwik strain hardening law given by Equation (3.7a) the instability strain is then calculated and approximated by

$$\bar{\epsilon}^* \doteq \frac{4}{11}(2n+1). \qquad (3.41)$$

Experimental work was performed by Mellor [3.8] on various materials and the results were found to be in good agreement with

Hill's instability strain given by relation (3.41).

ii) Diffuse Necking in Circular Bulge - Swift's Model

Assuming that the particle path and the bulge profile are circular, Swift [2.39] derived approximate expressions for the instability at the pole and at the rim of a circular diaphragm. For diaphragms which failed at the pole, the instability criterion was taken as the maximum pressure, and the critical strain at instability was approximated as

$$\bar{\varepsilon}^* = \frac{1}{2}\left[\frac{33}{10} + n - \left(\frac{729}{100} - \frac{3}{5}n + n^2\right)^{1/2}\right] . \qquad (3.42)$$

A comparison of Hill's and Swift's results of the instability strain for different strain hardening indices is given in Figure 3.11.

3.4. Deformation of Metal Diaphragms in Hydrostatic Bulging Processes

The deformation and failure of anisotropic steel diaphragms bulged in rectangular and square dies was studied by Duncan [3.9], and it was shown that material normally failed near the edge of the rectangular dies due to localized necking. Much larger strains can be obtained in the elliptical and circular bulge, and it was shown [3.2] that the circular bulge test can be employed to obtain the stress-strain characteristics of a material in the region of biaxial stretching.

Early work on elliptical diaphragms was done by Sachs and his co-workers [3.10]. Detailed experimental study was later performed by Yousif et al. [3.12]. However, as the deformation

and failure characteristics of elliptical diaphragms are mainly dependent upon the geometry of the die, a preliminary investigation of this type of bulging process is required in this work. This investigation was carried out for steel diaphragms and the deformation characteristics were analysed.

3.4.1. The Hydrostatic Bulging Processes

In the investigation of hydrostatic bulging processes, rectangular specimens were rigidly clamped in dies of elliptical apertures with different aspect ratios. This die ratio is defined as the ratio of the major to minor axis, i.e., a/b. The major axis of each die was 6 inches while the minor axes were 1.5, 3.0, 4.5 and 6 inches and these dies are thus designated 4:1, 2:1, 4:3 and 1:1 ratio respectively. The bulging dies and the apparatus employed are shown in Figures 3.12 and 3.13. The strain-ratios resulting from the bulging of specimens in these dies were from 0.1 to 1.0. The edge of each die was machined to 1/4 in. radius (about 8 times the thickness of the metal sheet used) which was considered to be sufficient to reduce the possibility of failure by bending under tension. To prevent drawing in of the specimens, a steel wire was soldered to the die base and a matching groove was machined in the die just beyond the die radius.

Before bulging, the specimens were clamped securely between the die and the die base to prevent any slippage, and although there was some relative movement between the specimen and the die edge, no local thinning was observed before diffuse

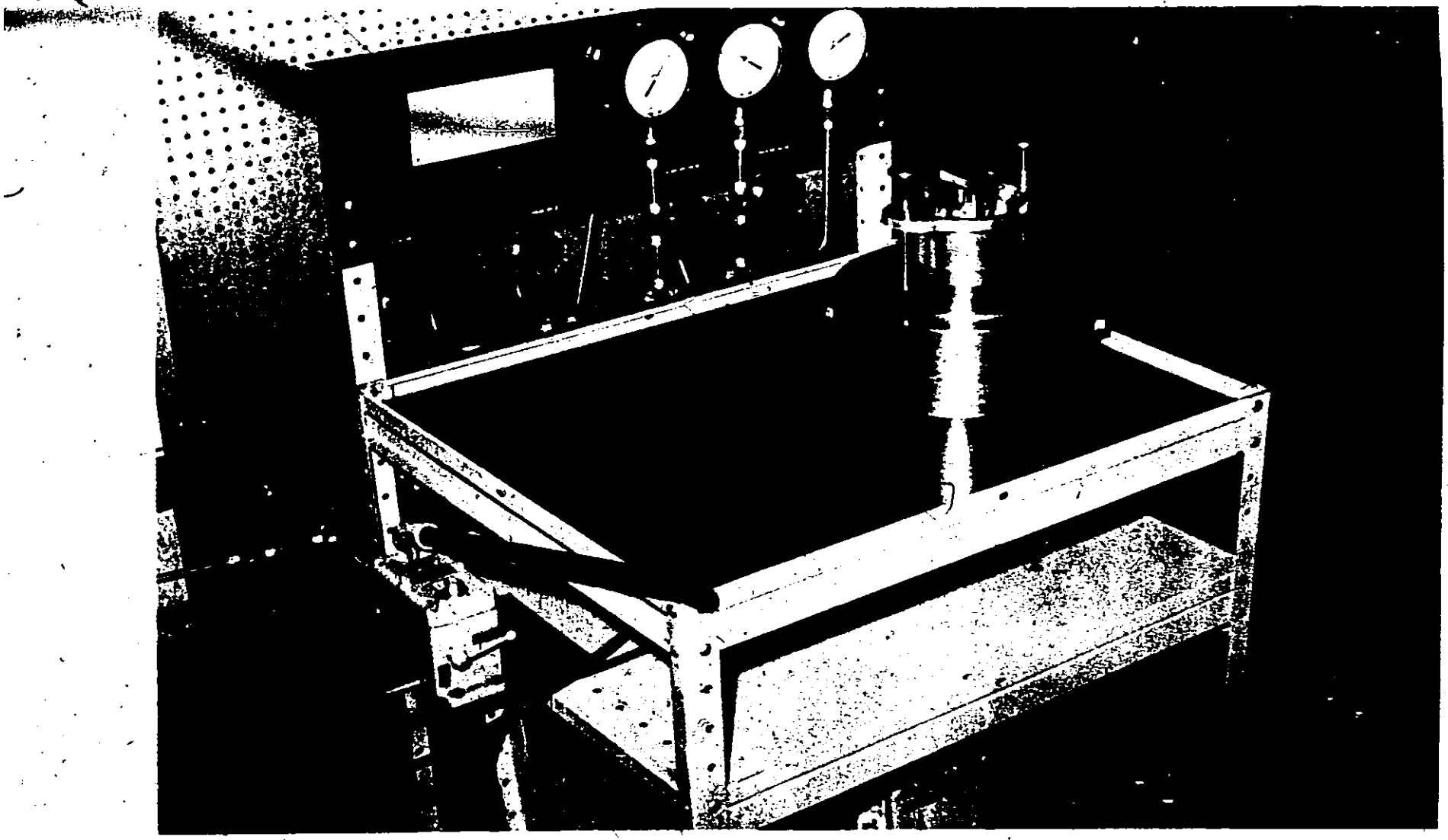

Figure 3.12. Circular Bulging Die and Bulge Testing Apparatus.

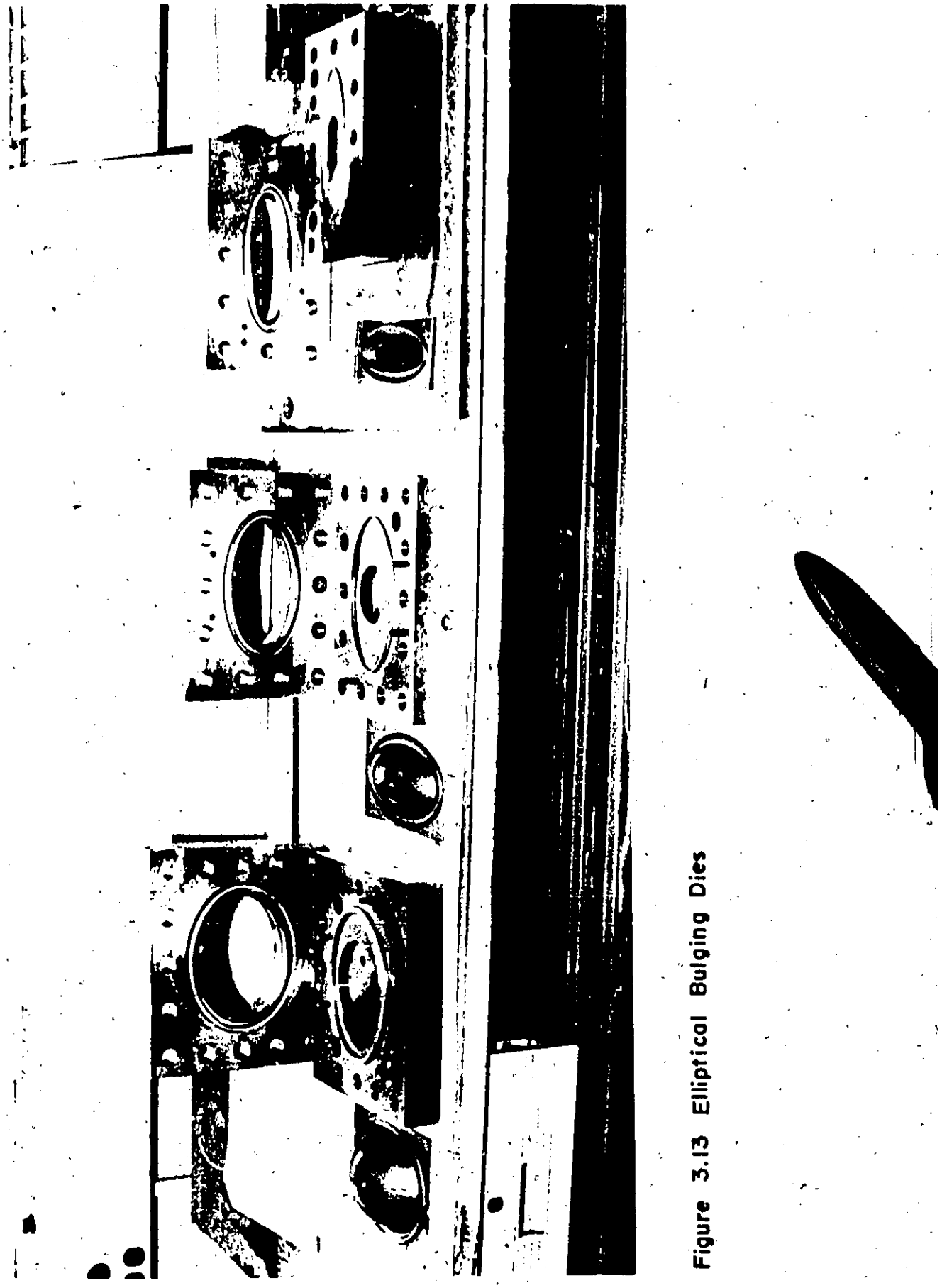

Figure 3.13 Elliptical Bulging Dies

instability. Oil pressure was applied to one side of the specimen by a manually-operated handpump and a series of Bourdon gauges were used for measuring the pressure (See Figure 3.12).

3.4.2. Characteristics of Elliptical Diaphragms

A typical deformed specimen in the elliptical die described above is shown schematically in Figure 3.14. The major and minor axes of the diaphragm are oriented in the directions oa and ob respectively, and oc is the axis of the dome as shown. The stress and strain system on the cross-section of the bulge aligned along the major and minor axes can be described by a moving coordinate system (1, 2, 3) as indicated in Figure 3.14.

a) Strain-Path

The straining process in the hydrostatic bulging can be described as a proportional straining process and at a point on the top of the bulge, the strain path can be approximated as a straight line. Typical strain paths for an anisotropic mild steel sheet bulged in a 2:1 aspect ratio die are shown in Figure 3.15. Isotropic materials produce similar strain paths when bulged in a particular die, and typical polar membrane strain ratios for the three elliptical dies are shown in Figure 3.16.

Away from the pole of the deformed diaphragm the strain ratio changes and the strain path may not be linear. Figure 3.17 shows the strain ratios at different locations with respect to

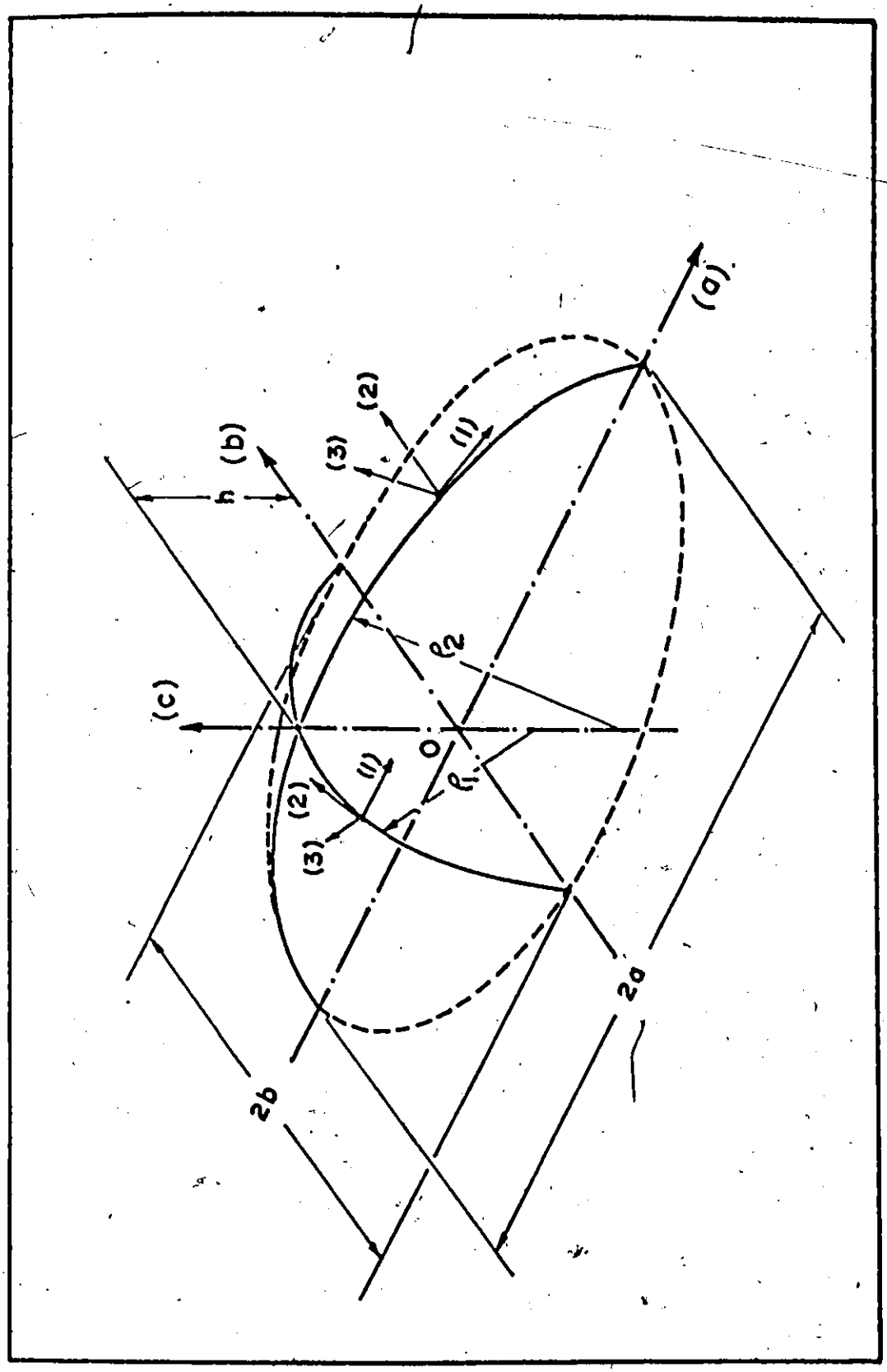

Figure 3.14. Schematic Representation of Deformed Elliptical Diaphragm.

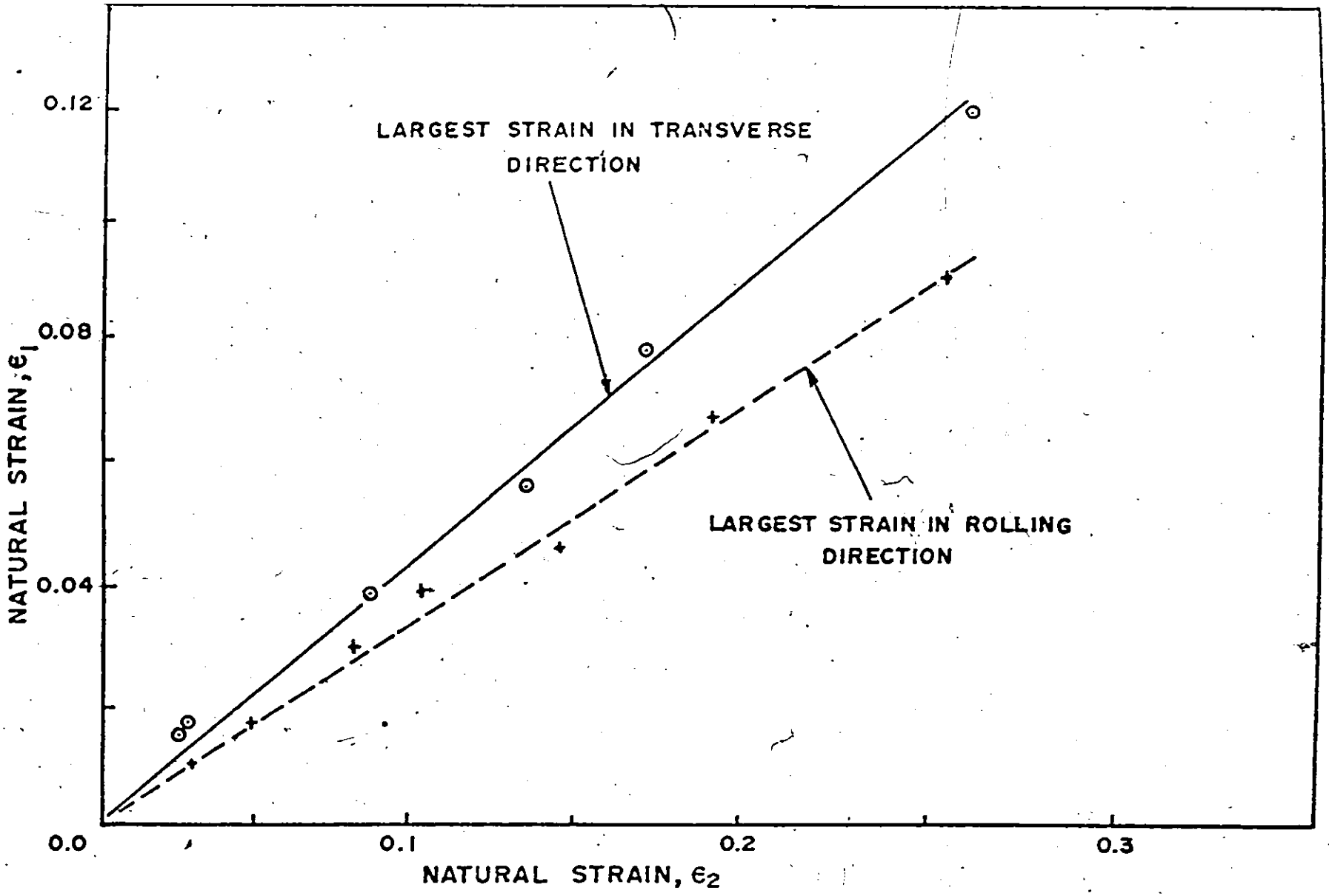

Figure 3.15. Polar Strain Paths for an Anisotropic Mild Steel Sheet Bulged in 2:1 Aspect Ratio Die.

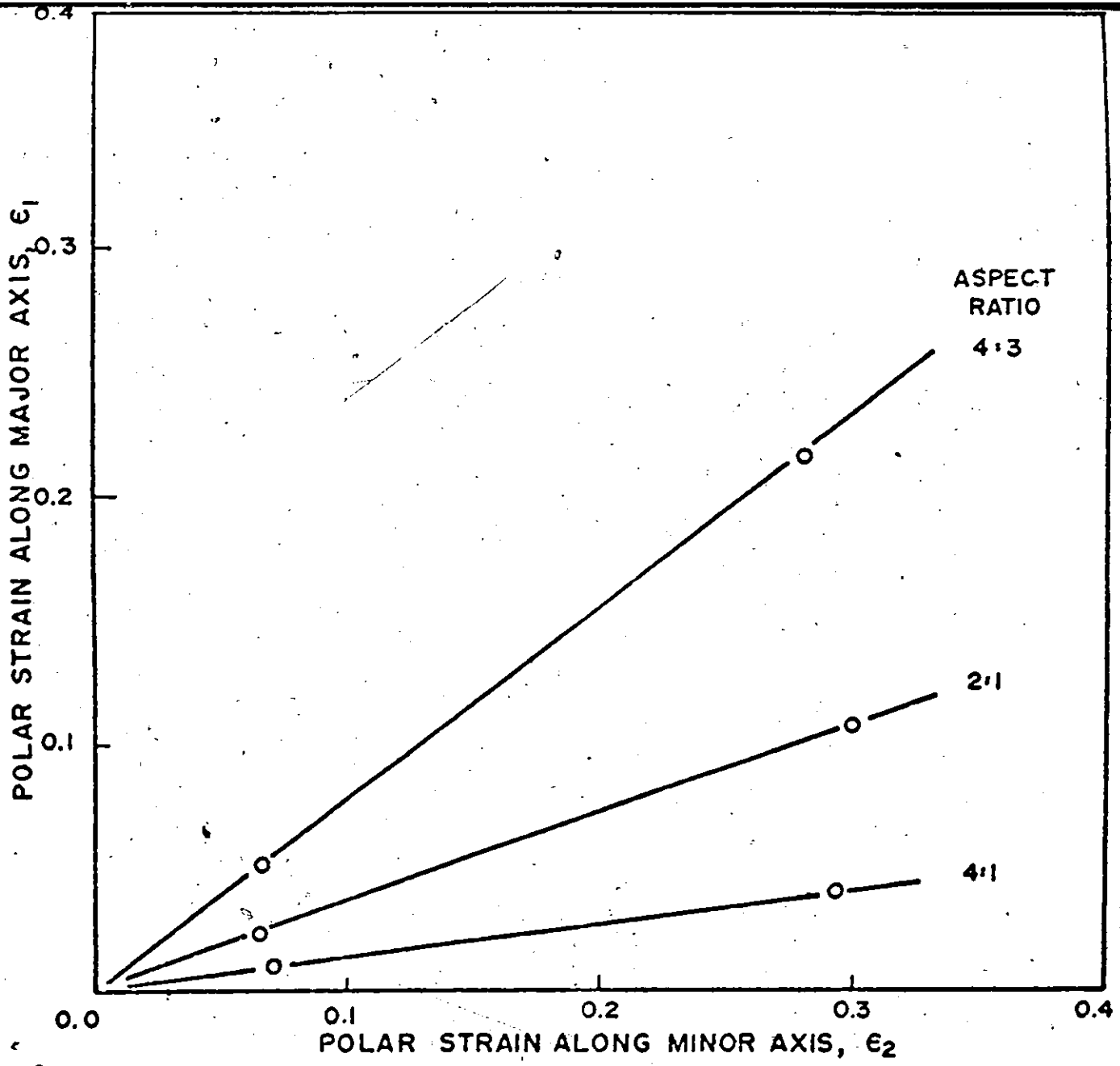

Figure 3.16. Mean Polar Strain Paths for Mild Steel Diaphragms Bulged in Elliptical Dies.

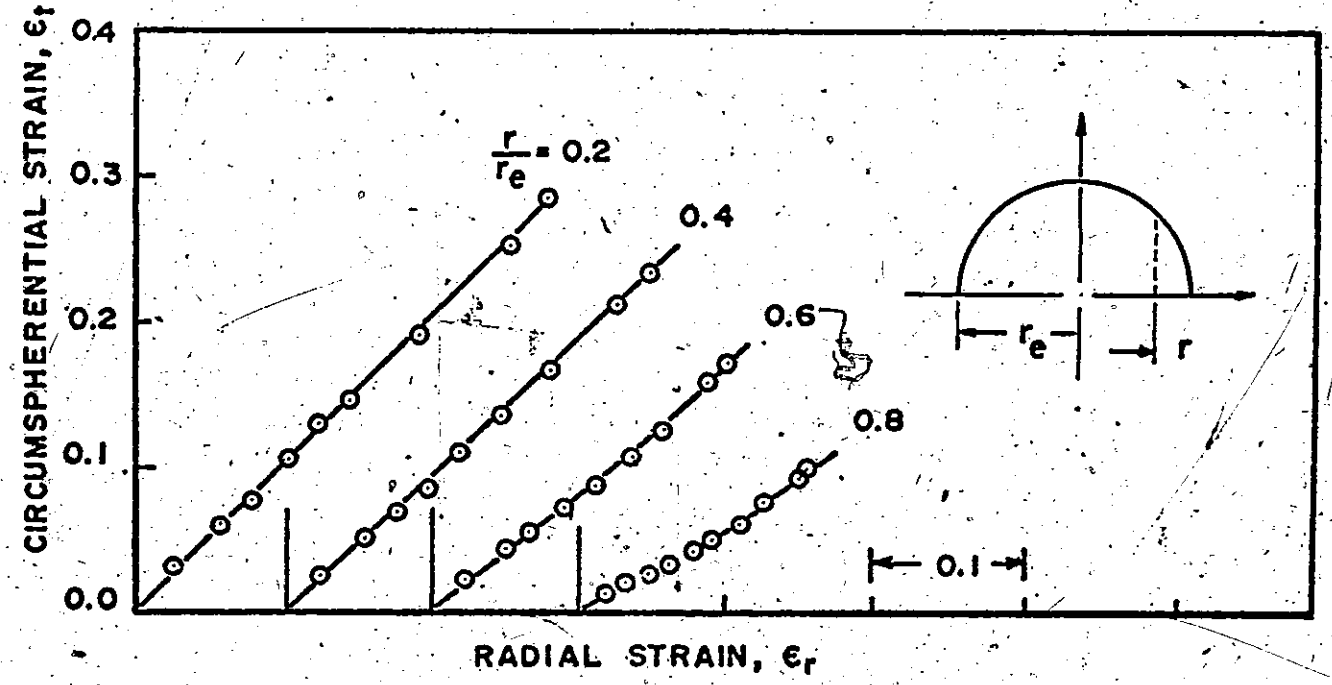

Figure 3.17. Strain Paths for Circular Diaphragm of Aluminum-Killed Steel at different Radial Distances [3.11].

the center of a circular bulge of aluminum-killed steel sheet [3.11]. It is observed that the deviation of the strain path from linearity is not large even at a point very close to the edge.

b) Diaphragm Profiles

Profiles of steel diaphragms at the deformed axes are approximately circular. Figure 3.18 shows the mean radius of curvature at various points along the major and minor axes of the steel diaphragm bulged to different heights in the 4:3 aspect ratio die. The minor axis is approximately circular and the major axis has a larger radius of curvature at the pole and a smaller one at the edge at small polar height.

c) Strain-Profiles and Strain-Ratios

The strain distributions of highly anisotropic steel diaphragms bulged in different aspect ratio dies are shown in Figures 3.19 to 3.23. The membrane strains along the major and minor axes are largest at the pole and decrease towards the edge, thus for these diaphragms the thickness is smallest at the pole where fracture is likely to occur.

Strain data from Figures 3.19 to 3.23 are replotted in the principal strain diagrams, Figures 3.24(a) and (b). It is seen from these figures that the strain ratio along the axes of the diaphragm decreases from the center to the edge. However, the change of strain-ratio along the major axis is smaller than that along the minor axis and for the 4:1 aspect ratio die the transverse strain on the major axis is nearly constant.

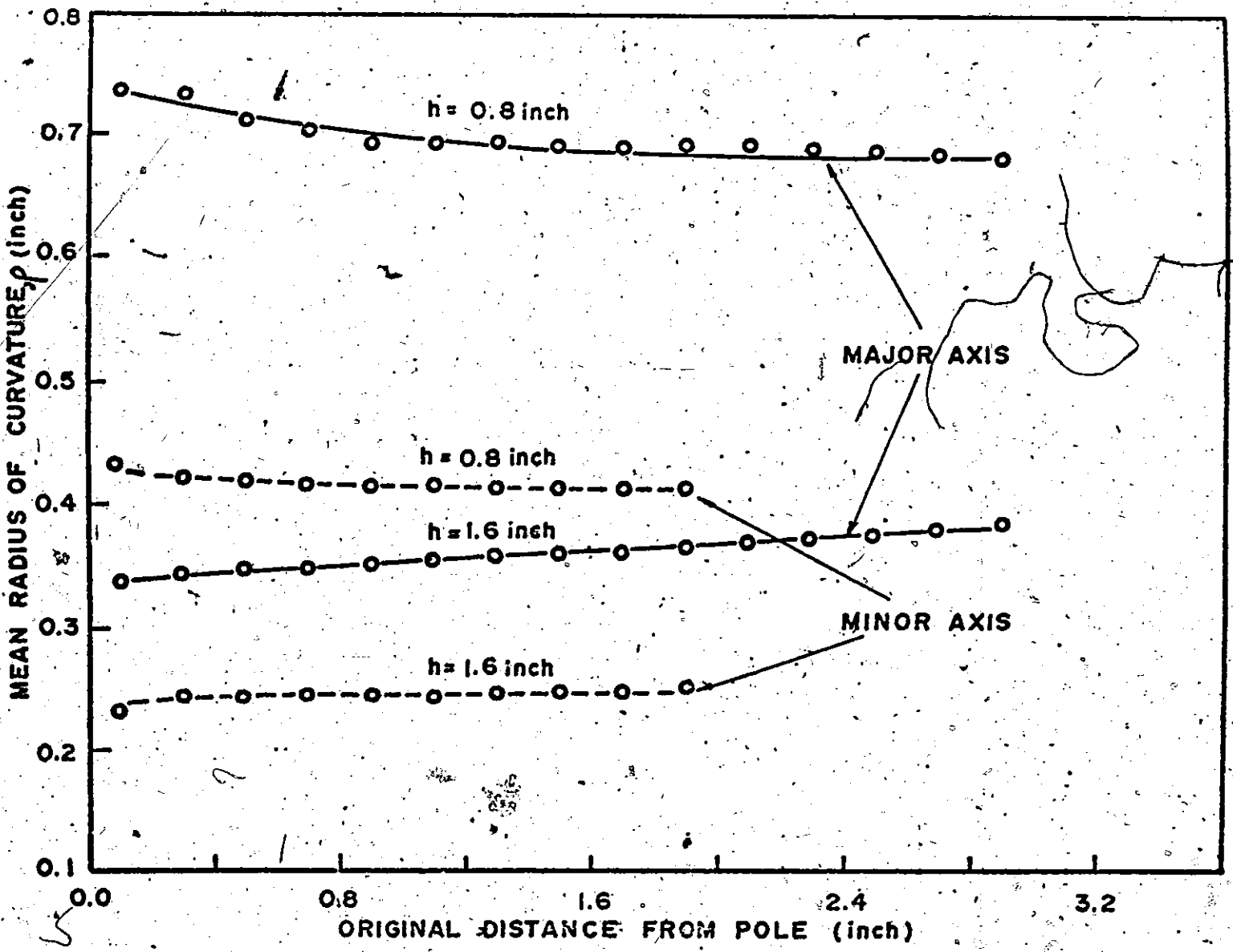

Figure 3.18. - Mean Radius of Curvature of Mild Steel Diaphragm Bulged to different Heights in 4:3 Aspect Ratio Die.

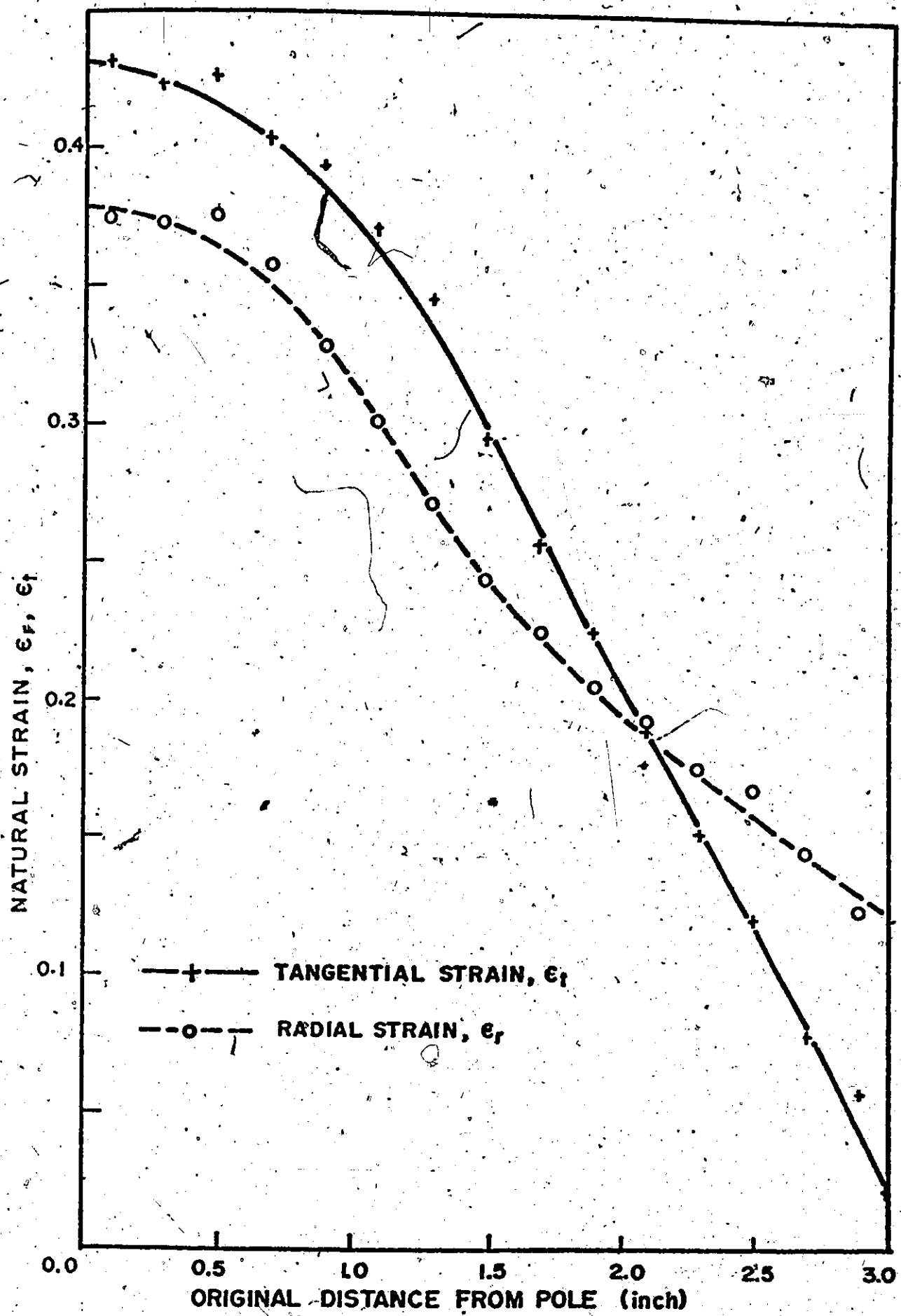

Figure 3.19. Strain Profiles of Anisotropic Mild Steel Diaphragm Bulged in Circular Die.

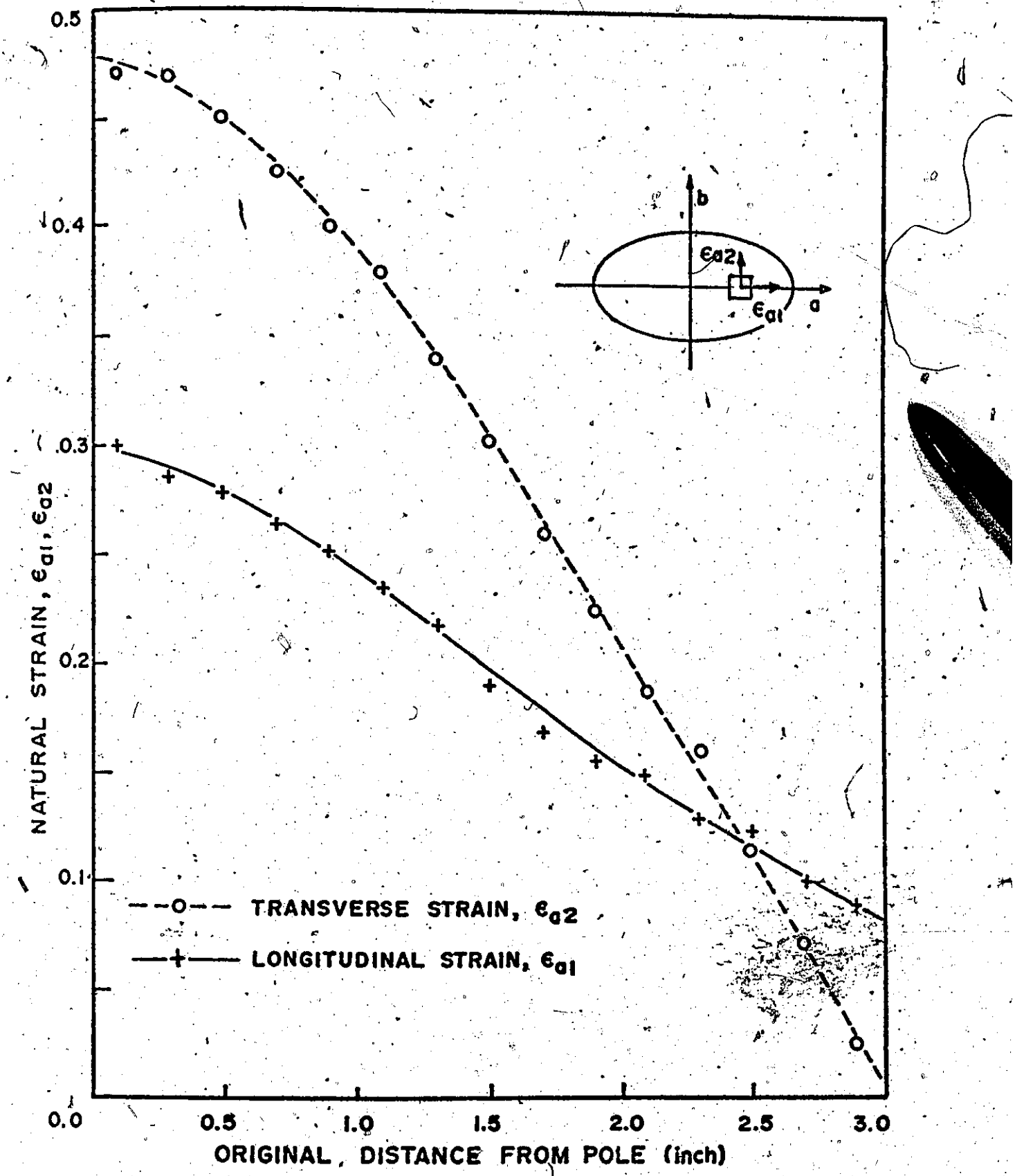

Figure 3.20a. Strain Profiles of Mild Steel Diaphragm Bulged in 4:3 Aspect Ratio Die.
a) Along Major Axis.

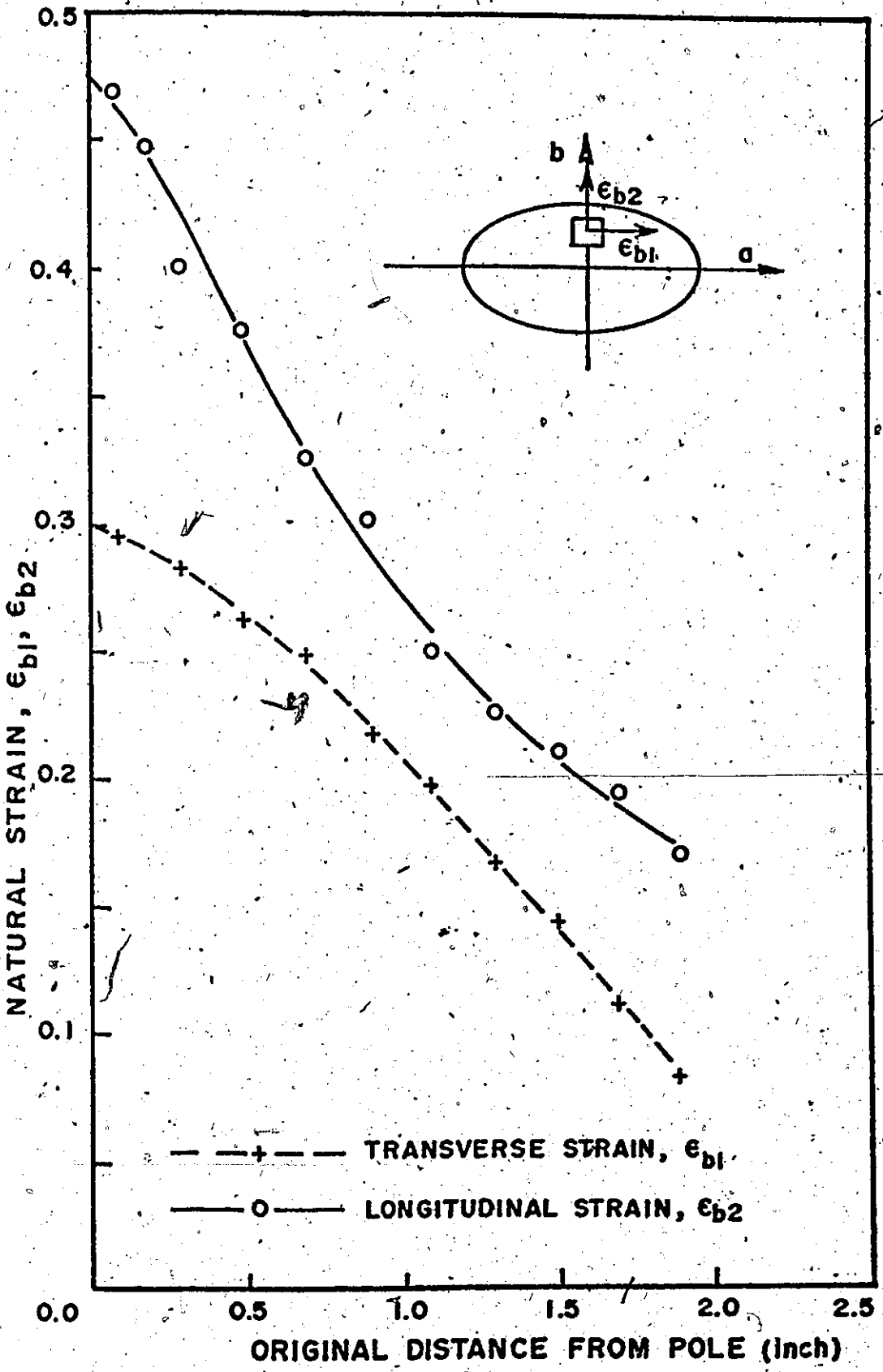

Figure 3.20b. Strain Profiles of Mild Steel Diaphragm Bulged in 4:3 Aspect Ratio Die.

b) Along Minor Axis.

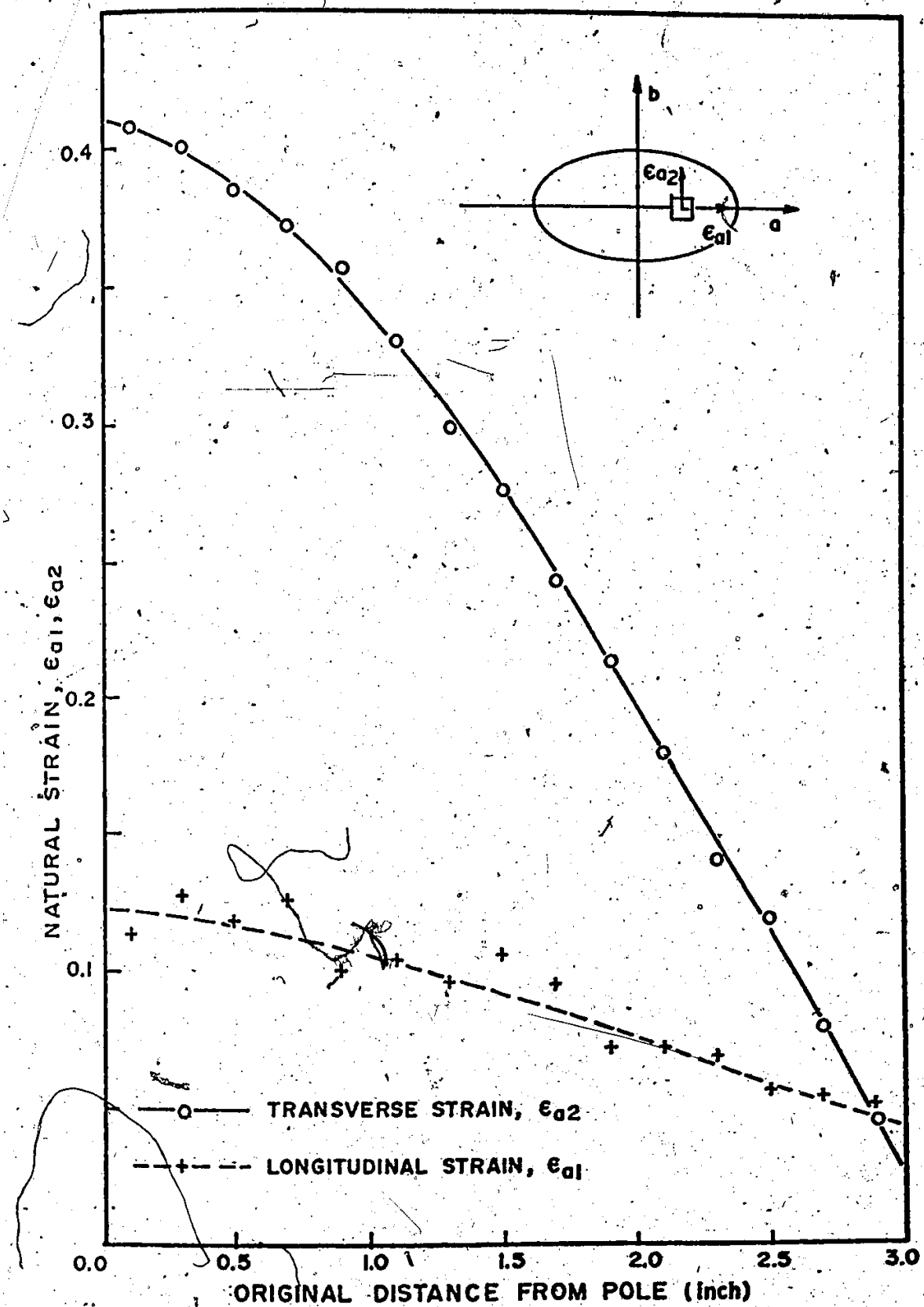

Figure 3.21a. Strain Profiles of Mild Steel Diaphragm Bulged in 2:1 Aspect Ratio Die.

a) Along Major Axis.

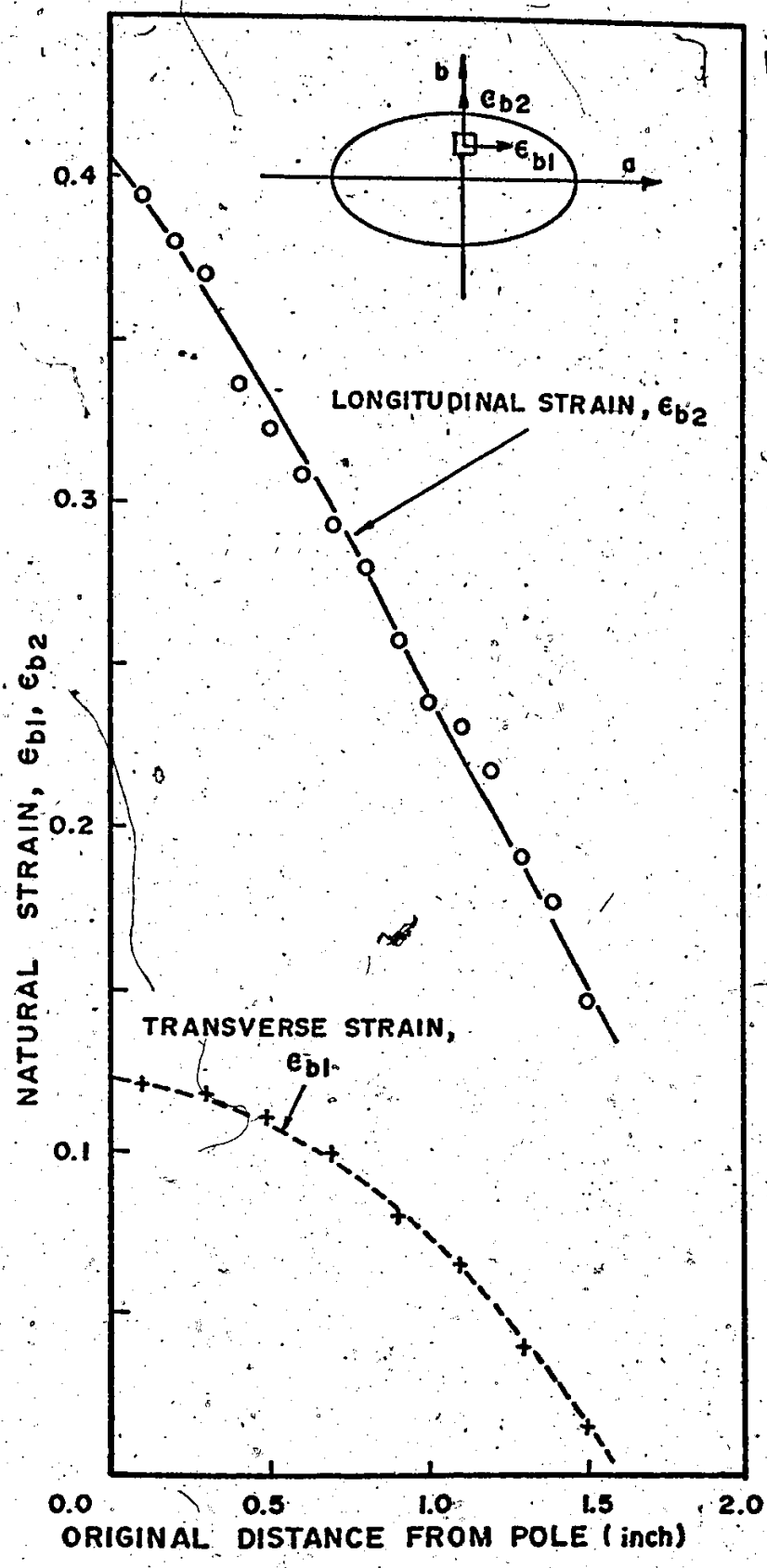

Figure 3.21b. Strain Profiles of Mild Steel Diaphragm Bulged in 2:1 Aspect Ratio Die.
b) Along Minor Axis.

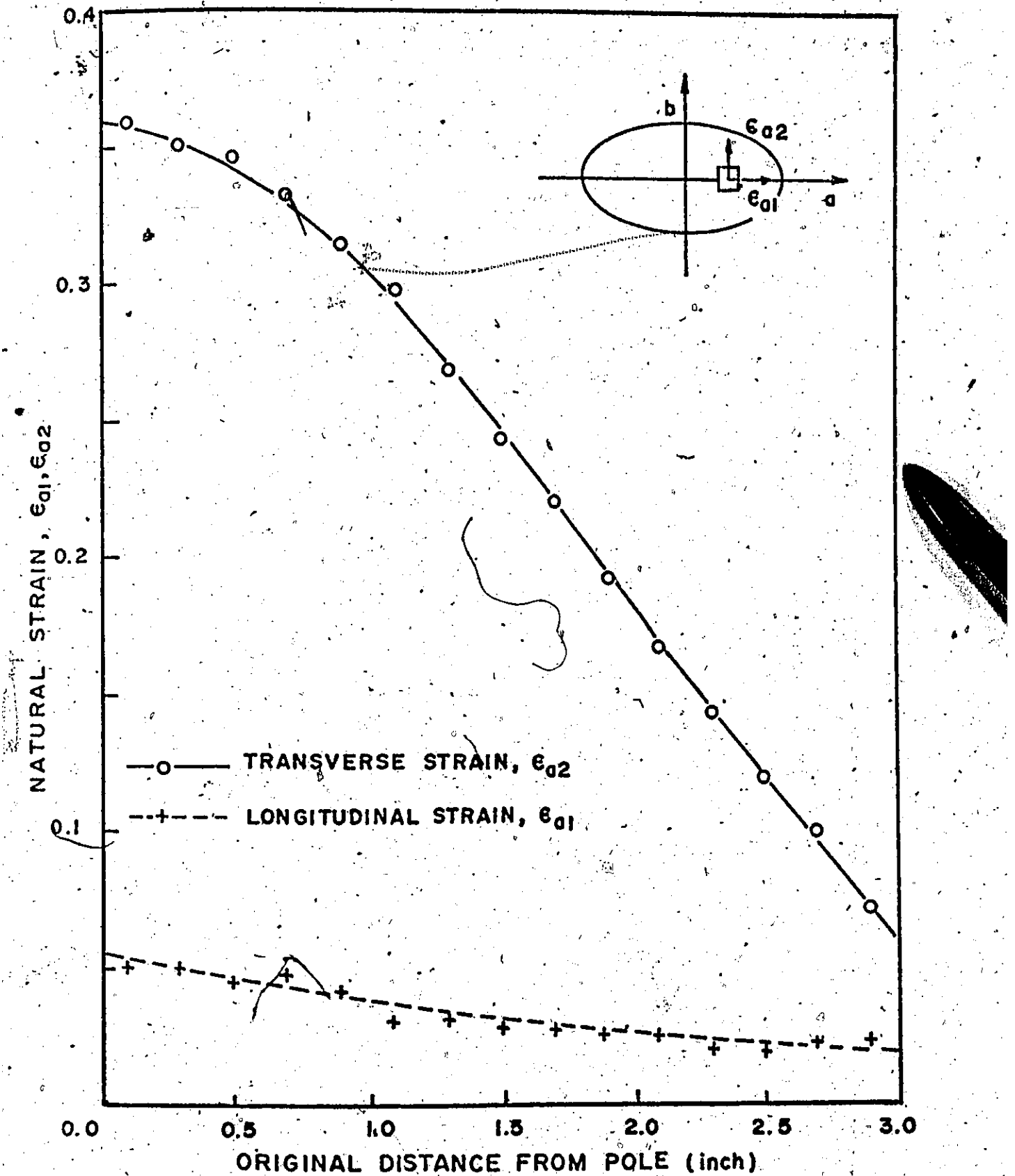

Figure 3.22a. Strain Profiles of Mild Steel Diaphragm Bulged in 4:1 Aspect Ratio Die.

a) Along Major Axis.

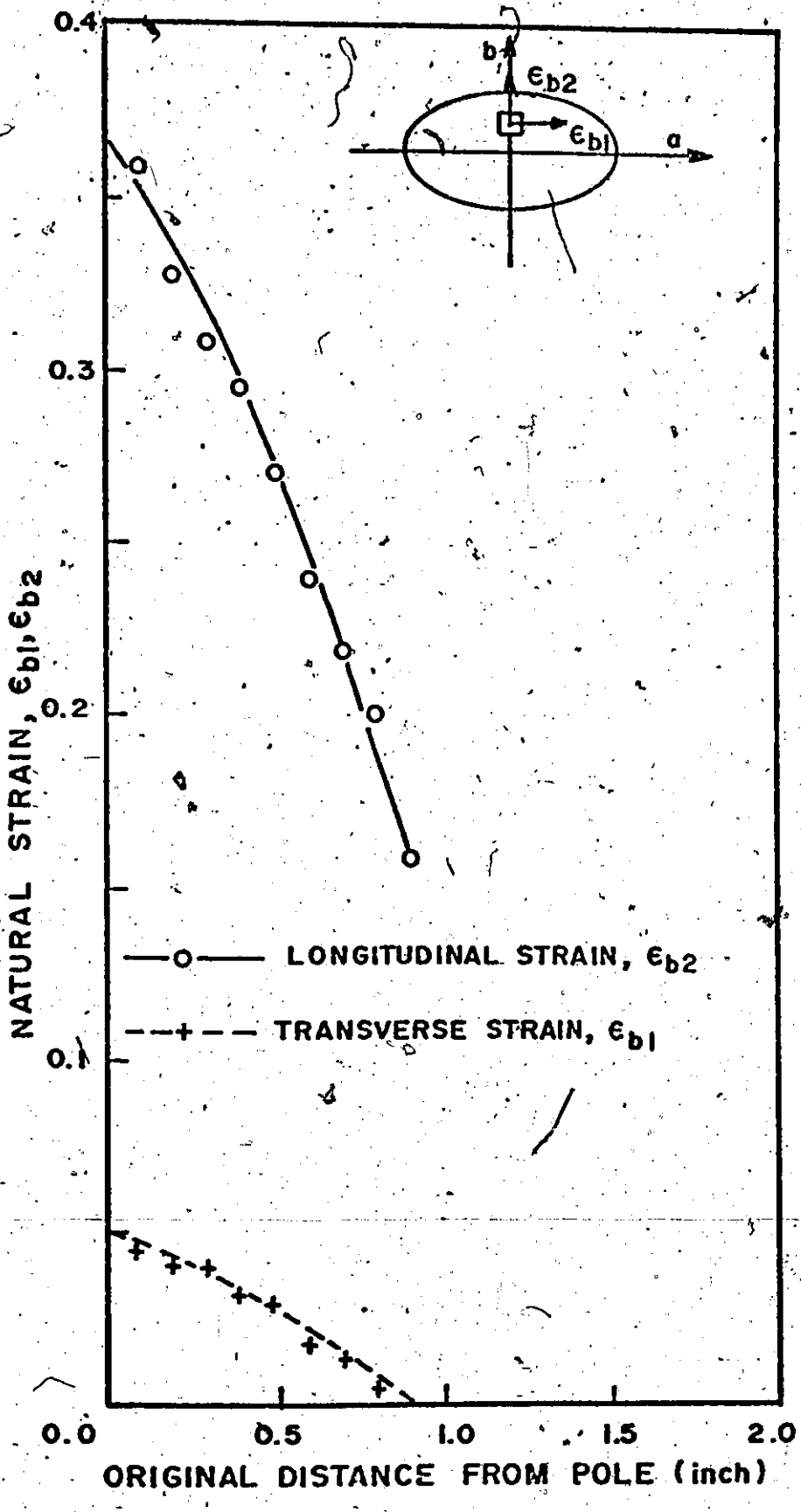

Figure 3.22b. Strain Profiles of Mild Steel Diaphragm Bulged in 4:1 Aspect Ratio Die.

b) Along Minor Axis.

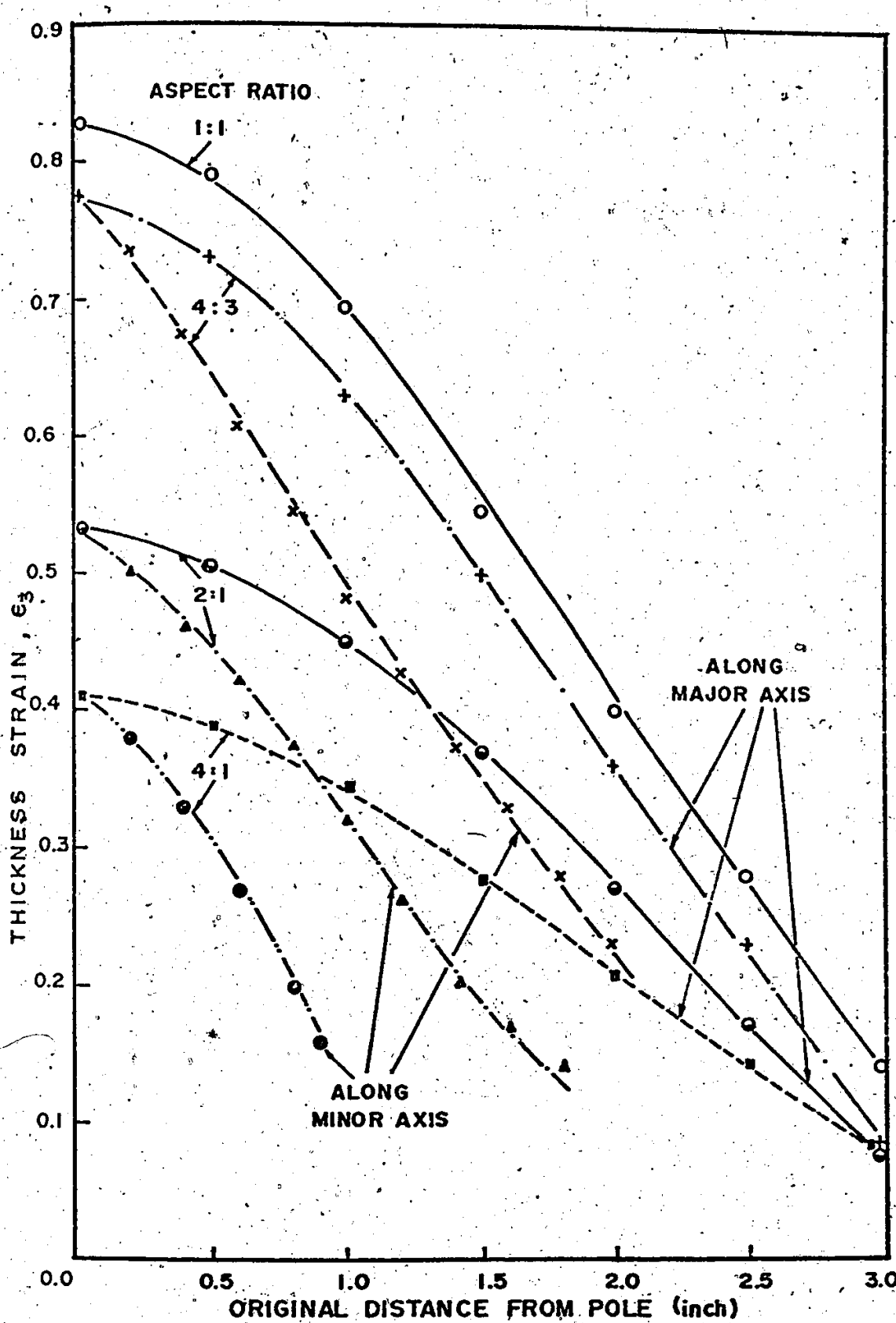

Figure 3.23. Thickness Strain Profiles for Mild Steel Diaphragms Bulged in Elliptical Dies with different Aspect Ratios.

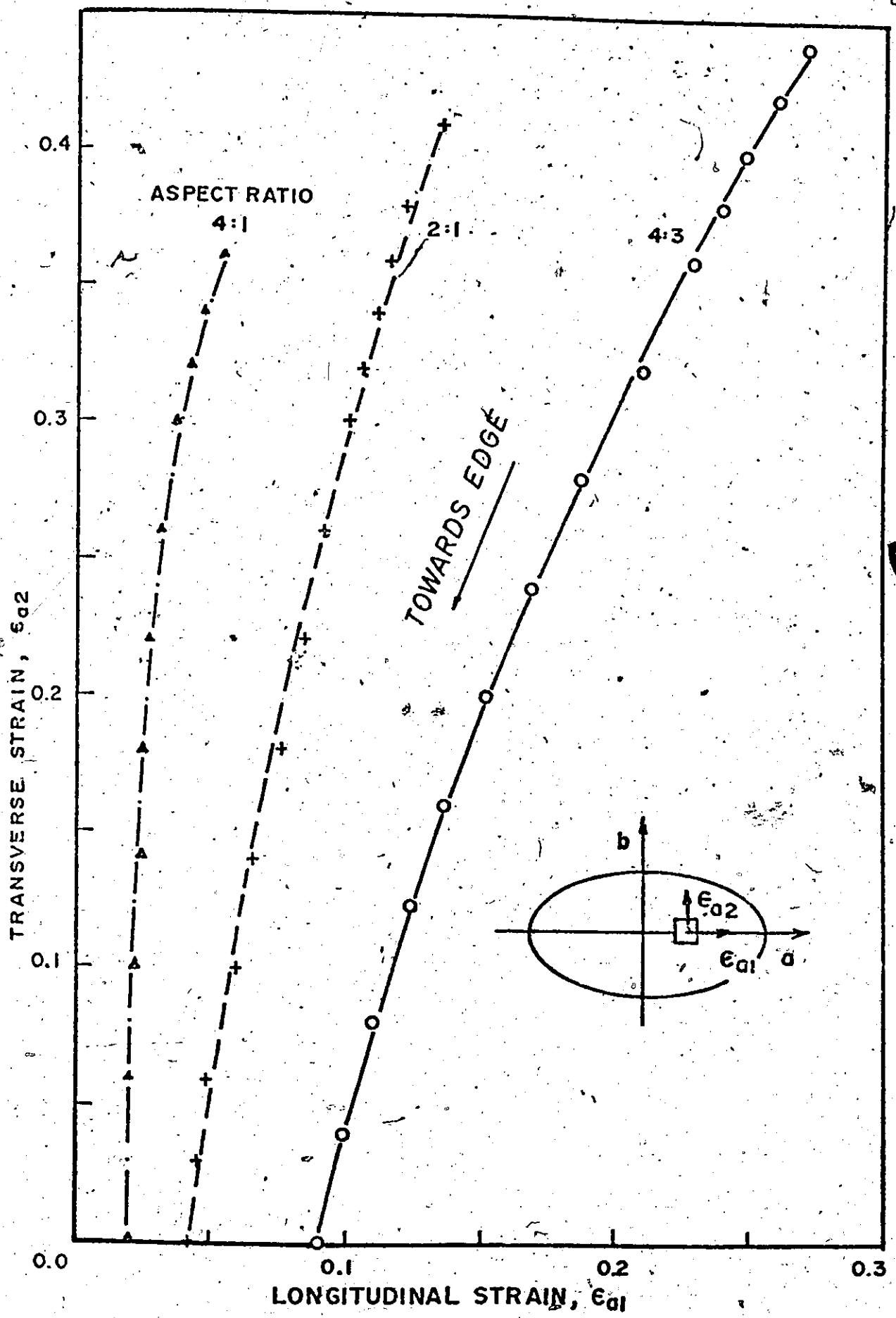

Figure 3.24a. Membrane Strain-Ratios in Elliptical Diaphragms Along
a) Major Axis

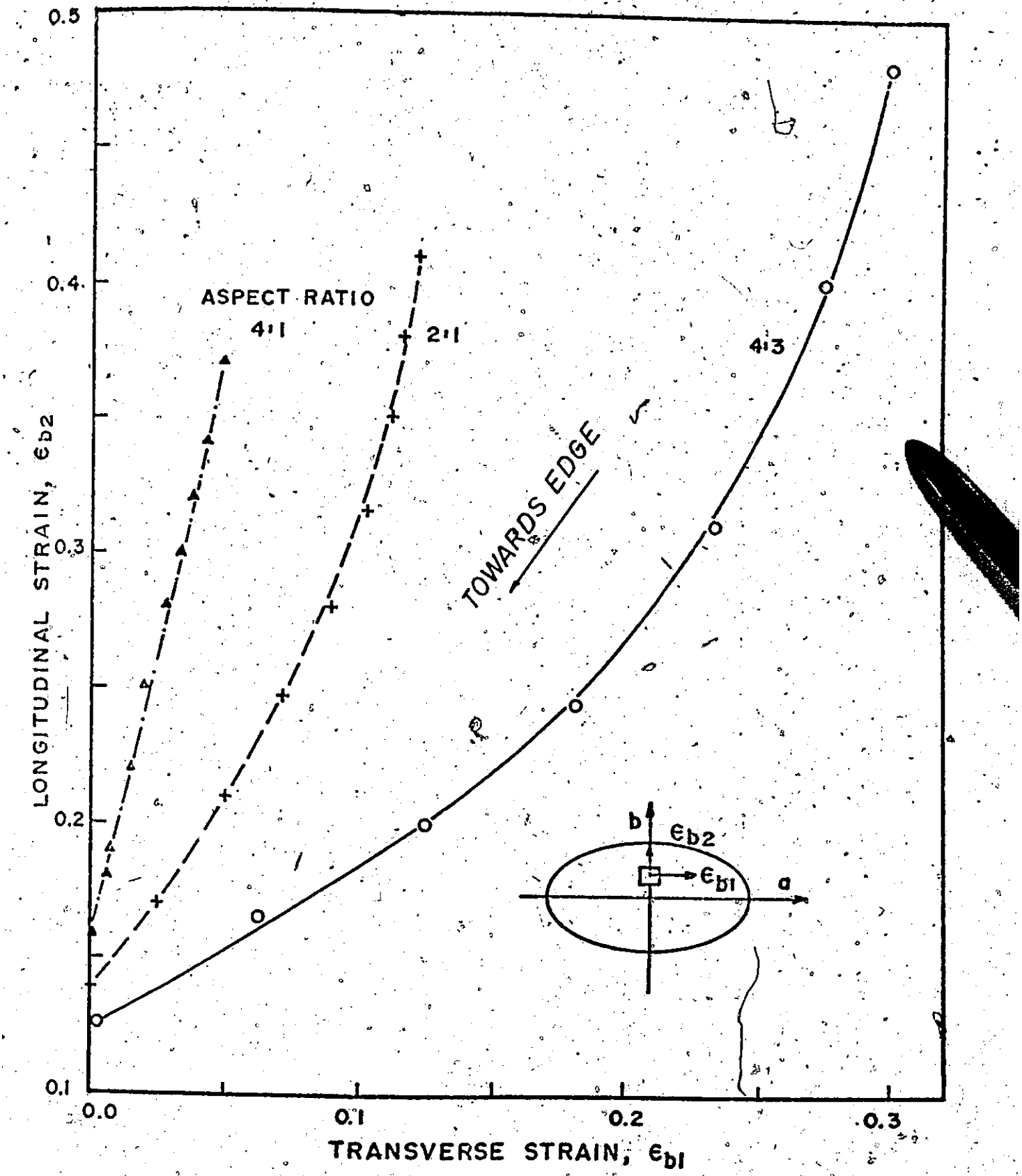

Figure 3.24b. Membrane Strain-Ratios in Elliptical Diaphragms Along
b) Minor Axis

3.5. Analysis of Failure of Diaphragms in Hydrostatic Bulging Processes

The failure of metal diaphragms in hydrostatic bulging processes can be described in terms of either diffuse or localized necking, and the probability of occurrence of either of these modes is dependent on the straining condition. For diaphragms which failed at the pole, the Marciniak groove can be applied to calculate the limit strains; these are a function of strain-ratio as mentioned earlier.

3.5.1. Diffuse Instability

Hill's and Swift's analysis of diffuse necking in the bulging of circular diaphragms was based on an arbitrary but reasonable assumption that the diaphragm's profile is circular. This assumption, however, cannot be applied to the elliptical bulge as it was shown that the profile of these diaphragms deviates from circularity.

It can be demonstrated also that the diffuse instability strain is influenced by the shape of these profiles. In elliptical diaphragms, there are three possible profile shapes: circular, elliptical or a combination of the two.

a) Diaphragms with Circular Profiles

This is a generalization of Hill's analysis of the circular bulge [3.7]. The profiles of elliptical diaphragms along both major and minor axes are assumed to be circular and the particle path of any point on these axes is assumed to be orthogonal to the current diaphragm's surface.

Using the assumption of a circular particle path, the strain at the pole along the major and minor axes can be approximated by

$$\epsilon_1 = \ln\left(1 + \frac{h^2}{a^2}\right) , \qquad (3.43)$$

and $$\epsilon_2 = \ln\left(1 + \frac{h^2}{b^2}\right) ,$$

where h is the height of the dome.

At the pole, the radii of curvature along the major and minor axes are

$$\rho_1 = \frac{a^2}{2h}\left(1 + \frac{h^2}{a^2}\right) , \qquad (3.44)$$

and $$\rho_2 = \frac{b^2}{2h}\left(1 + \frac{h^2}{b^2}\right) .$$

Let p be the applied pressure and if σ_1 and σ_2 are the principle stresses, then the equilibrium equation for an element near the top of the bulge is

$$\frac{\sigma_1}{\rho_1} + \frac{\sigma_2}{\rho_2} = \frac{p}{t} , \qquad (3.45)$$

where t is the thickness at the pole.

Differentiating Equation (3.45) and noting that at instability $\frac{dp}{p} = 0$, one obtains

$$\frac{d\sigma_2}{\sigma_2} = -\frac{dt}{t} + \frac{d\rho_2}{\rho_2} - \frac{\frac{\rho_2}{\alpha\,\rho_1}}{1 + \frac{\rho_2}{\alpha\,\rho_1}}\left(\frac{d\rho_2}{\rho_2} - \frac{d\rho_1}{\rho_1}\right) , \qquad (3.46)$$

where

$$\frac{dt}{t} = d\varepsilon_3 = -(d\varepsilon_1 + d\varepsilon_2),$$

Substituting Equations (3.44) and (3.45) into Equation (3.46) one can deduce that

$$\frac{d\sigma_2}{\sigma_2 d\varepsilon_2} = 2 - \frac{1}{2}\frac{e^{\varepsilon_2}}{e^{\varepsilon_2}-1} + \frac{\rho_2}{\rho_1} + \frac{\frac{\rho_2}{\alpha\rho_1}}{1-\frac{\rho_2}{\alpha\rho_1}}\left[\frac{\rho_2}{\rho_1} - 1\right], \qquad (3.47)$$

where

$$\frac{\rho_2}{\rho_1} = \frac{e^{\varepsilon_2}}{e^{\varepsilon_1}}\,\frac{e^{\varepsilon_1}-1}{e^{\varepsilon_2}-1} = \frac{2-\alpha}{2\alpha-1}.$$

Using the empirical stress-strain relationship, Equation (3.7a) and the equivalent stress and strain, Equations (3.2) and (3.5), one obtains

$$\frac{d\sigma_2}{\sigma_2 d\varepsilon_2} = \frac{n}{\varepsilon_2}. \qquad (3.48)$$

Combining this with Equation (3.47) gives

$$\frac{n}{\varepsilon_2} = 2 - \frac{1}{2}\frac{e^{\varepsilon_2}}{e^{\varepsilon_2}-1} + \frac{2-\alpha}{2(2\alpha-1)}\,\frac{(2\alpha^2-5\alpha+5)}{(\alpha^2-\alpha+1)}. \qquad (3.49)$$

Recalling the Taylor Series expansion of an exponential is given by

$$e^u = 1 + \frac{u}{1!} + \frac{u^2}{2!} + \frac{u^3}{3!} + \ldots,$$

equation (3.49) for ε_2, can be approximated as

$$\varepsilon_2^* = \frac{2n+1}{2}\left(\frac{7}{4} + \frac{(2-\alpha)}{2(2\alpha-1)}\,\frac{(2\alpha^2-5\alpha+5)}{(\alpha^2-\alpha+1)}\right)^{-1},$$

(3.50)

and

$$\varepsilon_1^* = \frac{2-\alpha}{2\alpha-1}\,\varepsilon_2^*.$$

These are the critical strains at diffuse instability.

Special cases

For equal-biaxial tension $\alpha = 1$ and Equations (3.50) become

$$\varepsilon_1^* = \varepsilon_2^* = \frac{2}{11}(2n+1),$$

which of course is the relation obtained by Hill.

For the plane-strain condition, $\alpha = 2$. Equations (3.50) give

$$\varepsilon_1^* = 0,$$

and

$$\varepsilon_2^* = \frac{2}{7}(2n+1).$$

b) Diaphragms with Elliptical Profiles

In cases where the diaphragm profiles along the axes are elliptic rather than circular, the instability analysis takes a different form. The local radii of curvature at the pole of the profiles along the major and minor axes can be approximated as

$$\rho_1 = \frac{a^2}{h},$$

and (3.51)

$$\rho_2 = \frac{b^2}{h}.$$

From the assumption of orthogonality of the particle paths and diaphragm's profile, the principal strains at the pole along the axes of the diaphragm are derived to be

$$d\varepsilon_1 = \frac{dh}{\rho_1},$$

and (3.52)

$$d\varepsilon_2 = \frac{dh}{\rho_2}.$$

Using the equilibrium Equation (3.45) and performing the same analysis, one can obtain the pole strain at instability as

$$\varepsilon_2^* = \frac{2\alpha-1}{2(\alpha+1)} \quad (2n+1),$$

and (3.53)

$$\varepsilon_1^* = \frac{2-\alpha}{2\alpha-1} \quad \varepsilon_2^*.$$

Special cases

For equal-biaxial tension, $\alpha = 1$,

$$\varepsilon_2^* = \varepsilon_1^* = \frac{1}{4}\,(2n+1).$$

And for the plane-strain case, $\alpha = 2$,

$$\varepsilon_1^* = 0,$$

and

$$\varepsilon_2^* = \frac{1}{2}(2n+1).$$

c) Diaphragms with Elliptical and Circular Profiles

It was shown in section 3.4 that, for elliptical diaphragms, the profile on the major axis deviates markedly from a circle. Let us assume then that the profile on the major axis is a part of an ellipse while the profile on the minor axis is circular. The instability strains for such a diaphragm can be derived as follows.

At the pole, the local radii of curvature along the major and minor axes are

$$\rho_1 = \frac{a^2}{h},$$

and (3.54)

$$\rho_2 = \frac{b^2+h^2}{2h}.$$

The polar principal strains along these axes are

$$\varepsilon_1 = \frac{h^2}{2a^2},$$

and (3.55)

$$\varepsilon_2 = \ln\left(1 + \frac{h^2}{b^2}\right).$$

From the equilibrium Equation (3.45) and by a similar analysis, one can derive that

$$\frac{d\sigma_2}{\sigma_2 d\varepsilon_2} = 2 - \frac{1}{2\varepsilon_1} + \frac{2-\alpha}{2\alpha-1} - \frac{2-\alpha}{2(\alpha^2-\alpha+1)} , \qquad (3.56)$$

and also that

$$\frac{d\sigma_2}{\sigma_2 d\varepsilon_2} = \frac{n}{\varepsilon_2} .$$

The instability strains are then

$$\varepsilon_2^* = \frac{2n+1}{2} \left[2 + \frac{(2-\alpha)(3-3\alpha+2\alpha^2)}{2(2\alpha-1)(\alpha^2-\alpha+1)}\right]^{-1}$$

and (3.57)

$$\varepsilon_1^* = \frac{\alpha-2}{2\alpha-1} \varepsilon_2^* .$$

Special case

For the plane-strain condition, $\alpha = 2$, Equations (3.57) become

$$\varepsilon_1^* = 0,$$

and

$$\varepsilon_2^* = \frac{1}{4} (2n+1).$$

Equations (3.50), (3.53), and (3.57) represent the instability strains for diffuse necking of elliptical diaphragms having different profiles and are dependent on the assumption that the pressure reaches a maximum at this point. For an n-value

of 0.25 the instability strains can be plotted in the principal strain diagram as shown in Figure 3.25.

3.5.2. Localized Instability

In hydrostatic bulging of elliptical diaphragms, failure occurs most frequently at the pole where the thickness strain is the highest. In some cases, however, a strain concentration initiates near the edge of the die on the long side of the specimen and finally causes rupture at the edge. This is usually the case when brass, copper and sometimes steel diaphragms are tested in large aspect-ratio dies. An inspection of the specimen which failed in this mode reveals that a plane-strain condition exists at the failure zone and that the membrane strain measured at the pole was much smaller than that measured when the rupture was at the top of the dome.

At the edge of the specimen, the principal membrane stresses are not parallel to the axes of the ellipse due to the shear stresses which are of the same magnitude as the tensile stresses. Thus to calculate the pole strain at instability, a simplified analysis is attempted.

Consider the strain distribution on the minor axis of the elliptical diaphragm shown in Figure 3.24b. It is seen that for specimens bulged in a large aspect-ratio die, the ratio of the longitudinal to transverse strain is nearly constant, i.e., the relationship between the longitudinal and transverse strain on the minor axis can be approximated by

$$\epsilon_2 = C_1\epsilon_1 + (\epsilon_2)_e, \qquad (3.58)$$

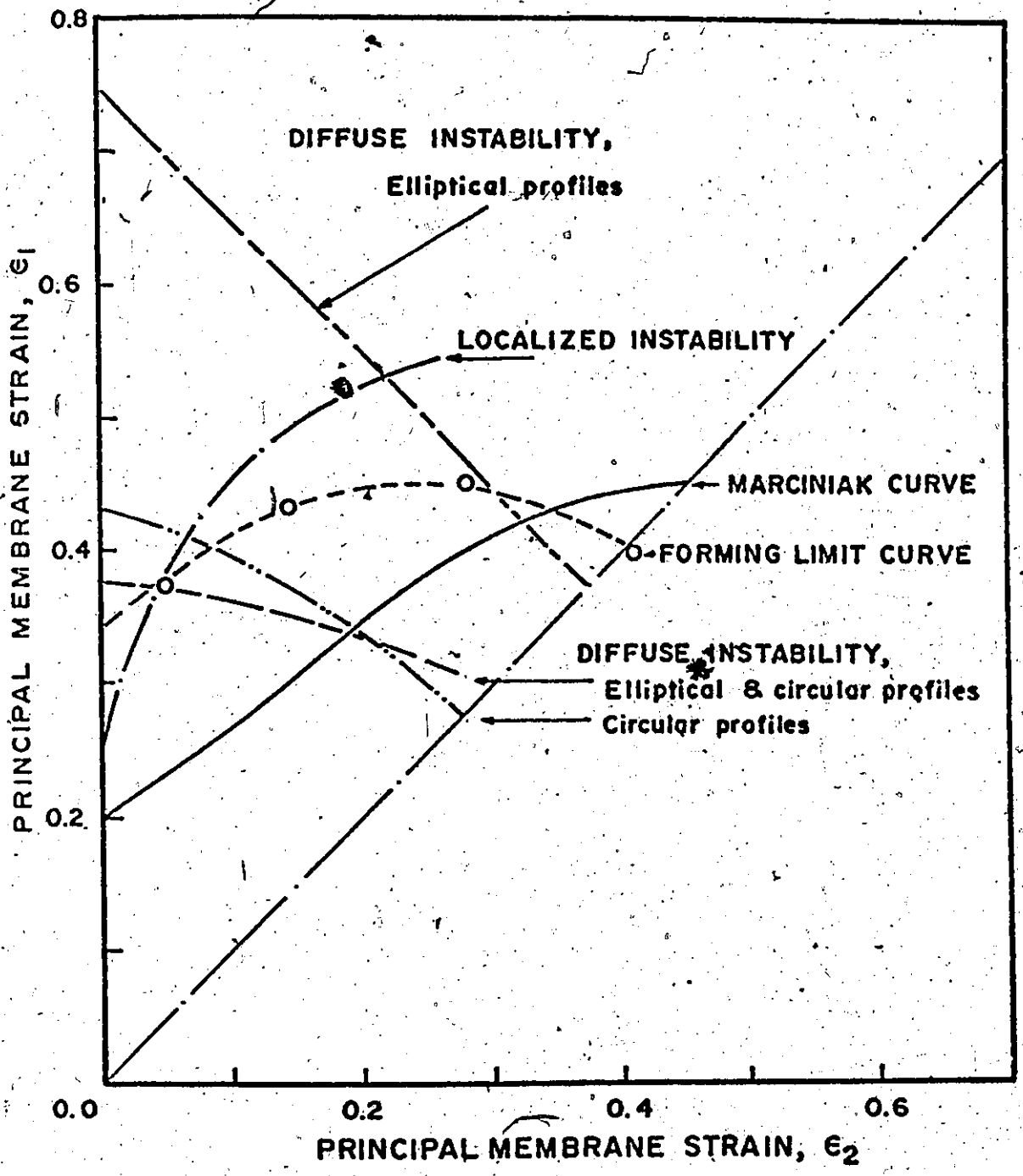

Figure 3.25. Critical Strains at Different Failure Modes and Forming-Limits of Mild Steel Diaphragms (n = 0.25, R = 1).

where ε_1 and ε_2 are the transverse and longitudinal strains respectively, $(\varepsilon_2)_e$ is the longitudinal strain at the edge of the diaphragm and C_1 is a constant dependent on the die geometry. Since diaphragm failure is due to plane strain at the edge, the longitudinal strain $(\varepsilon_2)_e$ at instability is given by

$$(\varepsilon_2^*)_e = n. \qquad (3.59)$$

For a particular die, the strain ratio at the pole is a constant, i.e.,

$$\frac{\varepsilon_1}{\varepsilon_2} = C_2 \qquad (3.60)$$

Combining the three Equations (3.58), (3.59) and (3.60) gives the pole strain at edge instability of the diaphragm, viz.,

$$\varepsilon_2^* = \frac{n}{1-C_1C_2} \qquad (3.61)$$

Table 3.1

Critical Strains for Localized Instability in Elliptical Bulging in Different Aspect Ratio Dies.

Die Aspect Ratio	C_1	C_2	ε_1^*	ε_2^*
Large A.R.	-	0	0	n
4:1	3.7	.13	.52n	1.9n
2:1	2.0	.27	1.07n	2.15n

Table 3.1 gives typical values of ε_1^* and ε_2^* for different aspect-ratio dies. These critical strains are plotted on a principal strain diagram, for n = 0.25, as shown in Figure 3.25.

3.5.3. Marciniak's Groove and Forming-Limit Curves

The Marciniak analysis described earlier can be applied to predict failure of elliptical diaphragms. The limit strains were calculated for different strain ratios ranging from zero to unity and with arbitrarily chosen material parameters. The parameters used were n = 0.25, f_o = .995, ε_o = .0075 and R = 1 and the results are plotted in the principal strain diagram as shown in Figure 3.25.

An experimental forming-limit curve was also obtained by measuring the limit strains on various elliptical and circular diaphragms tested. The results are indicated in Figure 3.25.

3.5.4. Discussion of Failure Modes

It is observed from Figure 3.25 that the diffuse instability curves in general have a similar trend; the instability strains decrease as the biaxiality is increasing and at equal-biaxial tension, the instability strains are lower than the forming limits. This indicates that in the deformation of circular diaphragms or that of elliptical diaphragms with polar strain ratio near unity, failure is normally preceded by a diffuse instability characterized by a pressure maximum.

As it is borne out by many experiments, the diffuse instability curve with assumed circular profiles does describe the failure characteristics of metal diaphragms well, near equal-biaxial tension. In the region near plane strain, however, the curve with mixed circular and elliptical profiles is closer to reality.

The localized instability curve shown in Figure 3.25 represents the polar strain for diaphragms failed at the edge. It is seen that edge failure can only occur in specimens bulged in large aspect-ratio dies and under this condition rupture takes place under rising pressure. The localized instability strain is thus smaller than the forming limit in the region near plane strain as indicated in Figure 3.25.

The Marciniak curve predicts the limit strains for elliptical diaphragms tested in various strain ratios. As the parameters used in the analysis are arbitrary, the Marciniak curve shows only the trend of the experimental forming limits.

From the above observation, one can distinguish three possible deformation modes which lead to fracture of metal diaphragms; these are described schematically in the following cases:

Case 1 Near plane strain.

As it was shown that the straining at the pole in the bulging process is a proportional process, the deformation of elliptical diaphragms can be represented by a straight line.

For specimens bulged in large aspect-ratio dies, the strain at the pole is near plane strain. The strain path in

this process is described by line OA as shown in Figure 3.26. Edge failure is likely to occur at A_1, the intersection of the strain path and the localized instability curve.

Diffuse instability is predicted by a combination of the two curves as shown in Figure 3.26. The first is for diaphragms with circular profiles on one axis and elliptical on the other, while the second is for diaphragms with circular profiles on both axes. The diffuse instability strain in the case where a near-plane-strain condition exists, is greater than the forming-limit and thus the diaphragms tend to fail under increasing pressure.

Case 2 Intermediate strain ratio.

When the polar strain ratio is between zero and unity, elliptical diaphragms usually fail at the pole. The straining process in this case is described by the line OB and the limit strain measured is indicated by point B_1. Diffuse instability cannot be used to describe the failure mode in these diaphragms as the sheet ruptures by a Marciniak groove process before the applied pressure reaches a maximum. The bulging of steel sheets in a 4:1 aspect-ratio die probably falls into this category (see Figure 3.25).

Case 3 Equal-biaxial tension.

For deformed diaphragms having a strain state approaching equal-biaxial tension, it is found that edge failure is unlikely to occur; this was in fact proved by Swift for circular diaphragms. The bulging pressure usually passes through a maximum where diffuse instability starts. Such a process is

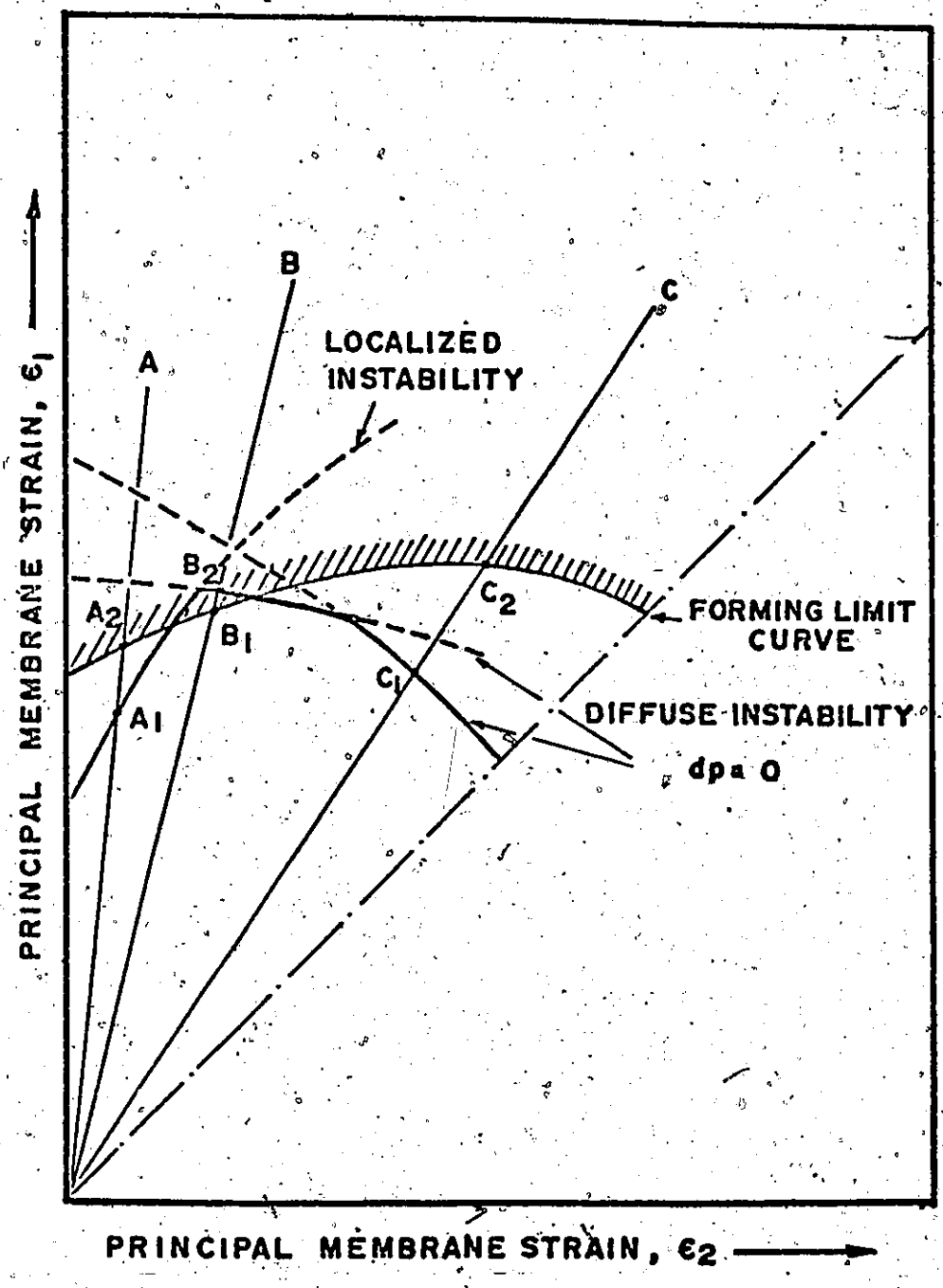

Figure 3.26. Schematic Description of the Deformation and Failure Modes of Mild Steel Diaphragms in Hydrostatic Bulging Processes.

described by line OC in Figure 3.26 with C_1 and C_2 being the instability and fracture points respectively.

3.6. Conclusions

The deformation and failure characteristics of metal diaphragms bulged in elliptical dies were investigated. The linearity of the strain path and the absence of friction in the process tends to make the bulging process more suitable than other formability tests where repeatability is of prime interest.

The instability theory of plane strain deformation was analysed and applied to the deformation of elliptical diaphragms. Diffuse necking associated with a pressure maximum can only occur when the strain ratio is near unity. Localized necking however, is related to edge failure of diaphragms bulged in large aspect-ratio dies.

The Marciniak analysis was also applied to predict failure in these diaphragms and it is recognised that the amount of stable straining in a process is not only dependent upon the strain-ratio and strain-hardening index, but also related to other material plastic properties.

CHAPTER 4

EXPERIMENTAL INVESTIGATION OF THE VARIABILITY OF THE FORMING LIMIT CURVES

4.1. Introduction

When sheet metal is stretched in biaxial tension so that both principal strains in the plane of the sheet are tensile, failure is believed to be preceded by a localized plastic strain-concentration process. The description of localized necking given by Hill [3.3] does not apply to biaxial stretching as there is no line of zero extension in the sheet. A hypothesis for strain concentration and failure was given by Marciniak [3.5] who assumed a pre-existing inhomogeneity in the sheet which gradually developed into a strain concentration or "groove"; failure occurs eventually by fracture in the trough of this groove. He identified a useful quantity called the "limit strain"; this is the maximum uniform strain adjacent to a tear in a given material when it is biaxially stretched in a proportional straining process. The limit strain is a measure of the maximum amount of useful stretching which can be achieved in a pressing without rupture. It was shown that this depended not only on the strain-ratio of the process and on the plastic and fracture properties of the sheet but also on the severity of the initial inhomogeneity in the material.

Using this hypothesis, the variation of limit-strain with strain-ratio can be calculated and drawn in the principal

membrane strain space. This is known as a "forming-limit diagram" and following the work of Keeler and Backofen [1.3], these diagrams have been used extensively in the failure analysis of industrial pressings.

Forming-limit curves can be regarded as material property curves and industrially the curve for a particular material is always established experimentally. Samples of the sheet are stretch-formed in a test in which adjustment of the test piece shape or the test conditions gives rise to different proportional loading processes. Forming limits are also obtained from strain measurements near tears in actual pressings or from hydrostatic bulging of diaphragms of different plan shape. It is recognized that different test procedures do not necessarily lead to identical forming limit curves and that the differences are due to the steepness of the strain gradient in the region of failure, the gauge length employed in membrane strain measurements and possibly to the effect of friction between the sheet and the tooling.

In spite of the known discrepancies between forming limit curves determined by different methods, the forming-limit for a particular strain ratio is generally interpreted as being a single-valued material property. Following Marciniak's hypothesis it can be proposed however that as tearing results from defects which are distributed throughout the sheet, the forming limit is not single-valued but can only be described in statistical terms. The maximum uniform strain which can be achieved adjacent to a tear will depend on the probability of a

defect of a certain severity falling inside a region of critical straining within a pressing.

The work presented in this chapter is an experimental study aimed at testing this hypothesis. Forming limits were obtained for four different samples of cold-rolled mild steels using elliptical bulging dies; three dies of different aspect-ratios were used and also a circular die. The material was stretch-formed to rupture in proportional loading processes with a strain ratio between 0.1 and 1.0. Approximately 20 test pieces from any one sheet were bulged to failure in each die and the limit strains were measured. The mean and standard deviation of each set were obtained. The error in terms of a standard deviation which could be attributed to the experimental technique was also calculated and the deviations for each grade of material were compared.

A micro-structural analysis was also performed for the four materials with a view of correlating formability and material structure. Structural parameters such as grain size and shape, the number of inclusion and inclusion morphology, were determined using a "Quantimet"-analyser and the results obtained were compared with the mechanical tests.

4.2. Materials and their Properties

All the mild steel sheets tested were of approximately the same thickness, see Table 4.1; thus the effect of thickness variation on forming limits was minimized. Four samples were used; one sample was a mechanically capped steel, another

Table 4.1

Material Properties from Tensile and Bulge Tests

Material	Notation	Thickness t (in.)	"n" Values		R_0	R_{45}	R_{90}	$\bar{R}$	ΔR
			Tensile	Circular Bulge					
Rimming Steel	A	0.035	0.21	-	1.12	0.89	1.55	1.11	0.59
Rimming Steel	B	0.036	0.21	0.18	1.11	0.84	1.51	1.07	0.47
Capped Steel	C	0.037	0.22	-	0.91	0.81	1.28	0.95	0.28
Al. Killed Steel	D	0.035	0.25	0.21	1.65	1.15	1.81	1.44	0.58

aluminium-killed steel and the other two were two different samples of rimming steel. The chemical composition of these samples are presented in Table 4.2.

Tensile and circular bulge tests were used to determine the mechanical properties of the steel samples.

4.2.1. Tensile Tests

Tensile test pieces were prepared according to IDDRG specifications, in which rectangular strips were cut from sheets along, at 45 degrees to and at 90 degrees to the rolling direction. They were then machined to a constant width of 1/2 inch. Care was taken to ensure the edge of the strips were parallel and no additional hardening was imparted to the test piece during machining. A gauge length of 2 inches was taken for extension measurement. The test pieces were pulled to failure in a 30-ton Tinius Olsen machine with a cross-head speed of about 0.2 in./min. and the applied loads were read off when the extension reached a predetermined amount.

The current stress and strain were calculated from

$$\bar{\sigma} = \frac{P\,\ell}{w_o \ell_o t_o} ,$$

and

$$\bar{\varepsilon} = \ln\left(\frac{\ell}{\ell_o}\right) ,$$

where P is the applied load, ℓ is the current gauge length and ℓ_o, w_o, t_o are the original gauge length, width and thickness of the test piece respectively. Typical stress-strain curves

Table 4.2

Composition of Steels

Materials / Elements	A	B	C	D
C	.030	.090	.065	.060
Mn	.285	.330	.350	.240
P	.006	.004	.006	.004
S	.029	.015	.035	.022
Si	.005	.004	.009	.013
Cu	.019	.033	.043	.066
Ni	.014	.013	.027	.025
Cr	.034	.010	.036	.035
Sn	.001	.001	.002	.005
Al	.007	.011	.017	.072
N_2	.002	.003	.003	.007

for specimens aligned at 0, 45 and 90 degrees to the rolling direction are presented in Figure 4.1. These curves were replotted in a log-log scale as shown in Figure 4.2 and the strain hardening indices were determined. These are given in Table 4.1.

The anisotropy coefficients were determined from the width and the gauge length of the specimen at 15% elongation. The normal anisotropy coefficients were then calculated for different orientation of the specimen by using Equation (3.8a) and an average value was obtained. Meanwhile the coefficient of planar anisotropy was determined from Equation (3.10) and a summary of the results is presented in Table 4.1.

4.2.2. Circular Bulge Tests

The stress-strain characteristic of a material is related to formability and is normally determined from the tensile tests. It was shown [4.1], however, that the plastic properties are dependent on the strain path of the test and this dependency is different from one material to the other. Thus, the material parameters obtained from tensile tests may not be representative of the plastic behaviour in the region of biaxial stretching. To check this, circular bulge tests were carried out and the results were compared with the tensile tests.

The use of a biaxial test extensometer in the circular bulge test has been extensively developed by Duncan and Johnson. Details of the equipment and the testing methods are described in References [3.2] and [4.2]. From the analysis of an isotropic spherical shell subjected to an internal pressure, the equivalent

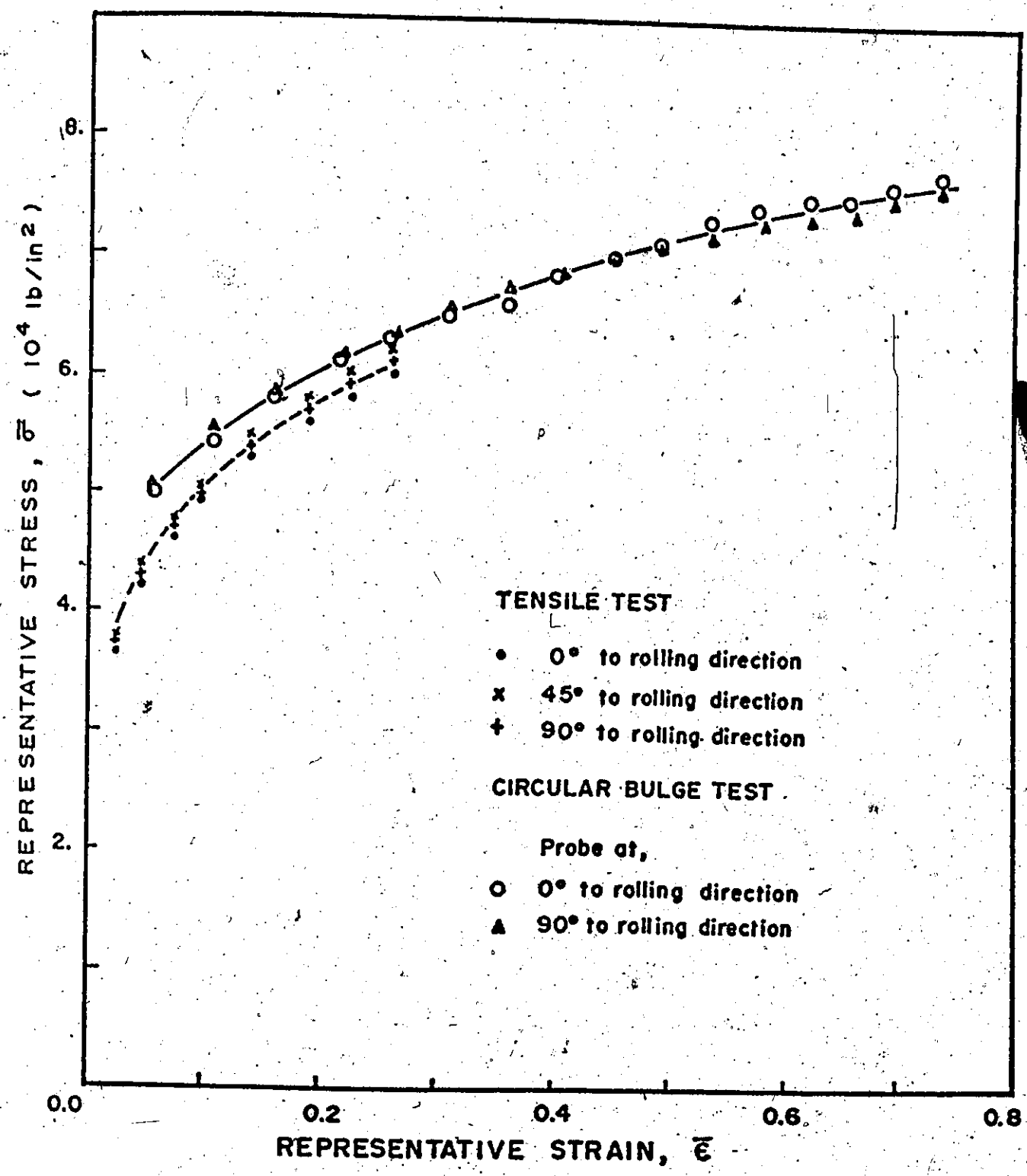

Figure 4.1. Stress-Strain Curves from Tensile and Circular Bulge Tests of Rimming Steel, Material B.

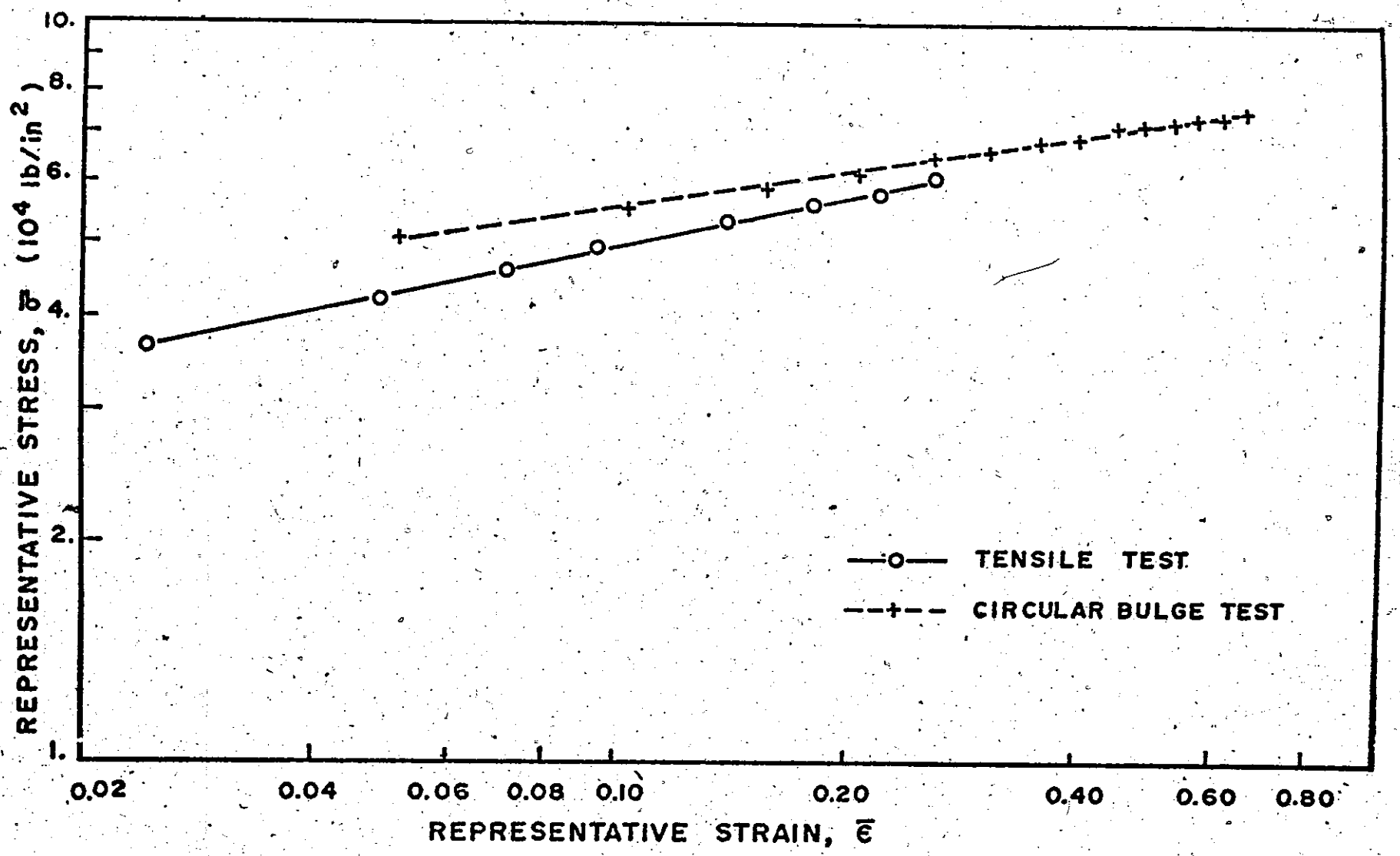

Figure 4.2. Determination of Strain-Hardening Index from Stress-Strain Curves of Rimming Steel, Material B.

stress and strain at the pole of the bulge can be derived as

$$\bar{\sigma} = \frac{p\rho}{2t_o} \exp(-\bar{\varepsilon}) ,$$

and

$$\bar{\varepsilon} = 2\varepsilon_\theta$$

where p is the pressure, ρ is the radius of curvature and ε_θ is the circumspherential strain.

The radius of curvature was measured using a spherometer, and the circumspherential strain at the pole of the bulge was determined from the extensometer readings as described in Reference [4.2]. Tests were performed with the extensometer probes in a line parallel and perpendicular to the rolling direction of the sheet. Stress and strain were calculated and plotted as shown in Figure 4.1. The strain-hardening index was determined by redrawing the stress-strain curve on a log-log paper as shown in Figure 4.2, and the results are tabulated in Table 4.1.

4.3. Hydrostatic Bulge Tests

4.3.1. Specimen Preparation

Specimens were tested to failure in a circular die and three elliptical dies. Photographs of these dies and the testing apparatus were shown in Figures 3.12 and 3.13. The deformation characteristics of metal diaphragms bulged to these dies were described in Chapter 3.

In rolled sheets, it is observed that material properties change considerably across the width of the sheet and the nature of this is not yet fully known. To reduce this variability

and to minimize the number of test samples, specimens were cut from approximately 9 inch wide strips located at one quarter of the width in from each edge of the sheet.

The determination of sample size for the test in each bulging die is influenced by the following considerations:

- The sample tested must represent the characteristic of the material which requires an indefinitely large number of specimens. For a finite sample and with a certain probability level, the confidence limits for the results are inversely proportional to the square root of the sample size.
- The difficulty and the amount of labor involved in producing a set of results is proportional to the number of specimens tested.

With the assumption that the defects are uniformly distributed along the rolling direction of the sheet, approximately 20 specimens were chosen for each sample as a compromise for the two factors above. Table 4.3 gives the list of the actual sample sizes for each material.

For the elliptical dies, two sets of samples were employed; one set having the rolling direction along the axis of the die and the other set with the rolling direction transverse to it. For the circular die, however, only one set was tested.

Before bulging, specimens were printed with square grids of 0.1 inch pitch using the Photo-Resist technique [4.3]. Square grids were used since the strain measured was along the

Table 4.3

Actual Sample Sizes for the Four Steels Tested

Direction	Material / Aspect Ratio	A	B	C	D
Largest Strain in Rolling Direction	4:1	24	13	-	19
	2:1	20	20	-	32
	4:3	19	20	17	14
	1:1	17	18	16	20
Largest Strain in Transverse Direction	4:3	19	-	16	-
	2:1	20	-	23	22
	4:1	23	-	20	30

principal axes of stress and strain; however, in industrial pressings fracture may not be along the axes of principal stress and therefore circular grids were employed instead. Also as the measurement of strain was made at the region away from the localized deformation, the grid size is not an important factor and thus a 1/10 inch grid was chosen.

4.3.2. Limit Strain Measurement

The specimens were clamped between a die and die plate and pressure was applied to one side of the specimens and they were bulged to failure. Nearly all specimens tested failed near the pole of the bulge and the fracture lines were more or less parallel to the major axis of the die regardless of the orientation of the rolling direction.

Specimens with visible scratches and those which slipped from the die were discarded. In a small number of cases, the diaphragms failed at the edge or at some distance away from the pole where strain gradients were high. These tests were also rejected although it might be argued that they indicated the presence of a small number of severe defects in the sheet.

To facilitate the strain measurement, a replica technique was used to transfer the deformed grid patterns from the specimen on to a flat surface. Technical details and the accuracy of the technique are described in Appendix A1.

Irregularities exist in the elongation of the grid system around the fracture due to the localization of strain and fracture lines are not always straight, especially when strain

ratio is close to unity. Thus, the selection of the strain data was therefore made in the following manner. Three adjacent grid squares at a distance roughly one grid spacing away from the fracture line and on either side of this line were measured. Thus the selected grids were adjacent to the tear but did not contain it or any highly localized straining associated with the tear. Care was also taken to make sure that the selected grids were located approximately at the middle of the line of fracture as shown in Figure 4.3.

In calculating the principal limit strains for a particular specimen, the two sets of three adjacent grid squares were considered as two rectangles. The lengths of each side of each rectangle were measured using a Toolmaker's microscope. The strain parallel to the tear was given by

$$e_1 = \frac{\bar{\ell}_1}{0.3} - 1 , \qquad (4.1)$$

where 0.3 is the length of three undeformed grids. Similarly the strain perpendicular to the groove was

$$e_2 = \frac{\bar{\ell}_2}{0.1} - 1 , \qquad (4.2)$$

where $\bar{\ell}_1$ and $\bar{\ell}_2$ were the average lengths of the long and the short sides of the rectangle respectively.

In these bulged diaphragms, there is a strain gradient everywhere except at the pole and it was observed that the average strains in each rectangle on either side of the tear were not always equal. Arbitrarily, the larger of the observed

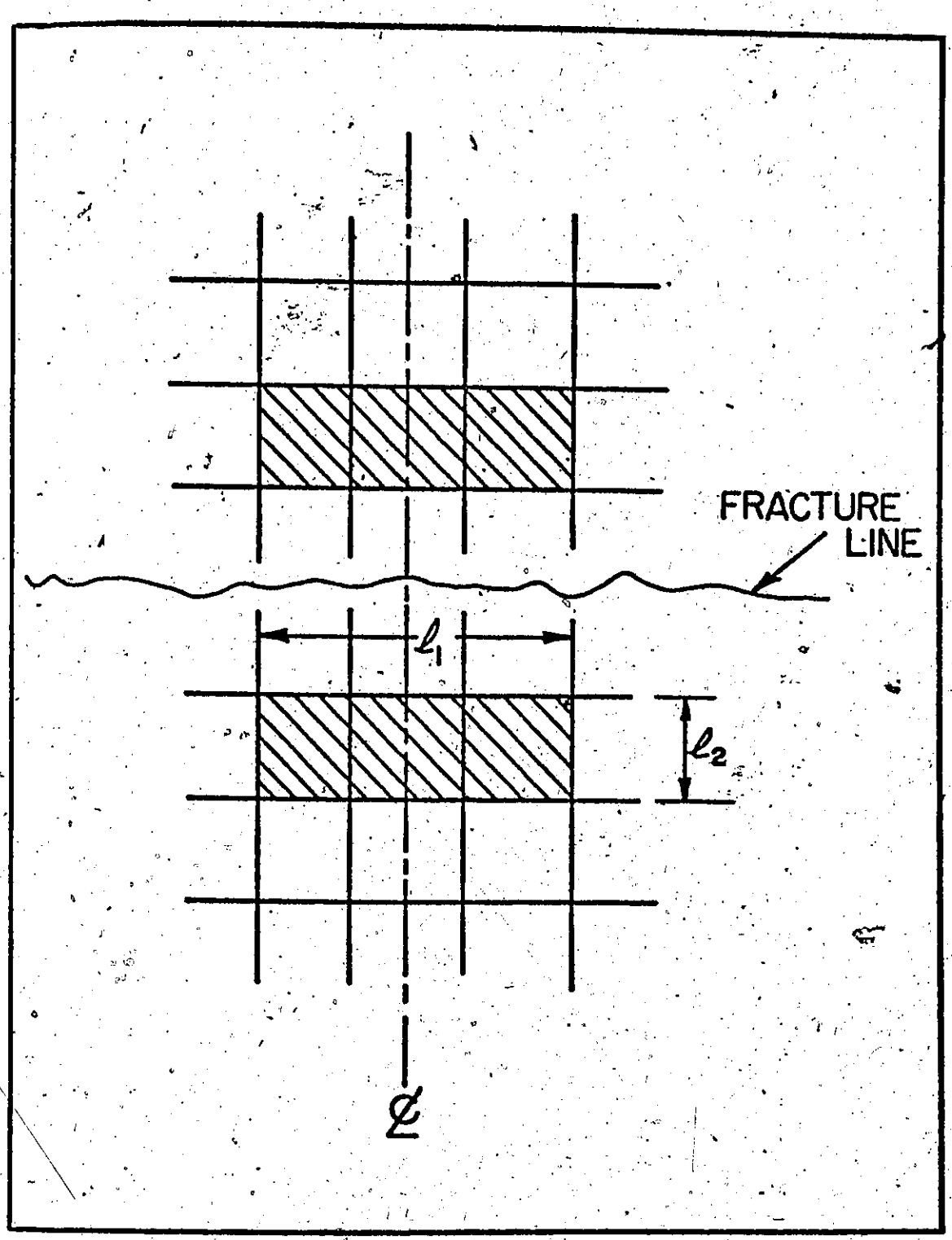

Figure 4.3. Selection of Deformed Grid Squares for Limit-Strain Measurement.

strains was selected and recorded; however, as the failures were all close to the pole the difference in strains on either side of the tear was not great.

4.4. Quantitative Metallographic Analysis

To assess the influence of microstructure on formability, a "Quantimet" analysis was performed on the four samples of steel using a 720 Image Analysing Computer [4.4]. The Quantimet analysis has been widely used by steel making industry as an automatic inclusion counting technique and the method, its accuracy and advantages are discussed in Reference [4.5].

In the Quantimet analysis, three samples were selected at random from each grade of steel and two sections were cut out from each sample; one was along the rolling direction and the other is perpendicular to it (See Figure 4.4(a)). These were polished before mounting in the microscope. The scanning was performed along a direction parallel and perpendicular to the thickness direction of the specimen, see Figure 4.4(b). Fifty fields were examined for each section and a magnification of 16 was applied to the scanner. The quantities measured were inclusion and grain size parameters. Figure 4.5 shows typical grain structures of the four steel samples and Figures 4.6 and 4.7, the inclusions in these steels. The following is a brief description of the parameters used in the Quantimet analysis.

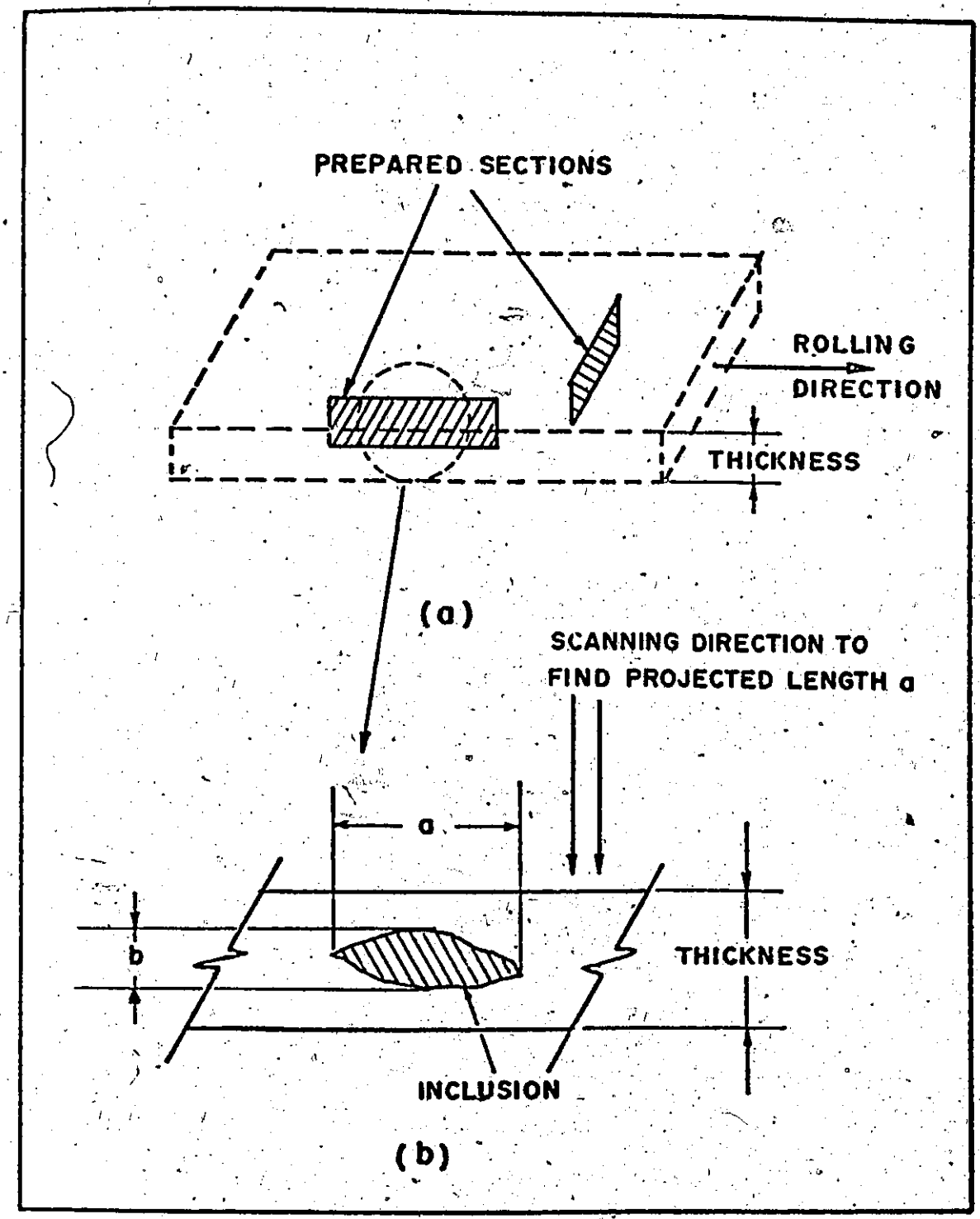

Figure 4.4. Specimen Preparation for Quantimet Analysis.

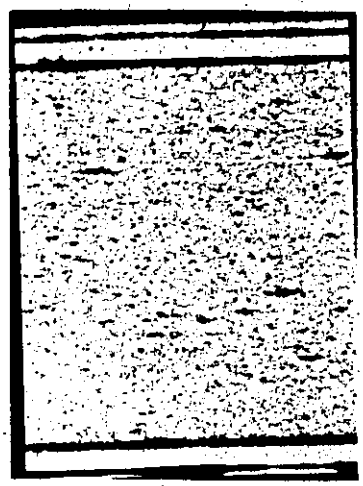

MATERIAL A

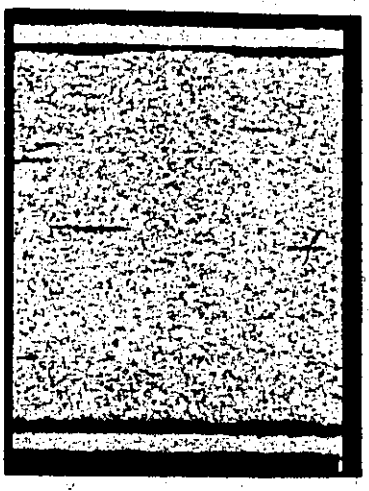

MATERIAL B

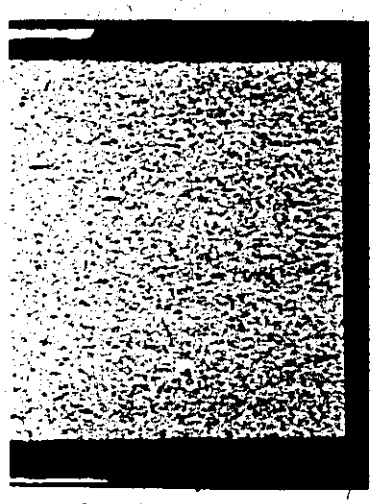

MATERIAL C

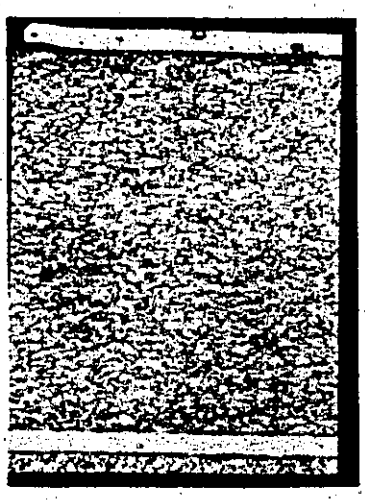

MATERIAL D

Figure 4.5 Grain Structures of the Four Steel Samples. Sections are Parallel to the Rolling Direction of the Sheet (Nital Etched, X100)

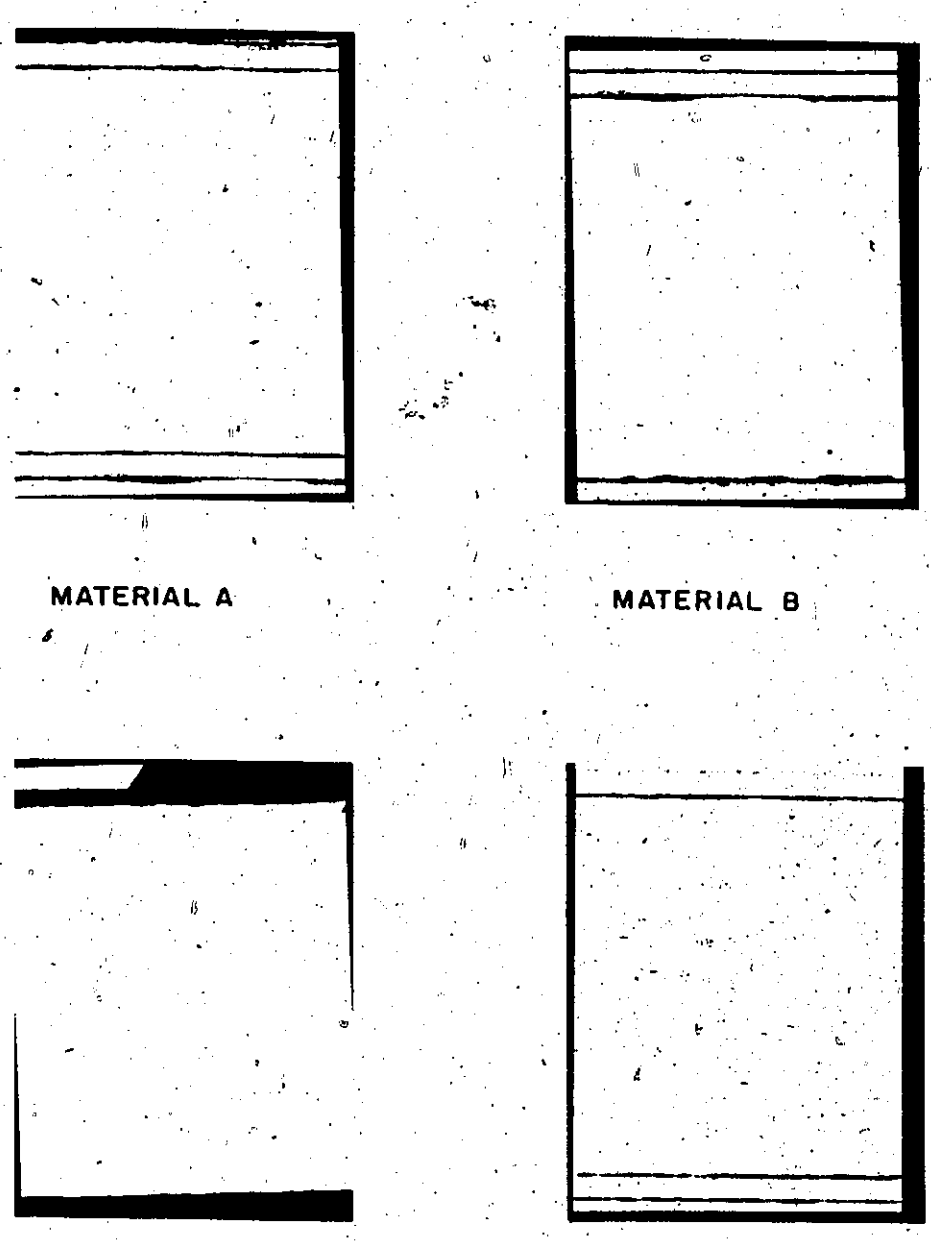

Figure 4.6 Voids and Non-Metallic Inclusions in the Four Steel Samples. Sections are Parallel to the Rolling Direction of the Sheet. (As Polished, X 100)

MATERIAL A

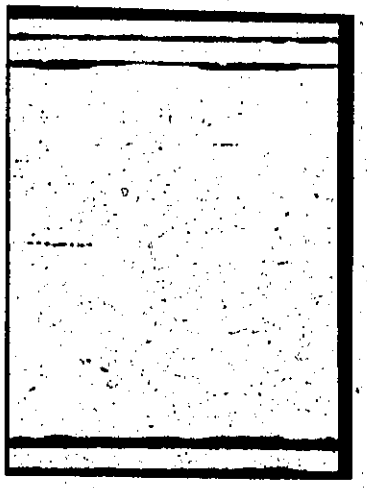

MATERIAL B

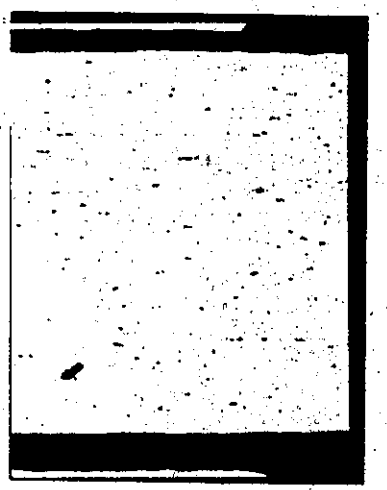

MATERIAL C

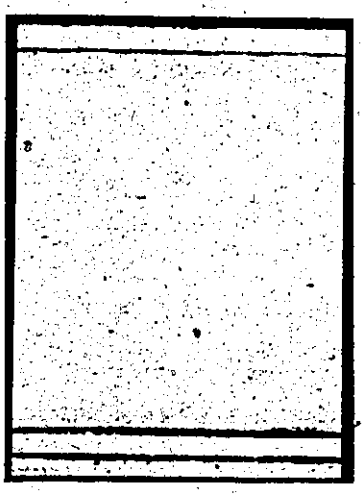

MATERIAL D

Figure 4.7 Iron Carbide in the Four Steel Samples. Sections are Parallel to the Rolling Direction of the Sheet (Picral Etched, X100)

4.4.1. Inclusion Parameters

a) Number of Inclusions

Inclusions with a size greater than 2 microns were recorded. These include oxide and sulphide inclusions and those features whose reflectivity was sufficiently different from the steel matrix. The number of inclusions per unit area is the number of inclusions detected in the area of field of view. It should be noted, however, that two adjacent features cannot be distinguished by the system unless they are separated by at least one scanning line.

b) Total Length

This is the sum of the projected lengths of all inclusions detected in the examined area. This projection refers to a length perpendicular to the scanning direction, see Figure 4.4(b).

c) Individual Length

The individual length is regarded as the average inclusion size which is equal to the total projection divided by the inclusion count.

d) Percentage Area

This parameter indicates the fraction area of the inclusions in the steel matrix. The measurement is based on the summation of the lengths of the linear intercepts expressed as a fraction of the total scanning line length. It can be shown that this linear fraction is statistically equivalent to the area fraction or volume fraction of the features detected.

e) Shape Factor

Shape factor is a measure of the degree of "pancaking" of the feature in the field of view and is defined as the average ratio of (a/b); see Figure 4.4(b). The quantity "a" corresponds to the individual length of the feature as defined above, while "b" depicts a similar measure obtained by rotating the specimen through 90 degrees.

f) Individual Area

This is the average area of the inclusions. It is the ratio of the total area of inclusions to the number counted.

g) Inclusion Factor

In studying the cleanliness of steel, a number of researchers have established a parameter called the "Inclusion factor" which was shown to have a certain correlation with both the "shelf energy" and the fracture toughness in certain steels. This parameter is defined as

$$I.F. = \ln \frac{1}{\ell\sqrt{N}} ,$$

where ℓ is the individual length and N is the number of inclusions per unit area.

4.4.2. Grain Size Parameters

In the grain size measurement, steels were assumed to have equi-axed grains, thus only a section parallel with the rolling direction, such as section 1 in Figure 4.4(a) was measured.

a) Ferrite Area

This parameter indicates the percentage of ferrite minus inclusions, carbides and features at grain boundaries. This fraction area was derived from the measurement of the non-ferrite features which have different reflectivity from the matrix. Thus, this parameter was determined in the same manner as the percentage area of inclusions.

b) Grain Size

The average grain size was measured in a similar fashion as the individual inclusion length and was obtained by dividing the chosen scan lengths by the number of grain boundaries encountered. This parameter can also be determined from the average projections of the grain boundaries.

c) Shape Factor

The shape factor for grain size was obtained in a similar manner to the shape factor of the inclusions as described above.

The inclusion and the grain size parameters were determined for each scanning field. The mean and the standard deviation of the fifty measurements were obtained and these were then finally averaged for each grade of steel. The results are shown in Tables 4.4(a) and 4.4(b).

4.5. Experimental Results

4.5.1. Forming Limit Diagram

The measured forming limit strain in each of approximately 140 test pieces of rimming steel, material A, are shown

Table 4.4(a)

Quantimet Results - Inclusion

Materials		Total Number (N/mm^2)		Total Length ℓ (mm/mm^2)		Individual Length (10^{-2} mm)		Total Area %		Individual Area (10^{-5} mm^2)		Shape Factor $\frac{a}{b}$		Inclusion Factor $\ell n(\frac{1}{\ell\sqrt{N}})$	
		Mean	S.D.*	Mean	S.D.	Mean	S.D.	Mean	S.D.	Mean	S.D.	Mean	S.D.	Mean	S.D.
A	Roll.+	330.	109.	1.105	.425	.335	.071	.363	.197	1.099	.523	1.081	.208	2.80	-
	Trans.≠	318.	89.	.928	.289	.294	.049	.290	.128	.919	.342	1.010	.169	2.95	-
B	Roll.	239.	87.	.853	.446	.360	.107	.288	.230	1.189	.816	1.200	.385	2.90	-
	Trans.	245.	87.	.798	.349	.328	.093	.269	.224	1.096	.827	1.122	.262	2.98	-
C	Roll.	297.	90.	1.039	.444	.351	.084	.286	.141	.984	.425	1.336	.261	2.80	-
	Trans.	337.	80.	.951	.257	.286	.055	.255	.107	.767	.275	1.120	.228	2.95	-
D	Roll.	99.	50.	.314	.175	.320	.115	.105	.069	1.075	.577	1.033	.328	3.44	-
	Trans.	70.	32.	.201	.112	.291	.107	.064	.050	.927	.654	1.079	.275	3.72	-

Note

* S.D.: standard deviation

\+ Roll: cross-section examined is parallel to the rolling direction

≠ Trans: cross-section is perpendicular to the rolling direction

Table 4.4(b)

Quantimet Results - Ferrite Grain

Steels	Ferrite Area %	Area Others %	Ferrite Grain Size (μm)		Shape Factor $\frac{a}{b}$	n	$\bar{R}$	ΔR
			Mean	S.D.*				
A	99.56	0.44	12.99	1.75	1.037	0.21	1.11	0.59
B	99.64	0.36	13.02	1.25	1.014	0.21	1.07	0.47
C	99.42	0.58	10.23	1.33	1.029	0.22	0.95	0.28
D	99.75	0.25	13.71	0.59	1.463	0.25	1.44	0.58

Note S.D.* = standard deviation

in Figure 4.8. In these tests, two sets of twenty specimens were prepared for each elliptical die. In one set, the direction of rolling was parallel to the minor axis of the die and was therefore aligned in the direction of the greatest principal strain in the failure area; the measured limit strains are plotted in the upper left hand part of the diagram. In the other set, the rolling direction was parallel to the major axis so that the greatest strain in the failure zone was perpendicular to the direction of rolling. These results are plotted in the lower right hand part of the diagram.

The forming limit diagrams for other steel samples are shown in Figures 4.9 to 4.11. In some cases, tests were performed with the direction of rolling along one axis of the elliptical die only. For details of the test data, the reader is referred to Appendix A2.

With each of the bulging dies employed it was possible to achieve an essentially constant ratio of the principal membrane strains, at the pole of the dome, throughout the course of the test. It is recognized that, in general, this is unlikely to be the case in an actual pressing.

a) Mean and Standard Deviation of Limit Strains

A "mean strain path" was established for each group of tests in a particular die by drawing a line from the origin through the coordinate of the mean of e_1 and e_2 for the group. Each particular point in the forming-limit diagram was then characterized by its projected length on the mean strain path, i.e., the length E as shown in Figure 4.12. This was done in

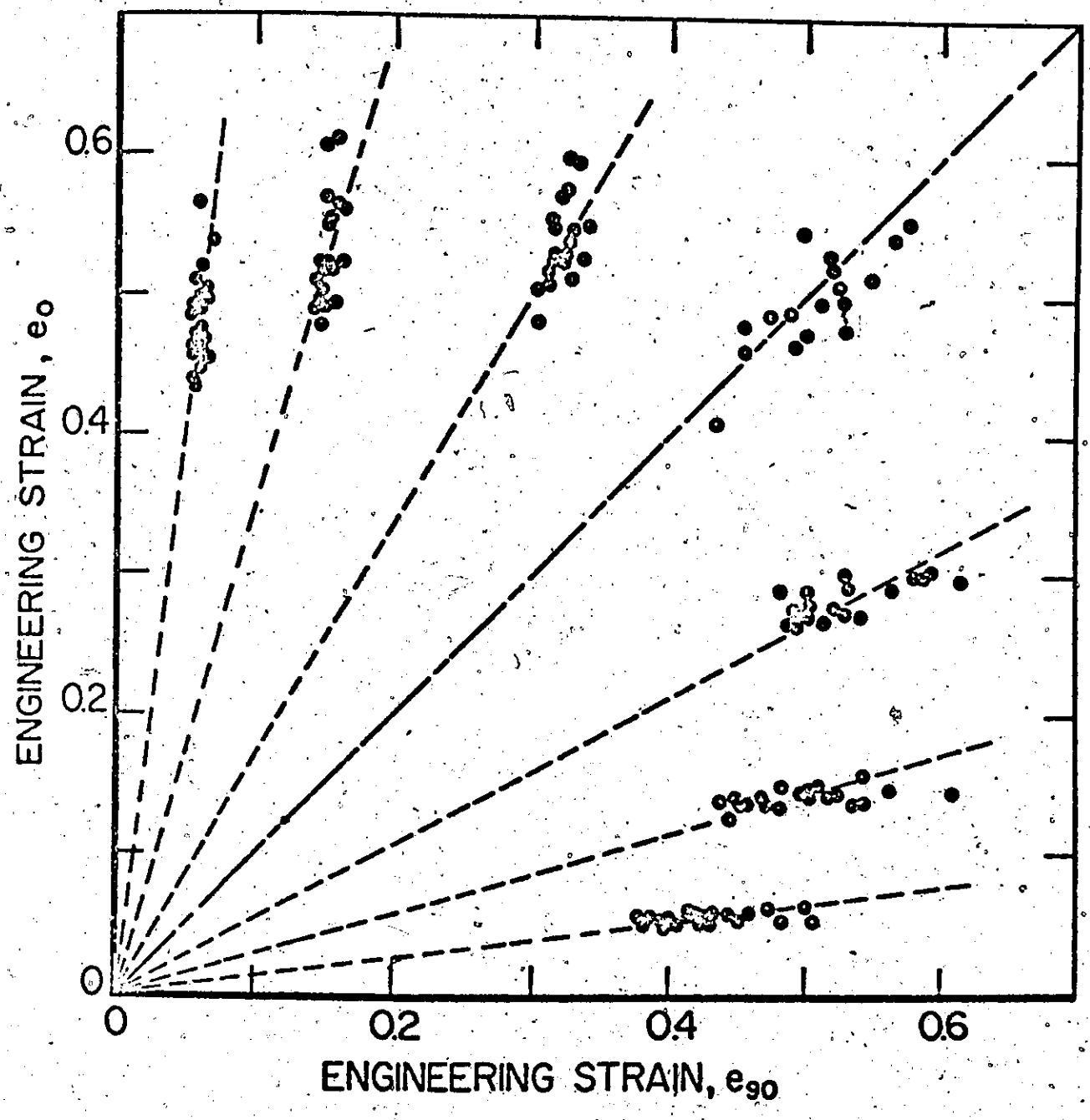

Figure 4.8. Forming-Limit Diagram for Rimming Steel, Material A.

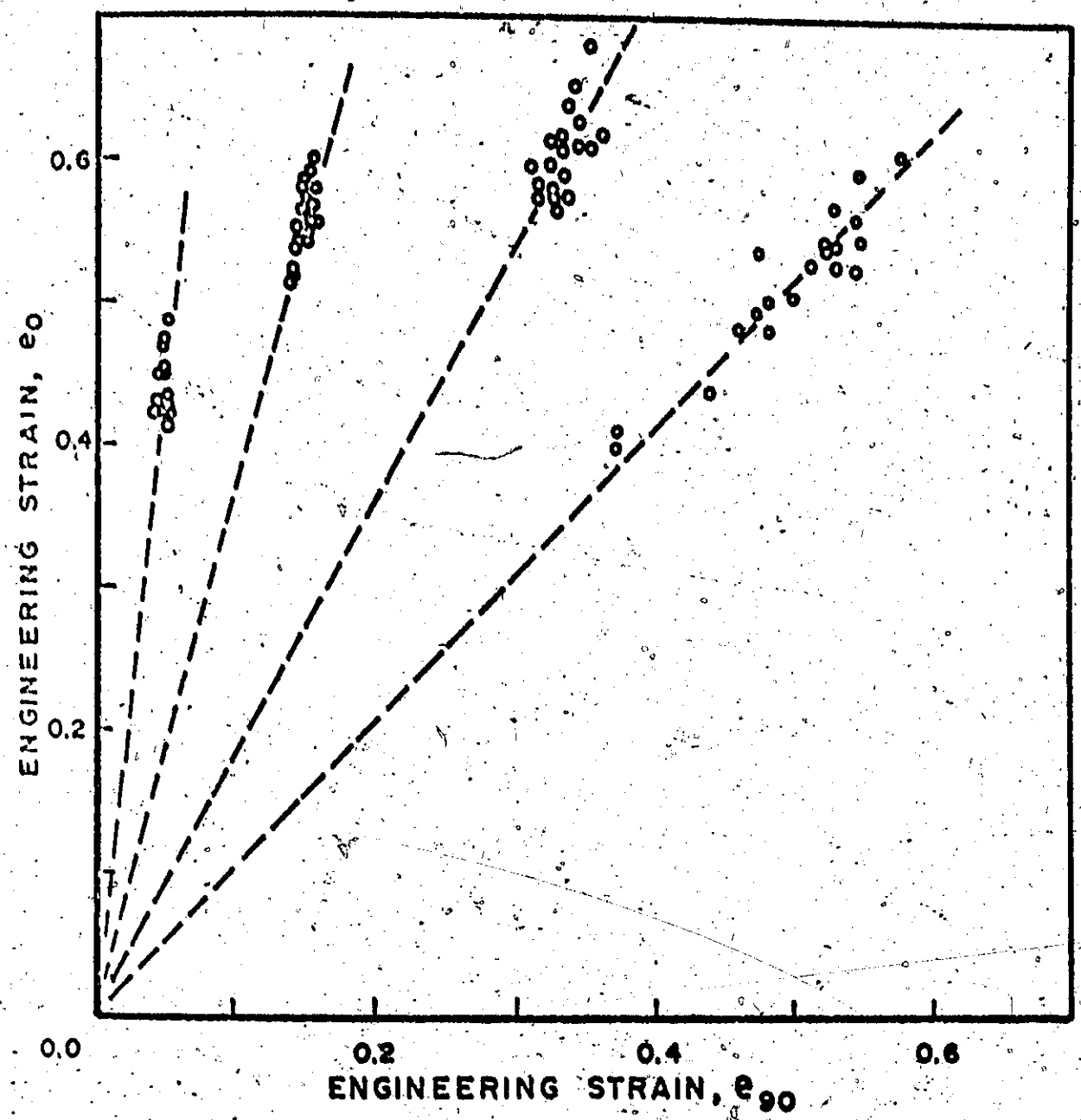

Figure 4.9. Forming-Limit Diagram for Rimming Steel, Material B.

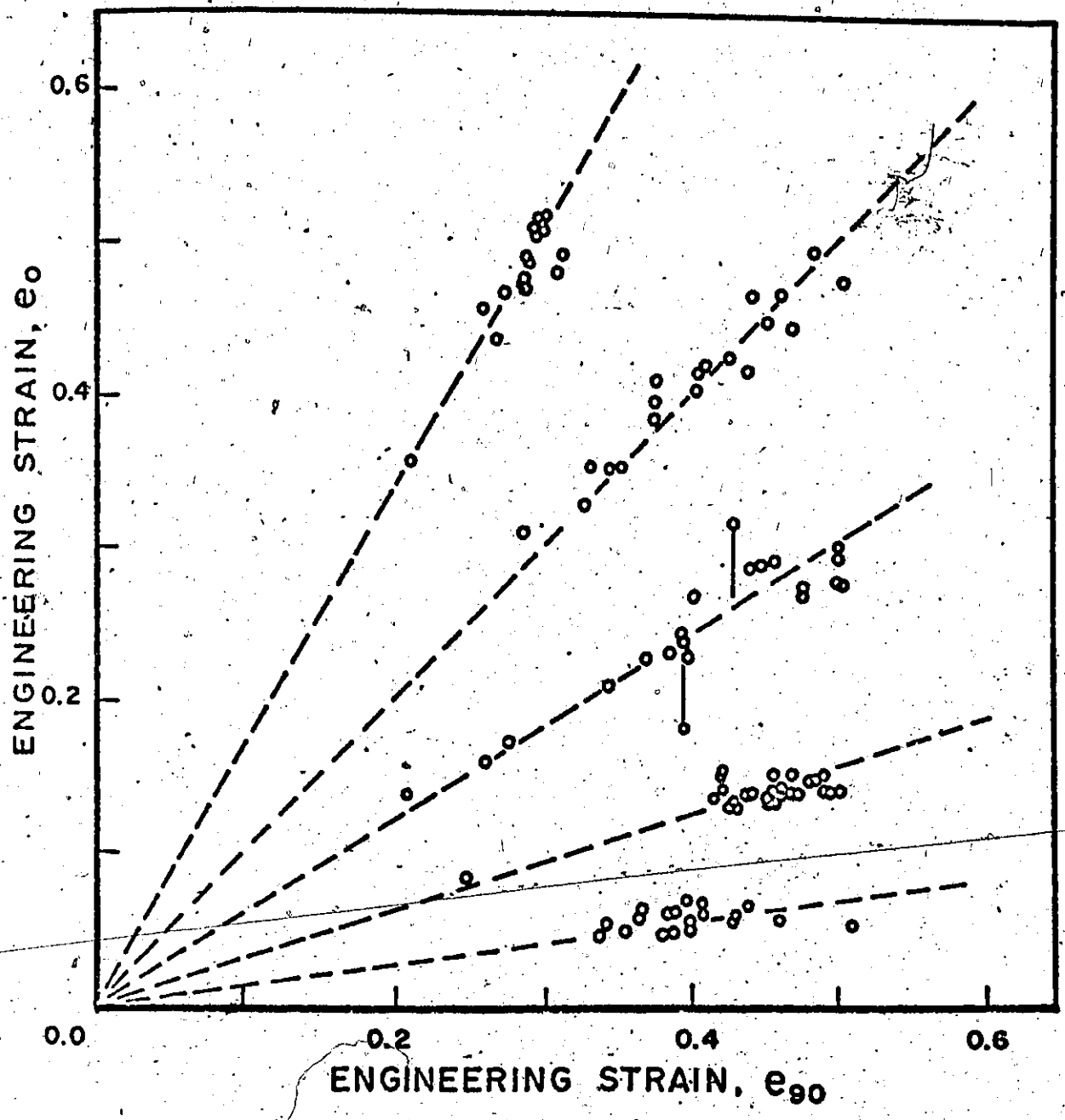

Figure 4.10. Forming-Limit Diagram for Capped Steel, Material C.

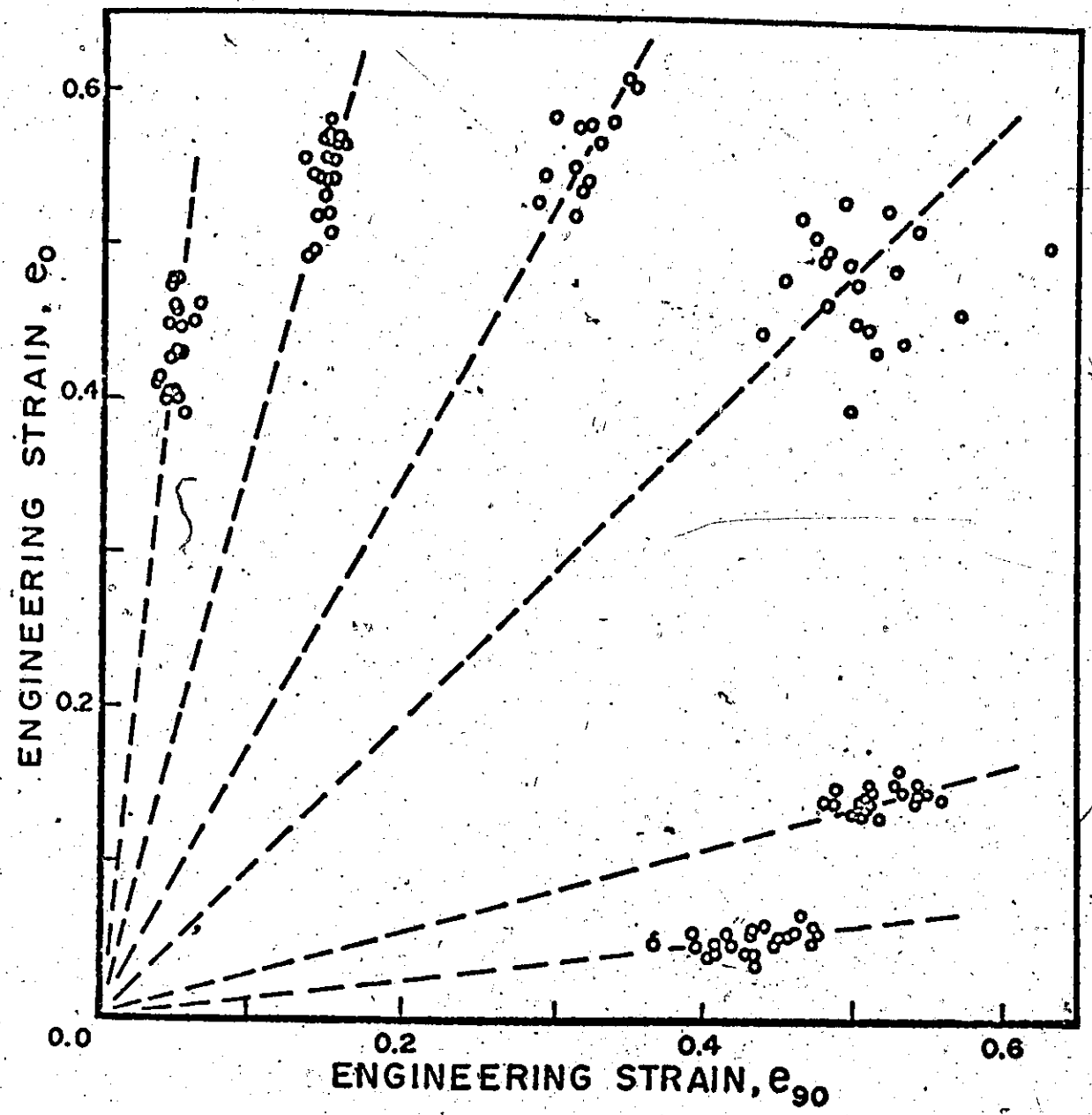

Figure 4.11. Forming-Limit Diagram for Aluminum-Killed Steel, Material D.

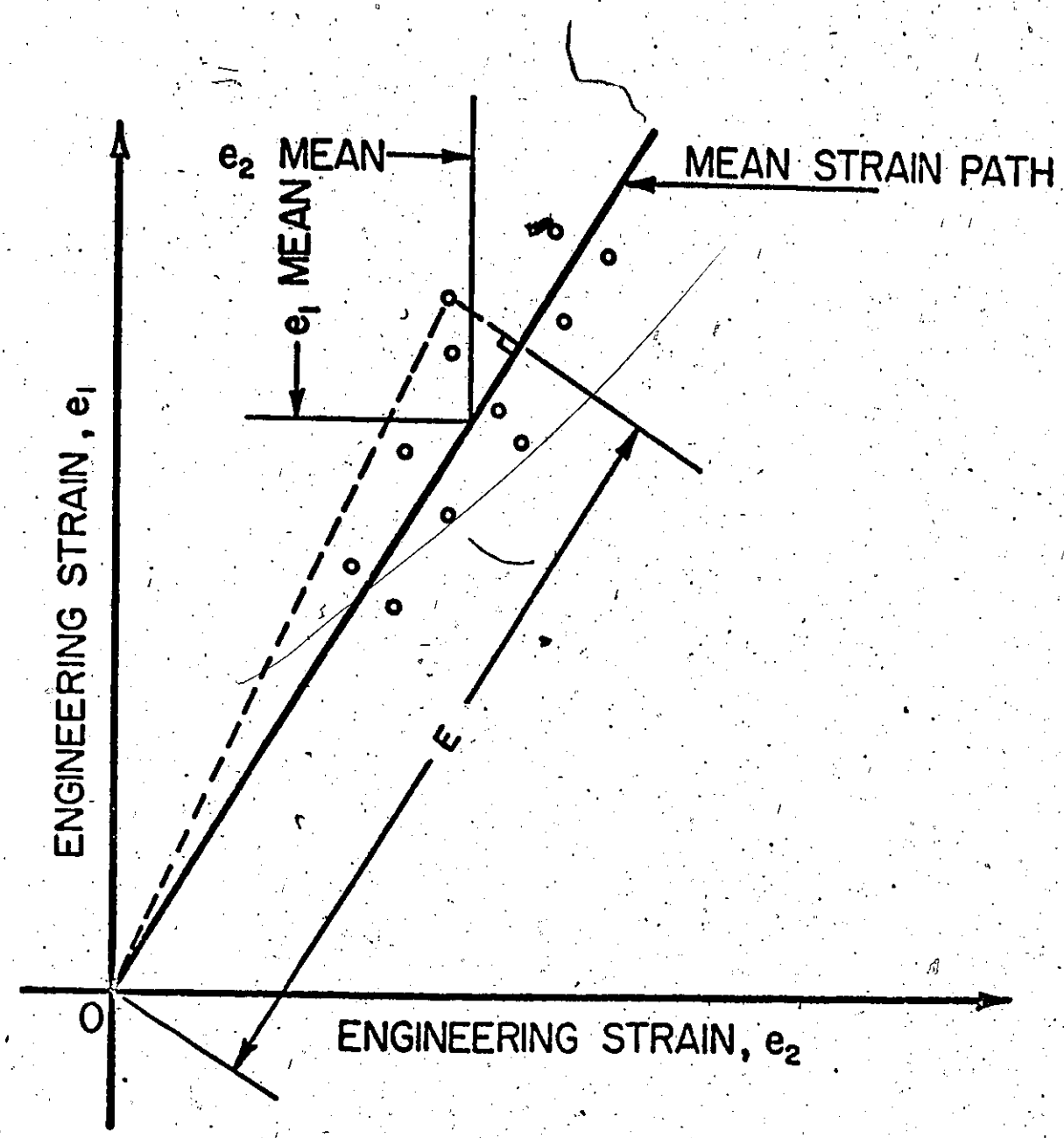

Figure 4.12. Schematic Representation of the Mean Strain Path for Specimens Tested in a Particular Die.

order to reduce the two variables for each point, e_1 and e_2, to a single variable, E, for the purposes of statistical analysis. In this manner it is possible to plot the frequency distribution of the projected strain vector E along each of the mean strain paths. The histograms of limit strains for rimming steel, material A, is shown in Figure 4.13. The normality of the distribution was tested by plotting the cumulative frequency of the vector E on a probability scale as shown in Figure 4.14. In most cases, it was found that the results could be reasonably fitted by a normal distribution curve. This might be fortuitous in view of the limited number of samples tested (about twenty for each die), however, it will be shown in Chapter 5 that this is a reasonable assumption.

The distribution of the limit-strains on the mean strain path can thus be described by the mean and either the variance or the standard deviation. The mean is defined as

$$\bar{E} = \frac{1}{N} \sum_{i=1}^{N} (E)_i \quad , \tag{4.3}$$

where N is the number of specimens in a sample; and the estimated variance is

$$S^2 = \left\{ \sum_{i=1}^{N} [\bar{E} - (E)_i]^2 \right\} / (N-1) \quad . \tag{4.4}$$

The mean and the standard deviation of the limit strains for the four steel samples tested were calculated and recorded in Table 4.5. Figure 4.15 shows the forming-limit diagram for the rimming steel in terms of the mean and three times the standard

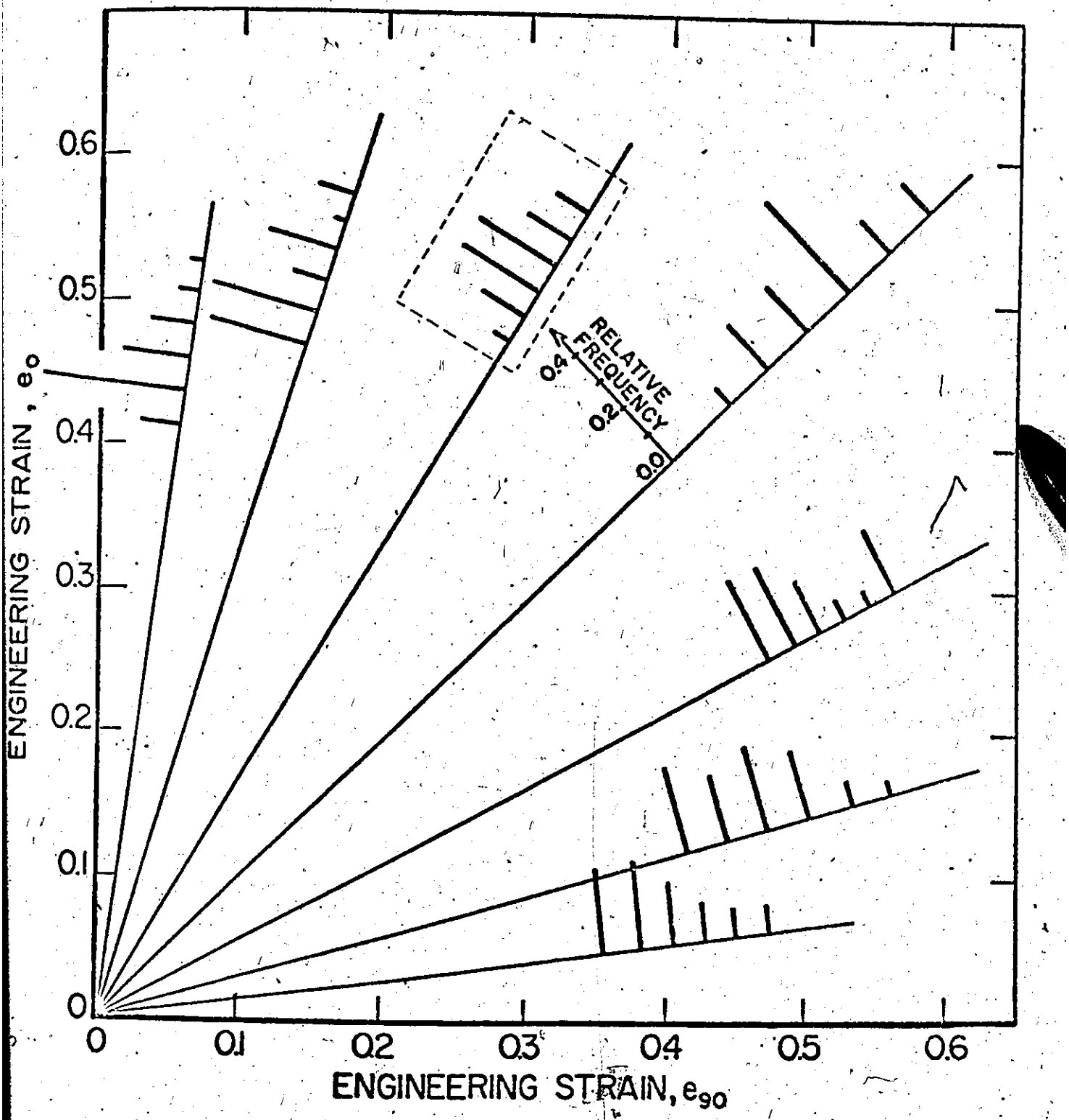

Figure 4.13. Frequency Distributions of Limit Strains on Mean Strain Path for Rimming Steel, Material A.

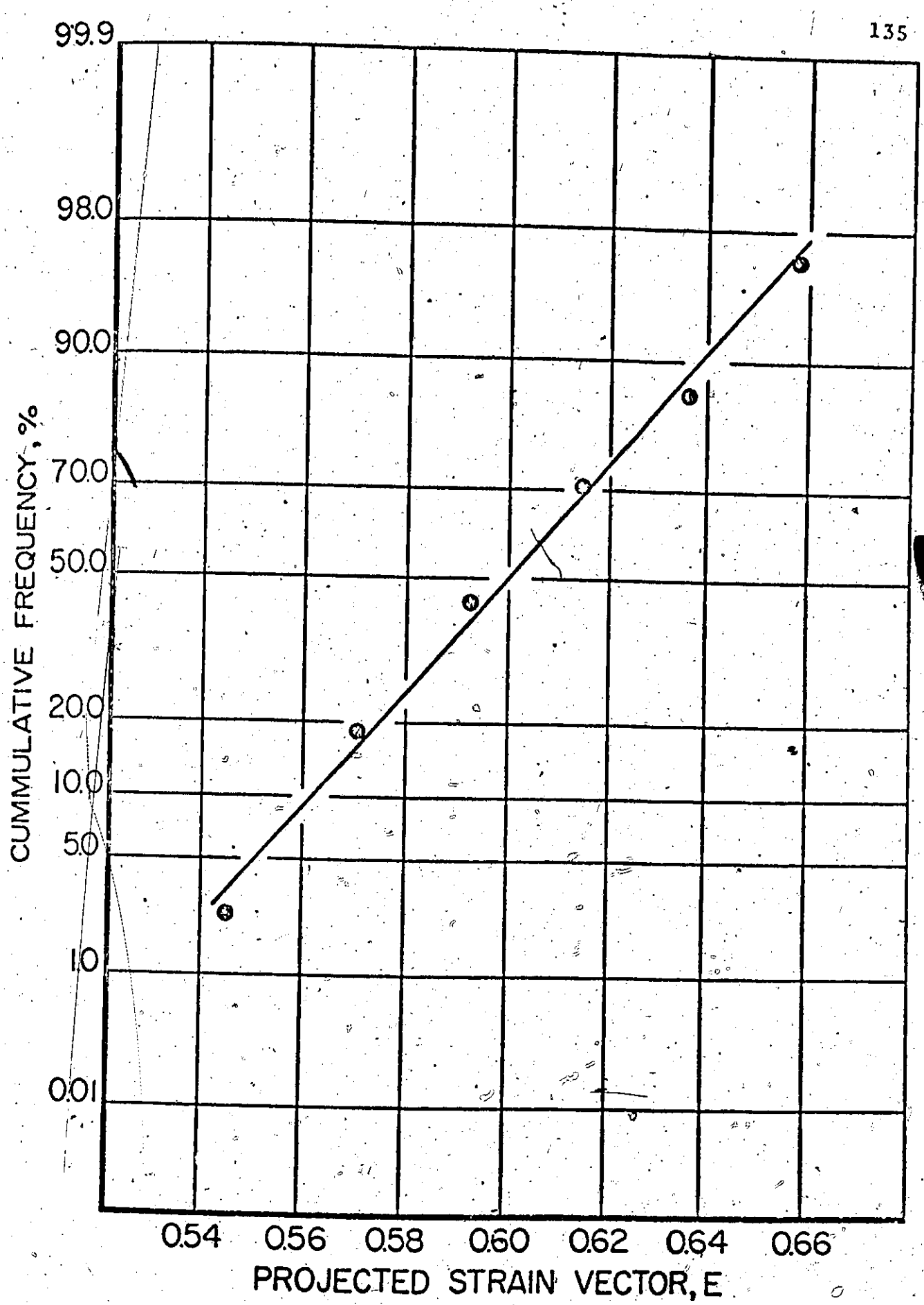

Figure 4.14. Typical Cumulative Frequency Distribution of Projected Strain Vectors on Mean Strain Path. (From the Case Marked in Fig. 4.13).

Table 4.5

Mean and Standard Deviation of the Limit Strains ($\bar{E}$) for the Four Steels Tested. (Confidence intervals for these are evaluated at 90% probability level.)

Material	Aspect Ratio / Quantity	Largest Strain in Rolling Direction				Largest Strain in Transverse Direction		
		4:1	2:1	4:3	1:1	4:3	2:1	4:1
A	Mean	0.48 ± 0.011	0.55 ± 0.014	0.63 ± 0.012	0.72 ± 0.025	0.60 ± 0.014	0.52 ± 0.017	0.43 ± 0.013
	S.D.*	0.031	0.037	0.030	0.058	0.036	0.044	0.037
	U.L., L.L.†	0.041,0.025	0.051,0.029	0.041,0.024	0.082,0.045	0.050,0.028	0.060,0.035	0.049,0.030
B	Mean	0.44 ± 0.012	0.57 ± 0.009	0.69 ± 0.011	0.75 ± 0.024	-	-	-
	S.D.	0.023	0.025	0.030	0.058	-	-	-
	U.L., L.L.	0.035,0.018	0.034,0.020	0.041,0.024	0.082,0.046	-	-	-
C	Mean	-	-	0.57 ± 0.011	0.61 ± 0.031	0.52 ± 0.026	0.48 ± 0.009	0.40 ± 0.013
	S.D.	-	-	0.025	0.072	0.059	0.025	0.033
	U.L, L.L.	-	-	0.035,0.019	0.103,0.056	0.084,0.045	0.033,0.020	0.046,0.026
D	Mean	0.44 ± 0.011	0.56 ± 0.008	0.65 ± 0.015	0.71 ± 0.016	-	0.54 ± 0.009	0.45 ± 0.007
	S.D.	0.028	0.026	0.032	0.043	-	0.024	0.023
	U.L., L.L.	0.039,0.022	0.034,0.022	0.047,0.024	0.058,0.034	-	0.032,0.019	0.030,0.019

* S.D.: standard deviation

† U.L., L.L.: upper and lower limits for the standard deviation

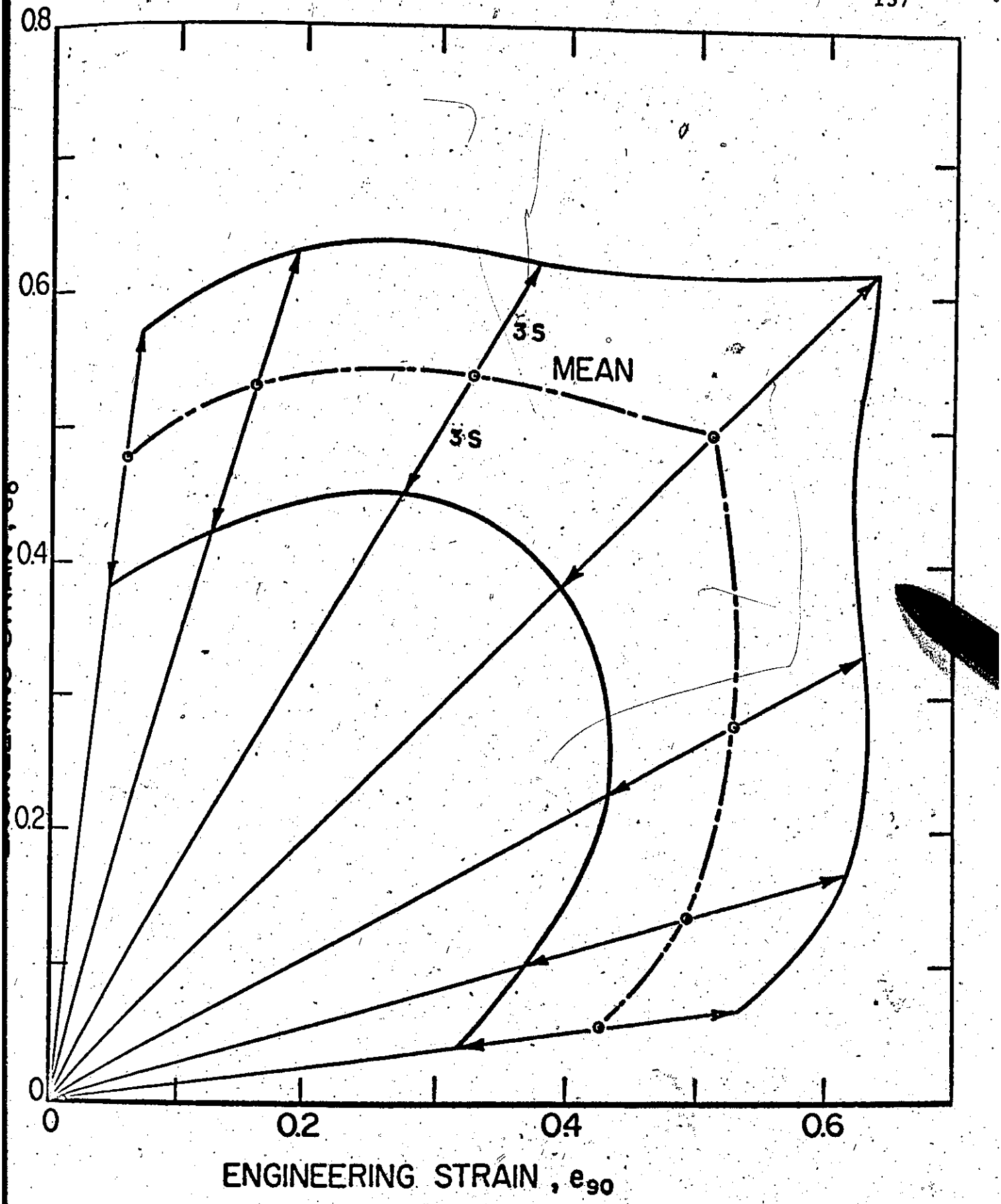

Figure 4.15. Forming-Limit Diagram for Rimming Steel, Material A, showing Mean Limit Strains and a Band of Three Times Standard Deviation on Either Side of the Mean.

deviation. If the sample had been very large, 99% of all limit strains observed would fall within a range of $\pm$ 3S. The number of tests for each case in these experiments was limited, therefore the confidence limits of the mean and the standard deviation were determined.

b) Confidence Limits

The values of the means of a limited number of samples of a normal population having a standard deviation S are distributed according to a student "t" distribution. Thus the confidence interval for the population mean $\bar{E}_M$ with a probability level of $(1 - \gamma)$ is

$$\Pr\{(\bar{E} - n_{\gamma/2}\frac{S}{\sqrt{N}}) < \bar{E}_M < (\bar{E} + n_{\gamma/2}\frac{S}{\sqrt{N}})\} = 1 - \gamma, \qquad (4.5)$$

where $n_{\gamma/2}$ is the student "t" variate with N degrees of freedom and having an upper tail area of $\gamma/2$.

The confidence interval for the population variance $(S_M)^2$ is

$$\Pr\{\frac{(N-1)\ S^2}{\chi^2_{\gamma/2}} < (S_M)^2 < \frac{(N-1)\ S^2}{\chi^2_{1-\gamma/2}}\} = 1 - \gamma \qquad (4.6)$$

where $\chi^2_{\gamma/2}$ and $\chi^2_{1-\gamma/2}$ are chi-square variates with (N-1) degrees of freedom.

For a 90% probability level, the confidence intervals for the mean and the standard deviation of the limit-strains

were calculated for the four steel samples and these are given in Table 4.5. The estimated mean and standard deviation, with a confidence interval of 90% for the rimming steel, material A, are shown in Figures 4.16 and 4.17 respectively.

c) Error Analysis

It could be argued that the scatter of the limit-strains observed in the forming-limit diagrams, Figures 4.8 to 4.11, is not a true reflection of variation in material performance but arises through measurement errors. To check this point a detailed experimental study was performed involving repeated measurements. The measuring instrument used was a Toolmaker's microscope graduated in divisions of 0.0002 in. and it was assumed that the major sources of experimental error were due to:- length measurement error, inaccuracy in grid printing and replica error.

i) Length Measurement:

To detect the random error in measuring the grid pattern in the microscope, thirty-one repetitive measurements were made on one grid and the observed standard deviation of the readings was

$$S_A = 0.0004 \text{ in.}$$

ii) Grid Printing:

Errors in the grid on the test piece could result from errors in the grid master and shrinkage or distortion of the master during printing. The length of the side of 41 grids

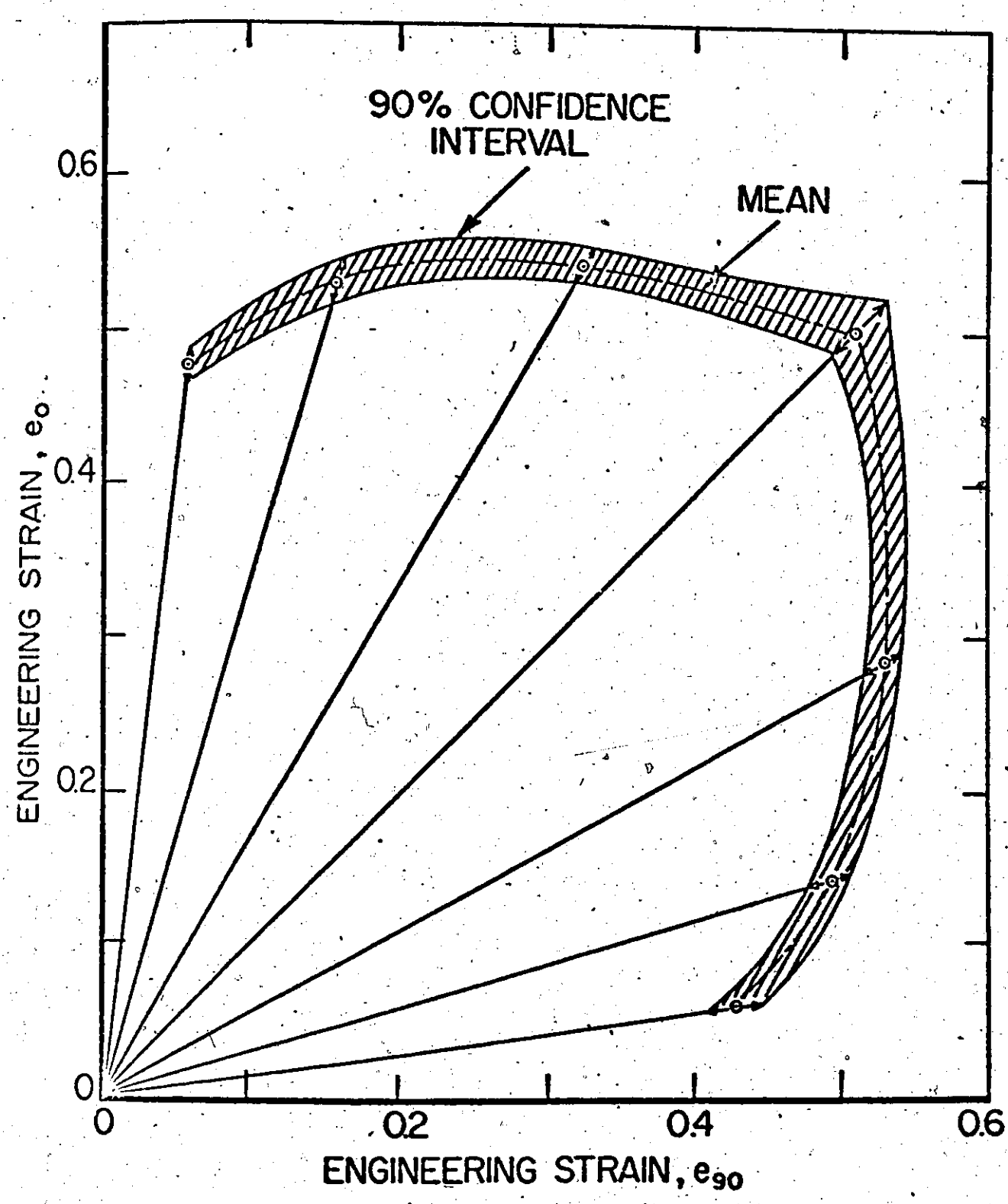

Figure 4.16. Mean Forming-Limits and its 90% Confidence Intervals for Rimming Steel, Material A.

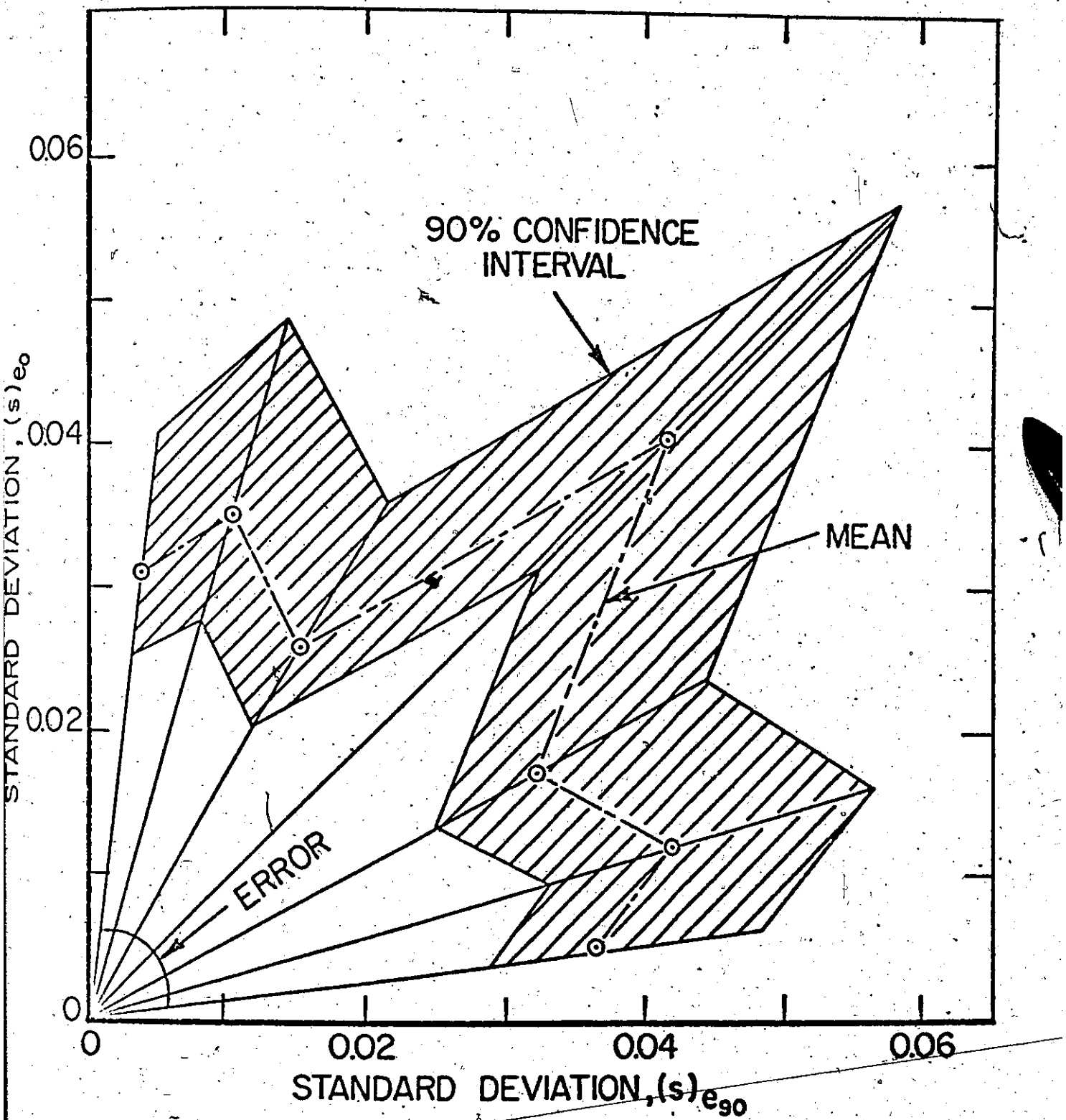

Figure 4.17. Standard Deviation of Forming-Limits and its 90% Confidence Interval for Rimming Steel, Material A.

squares were measured and it was found that the standard deviation was,

$$S_B = 0.00019 \text{ in.}$$

and the mean,

$$\bar{\ell}_o = .0996 \text{ in.}$$

It is assumed that the error in length measurement is zero for the undeformed grid. This is reasonable because the printed grid was extremely sharp and uniform before deformation.

iii) Replication Errors

A total of thirty-one replicas were taken repetitively and measured at different periods of time; the standard deviation was 0.00069 in.; however as this included measurement errors, it was assumed that the standard deviation in the replication technique was

$$S_C = \sqrt{(0.00069)^2 - S_A^2}$$

$$= 0.00056 \text{ in.}$$

The total error in determining the deformed grid length is the combination of the errors i) to iii) listed above and it is given by

$$S_T = \sqrt{S_A^2 + S_B^2 + S_C^2}$$

$$= 0.0009 \text{ in.}$$

As indicated in the Appendix A3, the standard deviation of the

projected strain vector, E, due to the above errors in determination of length can be calculated. This gives the scatter, in terms of a standard deviation, which can be accounted for by experimental technique, and for the rimming steel, material A, this standard deviation is shown in Figure 4.17. It is apparent that experimental errors play a small part in the observed scatter.

It may be assumed that the experimental error will be approximately the same for all of the different steels and for the purpose of comparison, the mean forming limits for all the materials are shown in Figure 4.18 and the standard deviations in Figure 4.19.

4.5.2. Results from Quantimet Analysis

The inclusion and the grain-size parameters from the Quantimet analysis were given in Tables 4.4(a) and 4.4(b) respectively.

4.6. Discussion

4.6.1. Forming-Limit Curves

In all the diaphragms tested the length of the major axis of the die was constant so that the region of critical or maximum strain in the centre of the diaphragm was approximately of constant length and increased in width as the die became more circular. The mean and the standard deviation of the forming limit would be expected to depend to some extent on the area of the region of greatest strain or on the strain gradients in a region. It would be useful therefore to perform tests

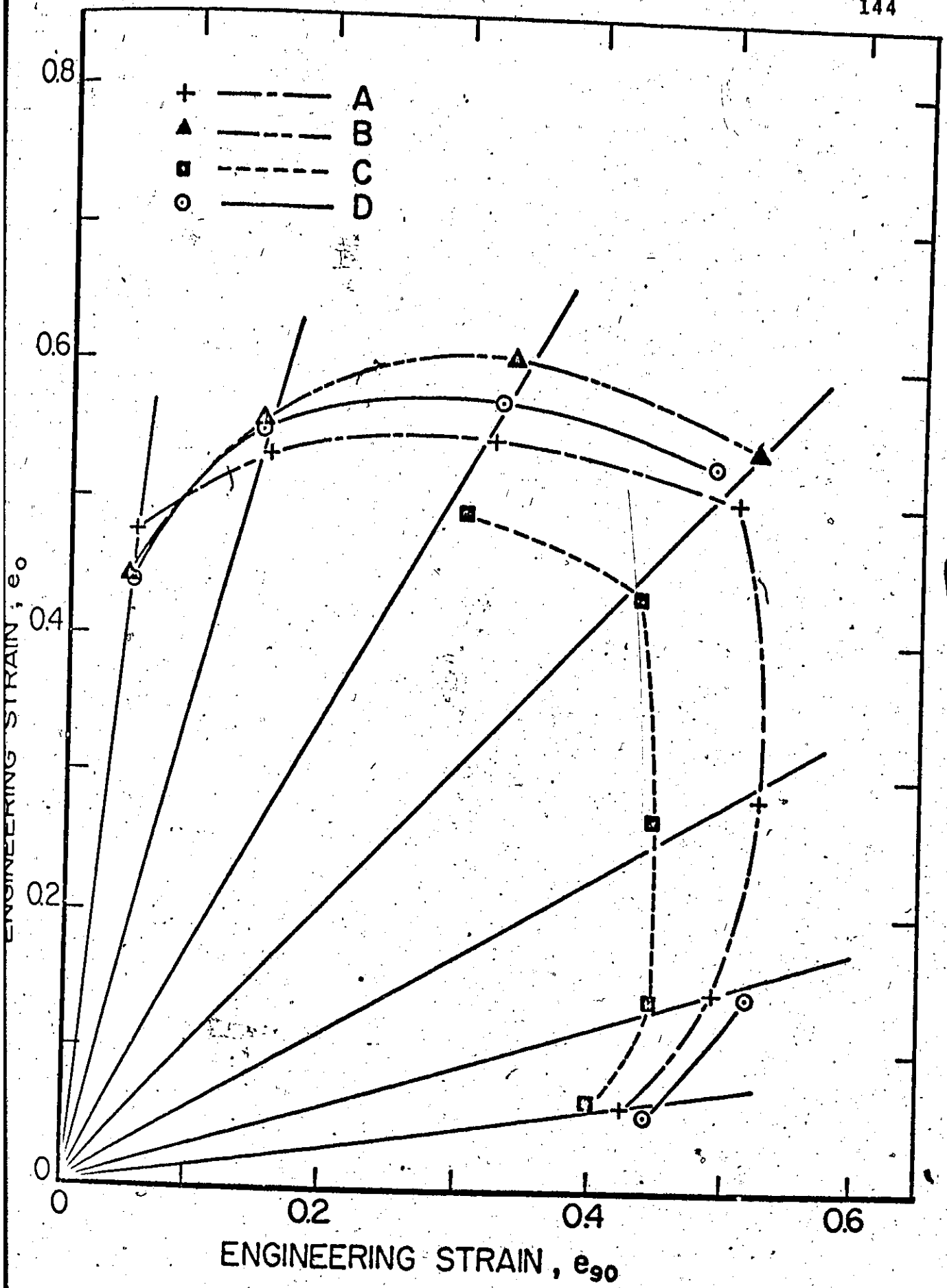

Figure 4.18. Mean Forming-Limit-Curves for the Four Steel Samples.

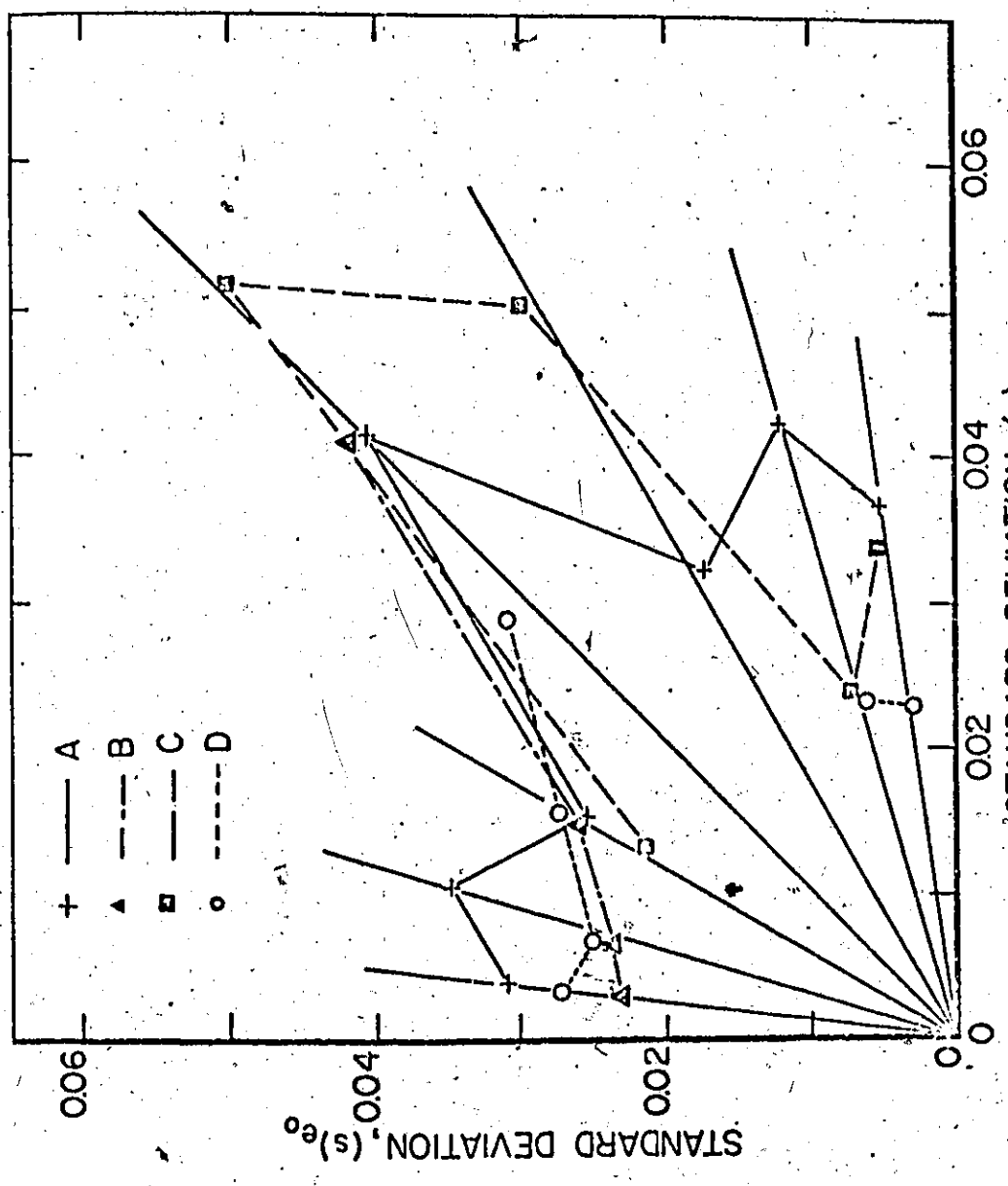

Figure 4.19. Estimated Standard Deviations of Limit Strains for the Four Steel Samples.

similar to the ones described using dies which were geometrically similar but of different size.

In this work, both the mean forming-limit and the scatter about the mean have been determined. This information could possibly be used to determine the probability of failure of an element of sheet stretched to a particular biaxial strain value. A three-dimensional forming-limit diagram as shown schematically in Figure 4.20 can be established from the mean and the standard deviation. In this diagram a point in the horizontal plane indicates the principal strains at a point in the sheet and the vertical ordinate represents the probability of failure which can be related to the percentage of rejects to be expected in a stamping operation. However, this relationship may not necessarily be a direct one as the probability of failure may be related to both strain level and strain gradient in a part.

In assessing the formability of a material it is suggested both the mean and the scatter in the forming-limits should be examined, i.e., the information in both Figures 4.18 and 4.19. From these figures, the means for both the rimming steel, material A, and capped steel, material C, are, in general, lower than for killed steel and even though the mean for the rimming steel, material B, is larger than for the killed steel, the scatter tends to be greater in the rimming steel. Thus the formability of both the rimming and capped steels can be considered to be lower than that of killed steel and this is usually observed in press shops.

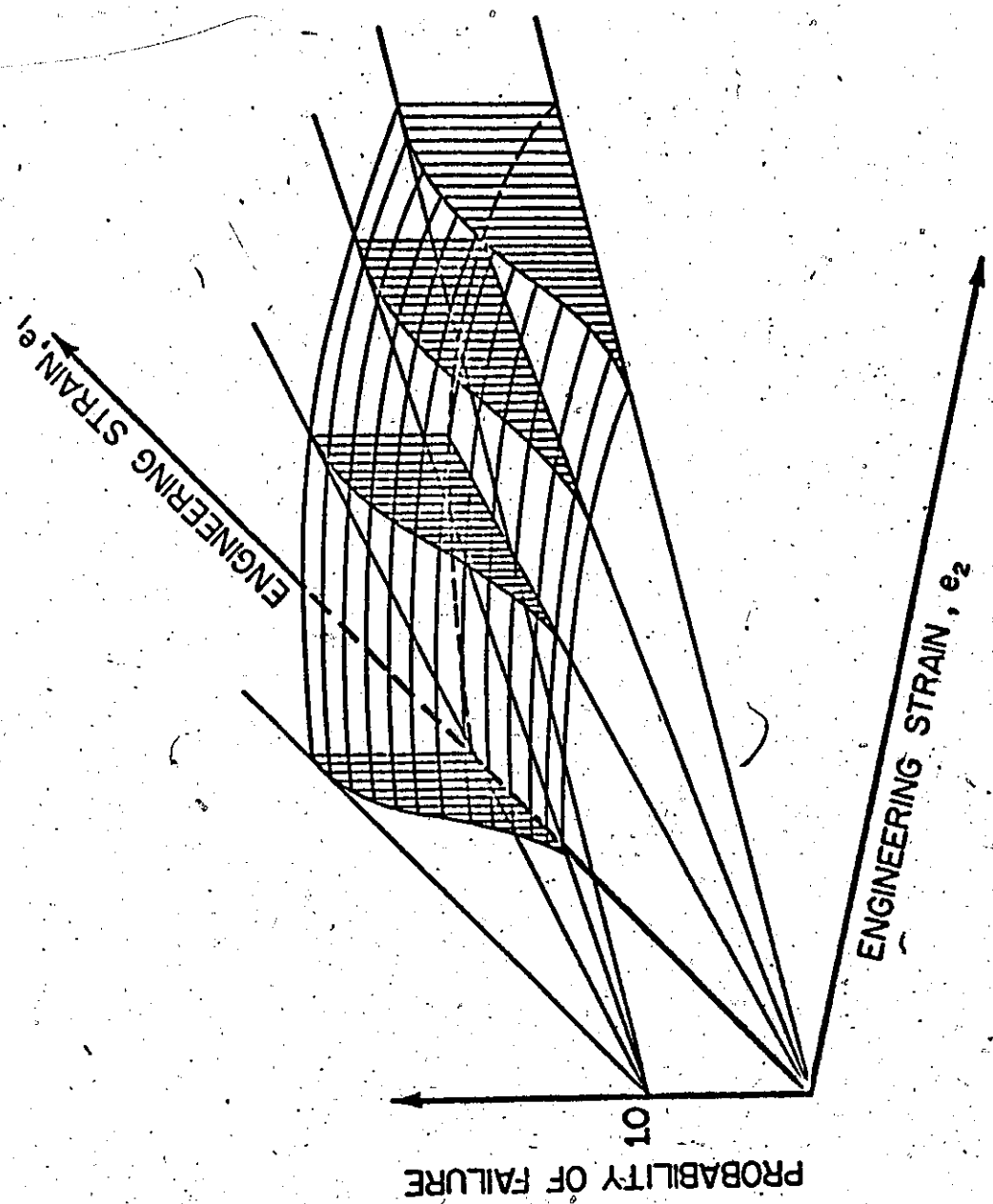

Figure 4.20. Three-Dimensional Forming-Limit-Diagram showing the Probability of Failure for a Particular Biaxial Strain State.

The impression that can be gained from Figure 4.19 is that the scatter seems to be the greatest in capped steel, and about the same magnitude in rimming steels. This has not been previously demonstrated and it is possible that this has as important an influence on overall formability as the mean value. In all cases, the scatter becomes larger as the process becomes closer to equal-biaxial tension and it is generally less when the greatest strain is in the direction of rolling than when it is in the transverse direction.

The method of determining the confidence interval of the mean forming limit was referred to previously and Figure 4.16 shows the 90% confidence interval on the mean forming limit for the rimming steel. Thus if repeated groups of tests were performed under the same conditions, there is a 90% probability that the mean of each group of tests would fall within the band indicated in Figure 4.16. The same analysis can be used to determine the number of tests, N, which must be performed to establish the mean forming-limit curve with a given accuracy (See Appendix A4). A convenient measure of accuracy would be to specify the width of the confidence interval as a percentage of the length of the mean strain path, E, in Figure 4.12. The results of such an analysis are shown in Table 4.6. This shows clearly that in order to establish a mean forming limit with reasonable certainty, for example to within $\pm$ 10%, five or more repeated tests should be performed for these particular materials. It also suggests that the results from one or two tests on a given material would not be very discriminating.

Table 4.6

Number of Tests to be Performed to Obtain a Given Accuracy at 90% Probability Level.

Die Ratio	Materials	Values of N			
		± 5% E	± 10% E	± 15% E	± 20% E
4:1	A. Rimming Steel	14	6	4	4
	B. Rimming Steel	6	3	2	2
	C. Capped	7	4	3	3
	D. Al.-Killed	6	4	3	3
1:1	A. Rimming Steel	12	5	4	3
	B. Rimming Steel	12	5	4	3
	C. Capped	24	8	5	4
	D. Al.-Killed	8	4	4	3

4.6.2. Quantimet Analysis

One result arising from the Quantimet analysis is the relationship between $\bar{R}$ values and the shape factor of the ferrite grain size, see Table 4.4(b). It is evident that the largest degree of normal anisotropy (arising from crystallographic texture) is exhibited by the aluminium-killed steel, material D, and this displays the largest shape factor as can be seen from the grain structure shown in Figure 4.5. For other materials, both the shape factor and $\bar{R}$ value are close to unity.

All evidence from the Quantimet analysis indicates that the capped steel, material C, should have the least formability. This material exhibits the largest percentage area of carbide plus inclusions, the smallest grain size, see Table 4.4(b) and the largest ratio of length of inclusion to ferrite grain size (i.e., 0.32).

The shape factor of the inclusions is known to influence the transverse ductility of steels and this mechanical fibering effect is clearly observed in the capped steel and in both samples of rimming steel. For these materials, the inclusion shape factors are much greater than unity (see Table 4.4(a)) as the inclusions are strung out in the rolling direction and this can be seen in the photo-micrographs presented in

Figures 4.5 to 4.7. Thus, in general, the forming limits for these materials tend to be lower when the largest strain is in the transverse direction than when it is in the rolling direction.

An examination of the fracture surfaces of the four steels under the electron-scanning microscope also gives support to the fact that the capped steel, material C, should give the least formability. For this steel, the fracture behaviour is less ductile and this is indicated by a stepping pattern in the fracture surface of this material (see Figure 4.21). This characteristic can also be observed at the cross-section profile of the failure zone of this material. Figure 4.22 shows the fracture profiles of capped steel and aluminium-killed steel specimens strained to rupture in various strain ratios and it can be seen that capped steel is comparatively less ductile than killed steel.

The Quantimet results of this work are of a preliminary nature and it is apparent that there is a great deal of scope for establishing more definitive structure and material property relationships.

4.7. Conclusions

The hydrostatic bulge tests in this work were performed on about 500 mild steel specimens. The results indicate that the scatter in the measured forming limits is greater than can be explained by an examination of errors inherent in the experimental method so that the scatter itself must be some manifestation of an intrinsic material property. This observation gives support to the Marciniak hypothesis that tearing in biaxial

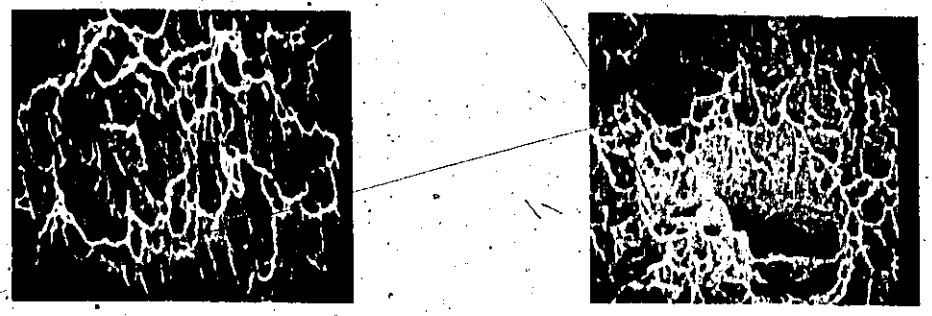

MATERIAL A

MATERIAL B

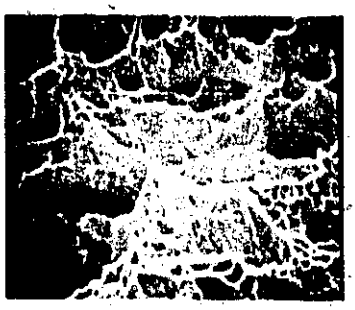

MATERIAL C

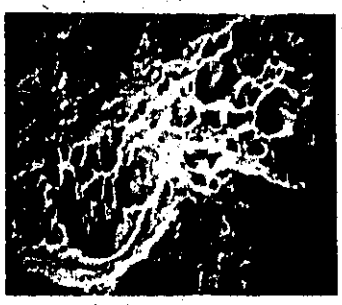

MATERIAL D

Figure 4.21 Scanning Electron Microscope Photographs of Fracture Surface of the Four Steel Samples (X500.)

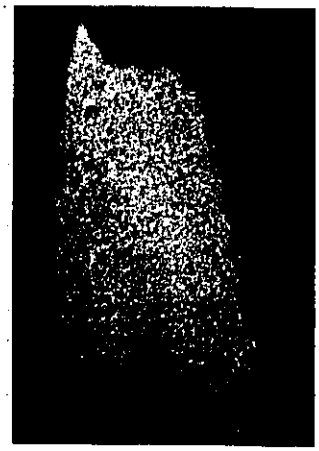

Strain ratio 0.15:1

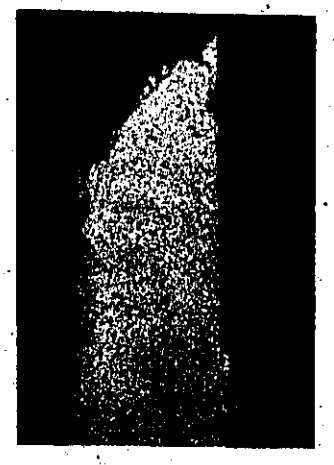

Strain ratio 1:1

(a)

Strain ratio 0.15:1

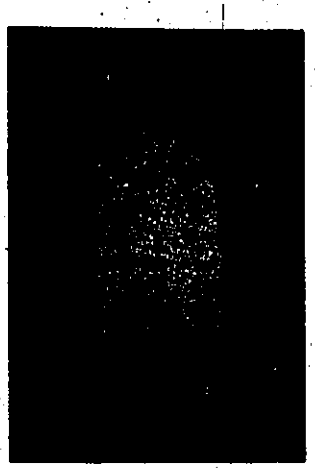

Strain ratio 1:1

(b)

Figure 4.22 Cross-Sections at Fracture Region of Specimens Strained in Different Strain Ratios,
a) Capped Steel (Material C)
b) Aluminium Killed Steel (Material D), (X80)

tension results from pre-existing inhomogeneity in the sheet.

There have been virtually no serious studies of the probabilistic nature of forming-limits prior to this work. A broad picture has been presented here dealing with different low C steels over a wide range of strain ratios. It is apparent that although a number of conclusions can be drawn, additional information could be obtained by taking a larger sample size. This would entail vast experimental effort and should perhaps be concentrated on those biaxial strain ratios which are most common in industrial pressings. The particular conclusions which can be made for the hydrostatic bulge tests, however, are:

a) The standard deviation of forming-limits was much greater than could be accounted for by an analysis of the experimental technique. This indicates that the failure process in sheet is itself a probabilistic phenomenon.

b) With the number of tests on one sample in this work, it was found that although there is some difference between the mean forming limits for the two different samples of rimming steels, the standard deviations of the forming limits for these two samples were roughly the same. The standard deviation was largest for the capped steel and smallest for the killed steel (for $\alpha=1$)

c) In general, the standard deviation increased as the degree of biaxiality of the process increased.

d) The mean forming limit when the greatest strain was in the direction of rolling was greater than when it was in the transverse direction; the standard deviation, however, was less in material A.

e) Using the materials and techniques similar to those described above, about four or five tests must be performed at each strain-ratio in order to obtain the mean forming-limit with reasonable accuracy.

The results from Quantimet analysis show that non-metallic inclusions exert some influence on fracture properties of the material and that these material inhomogeneities are partly responsible for the variability of the forming limits. Other correlations between the mechanical and metallographic tests are observed as pointed out above; however, in general, there does not seem to be a definite correlation with both the number of inclusions and inclusion size. It is possible that more discriminating metallographic examination is required. The failure process may be associated with certain types of inclusions and it may be possible that only inclusions above a certain size will affect failure.

Despite some uncertainties present in the investigation, this work provides a basis for a statistical analysis of forming-limit tests. It will assist in finding a quantitative relationship between the probability of tearing on a macroscopic scale and the morphology and distribution of inhomogeneities, particularly inclusions, at the micro-structural level, and this problem will be considered in the next chapter.

CHAPTER 5

DUCTILE FRACTURE IN SHEET METAL: A HYPOTHETICAL MODEL

5.1. Introduction

Non-metallic inclusions are inevitably present in all commercial steels; their amount, size, type, morphology and distribution have been shown to influence the mechanical properties of steels [5.1]. During the rolling of steel sheets, microscopic voids or holes are formed at the inclusion edges as a result of the difference between the deformability of the inclusions and the steel matrix. When subjected to a deformation in the elastic range, a system of inclusions (or holes) gives rise to a stress concentration which consequently changes the surrounding stress field. As the deformation proceeds into the plastic range, it is generally believed that the material goes through the following stages [5.2]:

a) After a certain plastic strain, additional microscopic holes may be nucleated at the inclusion edges or at grain boundaries where the shear stress is high.

b) These microscopic voids grow as the plastic strain increases and the distance between voids becomes smaller.

c) When this distance reaches a critical value, plastic deformation is concentrated in narrow regions which interconnect many holes and macroscopic deformation ceases.

d) Separation occurs in these regions and rupture finally takes place. Many dimple patterns resulting from voids or

inclusions can be observed on the fracture surface.

Thus non-metallic inclusions (or other material defects) are major factors affecting formability and their effect can be considered as equivalent to that of voids, the size of which are dictated by the type, morphology and size of the inclusions. Recently, various investigations [5.1, 5.3, 5.4] have concentrated on the effect of inclusions on material strength, ductility, fatigue properties and machinability; however there is only a limited knowledge of the relationship between inclusions and formability. The object of this chapter is to provide a failure model to rationalize the dependence of material formability on microscopic structure , and to give a quantitative relationship between formability and inclusions.

Assuming that failure is initiated from material defects, the prediction of material formability is basically a statistical problem as the defects are random in nature. Two major statistical theories have been developed to predict the strength of a material containing inclusions: the weakest link model [5.5] and the bundle fiber model [5.6]. The weakest link model seems to describe well the fracture behaviour of brittle materials such as glass and cast iron, while the other model has usually been applied to failure of more ductile materials. It is questionable, however, which model would be most suitable for a particular material and because of the advantage of a simple mathematical formulation, the weakest link type was chosen in the present analysis.

In this model, the rupture strength of a material is defined as being equal to the strength of its weakest part

subjected to a prescribed stress or strain system. From this assumption, a theory of extreme value was applied to determine the largest defects in a given population which is characterized by a prescribed distribution of defect size. Each defect was assumed to have zero strength and to grow independently of the neighbouring defects. The development of a defect during straining was assumed to follow the process described by Marciniak [3.5] and, as such, the fracture of the sheet can be related to the deformation of microscopic elements in the material.

The analysis was then applied to axi-symmetric forming problems to study the effect of strain-gradient, specimen thickness and size on the forming-limits so obtained. A computer aided simulation program was developed and forming-limits were obtained for materials having different degrees of cleanliness. It was found that the formability is not a unique function of the volume fraction of material defects but is dependent on both the density and the size distribution of the defects.

5.2. Description of the Model

The main purpose of the failure model is to predict the distribution of forming-limits for a sample of specimens subjected to a particular straining process. The specimens are considered to be from the same macroscopically uniform material which is described by:

i) a generalized stress-strain relation,

ii) zero rate sensitivity,

iii) a state of planar isotropy

and iv) a uniform apparent thickness t_o.

The material also possesses a state of non-uniformity characterized by a number of defects considered as spherical voids. The spatial distribution of these voids is assumed to be uniformly distributed in the material while the size (diameter) of the individual voids follows an exponential distribution law.

The straining process in the specimens is regarded as a biaxial-stretching process where a plane-stress condition exits. The process can also be described by a region of non-uniform strain intensity where all elements undergo a proportional straining process with the same biaxial strain ratio. The point of maximum strain in this region is identified and used as a reference point. The straining at this point is monotonically increasing during the straining process, while in the surrounding area the strain-rate is smaller and the local strain is a function of its distance to the reference point, i.e., the strain profile of the specimen in this process has an axis of symmetry which is normal to the sheet and passes through the sheet at the point of maximum straining.

The whole region surrounding the reference point is considered as being made up of a number of contiguous elements. At any instant the strain level in each element is known with respect to the strain at the reference point. Local strain concentrations are considered to develop independently in each element as a result of the inhomogeneities existing in the element.

failure of an element is deemed to occur when a particular value of the uniform strain in this element is reached. This uniform strain is determined from the state of initial inhomogeneity using the Marciniak analysis. The model then identifies which element would fail first as the straining of the specimen proceeds. The uniform strain in this element is determined and this is taken as the limit-strain for the particular specimen being considered. The model then operates on a number of specimens and a frequency distribution of the limit-strains is obtained.

5.3. Theoretical Considerations

5.3.1. Continum Properties of Material

For simplicity, Ludwik's constitutive equation is implemented; this is written as

$$\bar{\sigma} = \sigma_o (\bar{\varepsilon} + \varepsilon_o)^n.$$

Rate sensitivity is ignored, although it could be introduced into the analysis. Other constitutive equations are possible although the Marciniak analysis requires a material with a definite yield point, i.e., $\bar{\sigma} \neq 0$ at $\varepsilon_o = 0$. Plastic isotropy is assumed in the plane of the sheet, however the properties of the material in the thickness direction can be different from that in the plane of the sheet, i.e., $\Delta R = 0$ but $\bar{R}$ can differ from unity. The sheet is considered to have a superficially uniform thickness t_o but the effective thickness may vary locally due to the presence of voids which will be taken into account as indicated below.

5.3.2. Material Inhomogeneity

It is recognised that the principal mechanism of fracture in ductile material lies in either the opening of cracks (or voids) which were already present in the material before straining, or the development of micro-cracks which are initiated at inclusions (or other material defects) during plastic deformation. Thus it is conveniently assumed that material inhomogeneities, which include non-metallic inclusions, precipitates, voids and other defects can be categorized by equivalent holes or defects of zero strength. No attempt is made to relate the equivalent void distribution to an actual distribution of real imperfections but it is assumed that the state of the material can be represented by a density and size distribution of equivalent voids.

These voids are assumed to be distributed uniformly in the material with a density δ per unit area of the sheet. As a first approach to the problem, the voids are proposed to have a spherical shape of diameter D which follows a certain distribution function.

The distribution of non-metallic inclusions in steel ingots has been studied in detail by Bergh [5.7] and it was found that as the size increases, the spatial probability of finding large inclusions decreases exponentially as shown in Figure 5.1. In steel sheets, these inclusions are flattened out and re-oriented during the process, however, the shape of the frequency distribution curve of the inclusion size is not changed. Thus it may be assumed that the defect diameter D has an exponential distribution, viz.,

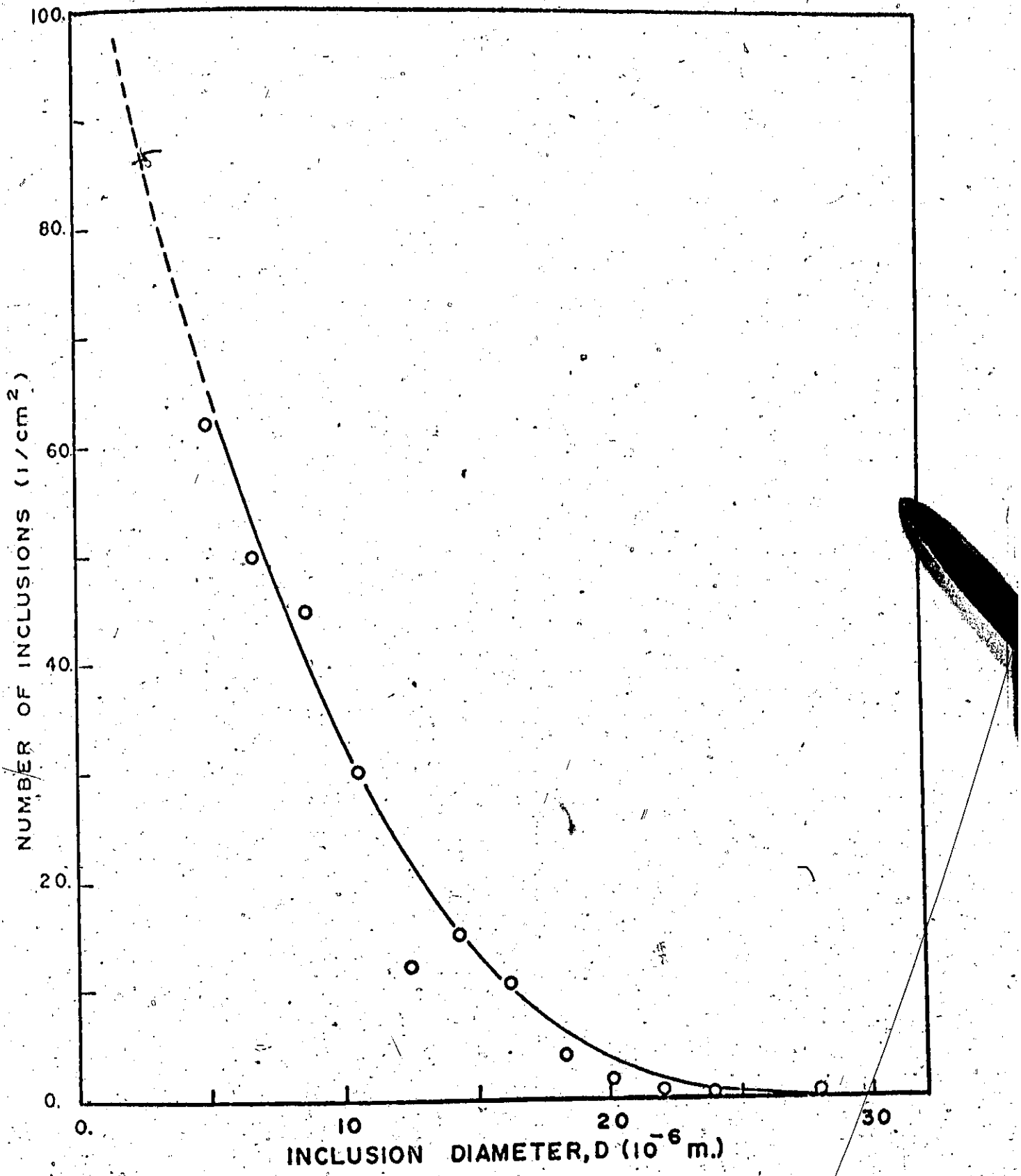

Figure 5.1. Frequency Distribution of Oxide Inclusion Size in Silicon-Steel Ingot [5.7].

$$g'(D) = D_0 \lambda e^{-\lambda D}, \qquad (5.1)$$

where λ is the distribution parameter and D_0 is a dummy variable which for convenience is taken as unity. A typical experimental distribution is given in Figure 5.1 and the effect of changing λ is shown in Figure 5.2. This may not be the most appropriate form of distribution for all materials and although it would be possible to accommodate some other forms in the model, Equation (5.1) is relatively simple and is used throughout this work.

5.3.3. The Elemental Area

The specimen considered can be divided into a number of elemental areas, each of which has an area A. The size of this area is chosen so that the localized deformation which causes failure of the specimen is contained within the element. The average number of voids in each element is then given by

$$N = \delta A, \qquad (5.2)$$

where δ is the defect density per unit area. During the straining of the element, the deformation of these voids contributes to the total uniform deformation of the element; strain concentration, however, is assumed to occur only in that region of the element which has the largest defect. Thus the deformation of the largest void in the element will cause rupture in the element and when the first element fails, the whole specimen is assumed to have failed.

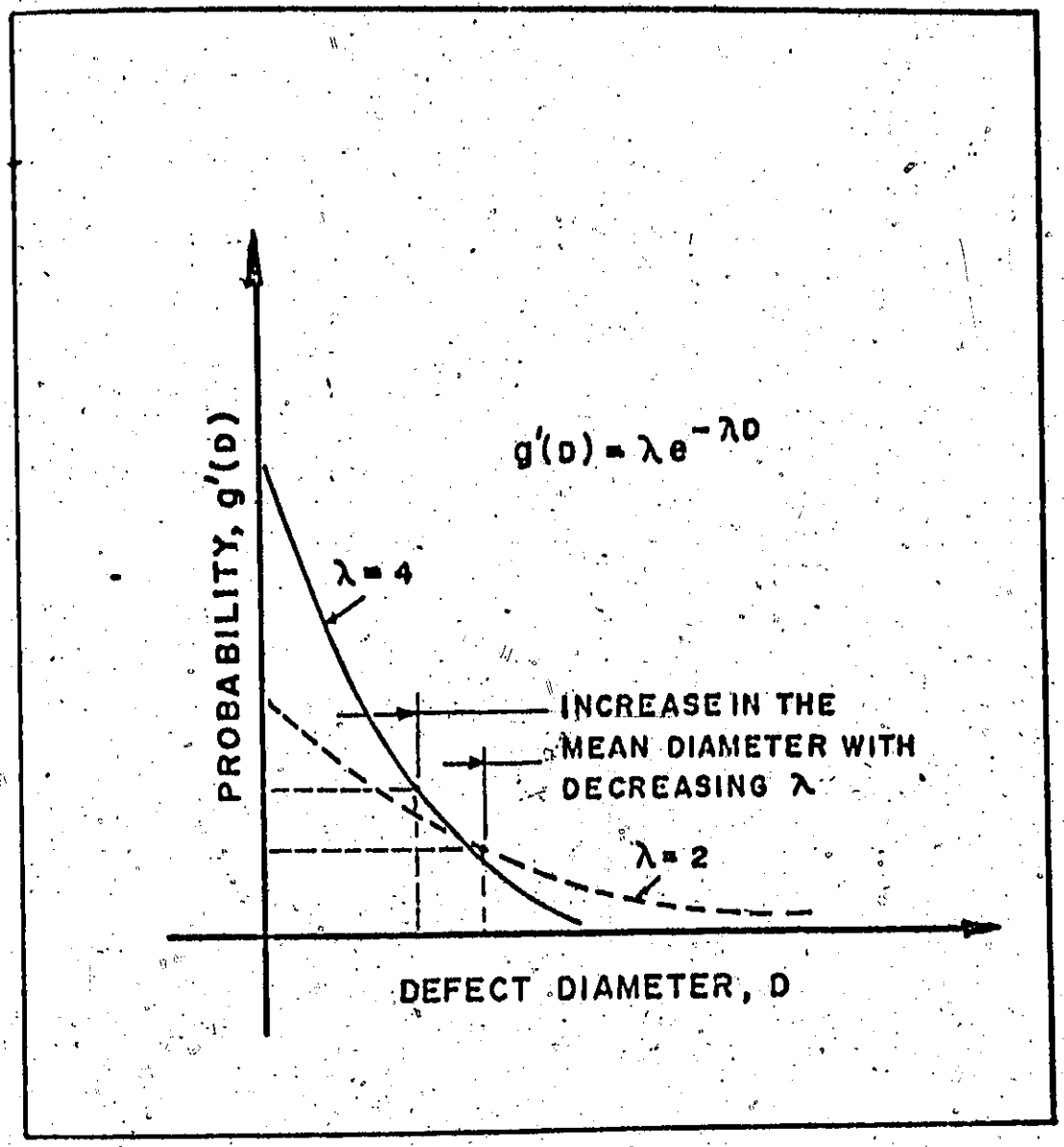

Figure 5.2. Proposed Density Distribution of Defect Size.

5.3.4. Determination of the Largest Defect Size

As failure of the element involves the largest defect, it is necessary to find the probability that the largest defect in an element will have a certain size. This is equivalent to determining the distribution of the largest defect D* amongst a sample of N defects drawn from a population of defects, the diameters of which are distributed according to an exponential function, Equation (5.1).

The theory of extreme value was first developed by Fisher and Tippett [5.8]; it has been used for studying the dielectric strength of capacitors [5.9], the pit depth in corrosion [5.10], [5.11] and also the critical stress at fracture of metals [5.5]. A brief description of the theory is given below.

The distribution of the mean values of samples drawn from a given population is a normal distribution regardless of the behaviour of the population. This is not true, however, for the case of the extreme values. Let us consider the distribution of the largest defect diameter D* in a sample of N defects where the distribution of D is given by g'(D). The function g'(D) and its derivative are continuous in the region where D is between zero and infinity. The cummulative distribution associated with g'(D) is given by

$$g(D) = \int_0^D g'(D)\, dD,$$

or

$$g(D) = 1 - e^{-\lambda D} \qquad (5.3)$$

Thus the probability of a defect D smaller than a given size D^* is $g(D^*)$. Assuming that the events occur independently, the probability that N defects are smaller than D^* is $g(D^*)^N$. This is also the probability that the defect D^* is largest amongst N defects. Therefore the distribution of the largest defect in samples each with N defects (where the sample is) taken from a given population (of samples) is

$$g_N(D^*) = \frac{d}{dD}\left(g(D^*)^N\right)$$

or

$$g_N(D^*) = N\, g'(D^*)\, g(D^*)^{N-1}.$$

Thus

$$g_N(D^*) = N\lambda e^{-\lambda D^*}\left(1-e^{-\lambda D^*}\right)^{N-1}, \qquad (5.4)$$

and the cumulative distribution is given by

$$g_N^i(D^*) = g(D^*)^N = \left(1-e^{-\lambda D^*}\right)^N. \qquad (5.5)$$

The most probable value (or the mode) of the largest value D^* in samples, each of size N, drawn from a population with a density function g'(D) can be found by equating $\frac{d}{dD^*}\left(g_N(D^*)\right) = 0$. If a solution D_N^* exists, then

$$(N-1)\, g'(D_N^*)^2 = -\, g''(D_N^*)\, g(D_N^*),$$

or

$$(N-1)\,\lambda^2 e^{-2\lambda D_N^*} = \lambda^2\, e^{-\lambda D_N^*}\left(1-e^{-\lambda D_N^*}\right),$$

Therefore

$$D^*_N = \frac{\ln N}{\lambda} \qquad (5.6)$$

For any given initial distribution function g'(D), one can use a similar procedure to derive the distribution of the extreme values. In some cases, however, direct calculation involves complex integrals and the asymptotic distributions for large N are used instead. Detailed analysis of these distributions is given in References [5.8] and [5.12].

It suffices here to note that for a population having the size distribution given by Equation (5.1) one can obtain the distribution function $g_N(D^*)$ for the largest defect in an element and this is shown in Figure 5.3.

5.3.5. Determination of Failure Strain in Elements

Equation (5.4) gives the distribution of the largest defect size D* in elements, each containing N defects. By establishing a relationship between D* and the failure strain, one can derive the distribution of failure strain in all the elements from Equation (5.4).

The development of localized strain concentration, initiated by the largest defect D* of an element, is assumed equivalent to the straining of a Marciniak groove with a thickness reduction factor given by

$$f_o = \frac{t}{t_o} = 1 - \frac{D^*}{t_o} \quad , \qquad (5.7)$$

where t is the effective thickness of the material (see Figure 5.4). Using the Marciniak analysis described in

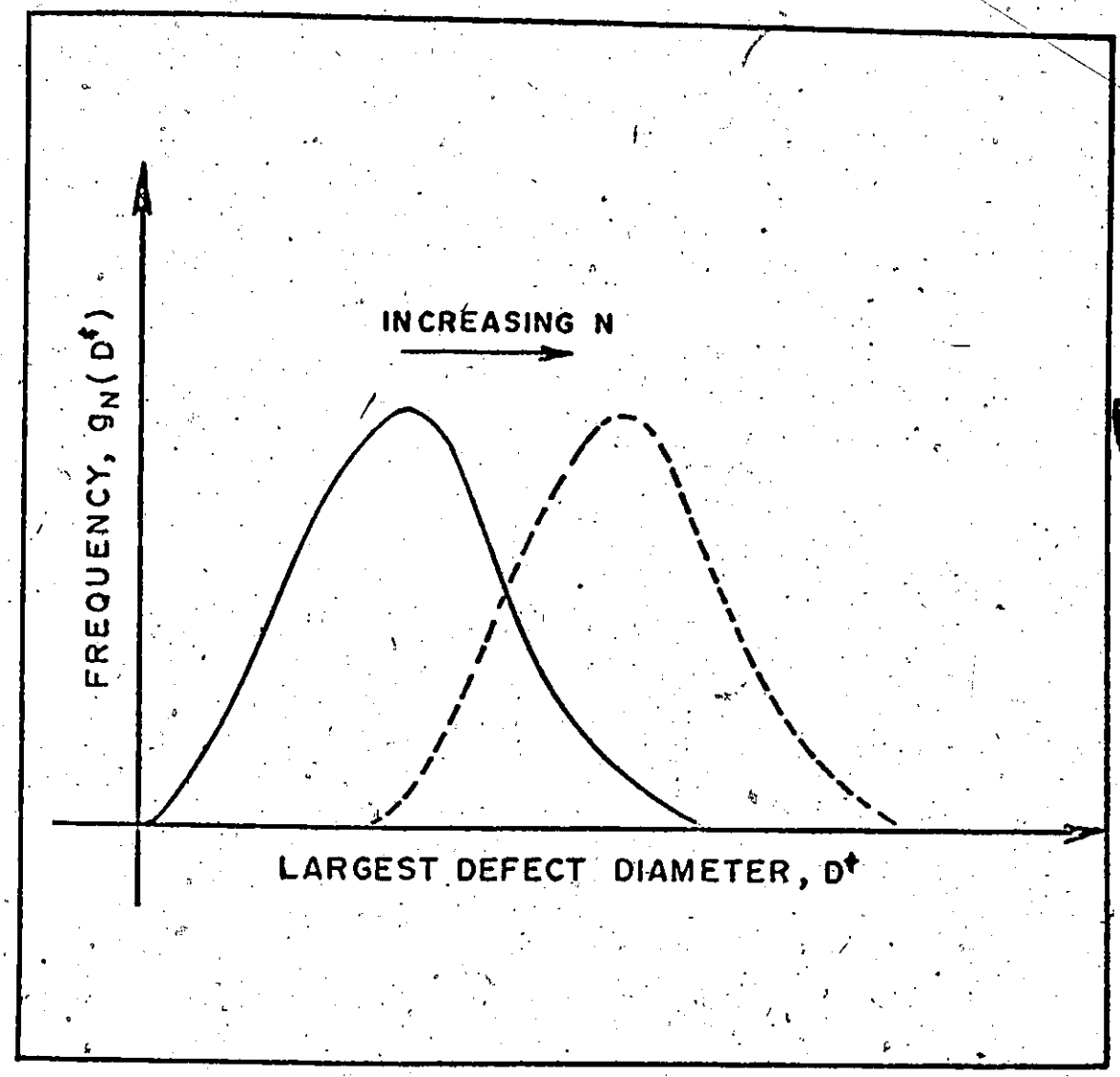

Figure 5.3. Frequency Distribution of the Largest Defect Size, D^*, for Different Sample Sizes, N.

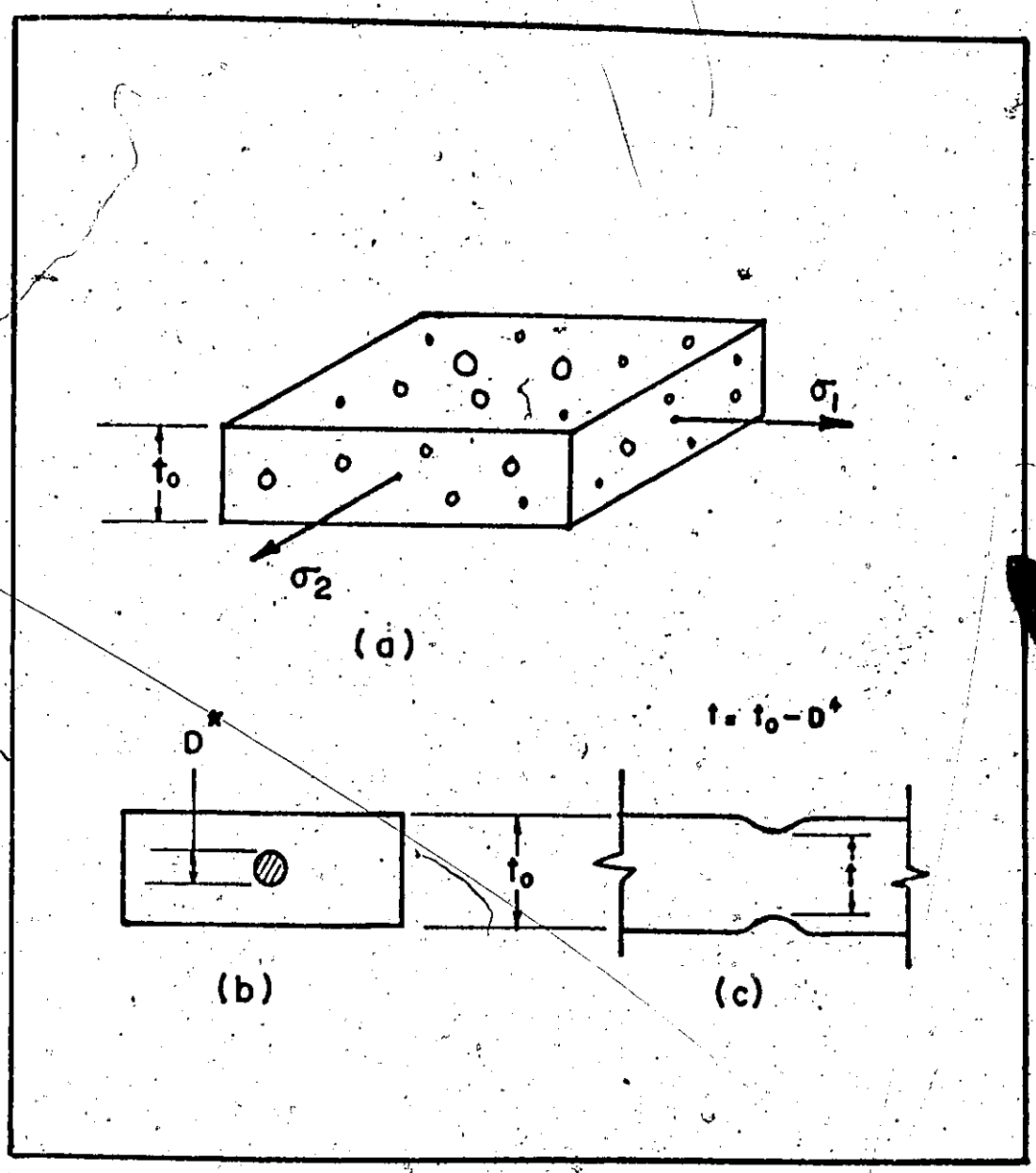

Figure 5.4. Ductile Fracture Model:

a) Schematic Representation of Voids in Elemental Area.

b) Cross-Section of the Elemental Area showing the Largest Defect, D*.

c) The Equivalent Marciniak Groove.

Chapter 3, the limit-strain can be calculated for an element subjected to a prescribed strain ratio. The calculated limit-strain is thus a function of the diameter of the defects, viz.,

$$\varepsilon_t = \varepsilon_t (D^*) ,$$

where ε_t is the limit-strain expressed in terms of thickness strain. For given plastic properties of the material, the limit-strains can be calculated and plotted against defect size as shown in Figure 5.5. It is observed from this figure that the limit strains can be approximated as

$$\varepsilon_t = - B_1 \ln \frac{D^*}{B_2 t_o} , \qquad (5.8)$$

where B_1 and B_2 are positive constants dependent on the strain ratio α, and the plastic properties characterized by n, $\bar{R}$ and ε_0.

Equation (5.8) shows that ε_t is a strictly decreasing function with respect to D^*, thus a method of variable transformation, viz.,

$$g_N(\varepsilon_t) = \frac{g_N(D^*)}{\left|\frac{d\varepsilon_t}{dD^*}\right|}$$

can be applied to Equation (5.4) and this becomes

$$g_N(\varepsilon_t) = - \frac{B_2}{B_1} N \lambda t_o \exp(-\varepsilon_t/B_1) \exp[-B_2 \lambda t_o \exp(\varepsilon_t/B_1)]$$

$$\{1 - \exp[-B_2 \lambda t_o \exp(-\varepsilon_t/B_1)]\}^{N-1} . \qquad (5.9)$$

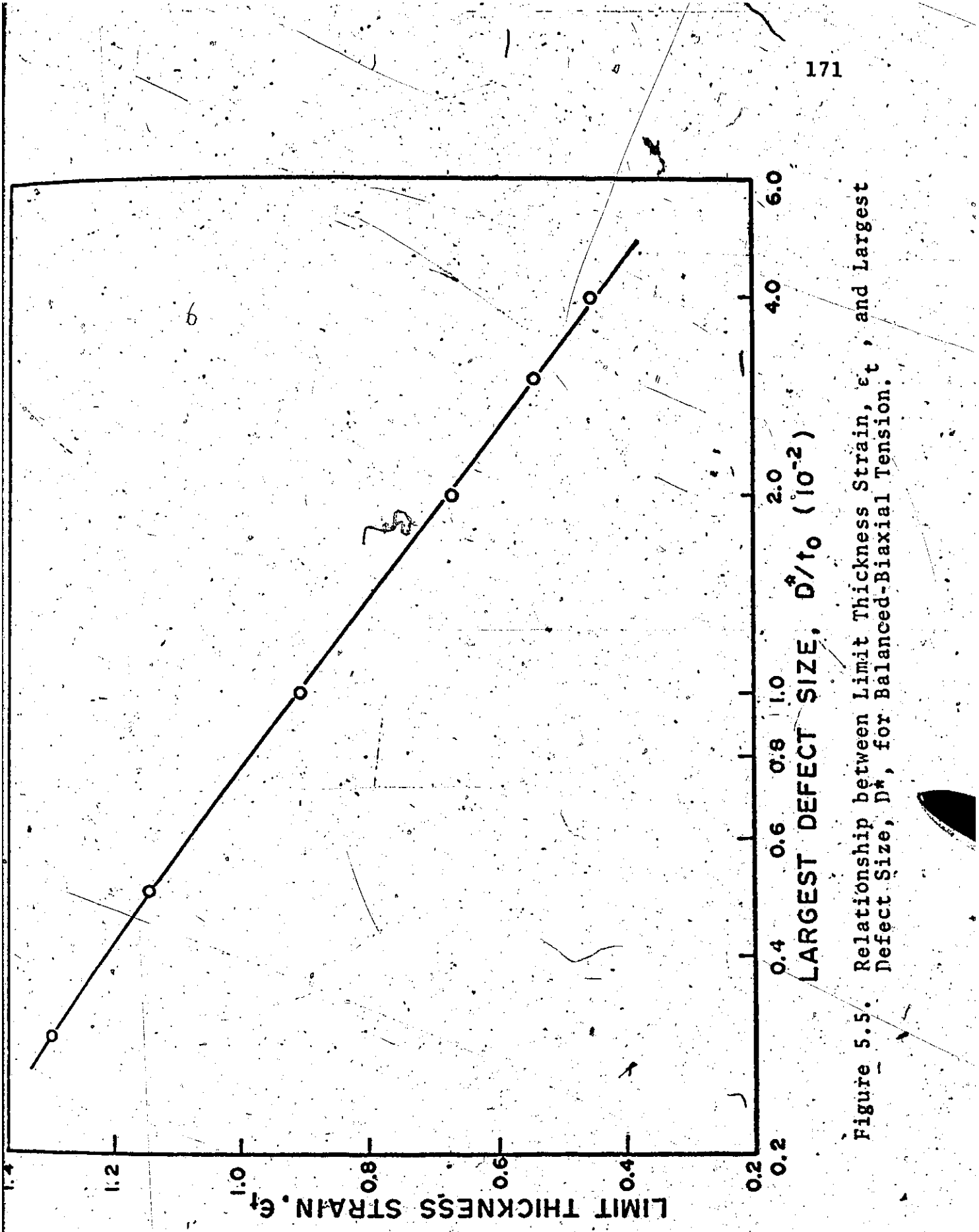

Figure 5.5. Relationship between Limit Thickness Strain, ϵ_t, and Largest Defect Size, D*, for Balanced-Biaxial Tension.

This relation defines the probability density of limit-strains in a large number of elemental areas, each of which has N defects.

5.3.6. The Deformation Process

The fracture model can be applied to non-uniform deformation processes characterized by a deformed surface which has an axis of symmetry passing through a point of maximum straining. A simple example of this type of deformation is the hydrostatic bulging of circular diaphragms where the reference point is the pole of the dome and the axis of symmetry is defined by a line perpendicular to the surface at the pole. Such a surface can be considered to be composed of a number of concentric annuli or rings (see Figure 5.6) within which the strain gradient is negligible. The strain level is different from one ring to the next; however, the biaxial strain ratio is assumed to be constant. As the ring radius becomes larger, the number of the elements in the ring increases and can be determined as a function of the radius in the undeformed specimen. The strain level within each ring is approximately constant and is related to the strain at the reference point by the strain profile of the specimen.

a) Distribution of Elemental Areas

The number of elemental areas in an annulus of width Δr and mean radius r in the undeformed configuration as shown in Figure 5.6 is

$$\Gamma(r) = \frac{2\pi r}{A} \Delta r \quad , \qquad (5.10)$$

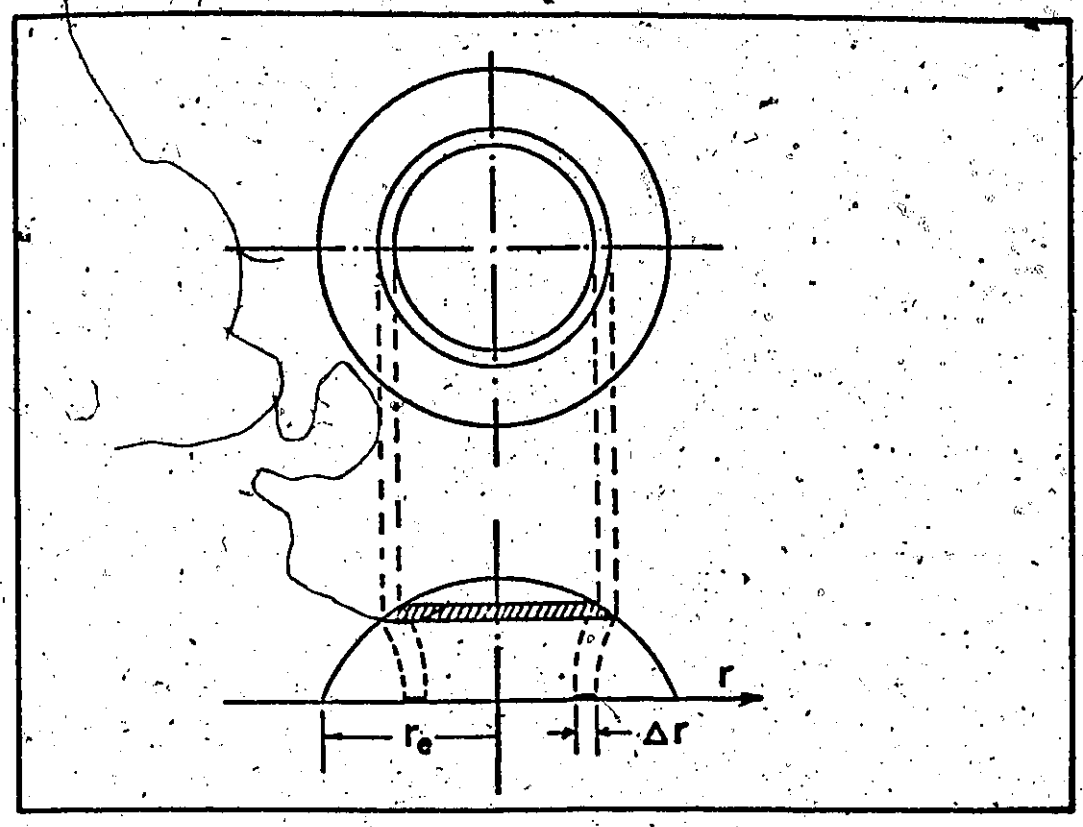

Figure 5.6. A Non-Uniform but Axi-Symmetric Deformation Process showing a Ring of (Assumed) Constant Thickness Strain.

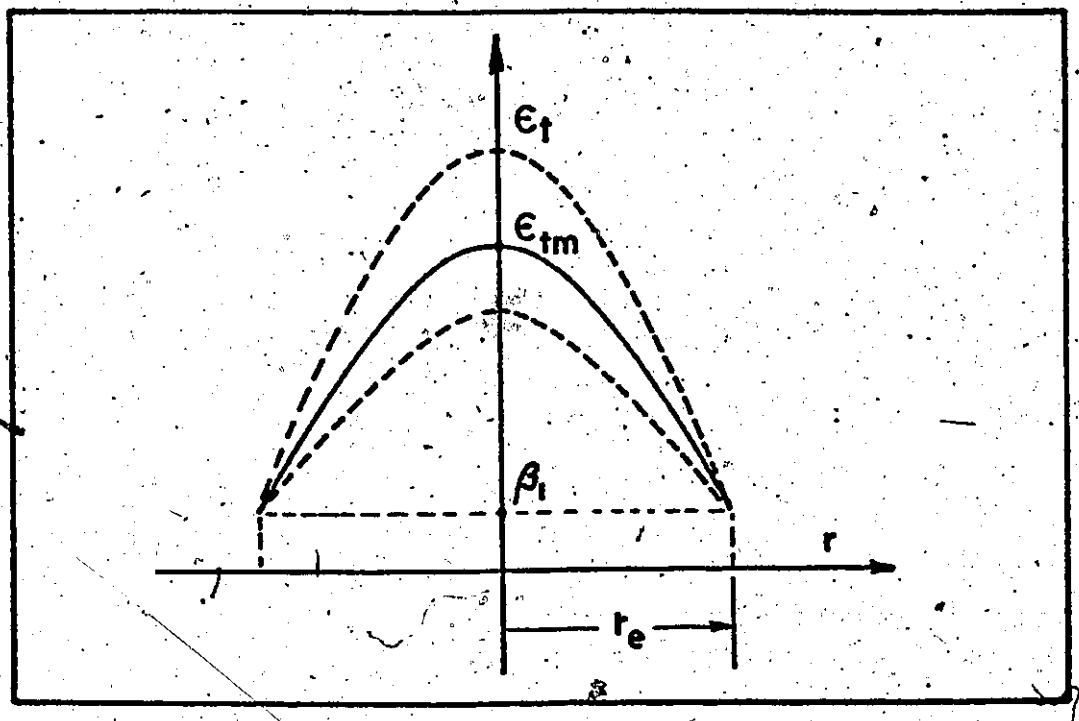

Figure 5.7. Thickness Strain Profiles of a Material in the Deformation Process shown in Figure 5.6.

where A is the area of the element. For a constant Δr, Equation (5.10) defines the distribution of elemental areas subjected to the same strain level.

h) Strain Profiles

The strain profile for a region is generally represented by a curve such as in Figure 5.7 which is referred to the undeformed radius of the point. A simple empirical relation, of a power law kind, can be fitted to this strain profile. For example the thickness strain profile could be described by

$$\varepsilon_t = -\beta_3 \left(\frac{r}{r_e}\right)^{\beta_2} + \beta_4 ,$$

where β_2, β_3 and β_4 are positive constants and r_e is the edge radius of the specimen in the undeformed configuration. This can be written in terms of the strain ε_{tm} at the reference point, i.e.,

$$\varepsilon_t = \varepsilon_{tm} \left[1 - \left(\frac{r}{r_e}\right)^{\beta_2}\right] + \beta_1 \left(\frac{r}{r_e}\right)^{\beta_2} \qquad (5.11)$$

where β_1 and β_2 are constants.

5.4. Method of Solution

The three Equations (5.9), (5.10) and (5.11) are governing equations for the determination of the probability density function of the limit strains for specimens tested in a process as described above. Based on these equations, a simulation process was employed to determine the failure point in the specimen and to calculate the resulting limit

strains. A computer program developed for this simulation process is given in Appendix B1 and the following is a brief description of the technqiue.

Consider a circular ring j at radius r on the specimen. The number of elements in this ring is M_j which can be calculated from Equation (5.10). The limit strain ε_t for each element is chosen in the following manner. For an element i, a pair of uniformly distributed random numbers Ω_{i1} and Ω_{i2} between zero and one are generated. Then, the limit strain for this element is defined as

$$\varepsilon_{ti} = \Omega_{i1} [(\varepsilon_t)_{max} - (\varepsilon_t)_{min}] + (\varepsilon_t)_{min} , \qquad (5.12)$$

where $(\varepsilon_t)_{max}$ and $(\varepsilon_t)_{min}$ are chosen as the upper and lower limits respectively for the limit strain density function $g_N(\varepsilon_t)$, given by Equation (5.9). Let $(g_N)_{max}$ be the maximum value of $g_N(\varepsilon_t)$. If

$$\Omega_{2i} \leq \frac{g_N(\varepsilon_{ti})}{(g_N)_{max}} \qquad (5.13)$$

then ε_{ti} is accepted as a member of the sample taken from the population described by $g_N(\varepsilon_t)$ and thus ε_{ti} is considered to be the limit strain in the element i. For more details of this rejection technqiue, see Appendix B2. This procedure is repeated for M_j elements in the ring j and the smallest value of ε_t is selected as the limit strain for this ring. (It should be noted that the values of ε_t so selected would approximate the original distribution $g_N(\varepsilon_t)$ for a large number

of values ε_t). Let this limit strain be $(\varepsilon_t)_j$. This can be related to the strain at the pole $(\varepsilon_{tm})_j$ using Equation (5.11). The value of $(\varepsilon_{tm})_j$ is thus the strain at the pole of the specimen when failure first occurs in ring j which is characterized by a failure strain $(\varepsilon_t)_j$.

This procedure is repeated for the next ring until all the region is covered and a distribution of the values such as $(\varepsilon_{tm})_j$ can be established. The least value of this distribution, $(\varepsilon^*_{tm})_j$, is the value of the strain at the pole when failure of the specimen - as a whole - occurs. Clearly, the value $(\varepsilon^*_t)_j$ associated with this minimum $(\varepsilon^*_{tm})_j$ is the limit strain for the specimen. The simulation process is then repeated for a number of specimens and the frequency distribution of the limit strains for these is determined.

5.5. Results and Discussion

The failure model was applied, as a numerical example, to a material with plastic properties defined as $n = 0.21$, $\bar{R} = 1$, and $\varepsilon_o = 0.0075$. (This would be similar to one of the steels described previously). Other parameters used in the numerical solution are shown in Table 5.1.

Samples of 50 specimens were used in the simulation process and the frequency distributions of limit strains for these samples were obtained. (The effect of sample size and the size of the elemental area on the results is indicated in Appendix B3). The following are typical results from the above analysis.

Table 5.1 Parameters Used in the Simulation Process

Material constants	$n = 0.21$, $\bar{R} = 1$, $\varepsilon_o = .0075$
Failure strain parameters	$B_1 = 0.332$, $B_2 = 0.155$, (Equation 5.9)
Simulation parameters	$A = 0.01$ in^2, $\Delta r = 0.1$ in. (Equation 5.10)
Process parameters	$\alpha' = 1.$ $\beta_1 = 0.14$, $\beta_2 = 1.5$, (Equation 5.11)

5.5.1. Frequency Distribution of Limit Strains

For a strain-ratio equal to unity, the probability density curves of the limit-strains in elemental areas determined from Equation (5.9) are shown in Figures 5.8(a) and 5.8(b). These curves may also represent the frequency distribution of limit-strains in individual specimens of area A which are tested in a uniform straining process, i.e., a strain gradient does not exist within the specimen. In general, these frequency distribution curves are skewed toward the left; however, they could be approximated by normal distribution curves. If the defect size distribution parameter λ is constant, the mean and spread of the distribution decrease as the defect density δ increases. This is shown in Figure 5.8(a). In increasing λ and keeping δ constant, however, the distribution curves have the same shape even though they are shifted to the right; this is indicated in Figure 5.8(b).

A typical calculated histogram of the limit strains ε_t^* in a sample of 200 specimens, simulated as being tested in the process determined by the parameters in Table 5.1, is shown in Figure 5.9. (The diameter of the specimen is 6 inches as defined by $r_e = 3$ inches and the apparent thickness is $t_o = 0.035$ inch.). This histogram appears to have similar characteristics to the distribution curves shown in Figures 5.8(a) and 5.8(b). If, however, the same number of specimens of the same diameter had been considered to be strained uniformly in biaxial tension, the histogram for the limit strains would be the one shown on the left (i.e., for zero strain gradient). It is observed from this figure that the mean and the spread

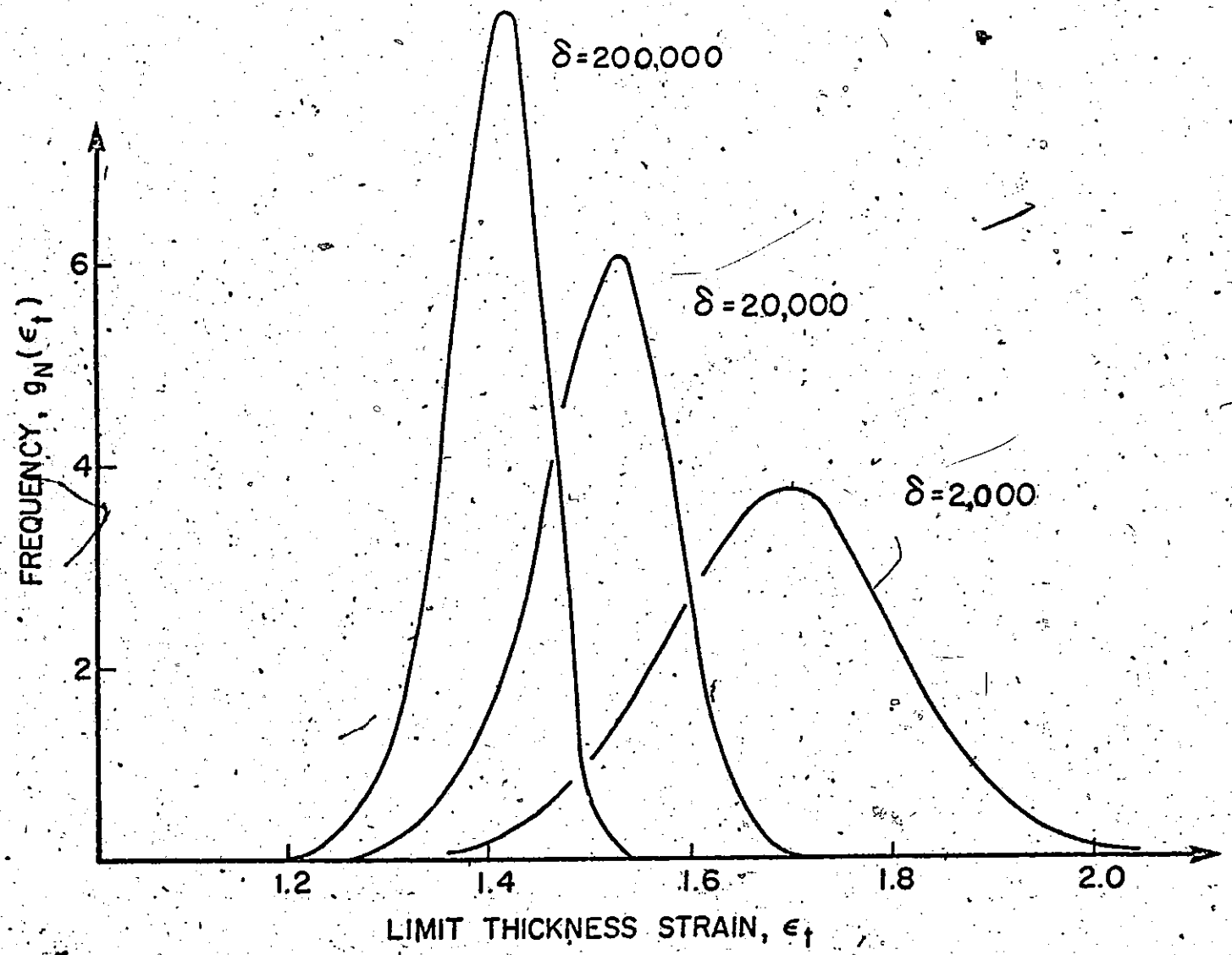

Figure 5.8a. Frequency Distributions of Limit-Strains for Elemental Areas; a) For $\lambda = .4$.

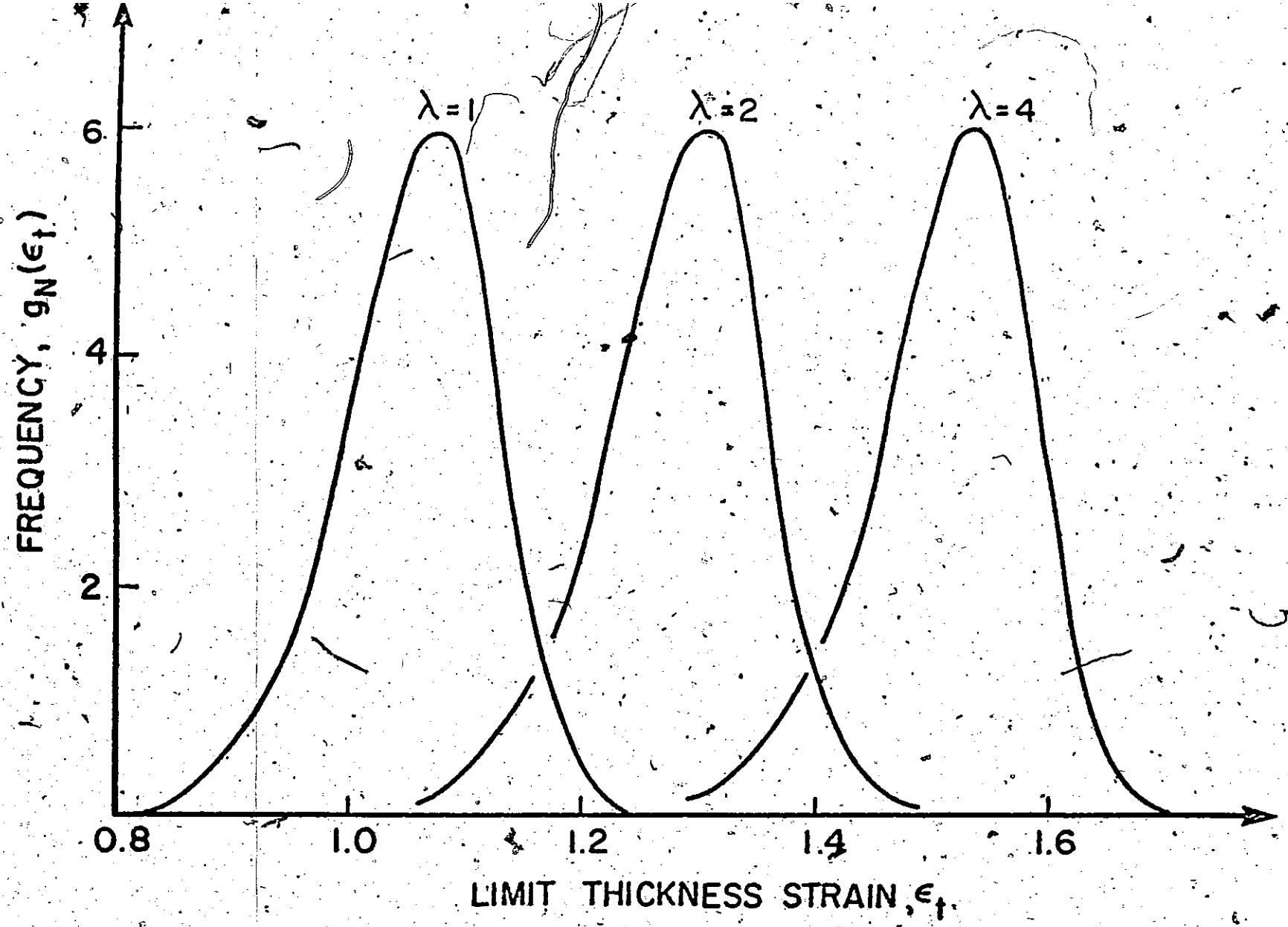

Figure 5.8b. Frequency Distributions of Limit-Strains for Elemental Areas; b) For $\delta = 20{,}000/in^2$.

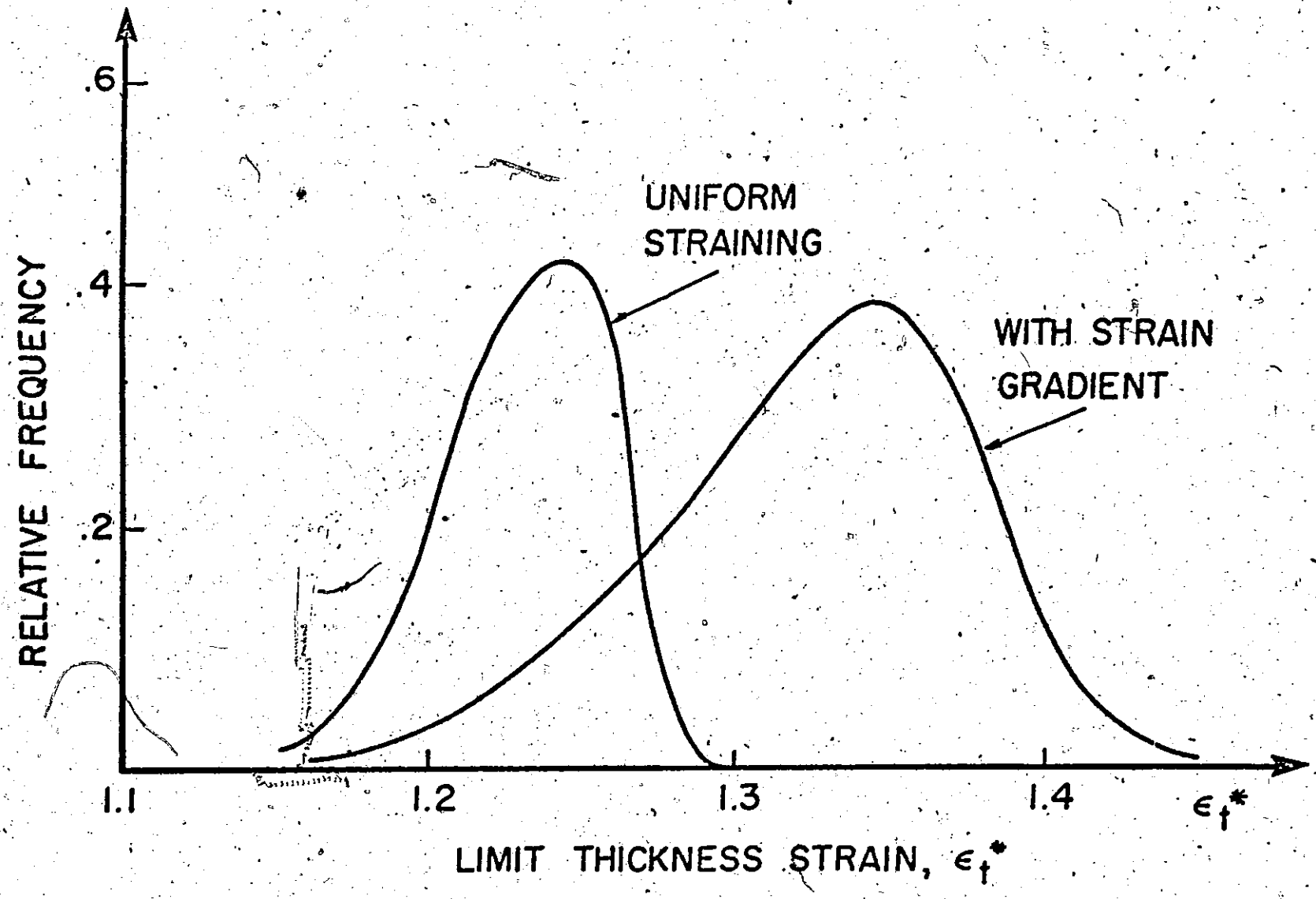

Figure 5.9. Influence of Strain Gradient on the Frequency Distribution of Limit Strains, ϵ_t^* (for $\lambda = 4$ and $\delta = 20{,}000/in^2$.).

of the frequency distribution curve for specimens where there is a strain gradient are both greater than for specimens strained uniformly.

As the defect size distribution parameter λ and the defect density δ used in the analysis were arbitrarily chosen, it is necessary to investigate the influence of λ and δ on the distribution of limit-strains of the sample. Histograms of the limit-strains in the specimens similar to those shown in Figure 5.9 were established for different λ and δ and the means and standard deviations for the resultant frequency distributions were determined.

5.5.2. Effect of Defect Size Distribution and Defect Density

The mean and the standard deviation of the limit-strains ε_t^* for materials having the same defect density but of different defect size distribution parameter λ were obtained and plotted on a semi-logarithmic paper as shown in Figure 5.10. It is seen in this figure that the mean increases with increasing λ while the standard deviation remains approximately constant. In the range of $0.5 \leq \lambda \leq 10$. the mean limit strains can be approximated by

$$(\varepsilon_t^*)_{ave} = C_1 \ln \left(\frac{\lambda}{C_2}\right) , \qquad (5.14)$$

where C_1 and C_2 are constants. A physical interpretation of the above observations is that as the probability of encountering a large defect in a material decreases, i.e.,

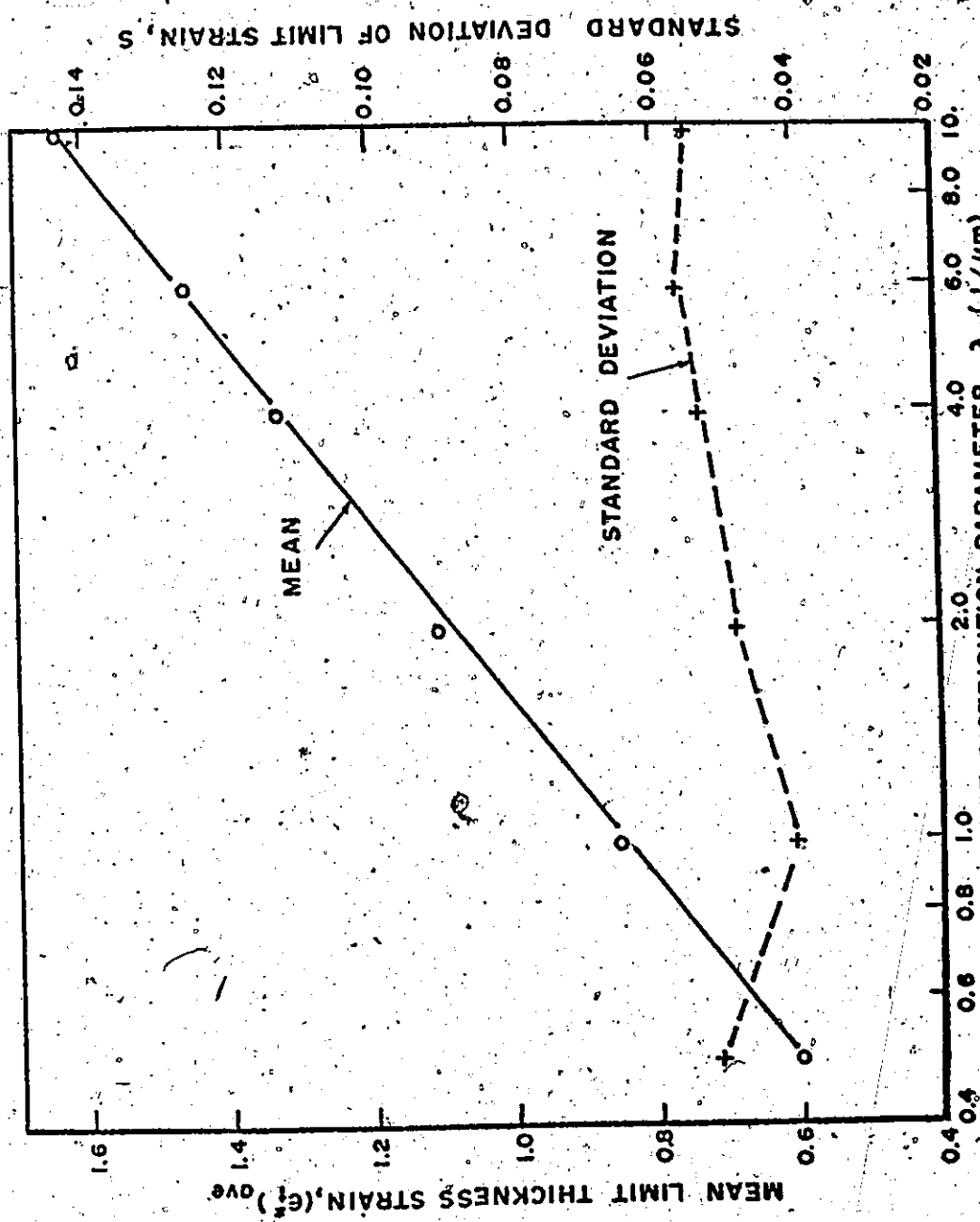

Figure 5.10. Effect of Defect Size Distribution Parameter, λ, on Frequency Distribution of Limit Strains, ϵ_t^*, for δ = 20,000/in.^{2}.

λ increases (see Figure 5.2), the formability is improved. This view has been supported by many metallurgists.

Figure 5.11 shows the effect of varying the defect density on the distribution of limit strains for material possessing the same λ. The mean and standard deviation of the limit-strains decrease as the defect density rises, thus fewer voids and inclusions lead to better formability - which again is well known.

5.5.3. Effect of Defect Volume Fraction

The volume fraction of the material defects which has a density δ/t_o per unit volume and obeys a distribution law given by Equation (5.1) can be derived as

$$V = \frac{\delta}{t_o} \int_o^\infty g'(D) \left(\frac{\pi D^3}{6}\right) dD,$$

or

$$V = \frac{\pi \delta \lambda}{6 t_o} \int_o^\infty e^{-\lambda D} D^3 \, dD.$$

so

$$V = \frac{\pi}{t_o} \left(\frac{\delta}{\lambda^3}\right) \qquad (5.15)$$

Data from Figures 5.10 and 5.11 are replotted in Figure 5.12 to show the influence of the defect volume fraction on forming limits. It is observed in Figure 5.12 that the limit strains decrease as the defect volume fraction increases and clearly for either δ or λ constant,

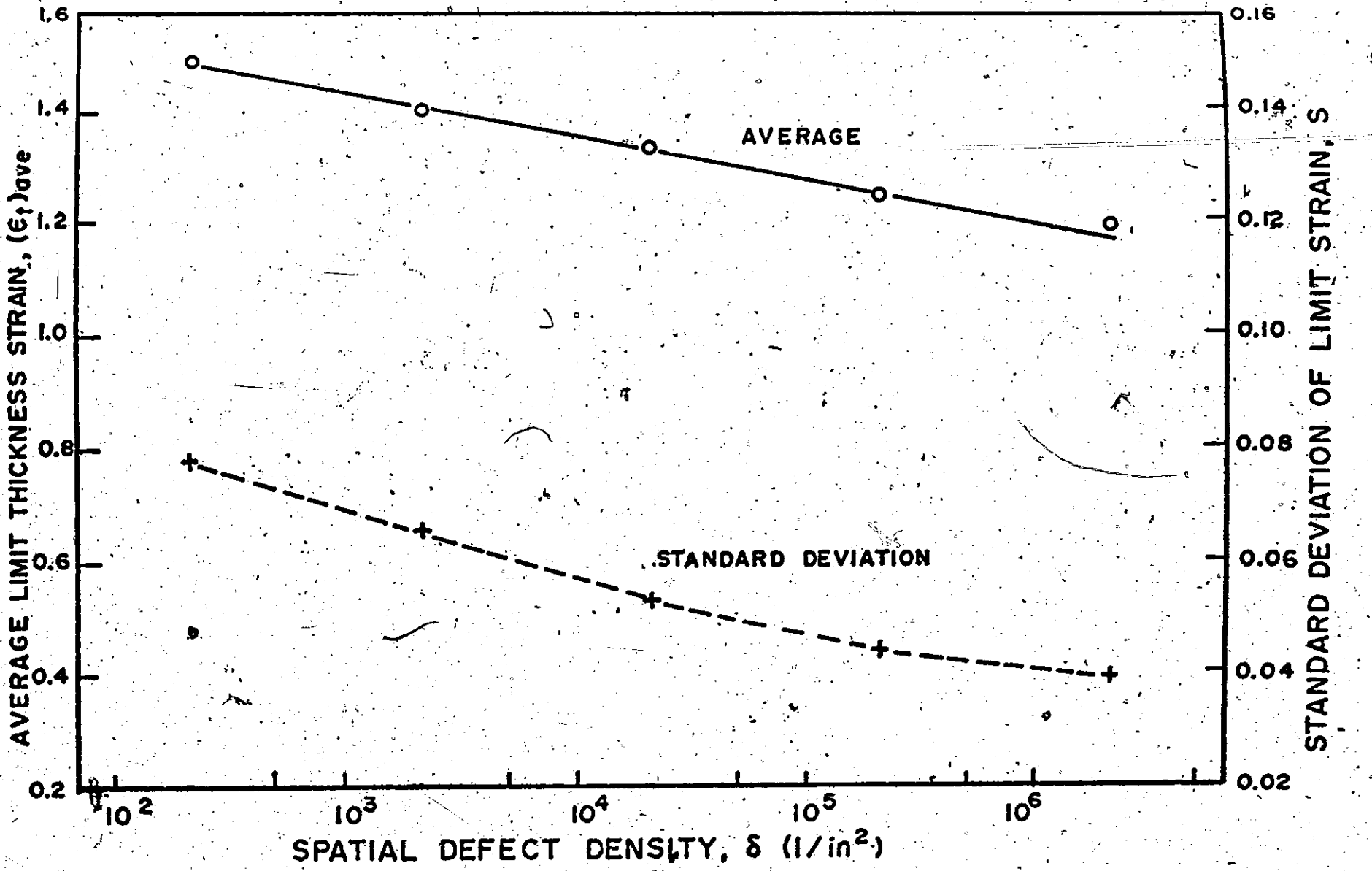

Figure 5.11. Effect of Defect Density, δ, on Frequency Distribution of Limit Strains, ϵ_t^*, for $\lambda = 4$.

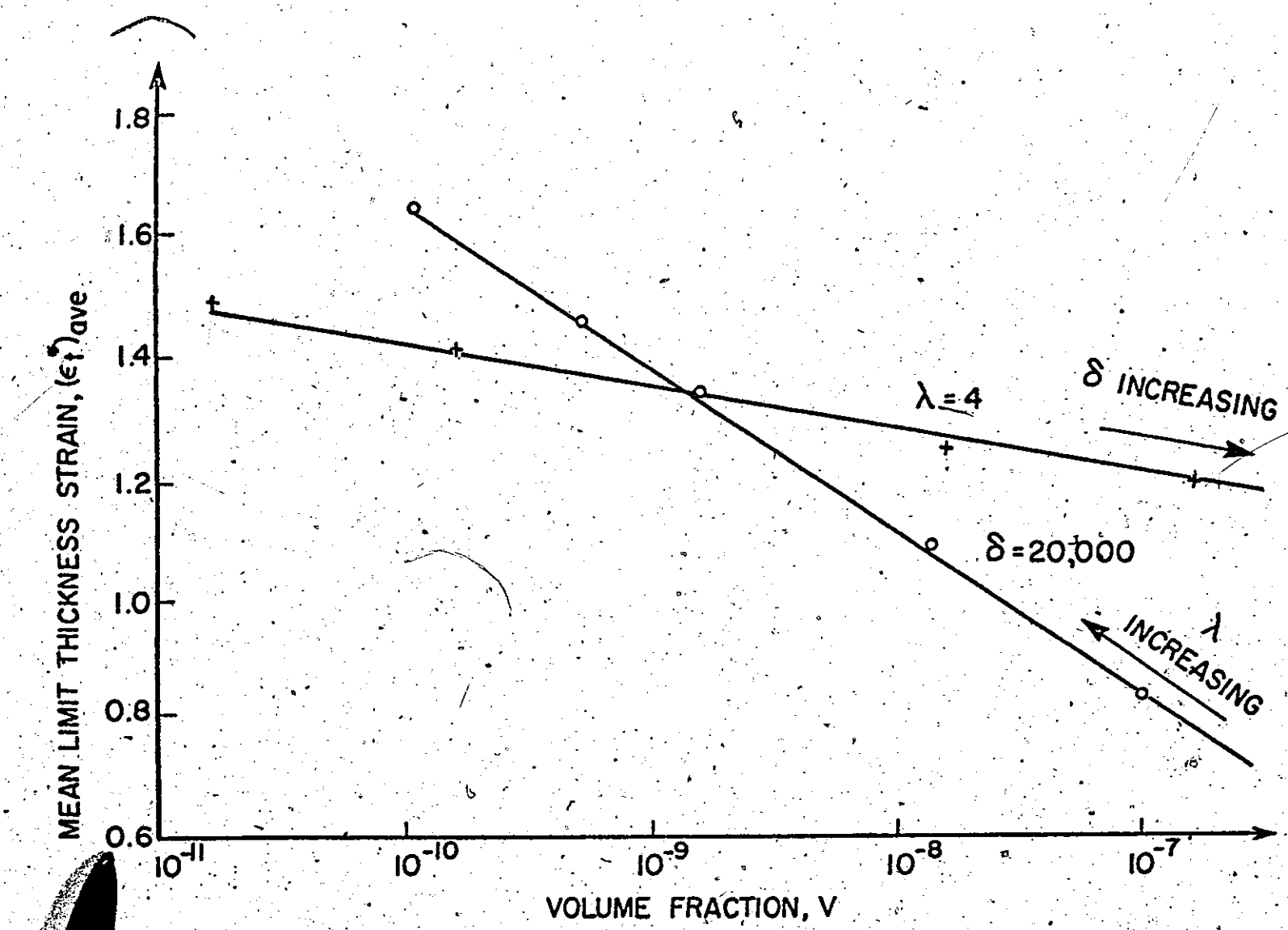

Figure 5.12. Effect of Defect Volume Fraction on Average Limit Strains, $(\epsilon_t^*)_{ave.}$, for Specimens having r_e = .3 in. and t_o = 0.035 in.

$$(\varepsilon_t^*)_{ave} \propto \ln\left(\frac{1}{V}\right) \qquad (5.14a)$$

Gurland and Plateau [2.56] analysed the uniform elongation of a tensile test piece containing inclusions and they showed that for material having spherical voids, a similar relationship, Equation (5.14a) exists. It must also be noted that this relationship is not unique since δ and λ are mutually independent; hence one obtains different limit-strain curves depending on whether λ or δ is kept constant. In the previous figures, Figures 5.10 and 5.11, the variation of limit-strain with each parameter was shown; however, in these cases the volume fraction was not constant. Curves which show the effect of δ and λ for constant volume fractions are indicated in Figures 5.13(a) and 5.13(b) respectively.

5.5.4. Effect of Size and Thickness of Specimens

As the specimen increases in size, it is expected that the formability will decrease since the larger the specimen, the greater is the number of defects which can be found in the critical straining region. This effect is shown in Figure 5.14. The solid line in this figure represents the mean limit strains for specimens of different sizes. In this example, size is varied by changing the edge radius, r_e in Equation (5.11), of the non-uniformly deforming specimen. As the diameter of the specimen increases, the mean limit strains decrease slightly and the standard deviations of the limit strains, shown as a dotted line in Figure 5.14, also

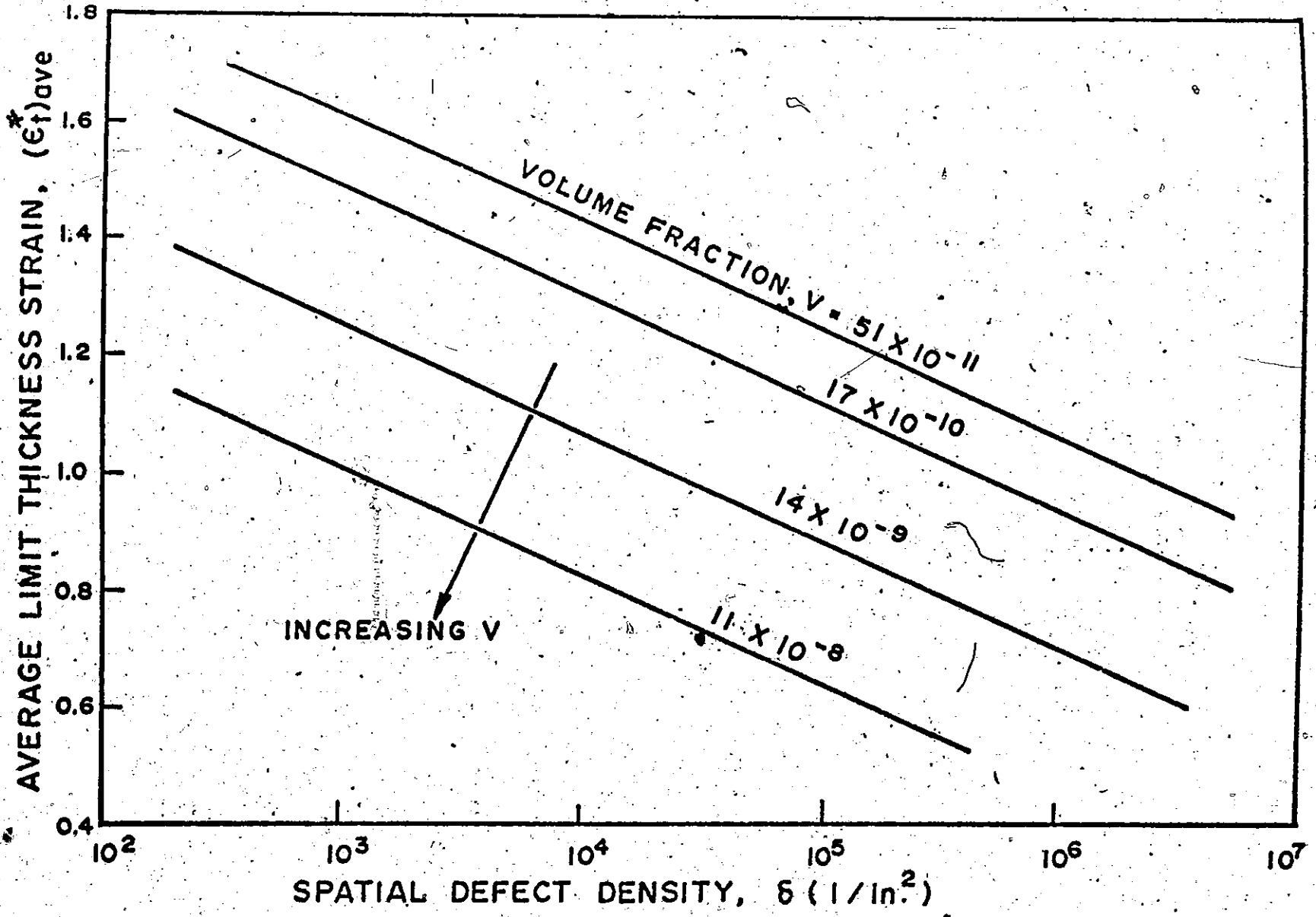

Figure 5.13a. Effect on Average Limit Strains, $(\varepsilon_t^*)_{ave.}$, (for Constant Defect Volume Fraction, V) of
a) Defect Density, δ.

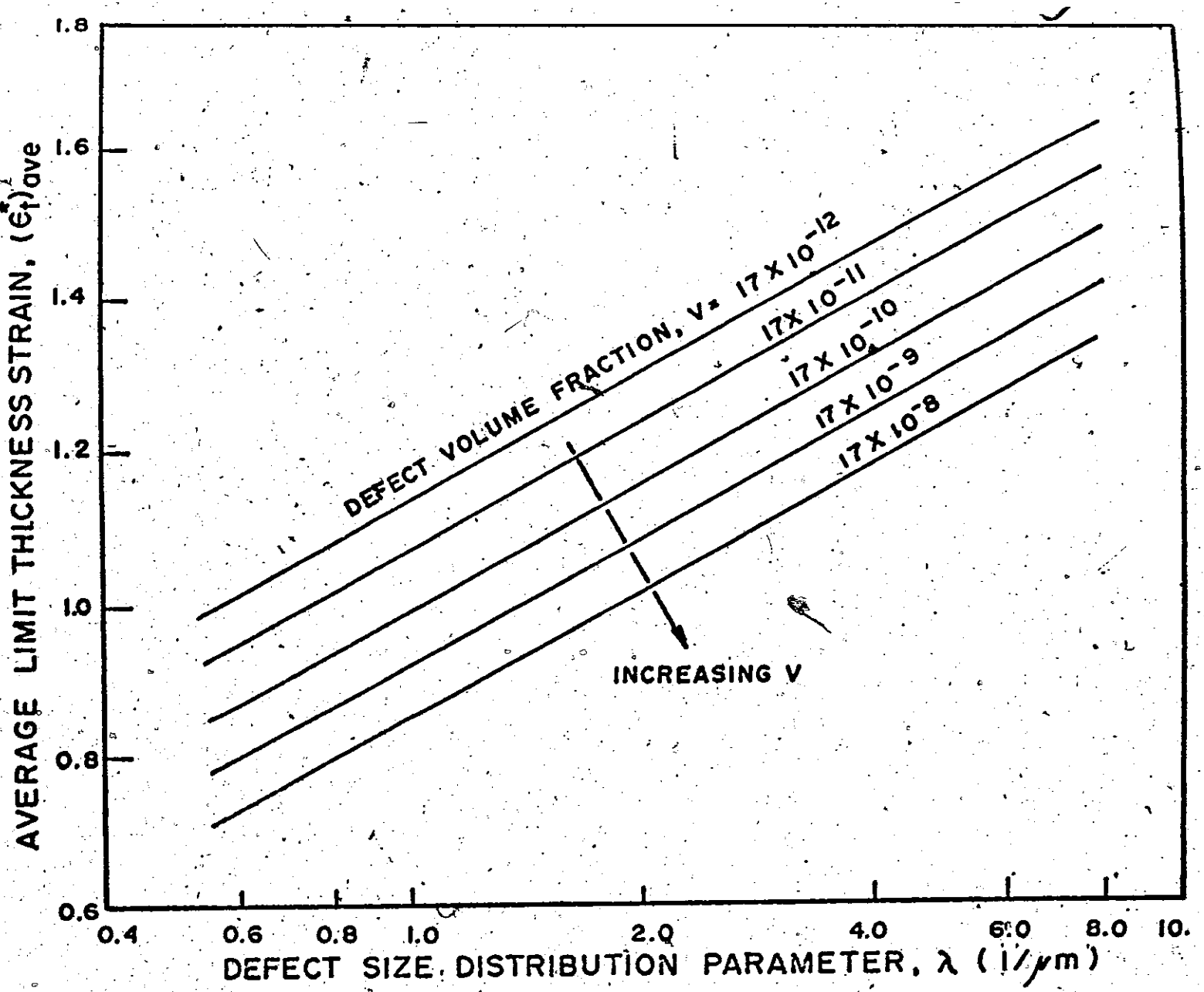

Figure 5.13b. Effect on Average Limit Strains, $(\epsilon_t^*)_{ave.}$, (for Constant Defect Volume Fraction, V) of
b) Defect Size Distribution Parameter, λ.

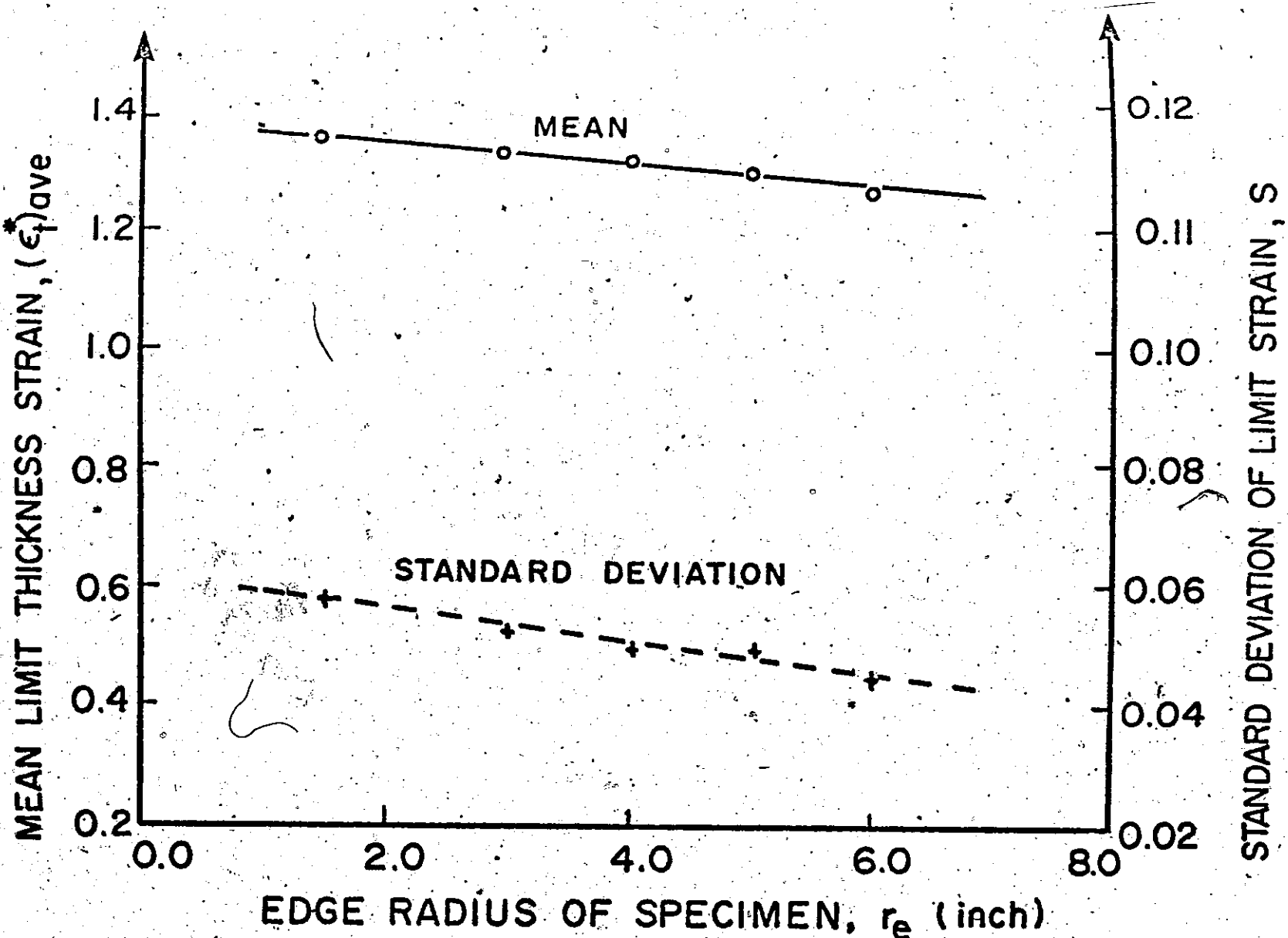

Figure 5.14. Effect of Specimen Size on Frequency Distribution of Limit-Strains for a Material with $\lambda = 4$, $\delta = 20{,}000/\text{in.}^2$ and $t_o = 0.035$ in.

decreases.

The formability of a material, on the other hand, can be improved by increasing the thickness of the sheet as indicated in Figure 5.15. The results in this figure were obtained for materials which have constant λ but δ increasing with t_o, i.e., the number of defects per unit volume of material remains constant.

Experimental results from stretch drawing of steel sheets using a hemispherical punch [5.13] presented in Figure 5.16 show a similar trend.

5.6. Conclusions

A failure model for ductile materials was developed and was used to predict the forming-limits of materials tested in a non-uniform biaxial straining process where the deformation geometry is axi-symmetric. Quantitative relationships were established between formability and material properties - both macroscopic and microscopic - and process variables which were intuitively known to have some influence on the failure of the material. The following are the particular conclusions derived from the above analysis.

a) The distribution of limit-strains for specimens tested in a non-uniform but axi-symmetric straining process can be approximated by a normal distribution curve and both the mean and the spread of the distribution are larger than those of specimens of the same size strained uniformly.

b) The formability of a material of given plastic properties is controlled by the spatial density and the size

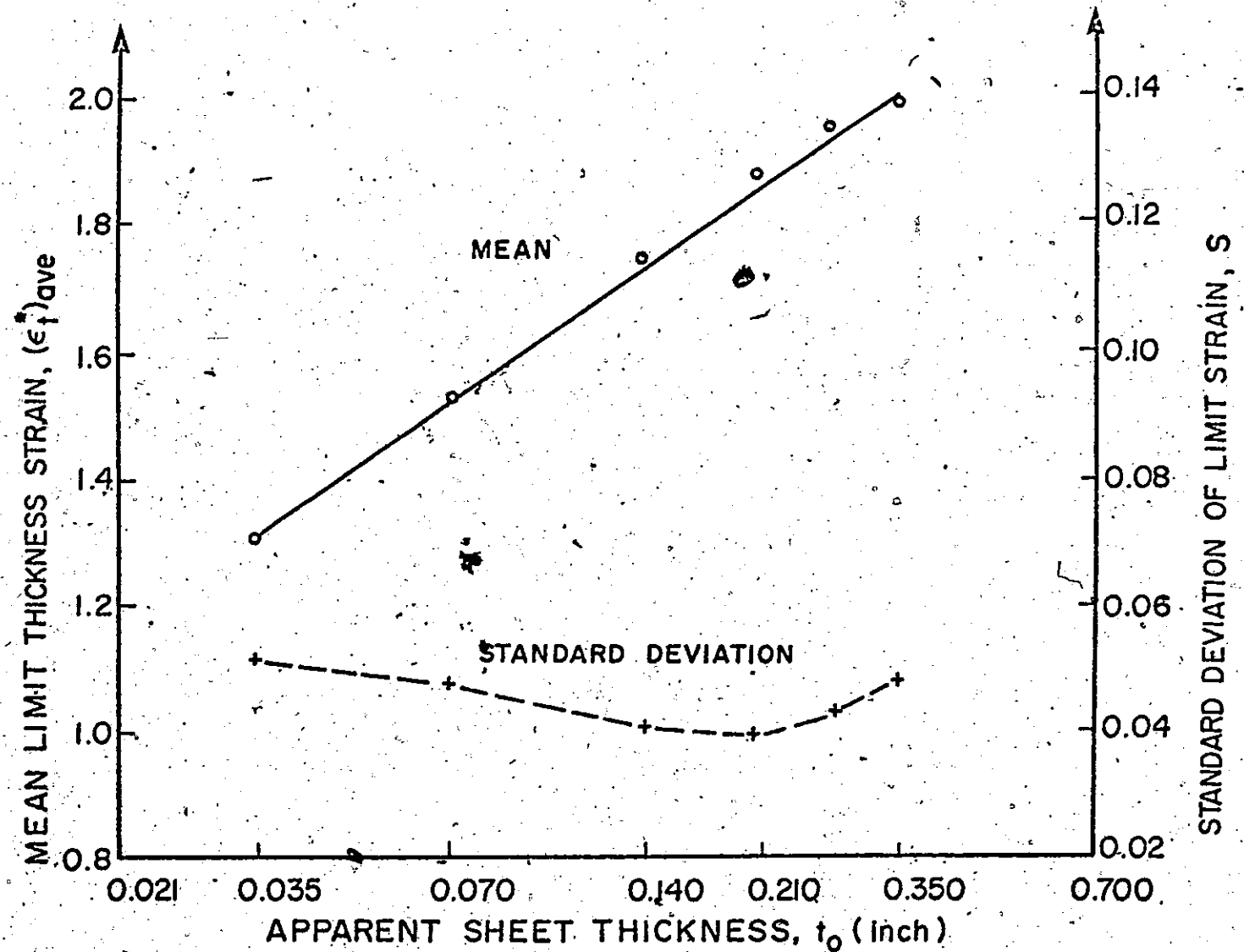

Figure 5.15. Effect of Sheet Thickness, t_o, on Frequency Distribution of Limit-Strains ϵ_t^*, for r_e = 3 in., λ = 4 and (δ/t_o) = Constant.

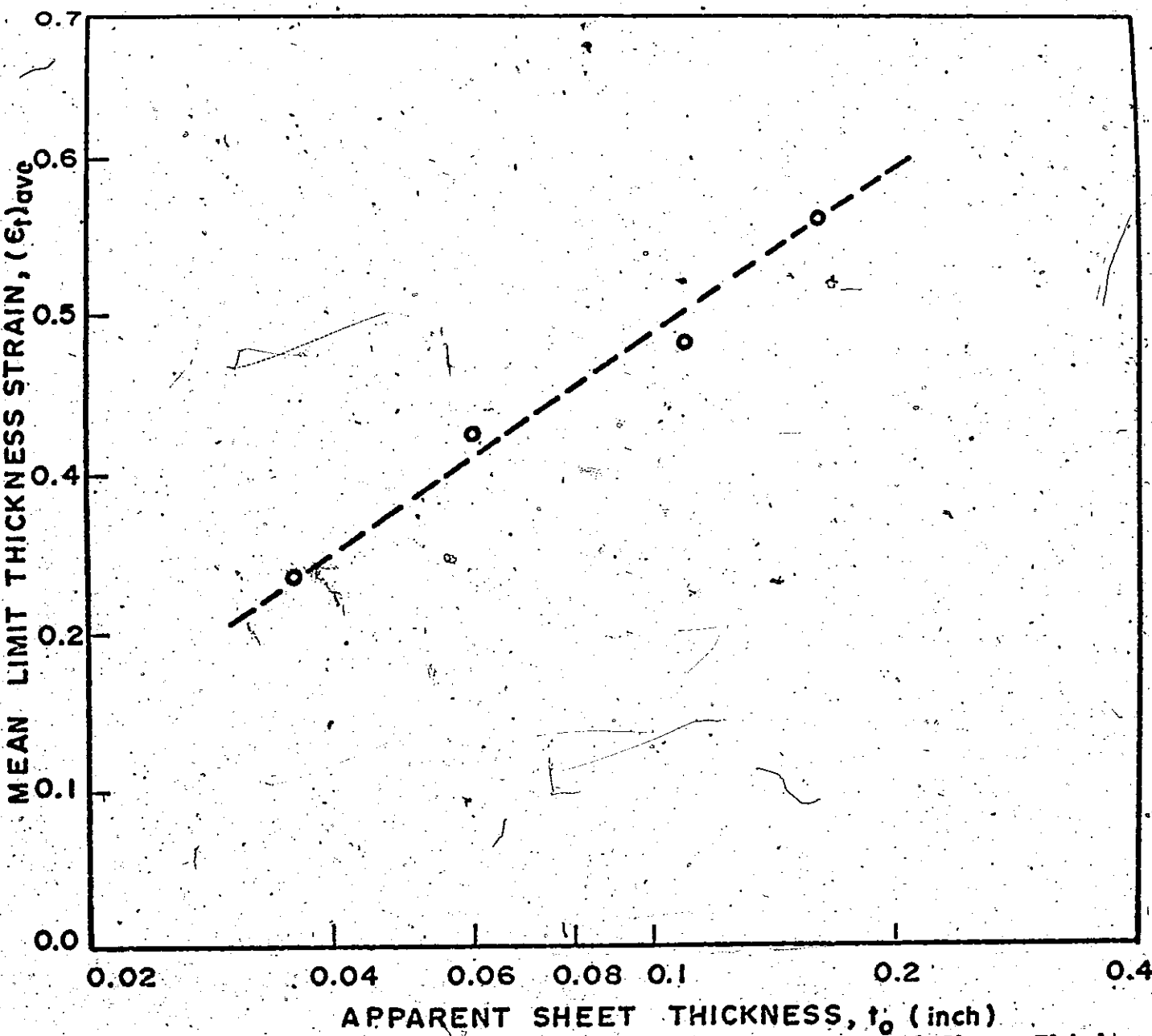

Figure 5.16. Experimental Results [5.13] showing the Effect of Sheet Thickness t_o on Average Limit Strains $(\epsilon_t^*)_{ave}$. Data were Obtained at Plane-Strain Condition.

distribution of material defects; increasing the probability of encountering large defects or increasing the defect density would produce lower limit strains.

c) The spread of the forming limits is larger for materials with few defects, although the mean is higher.

d) The forming limit decreases as the volume fraction of the inhomogeneity increases and logarithmic relations were found to exist between forming limits and volume fraction when either defect density or defect size distribution parameter is constant.

e) The limit strains are dependent not only on the material properties but also on the testing process. As the process strain gradient decreases, the limit strain decreases. The same effect is observed when the specimen size becomes larger.

f) Formability can be improved by using thicker materials.

The above failure model was applied to a simple axi-symmetric straining process. However, the model can be used to predict the failure in any forming process where the deformation geometry and the strain profile are defined. In the next chapter, this model will be utilized to determine the formability in the hydrostatic bulging processes.

CHAPTER 6

PREDICTION OF FORMING LIMITS IN HYDROSTATIC BULGING PROCESSES

6.1. Introduction

The failure model of a material subjected to a biaxial stretching process described in Chapter 5 applies to a non-uniform straining process characterized by a deformed surface which is rotationally symmetric about an axis. This model can be modified to predict failure strain in sheets which are hydrostatically bulged to rupture in elliptical dies as described earlier. The major axes of these dies are all the same dimension and by changing the length of the minor axes, different polar strain-ratios can be produced on the specimens; this gives rise to a dissimilarity in strain profiles along the major and minor axes of the elliptical diaphragms. Thus the deformation process of these diaphragms is not rotationally symmetric but is symmetric about two orthogonal planes.

The deformed specimens in this process can also be divided into a number of elemental areas in which straining is uniform. The failure strain in these elements are determined by the probability density function given by Equation (5.9). The deformation geometry of the process, however, is assumed to be the result of a linear transformation on that in an axisymmetric deformation process described in Chapter 5. From

this assumption, the strain at a point on the diaphragm can be related to that of the reference point (i.e., the pole of the bulge) and a distribution of the elemental areas subjected to the same strain intensity can be calculated accordingly.

The simulation process described in Chapter 5 was applied to four samples of specimens which were hypothetically tested in four elliptical dies having 1:1, 4:3, 2:1 and 4:1 aspect-ratios. The frequency distribution of limit-strains for each sample of specimens was obtained and a forming-limit diagram was established for a particular material characterized by given plastic properties (n, $\bar{R}$ and ε_o) and prescribed defect parameters (δ and λ).

As the aspect ratio of the elliptical die decreases, the critical area of the diaphragm strained in the die increases; thus, the limit strains resulting from the tests in these dies may be affected to a certain extent. To check this, a forming limit-diagram for specimens, tested in elliptical dies in which the major axis increases by the same factor as the die aspect-ratio to produce a constant critical straining area in the specimens, was obtained and compared with the former case. A comparison between the theoretical forming-limit diagram derived from the simulation process and the experimental results was also made for a material with similar plastic properties. It was found that a reasonable fit to the experimental curve can be obtained by a selection of suitable material defect parameters in the numerical solution.

6.2. The Deformation Process

The deformation characteristics of the major and minor axes of the elliptical diaphragms in hydrostatic bulging process were examined in Chapter 3. For a point which is not on these axes, the strain pattern is not yet fully known. To describe the deformation geometry and strain profiles of the elliptical diaphragms, a simplified approach was attempted.

Consider the thickness strains, ε_{ta} and ε_{tb}, along the major and minor axes of a deformed elliptical diaphragm. The quantities ε_{ta} and ε_{tb} can be described as

$$\varepsilon_{ta} = \varepsilon_{ta}(u) ,$$

and

$$\varepsilon_{tb} = \varepsilon_{tb}(v) ,$$

where u and v are distances measured from the axis of symmetry in the undeformed geometry as shown in Figure 6.1. Experimental results given in Chapter 3 show that ε_{tb} can be derived from ε_{ta} by the transformation

$$v \doteq u\left(\frac{b}{a}\right) ,$$

where a and b are the major and minor semi-axes of the ellipse respectively. From this observation, it is assumed that the strain profile on the elliptical diaphragms is a transformation of that of a circular diaphragm, and this transformation is given by

$$x = u,$$

and (6.1)

$$y = v\,\frac{a}{b} ,$$

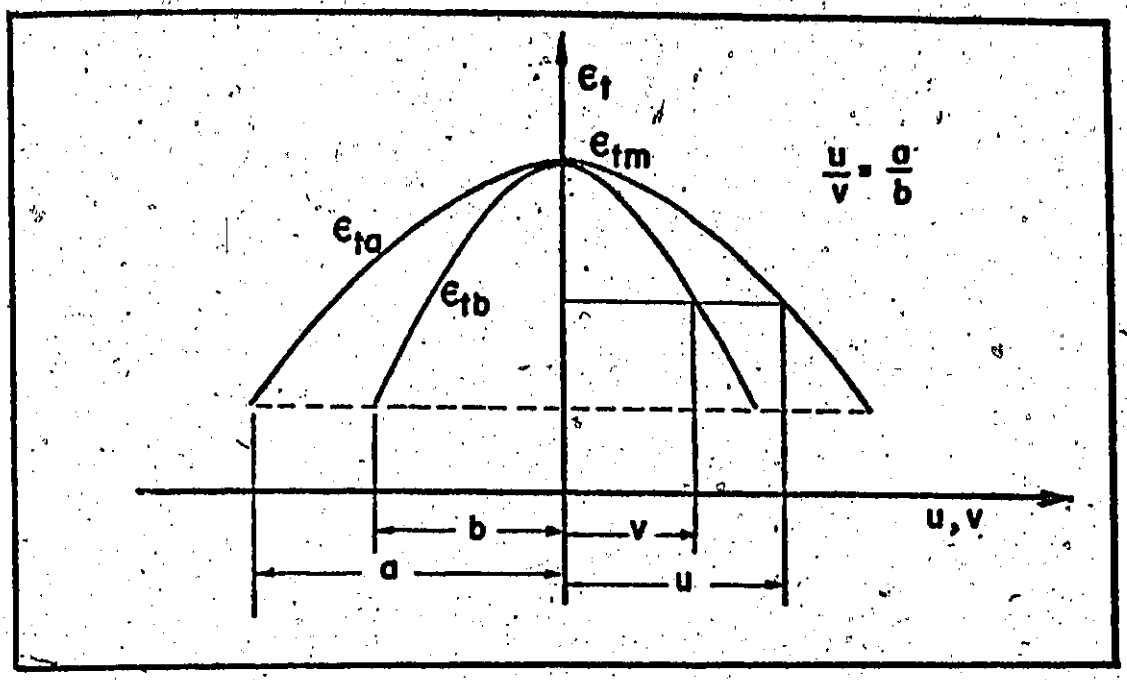

Figure 6.1. Schematic Representation of the Assumed Thickness Strain Profiles along the Major and Minor Axes of the Elliptical Diaphragm.

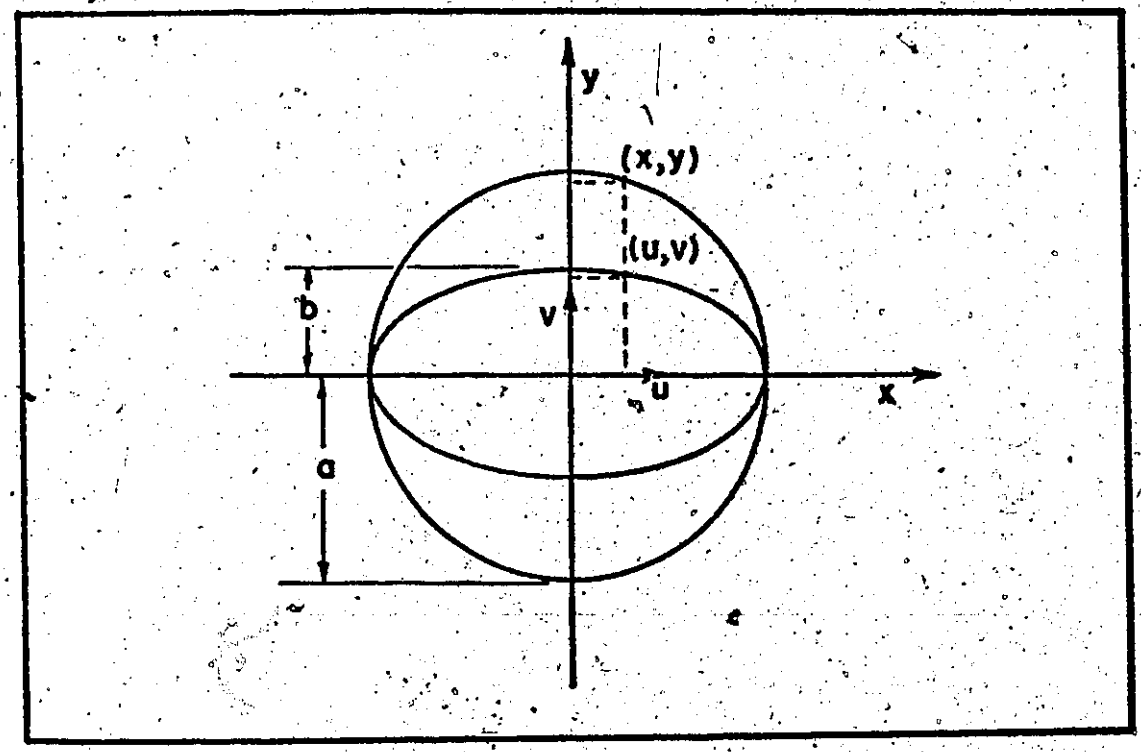

Figure 6.2. Schematic Representation of the Transformation of Circular Diaphragm into Elliptical Diaphragm in the Undeformed Configuration.

where (x,y) and (u,v) are the Cartesian coordinates describing the circular and elliptical diaphragms respectively. Such a transformation is depicted in Figure 6.2. (It should be noted that (x,y) and (u,v) are presented in the undeformed configuration).

Thus the strain profile of the elliptical diaphragm is derived from Equation (5.10), viz.,

$$\epsilon_t = \epsilon_{tm} \left[1-\left(\frac{r}{r_e}\right)^{\beta_2}\right] + \beta_1 \left(\frac{r}{r_e}\right)^{\beta_2} \qquad (6.2)$$

where $r = \sqrt{u^2 + v^2 \left(\frac{a}{b}\right)^2}$ and $r_e = a$.

From the above assumption, the elliptical diaphragms can be divided into concentric elliptical rings, within each ring the strain gradient is negligible. Thus the number of elemental areas in each ring is calculated by

$$\Gamma(r) = \frac{2\pi r\, \Delta r}{A} \frac{b}{a} \qquad (6.3)$$

where r is defined in a similar fashion as above, A is the area of the element and Δr is the width of the ring measured along the undeformed major axis of the ellipse.

6.3. Method of Solution

The distribution of failure strains in biaxially stretched elemental areas is given by Equation (5.9), viz.,

$$g_N(\epsilon_t) = -\frac{N\lambda B_2 t_o}{B_1} \exp(-\epsilon_t/B_1) \exp[-\lambda t_o B_2 \exp(-\epsilon_t/B_1)] \{1 - \exp[-\lambda t_o B_2 \exp(-\epsilon_t/B_1)]\}^{N-1} \qquad (5.9)$$

This equation is applied to the processes in which the strain profiles and the deformation geometry are described by Equations (6.2) and (6.3) respectively. The simulation technique described in Chapter 5 was then used to determine the limit-strains for a sample of specimens tested in a particular strain-ratio.

The strain-ratio of the specimens bulged in a given die is considered to be constant within the specimen and is determined experimentally. For a particular strain-ratio, the Marciniak analysis was utilized to calculate the limit-strains in elemental areas. These are plotted against the largest defect size of the elements as shown in Figure 6.3. From this figure, the parameters B_1 and B_2 in Equation (5.9) were determined for each strain ratio and these are indicated in Table 6.1. The strain profile parameters in Equation (6.2) were calculated from experimental data from the hydrostatic bulge tests and these are also given in Table 6.1.

6.4. Results and Discussion

Four samples each of 50 specimens, were simulated as being tested in the four dies of aspect ratios 1:1, 4:3, 2:1 and 4:1. The plastic properties of the material in these specimens are shown in Table 6.1. For each sample, the frequency distribution of limit-strains was established and the mean and standard deviation were evaluated.

Figure 6.4 shows the forming-limit diagrams for two materials which have the same plastic properties but have

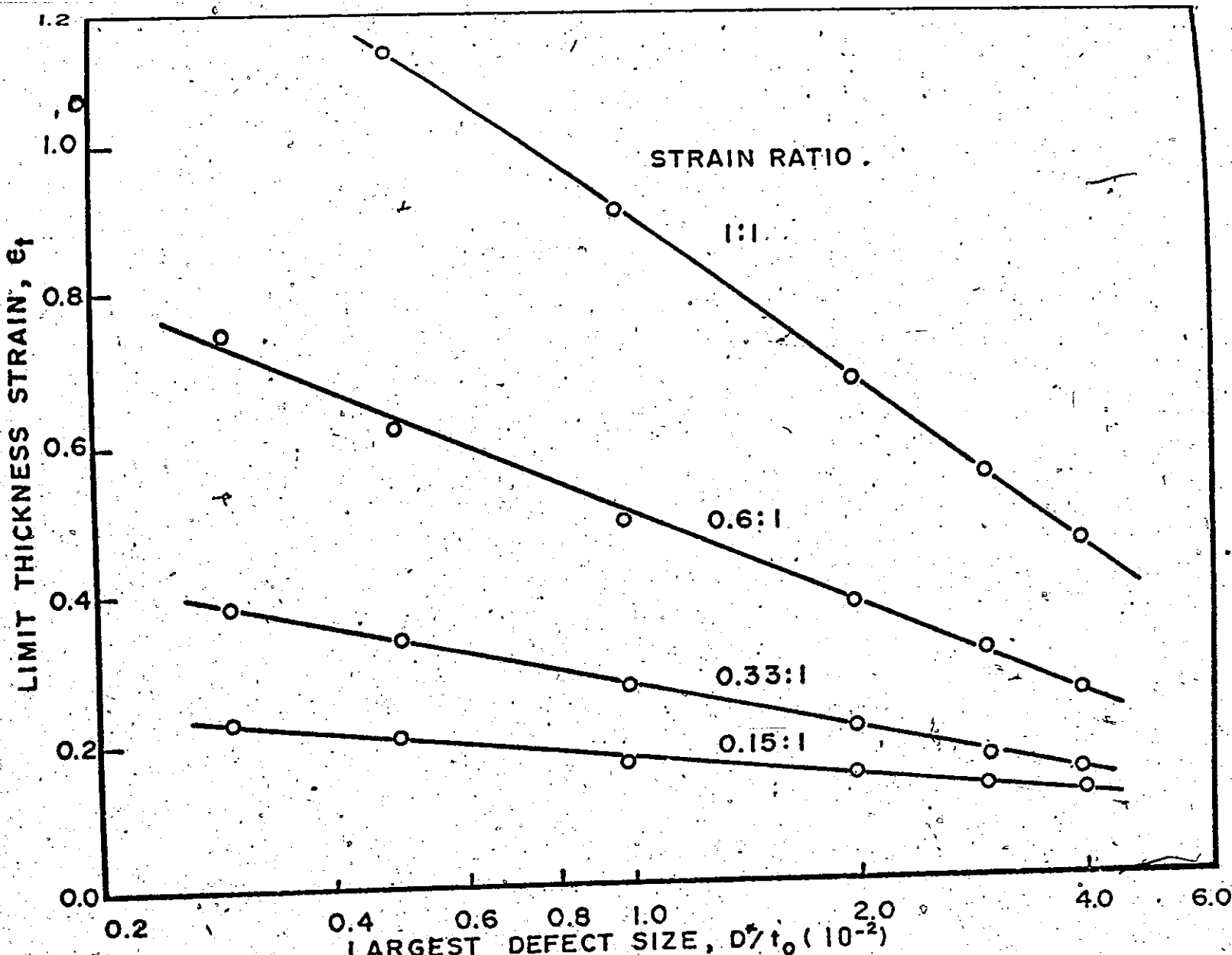

Figure 6.3. Limit Thickness Strain, ε_t, Versus Largest Defect Size, D*, for Different Strain-Ratios.

Table 6.1 Parameters used in the Prediction of Limit-Strains in the Hydrostatic Bulge Tests.

Die Aspect Ratio	Major Axis, 2a (in.)	Strain Ratio α'	Failure Strain Parameters Equation (5.9)		Simulation Process Parameters	Strain Profile Parameters, Equation (6.1)	Material Constants
			B_1	B_2			
1:1	6	1.0	0.332	0.155	A = 0.01 in^2.	β_1 = 0.14	t_o = 0.035 in.
4:3	6	0.6	0.185	0.155	Δr = 0.1 in.	β_2 = 1.5	n = .21
2:1	6	0.325	0.099	0.155			$\bar{R}$ = 1.
4:1	6	0.15	0.063	0.155			ε_o = .0075

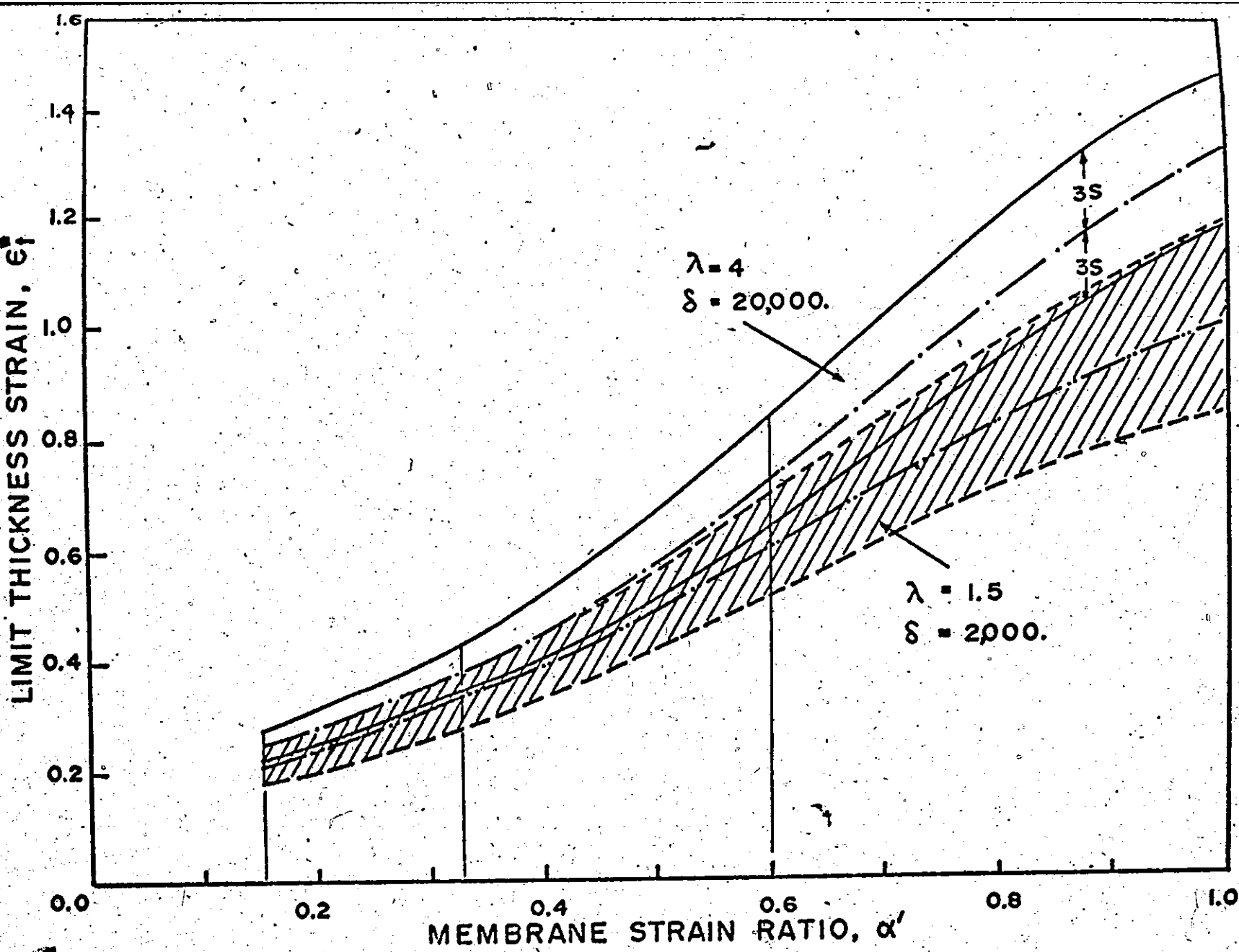

Figure 6.4. Theoretical Forming-Limit Curves for Materials of Similar Plastic Properties but Different Defect Parameters.

different defect parameters (i.e., spatial defect density δ and defect size distribution parameter λ). In this figure, three times the standard deviation was plotted on either side of the mean to show the range of the forming-limits. It is observed from these results that the mean and the spread of the limit strains increase as the degree of biaxiality increases.

The results presented in Figure 6.4 are for specimens tested in bulging dies described in Chapter 3. The major axes of these dies are of the same dimension, but the minor axes decrease in length as the aspect ratio of the die increases. Thus, the critical area in the specimens tested in these dies decreases with the strain-ratio. Forming-limit curves were also obtained for the elliptical bulge tests where the critical areas of the specimens were all equal to that in the circular bulge tests. These results together with the data plotted in Figure 6.4, are presented in Table 6.2. It is seen in this table that the difference in the means and the standard deviations of the limit-strains between the two cases is not great. This is reasonable because, as the die aspect ratio increases, strain gradient in the specimen will increase proportionally and this would offset any influence of the specimen size on the limit strains.

To confirm the validity of the fracture model, theoretical limit strains obtained were compared with the hydrostatic-bulge-test results for a material of the same plastic properties. This is shown in Figure 6.5. The theoretical forming-limits in this figure are for a material with defect

Table 6.2: Theoretical Forming-Limits in Hydrostatic Bulge Tests for

Case 1). Elliptical diaphragms of different critical areas,

Case 2). Elliptical diaphragms of the same critical area.

(Defect parameters: $\lambda = 1.5$, $\delta = 2{,}000/in^2$.)

Aspect Ratio	Case 1				Case 2			
	Die Dimensions		Limit Strains ε_t^*		Die Dimensions		Limit Strains ε_t^*	
	2a(in.)	2b(in.)	Mean	Standard Deviation	2a(in.)	2b(in.)	Mean	Standard Deviation
1:1	6	6	1.055	0.057	6	6	1.055	0.057
4:3	6	4	0.596	0.033	8	6	0.583	0.028
2:1	6	3	0.319	0.015	12	6	0.304	0.013
4:1	6	1.5	0.205	0.011	24	6	0.188	0.007

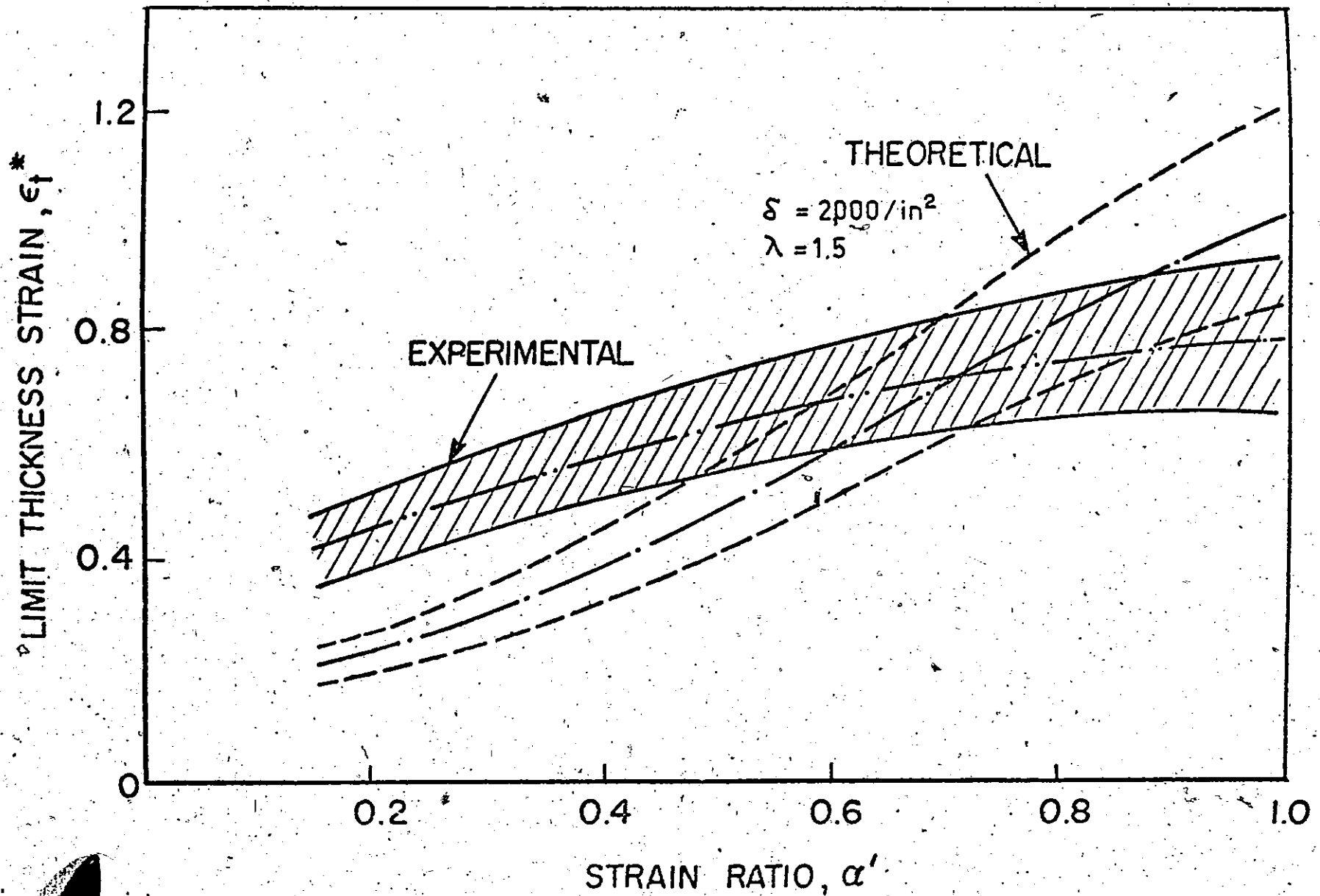

Figure 6.5. Comparison between the Theoretical and Experimental Forming-Limit Curves.

parameters chosen as $\lambda = 1.5$ and $\delta = 2000/in^2$. In view of the different combinations of λ and δ one can choose to calculate the limit strains, the theoretical results do show a similar trend to the experimental forming-limit curves. In addition, the mean and standard deviation of the theoretical limit strains are greater than the experimental results in the region near equal-biaxial tension. Near the plane-strain condition, however, this characteristic is reversed. This disparity is a shortcoming of the Marciniak analysis and is commonly observed for various materials.

6.5 Conclusions

The failure model of ductile material was employed to predict the forming limits of sheet metals in hydrostatic bulging processes. It was shown that for a particular process, the forming limits are not only a function of continum properties determined from mechanical tests, but also dependent upon the material's microscopic variables such as inclusion (or defect) distribution and inclusion density.

The results obtained from the simulation process indicate that in a process where the strain gradient is comparatively steep, the size effect of the specimen on forming limits is not very pronounced. Theoretical forming limits were obtained for a material with given plastic properties and, in general, these results are comparable with the experimental data, although some discrepancies between the theoretical and experimental results were observed.

It should be noted that the spatial defect density used in the determination of the theoretical forming limits, shown in Figure 6.5, is much smaller than the true value obtained from the Quantimet analysis as described in Chapter 4. This may indicate that only a small fraction of the total number of defects are large enough to influence the failure properties of the material. This supports the concept of "Macroscopic-Inclusions" proposed by Kiessling [2.57].

CHAPTER 7

CONCLUDING REMARKS

The forming-limit curve is a measure of local ductility of a material deformed in various proportional straining processes. It is subjected to a variation due to the intrinsic material property and is influenced by the testing process. In this work, the inherent variability of the forming-limit curve was determined experimentally from the measured limit-strains in sheets tested to failure in hydrostatic bulge processes. The deformation and failure characteristic of diaphragms in these processes were examined in detail. A hypothesis of ductile fracture was proposed to explain this variability and to predict the influence of the process variables on the experimentally determined forming-limit curve. The following are the particular remarks derived from this work, and these are listed according to the development of the program.

The deformation characteristics of mild steel diaphragms hydrostatically bulged in elliptical dies were investigated. The results showed that near the top of the bulge:

- The strain path is approximately linear,
- The membrane strain-ratio is nearly constant, and

- The diaphragm profiles along the axes of the ellipse are circular.

Strain profiles and strain ratios along the major and minor axes were also determined.

The different modes of failure of these diaphragms in the hydrostatic bulge process were analysed using the instability criteria and the Marciniak analysis, and the results were plotted on the principal strain diagram for comparison. The results showed that diffuse necking is associated with a pressure maximum and can only occur when the polar strain ratio is near unity, and that localized necking relating to edge failure of the diaphragm takes place when the strain at the pole of the bulge is near plane strain. This edge failure, however, did not occur in the mild steel diaphragms bulged in the largest aspect-ratio (i.e., 4:1) elliptical die.

Thus, in view of the linearity of the strain path and the absence of both friction and edge failure in the tests performed, the hydrostatic bulge test can provide a useful means to establish the forming-limit curves for sheet metal in biaxial stretching processes.

The inherent variation of the forming-limit curves was determined from the measured limit strains in about 500 mild steel diaphragms hydrostatically bulged to fracture in various elliptical dies, and a quantitative metallographic analysis was performed to relate formability to the microstructural variables. The results from the experimental

analysis indicate the following:

- Scatter in the measured forming limits is greater than the experimental error and this scatter is attributed to intrinsic material properties.
- The standard deviation of the distribution of forming limits is not constant for all strain ratios but increases with an increase of the degree of biaxiality.
- The overall variation of the forming-limit curve is larger at most strain ratios in steels having a larger volume fraction of inclusions, e.g., capped steel and generally smaller in the cleaner steels, aluminum-killed, and of the same magnitude in two similar grades of rimming steel.
- Formability of a material cannot be described by a single mean-value forming-limit curve as the scatter as well as the mean are important parameters which must be taken into consideration in evaluating formability.
- The mechanical fibering effect exerts a considerable influence on the distribution of forming limits in the various materials tested. The mean forming limit is generally lower when the largest principal strain is oriented in the transverse direction, and the scatter is generally higher when the largest strain is in the transverse direction.
- Inclusions play an important role in the fracture mechanism of steel, and thus have a considerable effect on the material formability.

From the above results, a three-dimensional forming-limit diagram was proposed to indicate the expected percentage of rejects due to parts failure in a particular stamping when the strain level in the process is known.

The results from the mechanical tests in this work definitely indicate that the overall limit-strains are subjected to variation, however, as the sample sizes of the specimens used in the tests were small, only limited conclusions could be drawn. Additional information regarding the behaviour of the distribution of the limit-strains in a material for different degrees of biaxiality can be made by performing tests similar to the ones described in this work, and perhaps these tests should be repeated for various materials having different combinations of plastic and fracture properties.

Some gross correlation between the results from the mechanical tests and those from the metallographic tests was observed. However, more research is needed in this area to establish more definite relationships between microstructural variables and material properties, e.g., formability. It is suggested that efforts should be concentrated on studying the type of inclusions which affect formability. These inclusions should be assessed in terms of morphology and both density and size distributions.

A hypothetical ductile fracture model was developed to predict the forming-limit of sheet metal subjected to a biaxial, non-uniform straining process. The material contains a certain population of voids which can be related to defects

present in the sheet. This model was then used to simulate the failure of elliptical diaphragms in hydrostatic bulge processes. From the analysis, a number of statements can be made about the relationship between voids in the microstructure and the macroscopic strains, or formability, achieved in deforming sheet metal. The effect of strain gradients in the process and sheet thickness can also be taken into account. The conclusions which arise from this analysis are as follows:

- The Marciniak model which has only been applied previously to determine a single-valued forming-limit curve at the point of maximum straining can be applied to smaller elements in the critical region of the sheet.
- Defects in the material microstructure can be represented by a distribution of equivalent voids. For the case where the density of voids is large and their diameter has an exponential distribution, the distribution of forming-limits in individual small elements is approximately normal.
- For a given deformation process, with or without strain gradient, the variation of limit-strain in a number of similar work pieces formed to failure can be predicted.
- An increase of severity of strain gradient (or a decrease of specimen size) leads to an increase in both the mean value of the forming-limit and its scatter.

- The distribution of forming-limits is influenced by the density and size distribution of voids. If either the density or size distribution is unchanged, the mean forming-limit is related to the volume fraction by an inverse logarithmic relation.
- An increase in sheet thickness (other factors kept constant) produces an increase in the mean forming-limit curve although scatter is approximately constant.
- A decrease in strain-ratio of the process from equal biaxial straining towards plane-strain condition will decrease both the mean forming-limit and the scatter.
- The theoretical forming-limits obtained from the simulation is comparable with that derived from the hydrostatic bulge tests of a material having similar plastic properties.

The model in this work is hypothetical in nature and the numerical results presented are based on arbitrary parameters. Nevertheless, the trends predicted by the model are in good agreement with experimental observations which hitherto have lacked any quantitative physical explanation. The method of analysis appears to have a generality beyond the particular process considered, and it is hoped that the model will help to establish a more precise relationship between defects in microstructure and formability of the sheet.

This work does indicate that tearing in a deformation process is a probabilistic phenomenon and is related to material defects. However, no attempt was made to establish a relation-

ship between the model's void population and real imperfections in the sheet. Further work in this area is necessary, although it may require continuous coordination of efforts from the overworked plasticians and the overburdened metallurgists.

REFERENCES

1.1 Keeler, S. P., S.A.E. paper No. 650635, 1965.

1.2 Goodwin, G. M., S.A.E. paper No. 680093, 1968.

1.3 Keeler, S. P. and Backofen, W. A., Trans. A.S.M., 56, 25, 1963.

1.4 Marciniak, Z. and Kuczyński, Int. J. Mech. Sci., 9, 609, 1967.

2.1 Lloyd, D. H., Sheet Metal Industries, 39, 712, 1962.

2.2 Musiol, K., Dinglers Polyt. Journal, 28, 445, 1900.

2.3 Siebel, E., "Forming in the Plastic Condition", Düseldorf, 1932.

2.4 Wilson, F. H. and Brick, R. M., Trans. A.I.M.E., 161, 173, 1945.

2.5 Baldwin, W. M., Howald, T. S. and Ross, A. W., Metals Technology, Sept., 1945.

2.6 Jackson, H., Polanyi, M. and Schmidt, E., Z. Physik, 12, 58, 1922.

2.7 Lankford, W. T., Snyder, S. C. and Bauscher, J. A., Trans. A.S.M., 42, 1197, 1950.

2.8 Whiteley, R. L., Trans. A.S.M., 52, 154, 1960.

2.9 Nelson, P. G. and Winlock, J., A.S.T.M. Bulletin, 156, 53, 1949.

2.10 Blickwede, D. J., 1968 A.S.M. Campbell Memorial Lecture, A.S.M. publication, 1970.

2.11 Keeler, S. P., Sheet Metal Industries, 683, 1965.

2.12 Keeler, S. P., S.A.E. paper No. 680092, 1968.

2.13 Keeler, S. P., A series of six articles, Machinery, 1968.

2.14 Goodwin, G. M., La Metallurgia Italiana, 8, 767, 1968.

2.15 Chatfield, D. A. and Keeler, S. P., Metal Progress, 60, 1971.

2.16 Woodthorpe, J. and Pearce, R., Sheet Metal Industries, 1061, 1969.

2.17 Grumbach, M. and Sanz, G., I.R.S.I.D. report No. 95-31-01-51, Oct., 1971.

2.18 Yoshida, K., Abe, K., Miyauchi, K. and Kakagawa, T., La Metallurgia Italiana, 8, 685, 1968.

2.19 Brozzo, P. and de Luca, B., Trans. of the Iron and Steel Inst. of Japan, 966, 1971.

2.20 Kobayashi, T., Ishigaki, H. and Abe, T., I.D.D.R.G. report, 1972 Conference, Amsterdam, 8.1, 1972.

2.21 Azrin, M. and Backofen, W. A., Metallurgical Trans., 1, 2857, 1970.

2.22 Levy, B. S., Sheet Metal Industries, 47, 527, 1970.

2.23 Hsu, T. C., Little John, G. S. and Marchbank, B. M., Proceedings A.S.T.M., 65, 874, 1965.

2.24 Burns, R. S. and Heyer, R. H., Symposium on the Annealing of Low Carbon Steel, Case Institute of Technology, Cleveland, Ohio, 1957.

2.25 Atkinson, M. and MacLean, I. M., Sheet Metal Industries, April, 1965.

2.26 Wright, J. C., Sheet Metal Industries, 39, 887, 1962.

2.27 Hazlett, T. H. and Robinson, A. T. and Dorn, J. E., Trans. A.S.M., 42, 1326, 1950.

2.28 Bramley, A. N. and Mellor, P. B., Int. J. Mech. Sci., 8, 101, 1966.

2.29 Heyer, R. H. and Newby, J. R., Sheet Metal Industries, 43, 910, 1966.

2.30 Duncan, J. L., Bull. Mech. Eng. Education, 1, 29, 1965.

2.31 Duncan, J. L., Goni, E. and Johnson, W., Journal of the Australian Institute of Metals, 12, 127, 1967.

2.32 Metsis, T., M.Sc. Dissertation, U.M.I.S.T., Manchester, 1970.

2.33 Marciniak, Z. and Kolodziejski, J., Proceedings I.D.D.R.G. Conference in Amsterdam, 1972, 6.1, 1972.

2.34 Kemmis, Q. H., Sheet Metal Industries, 203, March, 1957.

2.35 Schmidt, M., Archiv. f.d. Eisen, 3, part III, 213, 1929.

2.36 Weidemann, C., La Metallurgia Italiana, 8, 783, 1968.

2.37 Heyer, R. H. and Newby, J. R., S.A.E. paper No. 680094, 1968.

2.38 Goodwin, G. M., S.M.E. paper No. MF71-165, 1971.

2.39 Swift, H. W., J. of the Mechanics and Physics of Solids, 1, 1, 1952.

2.40 Warwick, J. O. and Alexander, J. M., Journal of the Institute of Metals, 91, 1, 1962.

2.41 Mellor, P. B., The Engineer, 209, 517, 1960.

2.42 Sachs, G. and Lubahn, J. D., Trans. A.S.M.E., 68, 271, 1946.

2.43 Moore, G. G. and Wallace, J. F., J. of the Institute of Metals, 93, 33, 1964.

2.44 Mir, W., Ph.D Dissertation, Waterloo University, Waterloo, 1967.

2.45 Venter, R. D., Ph.D. Dissertation, McMaster University, Hamilton, Ontario, 1971.

2.46 Sowerby, R. and Duncan, J. L., Int. J. Mech. Sci., 13, 217, 1971.

2.47 Marciniak, Z., Kuczyński, K. and Pokora, T., Int. J. Mech. Sci., 15, 789, 1973.

2.48 Cottrell, A. H., National Physical Symposium, 2, 456, 1963.

2.49 Lacy, C. E. and Gensamer, M., Trans. A.S.M., 32, 88, 1944.

2.50 Morrisson, W. B., A.S.M. Trans., 59, 824, 1966.

2.51 Hosford, W. F. and Backofen, W. A., "Fundamental Deformation Processing", Syracuse University Press, Syracuse, New York, 1964.

2.52 Backofen, W. A., "Fracture of Engineering Materials", A.S.M., 107, 1964.

2.53 Ferry, B. N. and Paliwoda, C.I.M. Conference of Metallurgists, Quebec City, paper No. 75, 1973.

2.54 Melbourne, S. H., Pietrowski, R. and Marsh, G. M., report No. 80, C.I.M. Conference of Metallurgists, Quebec City, 1973.

2.55 Mihelich, J. L., Bell, J. R. and Korchynski, M., J. of the Iron and Steel Institute, 469, June, 1971.

2.56 Gurland , J. and Plateau, J., Trans. A.S.M., 56, 442, 1963.

2.57 Kiessling, R., J. Metals, 10, 48, Oct., 1969.

2.58 Edelson, B. I. and Baldwin, W. M., Jr., Trans. A.S.M., 55, 230, 1962.

2.59 Gladman, T. and Pickering, F. B., J. Iron Steel Inst. (London), 203, 1212, 1965.

2.60 Alexander, J. M. and Brewer, R. C., "Manufacturing Properties of Materials", Van Nostrand, London, 1968.

3.1 Cole, H. R., "Underwater Explosions", Princeton University Press, New Jersey, Vol. I, II and III, 1948.

3.2 Johnson, W., Duncan, J. L., Komi, K., Sowerby, R. and Travis, F. W., "Advances in Machine Tool Design and Research", Pergamon Press, Oxford, Part II, 257, 1964.

3.3 Hill, R., "Mathematical Theory of Plasticity", Oxford Press, 1967.

3.4 Hill, R., J. Mech. Phys. Solids, 1, 19, 1952 .

3.5 Marciniak, Z., La Metallurgia Italiana, 8, 701, 1968 .

3.6 Painter, M. J. and Pearce, R., I.D.D.R.G. Amsterdam Conference, Section 1.1, 1972.

3.7 Hill, R., Phil. Mag., 41, 1133, 1950.

3.8 Mellor, P. B., J. Mech. Phys. Solids, 5, 41, 1956.

3.9 Duncan, J. L. and Johnson, W., Int. J. Mech. Sci., 10, 143, 1968.

3.10 Chow, C. C., Dana, A. W. and Sachs, G., J. Metals, 1, 49, Jan. 1949.

3.11 Shamamy, M. M. and Wang, N. M., Experimental Mechanics, 71, Feb., 1971.

3.12 Yousif, M. I., M.Sc. Dissertation, University of Manchester Institute of Technology, 1969.

4.1 Ghosh, A. K. and Backofen, W. A., Metallurgical Trans., 4, 1113, 1973.

4.2 Albertin, P. H., M.Eng. Thesis, McMaster U., 1972.

4.3 Baraya, G. L., Parker, J. and Flowett, J. W., Int. J. Mech. Sci., 5, 365, 1963.

4.4 Fisher, C., The Microscope, 19, 1, 1971.

4.5 Automatic Cleaness Assessment of Steel, ISI Publication 112, 1968.

4.6 Minh, H. V., Sowerby, R. and Duncan, J. L., Int. J. Mech. Sci., 16, 31, 1974.

5.1 Kiessling, R., "Non-Metallic Inclusions in Steels", ISI Publication 115, Part I, II and III, 1968.

5.2 Oyane, M., Bulletin J.S.M.E., Vol. 15, 90, 1507, 1972.

5.3 Thorton, P. A., J. of Material Science, 6, 347, 1971.

5.4 Duckworth, W. E. and Inerson E., "Clean Steel", Special Report No. 77, ISI, London, 87, 1963.

5.5 Fisher, J. C. and Hollomon, J. H., American Inst. of Min. and Met. Eng., No. 2218, 546, August, 1947.

5.6 Daniels, H. E., Proc. Roy. Soc., London, A183, 405, 1945.

5.7 Bergh, S., Jernkontorets Annaler, 146, 748, 1962.

5.8 Fisher, R. A. and Tippett, L. H. C., Proc. Camb. Phil. Soc., 24, 180, 1928.

5.9 Epstein, B. and Brooks, H., J. of Appl. Phys., 19, 544, 1948.

5.10 Aziz, P. M., Corrosion, 12, 495, 1956.

5.11 Eldredge, G. G., Corrosion, 13, 51, 1957.

5.12 Gumbel, E. J., Ann. of Math. Stat., 12, 163, 1941.

5.13 Lee, A. P. and Hiam, J. R., report No. 77, C.I.M. Conference of Metallurgists, Quebec City, 1973.

5.14 Mihram, G. A., "Simulation - Statistical Foundations and Methodology", Academic Press, N.Y., 118, 1972.

5.15 Hahn, G. J. and Shapiro, S. S., "Statistical Models in Engineering", John Wiley and Sons, 1967.

5.16 Tocher, K. D., "The Art of Simulation", English University Press, London, 1963.

5.17 Minh, H. V., Sowerby, R. and Duncan, J. L., Metal-working Research Group Report No. 33, McMaster University, 1973 .

5.18 Johnson, W. and Mellor, P. B., "Plasticity for Engineers", Van Nostrand Reinhold, New York, 1970.

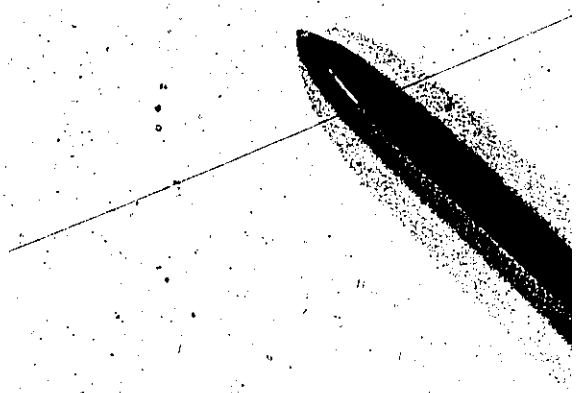

APPENDIX A1

Replica Technique and Its Accuracy

As strain gradient normally exists in laboratory tested specimens or in formed parts, it is often found that the surface at the critical area of these is not flat. To measure the limit-strains in these areas, the radius of curvature of the deformed surface is frequently neglected. This may produce an appreciable error in the quantity measured especially if the radius of curvature is relatively small. To eliminate this error and to facilitate the strain measurement, a replica technique was used.

In this technique, the specimen was gridded by using the Photo-resist method before forming. After being strained, the specimen was etched by using a suitable acid solution to produce grooves (or protrusions) along the grid lines in the region where strain measurement is to be made. A liquid-plastic was applied to the surface and allowed to harden. This plastic replica was then stripped using double-sided tape and mounted on a glass slide for measurement. Care was taken to avoid any excessive tension on the tape and to prevent the formation of bubbles between the tape and the plastic layer.

The replica produced by this method was found to be accurate and dimensionally stable. Table A1 shows the dimensions of several grid replicas measured at different time intervals. It is observed that the variation in the replica dimensions is small and can be accounted for by measurement error.

Table A1

Dimensional Stability of the Replicas
(Dimensions in inches)

Time Intervals \ Sample	1	2	3	4
0 hr.	0.2988	0.2980	0.2975	0.2980
40 hrs.	0.2988	0.2975	0.2975	0.2980
350 hrs.	0.2990	0.2970	0.2974	0.2978
Average	0.2989	0.2975	0.2975	0.2980

APPENDIX A2

Limit Strains of Steel Samples

This section contains the limit-strains in mild steel diaphragms tested in elliptical dies of aspect-ratios 1:1, 4:3, 2:1 and 4:1. The four materials tested were: two samples of rimming steel, A and B, capped steel, C, and aluminum-killed steel, D.

Material A

Specimen Number	Largest Strain in Rolling Direction								Largest Strain in Transverse Direction					
	4:1		2:1		4:3		1:1		4:3		2:1		4:1	
	ε_1	ε_2	ε_1	ε_2	ε_1	ε_2	ε_1	ε_2	ε_1	ε_2	ε_1	ε_2	ε_1	ε_2
1	.058	.411	.138	.389	.279	.451	.378	.378	.256	.447	.128	.386	.052	.353
2	.062	.418	.150	.476	.283	.455	.426	.422	.241	.432	.142	.446	.050	.340
3	.058	.375	.142	.417	.272	.409	.397	.387	.264	.433	.138	.423	.049	.335
4	.061	.369	.152	.446	.274	.441	.427	.432	.264	.459	.136	.476	.058	.367
5	.063	.377	.150	.401	.266	.392	.420	.432	.263	.458	.140	.394	.055	.338
6	.059	.383	.147	.440	.284	.431	.438	.438	.266	.464	.136	.404	.054	.334
7	.056	.375	.145	.405	.290	.466	.354	.358	.237	.397	.135	.422	.054	.327
8	.058	.396	.152	.447	.271	.416	.470	.457	.236	.401	.130	.429	.051	.358
9	.064	.375	.153	.421	.292	.423	.402	.398	.238	.413	.134	.383	.052	.411
10	.057	.397	.143	.421	.287	.436	.437	.426	.243	.423	.120	.368	.056	.347
11	.068	.429	.143	.403	.282	.467	.412	.412	.245	.419	.129	.362	.058	.378
12	.055	.363	.146	.436	.284	.413	.391	.381	.257	.426	.130	.433	.060	.407
13	.063	.402	.140	.419	.275	.423	.435	.413	.241	.405	.136	.408	.061	.387
14	.056	.380	.138	.411	.281	.423	.391	.407	.240	.406	.141	.412	.058	.359
15	.062	.383	.147	.475	.275	.437	.452	.449	.254	.406	.134	.417	.054	.335
16	.056	.361	.141	.391	.275	.423	.394	.401	.244	.399	.129	.376	.060	.348

Material A (Continued)

17	.056	.396	.144	.449	.266	.407	.417	.423
18	.062	.382	.149	.417	.295	.438		
19	.060	.383	.141	.403	.281	.421		
20	.062	.388	.140	.415				
21	.065	.408						
22	.061	.447						
23	.056	.373						
24	.061	.380						
25								
26								
27								
28								
29								
30								
31								
32								

.246	.408	.132	.371	.059	.350
.261	.457	.126	.394	.053	.371
.253	.405	.128	.373	.058	.356
		.137	.408	.053	.320
				.052	.396
				.051	.322
				.057	.352

Material B

Specimen Number	Largest Strain in Rolling Direction								Largest Strain in Transverse Direction					
	4:1		2:1		4:3		1:1		4:3		2:1		4:1	
	ε_1	ε_2	ε_1	ε_2	ε_1	ε_2	ε_1	ε_2	ε_1	ε_2	ε_1	ε_2	ε_1	ε_2
1	.050	.384	.140	.436	.287	.480	.432	.444						
2	.049	.350	.147	.470	.278	.453	.365	.377						
3	.053	.396	.143	.452	.282	.478	.425	.431						
4	.052	.373	.145	.464	.285	.455	.467	.465						
5	.047	.370	.139	.433	.276	.458	.427	.425						
6	.047	.358	.141	.435	.293	.476	.435	.450						
7	.053	.352	.136	.419	.273	.467	.436	.439						
8	.054	.345	.142	.460	.311	.481	.407	.406						
9	.051	.387	.146	.448	.286	.448	.401	.401						
10	.054	.346	.137	.438	.304	.519	.434	.432						
11	.052	.350	.141	.454	.288	.476	.427	.432						
12	.052	.371	.137	.416	.298	.487	.496	.473						
13	.053	.360	.136	.429	.283	.468	.387	.394						
14			.137	.429	.288	.463	.447	.430						
15			.150	.441	.303	.476	.428	.423						
16			.141	.447	.290	.464	.410	.409						

Material B (Continued)

17		.135	.414	.295	.501	.395	.404
18		.141	.436	.285	.453	.439	.446
19		.148	.441	.290	.453		
20		.148	.457	.292	.494		
21							
22							
23							
24							
25							
26							
27							
28							
29							
30							
31							
32							

Material C

Specimen Number	Largest Strain in Rolling Direction								Largest Strain in Transverse Direction					
	4:1		2:1		4:3		1:1		4:3		2:1		4:1	
	ε_1	ε_2	ε_1	ε_2	ε_1	ε_2	ε_1	ε_2	ε_1	ε_2	ε_1	ε_2	ε_1	ε_2
1					.254	.386	.388	.369	.209	.328	.124	.374	.050	.312
2					.263	.411	.370	.384	.206	.337	.139	.350	.054	.359
3					.256	.390	.368	.356	.259	.408	.136	.405	.053	.413
4					.239	.363	.411	.390	.257	.380	.133	.351	.059	.345
5					.256	.399	.322	.344	.277	.361	.130	.387	.063	.366
6					.256	.386	.343	.374	.255	.372	.135	.380	.065	.343
7					.243	.384	.286	.287	.214	.334	.122	.357	.058	.338
8					.261	.415	.321	.327	.245	.408	.131	.404	.048	.329
9					.254	.398	.359	.354	.254	.368	.133	.380	.061	.360
10					.274	.401	.398	.404	.205	.316	.137	.394	.056	.381
11					.260	.411	.383	.384	.244	.410	.127	.373	.052	.314
12					.262	.409	.321	.334	.191	.297	.124	.374	.059	.327
13					.265	.418	.346	.352	.263	.408	.129	.348	.045	.321
14					.272	.392	.288	.303	.238	.340	.126	.359	.056	.356
15					.263	.415	.376	.372	.239	.394	.121	.357	.059	.329
16					.257	.396	.343	.351	.243	.393	.130	.387	.063	.328

Material C (Continued)

17	.232	.376	.132	.367	.049	.337
18			.131	.398	.047	.292
19			.143	.376	.051	.296
20			.131	.375	.049	.306
21			.142	.384		
22			.131	.363		
23			.137	.394		
24						
25						
26						
27						
28						
29						
30						
31						
32						

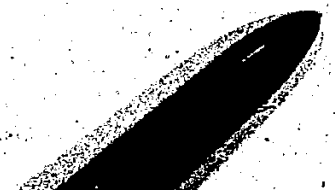

Material D

Specimen Number	Largest Strain in Rolling Direction								Largest Strain in Transverse Direction					
	4:1		2:1		4:3		1:1		4:3		2:1		4:1	
	ε_1	ε_2	ε_1	ε_2	ε_1	ε_2	ε_1	ε_2	ε_1	ε_2	ε_1	ε_2	ε_1	ε_2
1	0.055	0.356	0.144	0.433	0.285	0.451	0.416	0.368			0.133	0.411	0.052	0.391
2	0.051	0.377	0.133	0.417	0.276	0.428	0.431	0.365			0.129	0.411	0.051	0.377
3	0.046	0.390	0.137	0.434	0.282	0.457	0.436	0.435			0.126	0.415	0.047	0.371
4	0.051	0.386	0.143	0.411	0.273	0.420	0.408	0.410			0.132	0.445	0.045	0.388
5	0.049	0.356	0.140	0.426	0.292	0.459	0.494	0.409			0.141	0.414	0.050	0.351
6	0.043	0.339	0.141	0.458	0.274	0.457	0.408	0.394			0.141	0.426	0.039	0.339
7	0.040	0.345	0.134	0.435	0.255	0.424	0.404	0.419			0.130	0.395	0.041	0.356
8	0.046	0.336	0.145	0.443	0.300	0.475	0.367	0.369			0.123	0.406	0.039	0.361
9	0.048	0.389	0.134	0.402	0.304	0.473	0.406	0.412			0.139	0.435	0.030	0.361
10	0.040	0.344	0.141	0.441	0.274	0.441	0.409	0.376			0.135	0.438	0.046	0.349
11	0.052	0.375	0.145	0.451	0.264	0.461	0.421	0.427			0.127	0.408	0.055	0.360
12	0.055	0.370	0.141	0.442	0.259	0.437	0.411	0.403			0.129	0.398	0.055	0.389
13	0.048	0.371	0.133	0.401	0.279	0.433	0.400	0.406			0.129	0.415	0.050	0.372
14	0.048	0.338	0.141	0.419	0.314	0.449	0.395	0.395			0.135	0.415	0.050	0.360
15	0.050	0.358	0.140	0.446			0.434	0.428			0.130	0.433	0.062	0.383
16	0.051	0.338	0.140	0.448			0.410	0.343			0.134	0.436	0.048	0.388

Material D (Continued)

17	0.055	0.393	0.139	0.430		0.454	0.379		0.130	0.409	0.058	0.365
18	0.057	0.363	0.141	0.448		0.424	0.425		0.136	0.428	0.053	0.348
19	0.054	0.372	0.151	0.470		0.425	0.411		0.131	0.409	0.053	0.381
20			0.127	0.442		0.414	0.372		0.120	0.419	0.052	0.396
21			0.141	0.452					0.139	0.400	0.055	0.358
22			0.136	0.426					0.135	0.455	0.058	0.365
23			0.132	0.423							0.060	0.385
24			0.134	0.423							0.054	0.352
25			0.136	0.444							0.064	0.341
26			0.137	0.434							0.055	0.363
27			0.133	0.419							0.064	0.369
28			0.133	0.435							0.057	0.375
29			0.132	0.441							0.057	0.361
30			0.142	0.442							0.058	0.392
31			0.128	0.426								
32			0.130	0.392								

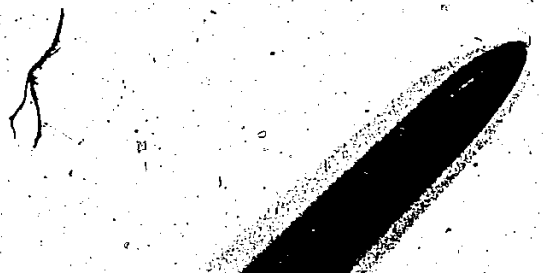

APPENDIX A3

Error Analysis for Strain Vector

The engineering strain of a specimen with original length ℓ_o being strained to ℓ is given by:

$$e = \frac{\ell}{\ell_o} - 1 \tag{1}$$

Since the errors in the measurement of ℓ and ℓ_o are independent random errors, the standard deviation of strain measurement can be derived from (1) as:

$$S_e = \sqrt{\left\{\frac{S_{\ell_o}}{\ell_o}\right\}^2 + \left\{\frac{S_\ell}{\ell}\right\}^2} \tag{2}$$

where S_{ℓ_o} and S_ℓ are errors in length measurement of the original and the deformed lengths respectively.

The magnitude of the projected strain vector $\bar{E}$ is computed from the strain components $\bar{e}_1$, and $\bar{e}_2$, i.e.,

$$\bar{E} = \sqrt{\bar{e}_1^2 + \bar{e}_2^2} \tag{3}$$

and since the errors in measuring $\bar{e}_1$ and $\bar{e}_2$ are random and independent, the expression for the error in $\bar{E}$ is:

$$S_E = \left[\frac{(\bar{e}_1 S_{\bar{e}_1})^2 + (\bar{e}_2 S_{\bar{e}_2})^2}{\bar{e}_1^2 + \bar{e}_2^2}\right]^{1/2} \tag{4}$$

where S_E, $S_{\bar{e}_1}$, $S_{\bar{e}_2}$ are errors in $\bar{E}$, $\bar{e}_1$ and $\bar{e}_2$ respectively.

For a given strain state ($\bar{e}_1$, $\bar{e}_2$), the error in $\bar{e}_1$ and $\bar{e}_2$ can be computed by using relation (2) and then substituted into (4) to find the error in the strain vector. For example; Rimming steel diaphragms bulged in a 4:1 ratio die:

$$\bar{e}_1 = .062 \qquad \bar{\ell}_1 = .1062 \text{ in.}$$

$$\bar{e}_2 = .477 \qquad \bar{\ell}_2 = .1477 \text{ in.}$$

$$s_{\bar{\ell}_1} = s_{\bar{\ell}_2} = s_T = .0009$$

$$s_{\bar{\ell}_o} = s_B = .00019 \approx .0002,$$

then

$$s_{\bar{e}_1} = .0087$$

$$s_{\bar{e}_2} = .0064,$$

and

$$s_{\bar{E}} = .0064.$$

APPENDIX A4

Sample Size Calculation

The accuracy of an estimated mean of a sample is proportional to the sample size. At a probability level of $(1-\gamma)$, the half width of the confidence interval for normal means is given by

$$\eta_{\gamma/2} \cdot \frac{S}{\sqrt{N}} .$$

If this quantity is restricted to a certain percentage (a) of the estimated mean $(\bar{x})$, then the value of N is governed by:

$$\eta_{\gamma/2} \cdot \frac{S}{\sqrt{N}} = a\bar{x}$$

or

$$\left(\frac{\sqrt{N}}{\eta_{\gamma/2}}\right) = \frac{S}{a\bar{x}}$$

A table for $\frac{\sqrt{N}}{\eta_{\gamma/2}}$ can be made for various N from student "t" table. By using this table, the value of N for a given $\frac{S}{a\bar{x}}$ can be evaluated.

APPENDIX B1

Computer Program for the Fracture Model

```
      PROGRAM TST(INPUT,OUTPUT,TAPE5=INPUT,TAPE6=OUTPUT)                    A    1
       -------------                                                        A    2
                                                                            A    3
                                                                            A    4
      TO FIND THE FREQUENCY DISTRIBUTION OF LIMIT-STRAINS IN SPECIMENS      A    5
      TESTED IN A NON-UNIFORM BUT AXI-SYMMETRIC FORMING PROCESS.            A    6
                                                                            A    7
      PARAMETERS                                                            A    8
      ----------                                                            A    9
      ARE= ELEMENTAL AREA (INCH SQUARE).                                    A   10
      ALAM= LAMBDA, DEFECT SIZE DISTRIBUTION PARAMETER.                     A   11
      DEL= DEFECT DENSITY PER UNIT AREA.                                    A   12
      T0= APPARENT THICKNESS OF THE SHEET(INCH).                            A   13
      A,AKK= PARAMETERS B1,B2 IN EQUATION (5.8).                            A   14
      E01, E02= LOWER AND UPPER LIMITS FOR THE FREQUENCY DISTRIBUTION OF    A   15
      LIMIT STRAINS IN ELEMENTAL AREAS,EQUATION (5.9).                      A   16
      RE= EDGE RADIUS OF THE SPECIMEN (INCH).                               A   17
      R0= RADIUS DEFINING THE CRITICAL REGION OF STRAINING IN THE           A   18
      SPECIMEN.                                                             A   19
      B,BETA= BETA1,BETA2 IN EQUATION (5.11).                               A   20
      ET= LIMIT THICKNESS STRAINS FOR SPECIMENS TESTED IN A NON-            A   21
      UNIFORM STRAINING PROCESS.                                            A   22
      ET0= THICKNESS STRAINS AT THE REFERENCE POINT.                        A   23
      ETS= LIMIT THICKNESS STRAINS FOR SPECIMENS STRAINED UNIFORMLY.        A   24
                                                                            A   25
      DIMENSION RAN(2), ET0(200), ETS(200), ET(200)                         A   26
      DATA BETA/8./                                                         A   27
                                                                            A   28
      CONSTANTS.                                                            A   29
                                                                            A   30
      B=.14                                                                 A   31
      NS=50                                                                 A   32
      M=100.                                                                A   33
      TEST1=.0001                                                           A   34
      ARE=.01                                                               A   35
      AKK=.155                                                              A   36
      A=-.332                                                               A   37
      AK=AKK/.00003937                                                      A   38
                                                                            A   39
       CALCULATE THE PROBABILITY DENSITY OF FAILURE STRAINS IN ELEMENTAL    A   40
      AREAS.                                                                A   41
                                                                            A   42
    1 READ (5,15) ALAM,DEL,E01,E02,R0,RE,T0                                 A   43
      DE=(E02-E01)/100.                                                     A   44
      IF (ALAM.LT.0.) GO TO 14                                              A   45
      WRITE (6,19)                                                          A   46
      WRITE (6,16) ARE,ALAM,DEL,AKK,T0,A                                    A   47
      WRITE (6,17) R0,RE,BETA                                               A   48
      AN=DEL*ARE                                                            A   49
                                                                            A   50
```

```
      ALAMN=AK*ALAM*T0                                                  A   51
      WRITE (6,20)                                                      A   52
      GN1=0.                                                            A   53
      GNM=0.0                                                           A   54
      RF0=0.0                                                           A   55
      DO 3 I=1,M                                                        A   56
      E=FLOAT(I)*DE+E01                                                 A   57
      EN=EXP(E/A)                                                       A   58
      GN=G(EN,A,AN,ALAMN)                                               A   59
      GN2=GN                                                            A   60
      RF=(GN1+GN2)/2./FLOAT(M)                                          A   61
      RF0=RF0+RF                                                        A   62
      GN1=GN                                                            A   63
      IF (GNM.GT.GN) GO TO 2                                            A   64
      GNM=GN                                                            A   65
      EM=E                                                              A   66
    2 CONTINUE                                                          A   67
      D=AK*T0*EN                                                        A   68
      F=1.-D/T0*.00003937                                               A   69
      WRITE (6,21) E,D,F,GN,RF0                                         A   70
      CALL PLOTPT (E,GN,4)                                              A   71
    3 CONTINUE                                                          A   72
C                                                                       A   73
C     FIND UPPER  AND LOWER LIMITS FOR THE FREQUENCY DISTRIBUTION.      A   74
C                                                                       A   75
      AMAX=E02                                                          A   76
      AMIN=E01                                                          A   77
      WRITE (6,18) AMAX,AMIN                                            A   78
      WRITE (6,22) EM,GNM                                               A   79
      CALL OUTPLT                                                       A   80
C                                                                       A   81
C     TEST FOR SUITABLE UPPER AND LOWER LIMITS.                         A   82
C                                                                       A   83
      E=AMIN                                                            A   84
    4 CONTINUE                                                          A   85
      EN=EXP(E/A)                                                       A   86
      GN=G(EN,A,AN,ALAMN)                                               A   87
      H1=GN/GNM                                                         A   88
      IF (H1.LT.TEST1) GO TO 5                                          A   89
      E=E-DE                                                            A   90
      AMIN=E                                                            A   91
      GO TO 4                                                           A   92
    5 E=AMAX                                                            A   93
    6 CONTINUE                                                          A   94
      EN=EXP(E/A)                                                       A   95
      GN=G(EN,A,AN,ALAMN)                                               A   96
      H2=GN/GNM                                                         A   97
      IF (H2.LT.TEST1) GO TO 7                                          A   98
      E=E+DE                                                            A   99
      AMAX=E                                                            A  100
```

```
      GO TO 6                                                           A  101
7     CONTINUE                                                          A  102
      WRITE (6,18) AMAX,AMIN                                            A  103
C                                                                       A  104
CC    SIMULATION BEGINS.                                                A  105
C                                                                       A  106
      SID=SQRT(ARE)                                                     A  107
      CALL FRANON (RAN,2,26)                                            A  108
C                                                                       A  109
CC    FOR NS SPECIMENS.                                                 A  110
C                                                                       A  111
      WRITE (6,23)                                                      A  112
      DO 13 J=1,NS                                                      A  113
      ET0(J)=5.0                                                        A  114
      ETS(J)=5.                                                         A  115
      R=-SID/2.                                                         A  116
C                                                                       A  117
CC    FOR 1 SPECIMEN                                                    A  118
C                                                                       A  119
8     CONTINUE                                                          A  120
      R=R+SID                                                           A  121
      IF (R.GT.R0) GO TO 12                                             A  122
      RAP=(R/RE)**BETA                                                  A  123
C                                                                       A  124
CC    CALCULATE THE NUMBER OF ELEMENTAL AREAS IN A RING.                A  125
C                                                                       A  126
      AM=6.2832*R/SID                                                   A  127
      MM=AM                                                             A  128
C                                                                       A  129
CC    CALCULATE FAILURE STRAIN FOR ONE RING.                            A  130
C                                                                       A  131
      DO 11 JJ=1,MM                                                     A  132
9     CONTINUE                                                          A  133
      CALL FRANON (RAN,2,0)                                             A  134
      ET1=RAN(1)*(AMAX-AMIN)+AMIN                                       A  135
      EN=EXP(ET1/A)                                                     A  136
      GNE=G(EN,A,AN,ALAMN)                                              A  137
      ET2=GNM*RAN(2)                                                    A  138
      IF (ET2.GT.GNE) GO TO 9                                           A  139
      E0=(ET1-B*RAP)/(1.-RAP)                                           A  140
      IF (ET0(J).LT.E0) GO TO 10                                        A  141
      ET(J)=ET1                                                         A  142
      ET0(J)=E0                                                         A  143
10    CONTINUE                                                          A  144
      IF (ETS(J).GT.ET1) ETS(J)=ET1                                     A  145
11    CONTINUE                                                          A  146
      GO TO 8                                                           A  147
12    CONTINUE                                                          A  148
      WRITE (6,24) ET(J),ETS(J),ET0(J)                                  A  149
13    CONTINUE                                                          A  150
```

```
C
CCC   PLOT HISTOGRAMS AND FIND THE MEANS AND STANDARD DEVIATIONS.                A 151
C                                                                               A 152
CCCCC                                                                           A 153
CCCCC                                                                           A 154
CCCCC DISTRIBUTION OF LIMIT-STRAINS FOR SPECIMENS  TESTED IN A NON-             A 155
CCC   UNIFORM STRAINING PROCESS.                                                A 156
C                                                                               A 157
      CALL HIST (ET,NS,0,1,XA,SD)                                               A 158
      WRITE (6,25) XA,SD                                                        A 159
C                                                                               A 160
CCCC   DISTRIBUTION OF LIMIT-STRAINS  FOR SPECIMENS WHERE THERE IS NO           A 161
CCCC  STRAIN GRADIENT.                                                          A 162
C                                                                               A 163
      CALL HIST (ETS,NS,0,1,XA1,SD1)                                            A 164
      WRITE (6,26) XA1,SD1                                                      A 165
C                                                                               A 166
CCC   DISTRIBUION OF STRAINS AT THE REFERENCE POINT.                            A 167
C                                                                               A 168
      CALL HIST (ET0,NS,0,1,XA,SD)                                              A 169
      WRITE (6,25) XA,SD                                                        A 170
      GO TO 1                                                                   A 171
14    CONTINUE                                                                  A 172
      STOP                                                                      A 173
C                                                                               A 174
15    FORMAT (F10.2,F15.2,5F10.2)                                               A 175
16    FORMAT (3X,*  AREA=*,F12.4,*  LAMBDA=*,F12.4,*   DEN=*,F12.2,*   K      A 176
     1=*,F12.4,*   T0=*,F12.4,*   A=*,F12.4,//)                                A 177
17    FORMAT (2X,*  R0=*,F12.4,*   RE=*,F12.2,*  BETA=*,F10.2,//)              A 178
18    FORMAT (3X,*  AMAX=*,F12.6,*  AMIN=*,F12.6)                               A 179
19    FORMAT (1H1,*   DISTRIBUTION OF FAILURE STRAINS IN ELEMENTAL AREAS      A 180
     1*,//)                                                                     A 181
20    FORMAT (3X,*       ET       *,*    SIZE D    *,*        F       *,*      A 182
     1 *,*  FREQ.      *,*     CUM FREQ.  *,//)                                A 183
21    FORMAT (3X,5E15.6)                                                        A 184
22    FORMAT (3X,*  EM=*,F12.6,*   GNM=*,F12.6)                                 A 185
23    FORMAT (1H1,5X,*LIMIT STRAIN *,*  LEAST STRAIN  *,* STRAIN AT POLE      A 186
     1 *,//)                                                                    A 187
24    FORMAT (3X,3E16.8)                                                        A 188
25    FORMAT (3X,*  XA=*,F12.6,*  SD=*,F12.6)                                   A 189
26    FORMAT (3X,*  XA1=*,F12.6,*  SD1=*,F12.6)                                 A 190
      END                                                                       A 191-
```

```
      FUNCTION G (EN,A,AN,ALAMN)                                        B
C     TO CALCULATE THE PROBABILITY DENSITY OF LIMIT STRAINS FOR         B
C     ELEMENTAL AREAS.                                                  B
      ELAMN=1./EXP(ALAMN*EN)                                            B
      GN=AN*ALAMN*EN/A*ELAMN*(1.-ELAMN)**(AN-1.)                        B
      G=ABS(GN)                                                         B
      RETURN                                                            B
      END                                                               B
```

```
      SUBROUTINE HIST (X,N,M,MM,XA,SD)
C
C     SUBROUTINE TO CALCULATE THE AVERAGE AND STANDARD DEVIATION AND
C     PLOT HISTOGRAM FOR A GIVEN DISTRIBUTION.
C
C     DEFINITION
C     ----------
C
C     X= INPUT ARRAY WITH DIMENSION N .
C     M= NUMBER OF DESIRED INTERVALS FOR THE HISTOGRAM,
C     IF M=0 , M WILL BE AUTOMATICALLY CALCULATED
C     MM=0 FOR NO HISTOGRAM
C     M= 1 HISTOGRAM WILL BE PRINTED OUT.
C     XA= AVERAGE.
C     SD= STANDARD DEVIATION.
C
      DIMENSION X(1), A(30), ICOUNT(30), XIC(30), XCU(30)
      IF (M.NE.0) GO TO 1
      AN=N
      AK=1.+3.3*ALOG10(AN)
      M=AK
      M=M+1
    1 CONTINUE
      M1=M+1
C
C     AVERAGING
C
      XA=0.
      DO 2 I=1,N
      XA=XA+X(I)
    2 CONTINUE
      XA=XA/FLOAT(N)
C
C     CALCULATE STANDARD DEVIATION.
C
      SD=0.
      DO 3 I=1,N
      SD=SD+(X(I)-XA)*(X(I)-XA)
    3 CONTINUE
      SD=SQRT(SD/FLOAT(N-1))
      IF (MM.EQ.0) GO TO 15
      XMAX=X(1)
      XMIN=X(1)
      DO 4 I=2,N
      IF (XMAX.LT.X(I)) XMAX=X(I)
      IF (XMIN.GT.X(I)) XMIN=X(I)
    4 CONTINUE
C
C     CALCULATE THE NUMBER OF INTERVALS IN  THE HISTOGRAM.
C
```

```
      Y1=ALOG10(XMAX)
      IF (Y1.LT.0.) Y1=Y1-1.
      L1=Y1
      L2=L1
      L3=L2-1
      L1=XMAX*(10.**(1-L1))
      XMAX=L1
      L2=XMIN*(10.**(1-L2))
      XMIN=L2
      XMAX=XMAX+1.
      DX=(XMAX-XMIN)/FLOAT(M)
      XMAX=XMAX*10.**L3
      XMIN=XMIN*10.**L3
      DX=DX*10.**L3
      DO 5 I=1,M1
    5 A(I)=XMIN+DX*FLOAT(I-1)
      CONTINUE
C
C     SET UP HISTOGRAM.
C
      DO 6 I=1,M
      ICOUNT(I)=0
    6 CONTINUE
      DO 8 I=1,N
      DO 7 J=1,M
      IF (X(I).GT.A(J).AND.X(I).LT.A(J+1)) ICOUNT(J)=ICOUNT(J)+1
    7 CONTINUE
    8 CONTINUE
      ITEST=0
      DO 9 I=1,M
      ITEST=ITEST+ICOUNT(I)
      XIC(I)=ICOUNT(I)
    9 XIC(I)=XIC(I)/FLOAT(N)
      XCU(1)=XIC(1)-.5/FLOAT(N)
      DO 10 I=2,M
      XCU(I)=XCU(I-1)+XIC(I)
   10 CONTINUE
      WRITE (6,16) N,ITEST,DX
      WRITE (6,17)
      DO 11 I=1,M
      A(I)=A(I)+DX/2.
      WRITE (6,18) I,A(I),ICOUNT(I),XIC(I),XCU(I)
   11 CONTINUE
      DO 14 I=1,M
      XX=A(I)
      YY=XIC(I)
C
C     PLOT HISTOGRAM.
C
```

```
C
      CALL PLOTPT (XX,YY,4)                                                  CCCCCC 101
      Y2=0.0                                                                 CCCCCC 102
      J=1                                                                    CCCCCC 103
12    CONTINUE                                                               CCCCCC 104
      Y2=.01*FLOAT(J-1)                                                      CCCCCC 105
      IF (Y2.GT.XIC(I)) GO TO 13                                             CCCCCC 106
      J=J+1                                                                  CCCCCC 107
      CALL PLOTPT (XX,Y2,2)                                                  CCCCCC 108
      GO TO 12                                                               CCCCCC 109
13    CONTINUE                                                               CCCCCC 110
14    CONTINUE                                                               CCCCCC 111
      CALL OUTPLT                                                            CCCCCC 112
15    CONTINUE                                                               CCCCCC 113
      RETURN                                                                 CCCCCC 114
C                                                                            CCCCCC 115
16    FORMAT (1H1,3X,* N= *,I3,*   ITEST=*,I3,*  INCREMENT=*,F12.8,//)       CCCCCC 116
17    FORMAT (*    NO.    *,*    INT. *,*     FRE.   *,* REL.  FREQ.*,*  CU  CCCCCC 117
     1M. FREQ.*)                                                             CCCCCC 118
18    FORMAT (3X,I4,F12.8,3X,I4,5X,2F10.5)                                   CCCCCC 119
      END                                                                    CCCCCC 120
                                                                             C  121-
```

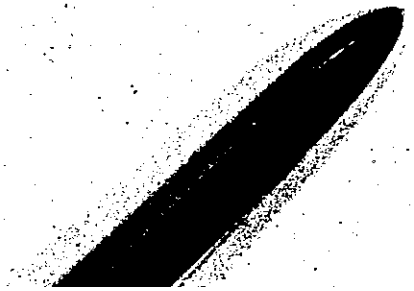

APPENDIX B2

Rejection Method in Monte-Carlo Simulation

The Monte-Carlo approach is one of the most powerful numerical techniques for obtaining the distribution of the general non-linear function of several random variables. In this technique, it is required to generate a set of random numbers from each of these variables. Such a set would represent a hypothetical sample of values for the variable. A histogram from this sample would approximate the original distribution. An illustrative example [5.16] for the theoretical sampling is given below.

Consider a manual technique in which the density distribution curve g(x) is divided into discrete intervals from 1 to M. The area under the curve in each interval gives the probability that x will occur in that interval. A set of N discs were made up so that if the probability of x occurring in the j^{th} interval is Pr_j, then the number of discs which are marked x_j is given by $(Pr_j \times N)$. A series of discs were drawn randomly from the whole set, using replacement. The number on the discs then are the derived set of variable x. A simple rejection technique can be used to select the number from the sample representing a given distribution density function. Let g(x) be the original distribution which has a maximum value of g_M. Two random numbers Ω_{1i} and Ω_{2i} are generated from a uniform distribution having a range from 0 to 1. The value of x is chosen as

$$x_i = \Omega_{1i} \text{ (Max - Min) + Min ,}$$

where Max and Min are the upper and lower bounds of x.

If $\Omega_{2i} \leq \frac{g(x_i)}{g_M}$ then x_i is accepted as a member of the sample.

APPENDIX B3

Effect of Sample Size and Size of Elemental Areas on Limit-Strains

The limit-strains obtained from the simulation process may depend on the size of the sample (of specimens) and also on the size of the elemental areas. To check this, the simulation process was applied to a larger sample size and then to smaller elemental areas, and the results were obtained as shown in Table B.3. It is observed that the difference in the results between these is not significant.

Table B.3

Effect of Sample Size and Size of Elemental Areas on Limit-Strains (For $\lambda=4$, $\delta=20{,}000/\text{in.}^2$, $r_e=3$ in. and $t_o = 0.035$ in.)

Sample Size N_S	Size of Elemental Area A (in.^2)	Mean Limit-Strain ε_t^*	Standard Deviation of ε_t^*
50	0.01	1.33	0.053
200	0.01	1.32	0.049
50	0.005	1.32	0.045